Nonadiabatic Quantum Dynamics of Carbon Chains and Fluorinated Phenol

A Thesis

Submitted for the Degree of

Doctor of Philosophy

By

Arpita Ghosh

SCHOOL OF CHEMISTRY

UNIVERSITY OF HYDERABAD

HYDERABAD 500 046

INDIA

March 2018

Dedicated

To
My Parents

STATEMENT

I hereby declare that the matter embodied in this thesis is the result of investigations carried out by me in the School of Chemistry, University of Hyderabad, Hyderabad, under the supervision of Prof. Susanta Mahapatra.

In keeping with the general practice of reporting scientific observations, due acknowledgment has been made whenever the work described is based on the findings of other investigators.

(Arpita Ghosh)

March 2018

Hyderabad-500046

School of Chemistry
University of Hyderabad
Hyderabad-500 046
India

CERTIFICATE

This is to certify that the thesis entitled "**Nonadiabatic Quantum Dynamics of Carbon Chains and Fluorinated Phenol**" submitted by **Arpita Ghosh (Reg.No. 12CHPH15)**, in partial fulfilment of the requirements for award of Doctor of Philosophy in the School of Chemistry is a bonafied work carried out by her under my supervision and guidance.

This thesis is free from plagiarism and has not been submitted previously in part or in full to this or any other University or Institution for award of any degree or diploma.

Parts of this thesis have been published in the following publications:

1. **Arpita Ghosh**, Samala Nagaprasad Reddy, S. Rajagopala Reddy, and S. Mahapatra*, J. Phys. Chem. A **120**, 7881 (2016), **Chap. 5**.
2. Karunamoy Rajak, **Arpita Ghosh** and S. Mahapatra*, J. Chem. Phys. **148**, 054301 (2018), **Chap. 6**.

and presented in following conferences :

1. Theoretical Chemistry Symposium (TCS-2014), 18-21 December, 2014, at CSIR - National Chemical Laboratory in association with Indian Institute of Sci-

ence Education and Research, Pune (National).

2. A Tributary Symposium on 100 Years of Chemical Bonding-2016, 4-5 August, 2016, at CSIR-Indian Institute of Chemical Technology, Hyderabad (National).

3. 15^{th} Indian Theoretical Chemistry Symposium (TCS-2016), 14-17 December, 2016, at University of Hyderabad, Hyderabad (National).

4. 8^{th} International Collaborative and Cooperative Chemistry Symposium, 18-19 December, 2017, at University of Hyderabad, Hyderabad (International).

Further, the student has passed the following courses towards fulfilment of coursework requirement for Ph.D.

Course code	Name	Credits	Pass/Fail
1. CY-801	Research Proposal	3	Pass
2. CY-802	Chemistry Pedagogy	3	Pass
3. CY-806	Instrumental Methods B	3	Pass
4. CY-822	Symmetry and Spectroscopy	4	Pass

Dean
School of Chemistry
University of Hyderabad

Prof. Susanta Mahapatra

Acknowledgement

First, I thank **Prof. Susanta Mahapatra** for giving me the opportunity to join his group and also for his guidance. I am really grateful for the patience and support that he has shown since I joined his group.

I thank my doctoral committee members, Prof. M. Durga Prasad and Prof. T. P. Radhakrishnan for their valuable suggestions and encouragements.

I am particularly grateful to Prof. Samudranil Pal and Ms. Sabari Ghosh for giving me the opportunity to work with them as it was an interesting experience for me.

I extend my sincere thanks to the former and present Deans, School of Chemistry, for providing all necessary facilities to carry out my research work. I also thank all the faculty members of School of Chemistry.

I thank Council of Scientific and Industrial Research (CSIR), New Delhi for financial support and Center for Modelling Simulation and Design (CMSD) for computational facilities.

I thank my former and present group members, Dr. T. Rajagopal Rao, Dr. S. Rajagopal Reddy, Dr. S. Nagaprasad Reddy, Dr. Karunamoy Rajak, Dr. Tanmoy Roy, Dr. Satyendra Gupta, Dr. Rudraditya Sarkar, Dr. Sugata Goswami, Dr. N. Krishna Reddy, Arun, Jayakrushna, Daradi, Nitai, Jhansi, Ranita and Soubhik for the great and stimulating atmosphere in the group.

I am grateful to Tulikadi, Subratada, Sanghamitradi, Pramitidi, Lalithadi for their help and support in my initial days in hyderabad.

I feel lucky to be surrounded by few wonderful persons during my Ph.D time. I thank Debparna, Sabari, Sneha, Tasnim, Suchana and Meena for their warm company on various occasions that will remain forever in my memory.

I consider myself fortunate to have a friend like Dr. Debparna Datta. My heartfelt thanks to her for all her support and guidance regarding various matters during my Ph.D days.

I thank all my friends of this school with a very special thanks to Srujana, Navendu and Sudipta for helping me in many ways.

Finally, I thank my parents, my husband and all my family members for their love, care and unconditional support.

(**Arpita Ghosh**)

List of Abbreviations

aug-cc-pVDZ	augmented correlation-consistent polarized Valence Double-ζ
aug-cc-pVTZ	augmented correlation-consistent polarized Valence Triple-ζ
ADT	Adiabatic to Diabatic Transformation
BO	Born-Oppenheimer
B3LYP	Becke 3-Parameter (exchange), Lee, Yang and Parr
Bz	Benzene
CASSCF	Complete Active Space Self Consistent Field
CAM-B3LYP	Coulomb-attenuating method-Becke 3-Parameter (exchange), Lee, Yang and Parr
CIs	Conical Intersections
cc-pVDZ	correlation-consistent polarized Valence Double-ζ
CRDs	Cavity Ringdown Spectroscopy
DFT	Density Functional Theory
DIBs	Diffuse Interstellar Bands
DOF	Degrees of Freedom
DVR	Discrete Variable Representation
EOM-CCSD	Equation of Motion-Coupled Cluster Singles and Doubles
FC	Franck-Condon
FWHM	Full Width at the Half Maximum
GIs	Glancing Intersections
HFBz	Hexafluorobenzene
HO	Harmonic oscillator
HOMO	Highest Occupied Molecular Orbital

Continued in next page

– continued from previous page

IREP	Irreducible Representation
ISM	Interstellar Medium
JT	Jahn-Teller
LIF	Laser-Induced Fluorescence
LVC	Linear Vibronic Coupling
MCTDH	Multi-Configuration Time-Dependent Hartree
MO	Molecular Orbital
MP2	Møller-Plesset Perturbation Theory
MRCI	Multi-Reference Configuration Interaction
MIS	Matrix Isolation Spectroscopy
MFBz	Metafluorobenzene
o-DFBz	Orthodifluorobenzene
PAHs	Polycyclic Aromatic Hydrocarbons
PESs	Potential Energy Surfaces
PFP	Pentafluorophenol
PJT	Pseudo-Jahn-Teller
PRT	Pseudo-Renner-Teller
PANH	Nitrogenated PAH molecule
QVC	Quadratic Vibronic Coupling
RT	Renner Teller
REMPI	Resonance Enhanced Multiphoton Ionization
REMPD	Resonance Enhanced Multiphoton Dissociation Spectroscopy
R2C2PI	Resonant Two-Color Two-Photon Ionization
SPFs	Single Particle Functions

Continued in next page

– **continued from previous page**

SCF	Self Consistent Field
TDDFT	Time-Dependent Density Functional Theory
TFBz	Trifluorobenzene
VC	Vibronic Voupling
VIEs	Vertical Ionization Energies
VEEs	Vertical Excitation Energies
VUV	Vacuum Ultraviolet
WP	Wave Packet

Contents

Chapter 1

Introduction

Study of nuclear motion on coupled multi-sheeted electronic potential energy surfaces (PESs) is a growing field of research in chemical dynamics. The study encompasses a wide variety of physico-chemical process like photochemistry, collisions dynamics of electronically excited species, chemiluminescence excited state processes like radiationless decay, energy and charge transfer and recombination reactions, heterocyclic dissociations, and electron transfer processes etc. to a name few. Understanding of coupling between the electronic states and the associated nonadiabatic effects is important in these investigations. On the dynamical front much of the challenge lies in monitoring nuclear motion on multiple electronic states concurrently from first principle. The adiabatic **Born-Oppenheimer (BO) approximation** [1–4], breaks down in this situation, which represents one of the cornerstones of molecular physics and chemistry. Within the BO approximation electronic motion and nuclear motion are treated separately i.e. they are independent to each other. According to this approximation, the calculation of dynamical processes in molecules can be divided into two steps. The *first step* involves the solution of the electronic Schrödinger equa-

tion by keeping the nuclei fixed in space, which gives adiabatic potential energy surfaces corresponding to the different electronic states. While in the *second step* the treatment of nuclear motion on the calculated electronic potential-energy surface (PES) is performed. Mainly this approximation is based on the fact that the spacing of electronic states is generally large. Also the electrons with much lighter mass move very fast as compared to the nuclei (a factor of 10^3 heavier) and therefore a small displacement in nuclear coordinate is quickly adjusted by the electrons completing a cycle of their motion. Therefore, it can be assumed that every instantaneous position (fixed) of the nuclei corresponds to a stationary electronic state and the average field of electrons governs the nuclear motion which is confined to a single adiabatic potential energy surface in the space of nuclear coordinate.

The BO approximation remains no longer valid when two or more electronic states becomes very close in energy i.e when the electronic states are degenerate. In this situation the electronic states change its character rapidly as a function of the nuclear geometry and it becomes necessary to go beyond the single surface approximation or in other words to consider the coupling between electronic and vibrational motion, which is neglected within the BO approximation. This coupling between vibrational and electronic motions is termed as **vibronic coupling (VC)**. It is mentioned that solving for the nuclear-electronic eigenstates variationally using the Hamiltonian for all the electrons and nuclei is computationally limiting. A practical way is to use a vibronic model Hamiltonian, which approximately describes the simultaneous nuclear dynamics on multiple potential energy surfaces and represents a nonadiabatic dynamical situation.

VC has great importance in molecular spectroscopy and it is ubiquitous in polyatomic molecular systems where there are large number of energetically close-

lying electronic states and many nuclear degrees of freedom (DOF) present. To name a few, VC covers a wide range in molecular spectroscopy, in particular, optical absorption and photoelectron spectroscopy. Vibronic coupling determines the splitting of degenerate electronic states. Nonadiabatic radiationless transitions between the states occur through vibronic coupling which are very important in photophysics and photochemistry.

The most significant deviations from the adiabatic BO approximation are the orbitally degenerate electronic states in polyatomic molecules. There are two different types of degeneracies observed depending on the dependence of electronic energy on the nuclear coordinate near their vicinity. When two electronic states cross and it forms a double cone topography, known as *Conical Intersections* (CIs). In other case, where two states do not cross but coincide and results a glancing topography which leads to *Renner effect or RT coupling*. Electronic degeneracies in molecules mostly yield CIs. Point group symmetry allows a classification of different types of CIs, the RT case is unique for the degenerate electronic states of linear polyatomic molecules with axial symmetry.

To discuss about *conical intersection* in detail one has to start from the noncrossing rule of Wigner and von Neumann [5], which showed that PESs of diatomic molecules do not cross unless the electronic states differ either in their symmetry or in their spin multiplicity. Minimum two nuclear DOF are required for two electronic states to be degenerate, when spin-orbit coupling is not taken into consideration. But for polyatomic molecules due to the presence of three or more nuclear DOF the noncrossing rule is not applicable. When two PESs of polyatomic molecules cross, a hyperline is formed in the vicinity of the crossing in the multidimensional nuclear coordinate space, known as conical intersections (CIs). CIs is a (3N-6-2)-dimensional seam of the electronic energy for an N-atom

molecule. In the early 1930s, CIs were reported [6–8] first. In 1934 Renner wrote about the nonadiabatic coupling in electronically excited states in CO_2 [6]. Teller in 1937 [7] showed that CIs are very important for the nonradiative decay in photochemical reaction, without performing any quantum dynamical simulation. He discussed the possibility that one can 'get a transition in a short time' by internal conversion via a CI. Moreover, in a semi-classical framework Landau [9] and Zener [10] quantified the fast radiationless decay that occur at CI. The first quantum dynamics simulation of internal conversion via conical intersection was carried out by Köppel et al. [11], demonstrating the internal deactivation on the sub-100-fs time scale. Since then, CIs are known to provide the important ultrafast mechanism for many photo-chemical reactions [12]. The identification and characterization of CIs were studied extensively by Teller [6], Herzberg and Longuet-Higgins [13]. They provide a deep insights into the subject predicting a variety of physical phenomena that emerge from PES crossing. The field has undergone an immense growth thereafter following the outstanding contributions of several research groups [3, 4, 14–16].

It is widely accepted that CIs serve as the *bottleneck* in photophysical and photochemical transitions [17, 18] and also referred to as photochemical funnels in the literature [19]. The book edited by Domcke, Yarkony and Köppel represents an excellent collection of articles in this emerging area of chemical dynamics [12, 20]. Strictly speaking, with respect to the mainstream computational chemistry which considers electronic structure calculations of polyatomic molecules with fixed nuclei and the nuclear dynamics along the adiabatic PESs, the CIs and the associated Jahn Teller (JT) and Pseudo Jahn Teller (PJT) vibronic coupling effects are important extensions which take into account the coupling between the electronic and nuclear motions.

The CIs of electronic PESs are classified into different groups depending on few factors which are as follows:

a) based on their electronic state symmetry : the noncrossing rule,

b) by topography and

c) by dimension of the branching space.

Molecular point group symmetry plays a very crucial role for the existence of CIs. Based on this molecular symmetry the CIs of electronic PESs are classified into as follows: i) symmetry required or symmetry enforced, ii) accidental symmetry allowed and iii) accidental same-symmetry intersections. Symmetry required (or enforced) CIs occur when two electronic states form the components of a degenerate irreducible representation(IREP). JT systems exhibit this type of CIs. For example, a doubly degenerate E electronic state in D_{3h} symmetry configuration splits into A_1 and B_2 when distorted to C_{2v} and forms CIs at the original undistorted D_{3h} configuration. Conical intersections which does not require symmetry are called accidental intersection. Accidental intersection which corresponds to two states of distinct spatial symmetry is known as accidental symmetry-allowed (different symmetry) CI. The two lowest excited singlet electronic states (A'') of $H-S-H$, generates this type of CI. For C_{2v} point group symmetry allowed accidental CI occurs as these electronic states are of $^1A_2$ and $^1B_1$ symmetry. Similarly, PESs of two states of same symmetry cross, the intersection is known as accidental same symmetry CI. An intersection of electronically excited electronic states (2^1A and 3^1A) of methyl mercaptan (CH_3-S-H) gives an example of this type of CI. [12, 20].

Based on the shape and orientation of the PESs, CIs are categorized as peaked and sloped CI [12, 21]. Peaked CIs originate when both the PESs are elliptical cones pointing towards each other with a common tip. In this case, the crossing

point is the minimum of the upper PES and the topology at this point looks like a double cone. At slopped CIs, both the PESs have downhill slope and touch each other at the crossing point in branching space. Here, the crossing point is always at higher energies compared to the minimum of the upper PES and the crossing appear as a seam of intersections. A large variety of photochemical reactions via excited-state reaction pathways are controlled by peaked CIs. Ring-opening and ring-closure reactions, hydrogen transfer reactions and $cis - trans$ isomerization are the standard photochemical reactions mediated via peaked CIs [12, 21]. The sloped CIs are the key factor for the unsuccessful chemical reactions and arrange decay channels for the ultrafast nonradiative deactivation of excited states [12,21].

Seams of the CI can also be categorized based on the dimension of the branching space, η, for intersection of two PESs with $\eta = 2$, 3 or 5 [22]. Among them $\eta = 2$ is the most common case of a two state CI for even electronic molecular system in a non-relativistic situation.

The first evidence of CIs came from the JT active systems [7]. In 1937, Jahn and Teller formulated the idea of instability and spontaneous distortion of the nuclear configuration of a nonlinear molecule in an orbitally degenerate electronic state (Γ) along the nontotally symmetric vibrational modes [8, 23]. This unique VC is known as the Jahn-Teller (JT) effect. It has great impact in complex electronic spectra of symmetric molecules. In the presence of the JT effect, the electrons do not follow the motions of the nuclei adiabatically and the nuclear states are determined by the averaged field of the electron as well as by the details of the electronic structure and their changes with nuclear displacements. The symmetry of the nontotally symmetric mode (e) is such that it contains in the direct product of $\Gamma \otimes \Gamma$. This VC is called as $\Gamma \otimes e$ -JT coupling model. For example, the $(E \otimes e)$-JT effect, that is, perturbation

of a doubly degenerate electronic state (E) by a doubly degenerate vibrational mode (e), has been extensively studied for molecules with trigonal symmetry [3, 8, 23–27]. In tetragonal systems, the JT perturbation of an E state is caused by the nondegenerate vibrational modes of b symmetry, known as ($E \otimes b$) - JT effect.

If the energy levels do not cross at Q_i =0 but they are very closely spaced, the molecule is still unstable in the sense of Jahn and Teller, and the terminology used is pseudo-Jahn-Teller (PJT) effect. Pseudo-Renner-Teller (PRT) effect terminology is used in case of linear molecules. PJT or PRT effect is the interaction between the degenerate and nondegenerate electronic states in a molecule that is prone to JT or RT effect. In 1957, Opic and Price [28], observed structural distortions and splitting in systems with near (quasi-degenerate or pseudo-degenerate) electronic states. While the JT or RT effect is the source of instability in high symmetry configuration of any polyatomic molecules in degenerate electronic states, the PJT or PRT effect is the only source of instability and distortions of high-symmetry configurations of any polyatomic system in nondegenerate states [29, 30]. The (pseudo) Jahn-Teller vibronic coupling effect can be described by a model Hamilton operator H. This operator takes the form of a $n \times n$ matrix in the case of n-fold degeneracy.

In the simplest case of two-fold degeneracy, H becomes:

$$H = \begin{bmatrix} H_{11} & H_{12} \\ H_{12}^{*} & H_{22} \end{bmatrix}$$

where the diagonal elements correspond to the electronic states, and the non-diagonal elements give the coupling between the two states.

Both the JT and PJT effect have been studied extensively over the past

decades [4,14-15,21-24,31-33] Although most of the applications of the JT effect has been in the field of spectroscopy, stereochemistry, and structural phase transformations, the JT effect has played the role of guiding idea [34] in one of the most important (Nobel prize winning) discoveries of modern physics: high-temperature superconductivity. This effect is also found instrumental in understanding the chemical reactions mechanisms, the properties of fullerenes, and the recent discovery of the colossal magnetoresistance [24].

Linear molecules are the exceptions from the JT theorem but like nonlinear molecules linear molecules also experience a similar type of instabilities in their degenerate or pseudo-degenerate states when quadratic terms of VC are considered [35]. For linear molecules, the nontotally symmetric displacements are described as ungerade with respect to reflection, whereas the product of wave functions of the degenerate terms (coming from symmetry considerations) is always gerade with respect to the same symmetry operation. Consequently, all the linear $W_{km}(k \neq m)$ terms are zero, and only the quadratic terms could play a role. This VC in linear molecules is known as the *Renner-Teller (RT) coupling or glancing intersection(GI)*. The RT effect is one of the best characterized violation of the the BO approximation in molecular spectroscopy. In its simplest manifestation, this vibronic interactions occurs in linear triatomic molecules in orbitally degenerate Π electronic states, it is caused by a coupling between the electronic orbital angular momentum and the nuclear vibrational angular momentum associated with the bending vibration [36]. Upon bending the molecule an additional dipole moment is set up in the molecular plane which lifts the electronic degeneracy. The motion on both potential surfaces remains, however, coupled through a coriolis type interaction between vibrational and electronic angular momentum. This interaction behaves singularly at the linear configuration and leads to the

breakdown of adiabatic approximation. In 1933 Herzberg and Teller [37] recognized that the potential of a triatomic linear molecule in a degenerate electronic state splits into two when the molecule is bent. A year later this effect was worked out in detail by Rudolf Renner [6], who gave an explanation of this splitting phenomenon and showed that the bending and electronic motion are coupled. He predicted that this coupling would give rise to anomalies in the vibrational side bands of electronic spectra. Herzberg refers to this as the "Renner-Teller" effect in one of his influential books [38] and consequently the effect is now generally called after Renner and Teller.

Renner's original theory [6] was restricted to a perturbation treatment of the lowest order terms of the Hamiltonian of three-atomic molecules when expanded in a Taylor series around the linear configuration. Later, his work has been extended to include higher order terms of this expansion, [23,28] to allow for electron spin [24] and for the effect of molecular rotation [4], anharmonic coupling and Fermi Resonances [39] and for the effect of magnetic coupling [40] as well. Δ electronic states [14] and tetra-atomic molecules [15] have also been considered. Several interesting applications of the RT effect including processes like protonation, charge transfer, photodissociation, etc. suggest the importance of the RT effect in chemical and molecular physics. For a detailed overview of the RT effect, a review by Rosmus and Chambaud [41] is recomended.

In all the above cases perturbation theory is used. Among the nonperturbative, i.e numeric approaches, the reader is directed to the works of Barrow et al. [42] and Jungen et al. [43]. All the above mentioned works successfully explained the interactions in an isolated doublet Π or Δ electronic state of many triatomic molecules. The perturbative methods known to fail when the respective nonadiabatic coupling is strong enough. Moreover, the interaction between

different electronic states is not accounted in these approaches. The quadratic vibronic coupling (QVC) approach developed by Köppel, Domcke and Cederbaum appears to provide a systematic way to understand the multimode dynamics in linear polyatomic molecules [44]. The RT effect was not observed until 1959, when K. Dressler and D. A. Ramsay [45] measured the electronic absorption spectrum of NH_2 and ND_2 . They revealed that the first electronically excited states of these triatomic molecules have a linear geometry and observed in these excited states an unusual type of vibronic structure: the RT effect. Theoretical studies on VC effects in molecular systems have been exercised in the literature with improved level of sophistication [3,11]. The theoretical approach is generally based on the so-called linear vibronic coupling (LVC) scheme, often augmented by quadratic vibronic coupling terms [3,24–26]. This is based on the use of a diabatic electronic basis, where the potential energy matrix is expanded in a Taylor series in suitable displacement coordinates, and linear or quadratic terms are retained. The pertinent coupling constants and the nuclear motion are computed within an *ab initio* quantum dynamical scheme. Vibrational structures in various electronic spectra have been studied as time independent observables. Time dependent quantities of interest are often electronic populations in the interacting manifold of states. Strong nonadiabatic coupling manifest themselves typically in diffuse (under low resolution) or very irregular (under high resolution) spectral structures and in the sub-picosecond time scale of electronic population transfer, thus signaling internal conversion processes [3].

The concept of VC and the associated JT, RT, PJT and PRT coupling effects is of a much wider relevance, however, and applies to essentially all symmetric polyatomic molecular systems. The applications of VC theory cover the full range of molecular spectroscopy, including, in particular, optical absorption and

photoelectron spectroscopy. Typical spectroscopic phenomena associated with vibronic interactions are the appearance of nominally forbidden electronic bands, the excitation of nontotally symmetric modes, or unusual and complex vibronic fine structures of electronic spectra [3,22,46-47] Some consequences of vibronic coupling interactions in molecular spectroscopy are :

i) loss of mirror symmetry of absorption and emission bands,

ii) appearance of forbidden bands in absorption spectrum,

iii) odd quantum excitation of non-totally symmetric vibrational modes,

iv) irregular and complex vibronic structure,

v) broad and diffuse vibronic bands and

vi) low quantum yield or lack of fluorescence emission.

vii) fluorescence quenching

viii) large stoke's shift.

As the absorption or photoelectron spectroscopy probes the excited state within the FC region, these features become dominant when the CIs appear near or within the FC zone. These phenomena in a wide variety of molecular systems are successfully explained theoretically within a multi-state and multi-mode vibronic coupling approach. **In chapter 2** of this thesis a detailed theoretical framework of multistate multimode vibronic coupling scheme is given. The concept of adiabatic approximation and the necessity of a diabatic electronic basis to investigate the RT and PRT interactions in multimode molecular systems is discussed. The vibronic coupling involving degenerate vibrational modes and degenerate electronic states has also been discussed in details in this chapter. Construction of diabatic electronic Hamiltonian utilizing elementary symmetry selection rules is explained with few representative examples. The calculation of vibronic eigenvalue spectrum by a numerically exact solution of the time-independent Schrödinger equa-

tion with the help of Lanczos algorithm [48] is discussed. Finally, the calculation of complex vibronic spectra of molecules with large electronic and vibrational DOF by a time-dependent wave packet (WP) propagation approach within the multi-configuration time-dependent Hartree (MCTDH) scheme [49] is illustrated.

Linear carbon chains and diacetylene radical cation which are supposed to be important in interstellar medium (ISM), and proposed as a potential *diffuse interstellar bands (DIBs)* carrier are studied. These linear molecules are RT active as well. At the same time the photophysics of phenol and fluorine substituted phenol compound i.e pentafluorophenol is also studied here in order to examine the fluoroeffect in phenol, known as *perfluoro effect* in literature.

The diffuse interstellar bands (DIBs) are a set of ubiquitous absorption features observed in the optical region of the spectra of stars that lie beyond, and are viewed through, interstellar clouds. The DIBs have been observed in over a hundred sightlines within our Galaxy [49], in the magellanic Clouds [50] and at cosmological distances too [51]. The number of known DIBs is more than 500 [52, 53]. The term 'diffuse' differentiates between the somewhat hazy appearance of DIBs compared with the relative sharpness of atomic transitions in the interstellar medium. The breadth of the DIBs appears to be an intrinsic property which is not caused by the physical conditions in the clouds in which they arise. Because of that diffuse character, it is generally assumed that DIBs are caused by molecules; the fact that their measured wavelengths do not agree with any known atomic transitions tends to support that assumption. The constancy of the DIB central wavelengths and profiles in many different sightlines, and the fine structure observed in some DIBs, also suggest that the molecular carriers are in the gas phase. Heger was the first to observe the DIBs at 5780 and 5797 A^0 in 1919 at Lick observatory. Later, in the period of 1924-36, Merrill and coworkers at

Mount Wilson observatory extensively studied DIBs [54]. They showed that the DIBs are caused by absorbers that are in between the stars ('interstellar'), rather than in, or associated with, the stars themselves, and their central wavelengths were 'stationary' in the spectrum of a binary star whose stellar lines were periodically Doppler-shifted by the orbital motion of the binary. Despite a tremendous amount of effort in the intervening for decades (for reviews, see Herbig [55], Snow and McCall [56], Sarre [57]), very little is known about the carrier of DIBs. Not a single feature has been positively identified with laboratory spectra, although there have been some close calls. When the DIBs are ultimately identified, the inventory of interstellar molecules will probably become more than double, and open up a new window of interstellar chemistry. Furthermore, it is likely that the DIBs will prove to be a 'powerful multidimensional probe' of the physical conditions in the interstellar medium [56]. The identification of the DIBs carriers has often been referred to as the longest-standing unsolved mystery in all of spectroscopy. The spectra observed by the astronomers are compared with those recorded in the laboratory under the typical conditions of ISM [58, 59], which is a collision free environment. It was not possible to create such an environment in a laboratory until the recent past. Therefore, most of the studies relied on the laboratory experiment (matrix isolation spectroscopy (MIS), resonance-enhanced multiphoton dissociation spectroscopy (REMPD), photo dissociation of van der Walls complexes) in matrix environments [58–60]. Understandably, collision with the host matrix causes an energy shift and broadening of the spectral lines and no unambiguous identification of DIBs could be made with the aid of these experimental results obtained in matrices. In recent years, breakthrough developments in the gas phase measurements such as cavity ring down spectroscopy (CRDS), made it possible to provide complementary evidence of

interstellar observations [61–64]. In recent years, very high resolution spectrograph's on the world's most powerful telescopes have been used to observe and analyze DIBs.

Identification of the carriers of DIBs has become one of the classic astrophysical spectroscopic problems. Origin of the DIBs were long believed to be due to polycyclic aromatic hydrocarbons (PAHs) [65] and there was no definite understanding of the origin of the additional bands due to carbon-bearing molecules [66]. The gas phase spectral measurements in the laboratory with support from theoretical studies of nuclear dynamics offer valuable aid to the astronomers in unraveling the mystery of the DIBs. Recent work suggests that they are caused by PAHs, or, most likely, their cations, since PAH ions of all sizes, long carbon-chain molecules, and fullerenes, absorb in the visible and near infrared, and such molecules are expected to be ionized by the intense ultraviolet field present in much of the interstellar medium. PAH molecules appears to have profound implications in the physics, chemistry and biology of ISM. Recently nitrogenated PAH molecule (PANH) also found in astrophysical environment. The observed broad and diffuse vibronic band, ultrafast internal conversion rate of low-lying excited electronic state and lack of fluorescence are in favour of PAH hypothesis. The PAH cation is highly photostable than their neutral counterpart. Their formation, fragmentation and reactions with the small molecules are being studied both theoretically and experimentally [67–72] in recent years.

Douglas in his seminal paper, suggested that the bare carbon chains C_n , where n may lie in the range 5-15 [66] could show spectroscopic features consistent with the DIB observations as their electronic transitions take place in the visible region of the spectrum as the majority of the DIBs lying in the 400-800 nm region with a few others to the red and the spectrum gets broadened due

to intramolecular processes. The first spectroscopic detection of C_3 in comets in the year 1881 [73] triggered curiosity among the astronomers, chemists and physicists on the structure and spectroscopy of carbon chains. Maier et al. investigated the spectroscopy of linear carbon chains extensively with the aid of wide variety of spectroscopic techniques ranging from neon matrix studies, CRD, R2C2PI, laser-induced fluorescence (LIF), trapped ion photofragmentation, and electron photodetachment processes [74–77] and concluded that absorptions of the carbon chains comprising upto 12 atoms do not correspond to any of the stronger DIB features. The following criteria are furnished by Maier et al. for a species to be a potential DIB carrier, "(a) absorptions in the 400-800 nm range, (b) oscillator strength (f) values in the 1-10 range, and (c) an excited electronic-state lifetime longer than a few picoseconds so that intramolecular broadening would still be compatible with the typical half-widths of the narrower DIBs (i.e., a few wave numbers)"[10]. The longer chains with an odd number of carbon atoms of length 15, 17, 19 and 21 are expected to satisfy the first two criteria because their transitions are in the 400-800 nm range and their f values scale with the chain length. It remains to be seen by doing nuclear dynamics study, whether the excited electronic state of $^1\Sigma_u^+$ symmetry has a lifetime longer than a few picoseconds to satisfy the third condition listed above. Taking the mentioned facts into consideration the electronic structure and dynamics of C_{2n+1} (n=7-10) cluster are studied in **chapter 3 and 4** in an attempt to examine their potentiality as a DIB carrier.

Among many hydrocarbons, **diacetylene radical cation**, has been proposed to be a potential DIBs carrier. From several spectroscopic and dynamics study of the $^2\Pi$ electronic state of this radical cation it is proposed that these are relevant in plasma chemistry. Inspired by the recent debate on its astrophysical impor-

tance, in **chapter-5** a detailed investigation of vibronic interactions within and between the doubly degenerate two energetically lowest electronic states ($\widetilde{X}^2\Pi_g$ - $\widetilde{A}^2\Pi_u$) of diacetylene radical cation ($C_4H_2^{\cdot +}$) and their impact on the vibronic structure of each state is carried out theoretically. The spectroscopy of these two electronic states of $C_4H_2^{\cdot +}$ has been a subject of considerable interest and measured in laboratory by various groups.

The perfluoro effect in phenol is studied in **Chapter-6**. Fluorine atom substitution in the aromatic ring leads to a stabilization of the σ type of molecular orbitals (MO) which consist mostly the fluorine orbitals. This phenomenon is known as perfluoro effect in the literature. As a result the energetic minimum of the seam of various CIs and the equilibrium minimum of a state varies with fluorine substitution, causing a difference in its absorption and emission properties for both the cation, neutral hydrocarbons and its fluorinated hydrocarbons. It is established that along with vibronic coupling, perfluoro effect [78] also plays an important role on the dynamics of the low-lying excited electronic states of the fluorobenzene molecules. Spectroscopic [79, 80] and photophysical [81, 82] studies on fluorobenzene molecules have revealed that the features of the electronic absorption and emission bands and lifetimes of fluorescence emission strongly depends on the number of substituted fluorine atoms. For example, fluorobenzene, C_6F_n with $n \leq 4$ exhibit structured $S_1 \leftarrow S_0$ absorption band, large quantum yield and nanosecond lifetime of fluorescence. On the other hand, C_6F_n with $n = 5$ and 6 exhibit structureless $S_1 \leftarrow S_0$ absorption band, [79, 80] low quantum yield, [81, 82] picosecond and nanosecond lifetime of fluorescence emission. [83] Furthermore, a biexponential decay of fluorescence is observed for the latter molecules. [83] Experimental measurements of Philis et al. [81] revealed that a lowering of D_{6h} symmetry of benzene (Bz) by fluorine substitution leads

to the appearance of additional bands within 8.0 eV which do not have a Bz parentage. For example, apart from three singlet-singlet transitions analogous to the $B_{2u} \leftarrow A_{1g}, B_{1u} \leftarrow A_{1g}$ and $E_{1u} \leftarrow A_{1g}$ transitions in Bz, one additional band has been observed in metafluorobenzene (MFBz) and in orthodifluorobenzene (o-DFBz) in the region of the $^1B_{1u}$ band [81]. This band correlates with the 3s ($^1E_{1g}$) Rydberg state of Bz molecule [81]. Likewise, one additional band has been identified in PFBz and HFBz at $\sim$ 5.85 and $\sim$ 5.36 eV, respectively, and is designated as the unassigned C-band. [81] . There is no clear-cut understanding of the origin of the additional bands (when compared to benzene). It is already established from experimental studies [94, 95] that 1,3,5-trifluorobenzene radical cation (TFBz+) shows considerable emission in contrast to the parent benzene radical cation (Bz+) and as the number of fluorine substituent increases the absorption spectra of the neutral fluorinated benzenes becomes increasingly congested and the well resolved vibrational spectra of its parent compound is almost completely lost [78]. This highly diffuse and complex pattern of molecular electronic spectra indeed bears the signature of complex entanglement of electronic and nuclear motion and indicates the paramount importance of the nonadiabatic effects on the spectral envelope and energy relaxation process [4]. Although the electronic structure and spectroscopy of these highly symmetric molecules have been collected in several experimental and theoretical studies [79–83], at the same time this perfluoro effect is not studied in any reduced symmetric molecules. A theoretical investigation of these reduced molecules yet to be explored. It is known from the recent experimental studies that rich vibronic structure of phenol in its optical absorption spectra completely disappears in pentafluorophenol which tempted us to do some theoretical investigation in phenol and pentafluorophenol which is done **in chapter 6**.

The summarizing remarks and outlook are given in **chapter 7**.

References

[1] M. Born and R. Oppenheimer, Ann. Phys. 84, 457 (1927).

[2] C. J. Ballhausen and A. E. Hansen, Ann. Rev. Phys. Chem. 23, 15 (1972).

[3] H. Köppel, W. Domcke, and L. S. Cederbaum, Adv. Chem. Phys. 57, 59 (1984).

[4] G. Fisher, *Vibronic coupling*, Academic press, London (1984).

[5] J. von Neumann and E. P. Wigner, Physik. Z. 30, 467 (1929).

[6] R. Renner, Z. Phys. 92, 172 (1934).

[7] E. Teller, J. Phys. Chem. 41, 109 (1937).

[8] H. A. Jahn and E. Teller, Proc. Roy. Soc. London, Ser. A **161**, 220 (1937).

[9] L. D. Landau, Phys. Sov. Union 2 (1932) 46.

[10] C. Zener, Proc. Roy. Soc., (London) A 137 (1932) 696.

[11] H. Köppel, L. S. Cederbaum, W. Domcke, S. S. Shaik, Angew. Chem. Int. Ed. (1983), 22, 210.

[12] *Conical Intersections: Electronic Structure, Dynamics and Spectroscopy*, edited by W. Domcke, D. R. Yarkony, and H. Köppel (WorldScientific, Singapore, 2004).

[13] G. Herzberg and H. C. Longuet-Higgins, Discuss. Farad. Soc. 35, 77 (1963).

[14] I. B. Bersuker, Plenum Press, New York, 1984

[15] I. B. Bersuker and V. Z. Polinger, Springer-Verlag, Berlin, 1989.

[16] W. Domcke and G. Stock, Adv. Chem. Phys. 100, 1 (1997).

[17] F. Bernardi, M. Olivucci, and M. A. Robb, Chem. Soc. Rev. **25**, 321 (1996).

[18] Chem. Phys. **259**, 121-337 (2000).

[19] J. Michl and V. Bonacic-Koutecky, *Electronic Aspects of Organic Photochemistry* (Wiley, New York, 1990).

[20] *Conical Intersections: Theory, Computation and Experiment*, W. Domcke, D. R. Yarkony, H. Köppel, Eds., (World Scientific: Singapore, 2011).

[21] M. J. Paterson, M. A. Robb, L. Blancafort and A. D. DeBellis, J. Phys. Chem. A **109**, 7527 (2006).

[22] W. Domcke, D. R. Yarkony, Annu. Rev. Phys. Chem. *63*, 325 (2012).

[23] H. A. Jahn, Proc. R. Soc. London, Ser. A **164**, 117 (1938).

[24] I. B. Bersuker, *The Jahn-Teller Effect* (Cambridge University Press, 2006).

[25] H. Köppel, L.S. Cederbaum, and S. Mahapatra, *Theory of the JahnTeller Effect*, in *Handbook of high-resolution spectroscopy*, John Wiley & Sons, (2011).

[26] S. Mahapatra, Acc. Chem. Res. **42**, 1004 (2009).

[27] I. B. Bersuker and V. Z. Polinger, *Vibronic Interactions in Molecules and Crystals* (Springer-Verlag, Berlin, 1989).

[28] U. Öpik and M. H. L. Pryce, Proc. R. Soc. London, Ser. A **238**, 425 (1957).

[29] I. B. Bersuker, Chem. Rev. *113*, 1351, (2013).

[30] P. Garcia-Fernandez and I. B. Bersuker, Int, Jou, Quant, Chem, **112**, 3025 (2012).

[31] I. B. Bersuker, Chem. Rev. 101 (2001) 1067.

[32] Y. E. Perlin, M. Wagner (Eds.), The Dynamical Jahn-Teller Effect in Localized Systems, North-Holland, Amsterdam, 1984.

[33] T. A. Barckholtz, T. A. Miller, Int. Rev. Phys. Chem. 17 (1998) 435.

[34] J. G. Bednorz, K. A. Mller, Perovskite type oxides: The new approach to high-Tc superconductivity, in: Nobel Lectures, Physics 1981-1990, World Scientifc, Singapore, 1993.

[35] J. Jortner, M. Bixon; J. Chem. Phys. 88 (1988) 167

[36] H. L. Dai and R. W. Field, Molecular Dynamics and Spectroscopy by Stimulated Emission Pumping (World Scientific, Singapore, 1995).

[37] G. Herzberg and E. Teller, Z. Phys. Chem. B21, 410 (1933).

[38] G. Herzberg, Molecular Spectra and Molecular Structure Vol. III, Reprint Edition (Krieger, Malabar, 1991).

[39] C. F. Chang, Y. N. Chiu, J. Chem. Phys. 53 (1970) 2186.

[40] J. T. Hougen, J. P. Jesson, J. Chem. Phys. 38 (1963) 1524.

[41] P. Rosmus, G. Chambaud, The Renner-Teller effect and the role of electronically degenerate states in molecular ions, in: C. Y. Ng (Ed.), Photoionization and Photodetachment, Vol. 10A, World Scientifc, Singapore, 2000, Ch. 5.

[42] T. Barrow, R. N. Dixon and G. Duxbuty, Mol. Phys. *27*, 1217 (1974).

[43] Ch. Jungen and A. J. Merer, Mol. Phys. *40*, 95 (1980).

[44] H. Köppel, W. Domcke and L. S. Cederbaum, J. Chem. Phys. **74**, 2946 (1981).

[45] K. Dressler and D. A. Ramsay, Phil. Trans. Roy. Soc. 251A, 553 (1959).

[46] H. Köppel and W. Domcke, Encyclopedia of Computational Chemistry, Ed., P. V. R. Schleyer, Wiley: New York, 1998, P. 3166.

[47] J. Cullum and R. Willoughby, *Lanczos algorithms for large symmetric eigenvalue problems*, Birkhäuser, Boston (1985), Vols. I and II.

[48] G. A. Worth, M. H. Beck, A. Jäckle, and H. -D. Meyer, *The MCTDH Package*, Version 8.2, (2000), University of Heidelberg, Heidelberg, Germany. H. -D. Meyer, Version 8.3 (2002), Version 8.4 (2007). See http://mctdh.uni-hd.de.

[49] McCall BJ et al. Astrophys. J. 708, 16281638, 2010.

[50] Ehrenfreund P et al. Astrophys. J. 576, L117L120, 2002.

[51] Junkkarinen VT, Cohen RD, Beaver EA, Burbidge EM, Lyons RW, Madejski G. Astrophys.J. 614, 658670, 2004.

[52] Hobbs LM et al. Astrophys. J. 680, 12561270, 2008.

[53] Hobbs LM et al. Astrophys. J. 705, 3245, 2009

[54] Merrill PW. Astrophys. J. 83, 126128, 1936

[55] Herbig GH. Ann. Rev. Astron. Astrophys. 33, 1973, 1995.

[56] Snow TP, McCall BJ. Annu. Rev. Astron. Astrophys. 44, 367414, 2006.

[57] Sarre PJ. J. Mol. Spectrosc. 238, 110, 2006.

[58] Shida. T, Iwata. S J Am Chem Soc 95,3473-3483 (1973).

[59] Salama. F, eds (1999) Solid Interstellar Matter: The ISO Revolution (Sciences, France).

[60] Szczepanski. J, Vala. M, Talbi. D, Parisel. O, Ellinger. Y J Chem Phys 98,4494-4511 (1993).

[61] Bréchignac. P, Pino. T Astron Astrophys 343,L49-L52 (1999)

[62] Biennier. L, Salama. F, Allamandola. LJ, J.Chem.Phys 118:7863-7872 (2003).

[63] Zhao. L et al. J Phys Chem A 108,25-31 (2004).

[64] Sukhorukov. O et al. Chem Phys Lett 386,259-264 (2004)

[65] T. P. Snow, A. G. G. M. Tielens, 'The Diffuse Interstellar Bands' Klüwer Acad. (1995).

[66] A. E. Douglas, Nature, **269**, 130, (1977).

[67] T. Allain, E. Sedlmayr and S. Leach, Astrophys. Space. Sci. 224, 417 (1995).

[68] A. Goeres, Rev. Modern Astron. 6, 165 (1993).

[69] K. Schroeter, D. Schrder and H. Schwarz 103, 4174 (1999).

[70] T. Allain, S. Leach and E. Sedlmayr, Astron. Astrophys. 305, 602 (1996).

[71] G. Granucci, Y. Ellinger and P. Boissel, Chem. Phys. 191, 165 (1995).

[72] F. Jolibois, A. Klotz, F. X. Gada and C. Joblin, Astron. Astrophys. 444,629 (2005).

[73] W. Huggins, Proc. R. Soc. Landon **33**, 1 (1982); G. Herzberg, Astophys. J. **96**, 314 (1942).

[74] J. P. Maier Chem. Soc. Rev. **17**, 45, (1988).

[75] J. P. Maier Chem. Soc. Rev. **26**, 21, (1997).

[76] J. P. Maier J. Phys. Chem. A **102** 3462 (1998).

[77] E. B. Jochnowitz and J. P. Maier, Annu. Rev. Phys. Chem. **59**, 519 (2008).

[78] C. R. Brundle, M. B. Robin, and N. A. Kuebler, J. Am. Chem. Soc. **94**, 1466 (1972).

[79] M. B. Robin, *Higher Excited States of Polyatomic Molecules*, Vol. III (Academic, New York, 1975), and references therein.

[80] J. Philis, A. Bolovinos, G. Andritsopoulos, E. Pantos, and P. Tsekeris, J. Phys. B: At. Mol. Phys. **14**, 3621 (1981).

[81] D. Phillips, J. Chem. Phys. **46**, 4679 (1967).

[82] G. L. Loper, and E. K. C. Lee, Chem. Phys. Lett. **13**, 140 (1972).

[83] D. V. O'connor, M. Sumitani, J. M. Morris, and K. Yoshihara, Chem. Phys. Lett. **93**, 350 (1982).

Chapter 2

Theoretical methodology

2.1 Vibronic coupling in polyatomic molecules

2.1.1 Born-Oppenheimer adiabatic approximation

The time-independent Schrödinger equation describing the quantum chemistry and dynamics can be illustrated within the Born-Oppenheimer (BO) approximation in the following way.

$$\mathcal{H}(q,Q)\Psi(q,Q) = \mathcal{E}\Psi(q,Q) \tag{2.1}$$

where $H(q,Q)$, $\Psi(q,Q)$ and $\mathcal{E}$ are the molecular Hamiltonian, wavefunction and energy, respectively. The former two quantities depends collectively on the electronic, q and nuclear, Q coordinates. The molecular Hamiltonian (the operator symbol $\hat{}$ is omitted for simplicity) can be expressed as

$$\mathcal{H}(q,Q) = \mathcal{T}_{el}(q) + \mathcal{T}_N(Q) + \mathcal{U}(q,Q) \tag{2.2}$$

where $\mathcal{T}_{el}$ and $\mathcal{T}_N$ represents the electronic and nuclear kinetic energy operators, respectively. The potential energy term $\mathcal{U}(q,Q)$ consists of the total potential energy between the electrons and nuclei where all electron-electron, nuclei-nuclei repulsion energy and electron-nuclei attraction energy is included. The Hamiltonian in Eq. (2.2) does not allow a separation of variables q and Q due to the potential energy which corresponds to electron-nucleus attraction. As a consequence, the above Schrödinger equation (2.1) can not be solvable as is. To overcome this problem of nonseparability of electronic and nuclear motions, the approximation due to Born and Oppenheimer was remarkable which lead to the birth of quantum chemistry way back in 1927 [1]. Within this approximation one computes the electronic wavefunctions for a fixed position of the nuclei. This approximation is based on the fact that the nuclear mass is much heavier than the mass of electrons. As a result, the electrons can complete a cycle of their motion before the nuclei can rearrange to a new configuration. The fast moving electrons can readjust to the change in the nuclear configurations. Therefore, the electronic motion is treated first for several fixed nuclear configurations and the electronic potential thus generated provides the force field for the nuclear motion. While the electronic wavefunction and energy become parametrically dependent on nuclear coordinates the energy becomes a function of the latter [2, 3]. To illustrate further, in this approximation ($\mathcal{T}_N$ =0), the orthonormal electronic eigenfunctions $\psi_n(q;Q)$ and electronic energy $\mathcal{V}_n(Q)$ at a fixed nuclear position which are known as BO adiabatic electronic states and adiabatic PESs, respectively, are calculated by solving electronic Schrödinger equation

$$\mathcal{H}_{el}(q,Q)\psi_n(q;Q) = (\mathcal{T}_{el}(q) + \mathcal{U}(q,Q))\psi_n(q;Q) = \mathcal{V}_n(Q)\psi_n(q;Q) \tag{2.3}$$

The total molecular wavefunction within the adiabatic theorem can be expanded as a product of electronic eigenfunction ($\psi_n(q;Q)$) and nuclear eigenfunction ($\chi(Q)$) dependent only on the nuclear coordinates

$$\Psi_i(q,Q) = \sum_n \psi_n(q;Q)\chi_n(Q) \tag{2.4}$$

In principle, this expansion is exact, since the set $\psi_n(q;Q)$ is complete. The total Schrödinger equation can be expressed as

$$\left[\mathcal{H} - \mathcal{E}\right] \Psi_i(q,Q) = 0 \tag{2.5}$$

From the above equation one readily obtains the coupled differential equations for the expansion coefficients $\chi_n(Q)$. By inserting the expression for vibronic wavefunction $\Psi_i(q,Q)$ which is defined in Eq. (2.4), into Eq. (2.5) and left multiplying with $\psi_m^*(q,Q)$ and integrating over the electronic coordinates leads to

$$\left[\mathcal{T}_N(Q) + \mathcal{V}_n(Q) - \mathcal{E}\right] \chi_n(Q) = \sum_m \Lambda_{nm}(Q)\chi_m(Q) \tag{2.6}$$

where

$$\sum_m \Lambda_{nm}(Q) = -\int dq \psi_n^*(q;Q) \left[\mathcal{T}_N(Q), \psi_m(q;Q)\right] \tag{2.7}$$

The operator Λ_{nm}, is known as the nonadiabatic operator in the adiabatic electronic representation and it defines the coupling of electronic states n and m through the nuclear kinetic energy operator. The nuclear kinetic energy operator takes non-diagonal form in this representation due to coupling between electronic

states. The nonadiabatic operator coupling $\Lambda_{nm}(Q)$ decomposes as [2, 4]

$$\Lambda_{nm}(Q) = -\sum_i \frac{\hbar^2}{M_i} A^{(i)}_{nm}(Q) \frac{\partial}{\partial Q_i} - \sum_i \frac{\hbar^2}{2M_i} B^{(i)}_{nm}(Q) \tag{2.8}$$

where M_i are nuclear masses and

$$A^{(i)}_{nm}(Q) = \langle \psi_n(q;Q) | \nabla_i | \psi_m(q;Q) \rangle \tag{2.9}$$

and

$$B^{(i)}_{nm}(Q) = \langle \psi_n(q;Q) | \nabla_i^2 | \psi_m(q;Q) \rangle \tag{2.10}$$

represent the derivative coupling and scalar coupling, respectively. When Λ_{nm} in Eq. (2.6) is set to zero altogether, one arrives at the well known BO or adiabatic approximation [1, 3, 5]. The molecular wavefunction is given by

$$\Psi^{BO}_i(q,Q) = \sum_n \psi_n(q;Q) \chi^{BO}_{ni}(Q)$$

The electronic and nuclear eigen value equations are given by

$$\left[\mathcal{T}_{el}(q) + \mathcal{U}(q,Q) - \mathcal{V}_n(Q)\right] \psi_n(q;Q) = 0;$$
$$\left[\mathcal{T}_N(Q) + \mathcal{V}_n(Q) - \mathcal{E}\right] \chi^{BO}_{ni}(Q) = 0;$$

respectively.

2.1.2 Breakdown of BO approximation

The adiabatic approximation is a very useful approach, but it fails when the PESs of different electronic states are energetically close. In this case the elements of

the nonadiabatic coupling matrix Λ_{nm} become extremely large and significant. The large ratio of nuclear and electronic mass is outweighted by the large derivative coupling $A^{(i)}_{nm}(Q)$ and the BO approximation remains no longer valid. The derivative coupling matrix elements diverge at the intersection region of the PESs according to Hellmann-Feynmann type of relation

$$A^{(i)}_{nm}(Q) = \frac{\langle\psi_m(q;Q)|\nabla_i\mathcal{H}_{el}(q;Q)|\psi_n(q;Q)\rangle}{\mathcal{V}_n(Q) - \mathcal{V}_m(Q)},$$

To know a bit details how the above form of $A^{(i)}_{nm}(Q)$ arises one should start from the electronic Schrödinger equation (Eq. 2.3),

$$\begin{aligned}\langle\psi_m(q;Q)|\mathcal{H}_{el}(q;Q)|\psi_n(q;Q)\rangle &= \langle\psi_m(q;Q)|\mathcal{V}_n(Q)|\psi_n(q;Q)\rangle \\ \langle\psi_m(q;Q)|\mathcal{H}_{el}(q;Q)|\psi_n(q;Q)\rangle &= \mathcal{V}_n(Q)\delta_{mn} \qquad (2.11)\end{aligned}$$

Differentiating the above equation (2.11) with respect to nuclear coordinate, Q we arrive at,

$$\begin{aligned}\frac{\partial}{\partial Q}[\langle\psi_m(q;Q)|\mathcal{H}_{el}(q;Q)|\psi_n(q;Q)\rangle] &= \frac{\partial\mathcal{V}_n(Q)}{\partial Q}\delta_{mn} \\ \langle\frac{\partial}{\partial Q}\psi_m|\mathcal{H}_{el}(q;Q)|\psi_n\rangle + \langle\psi_m|\frac{\partial\mathcal{H}_{el}(q;Q)}{\partial Q}|\psi_n\rangle + \langle\psi_m|\mathcal{H}_{el}(q;Q)|\frac{\partial}{\partial Q}\psi_n\rangle &= 0 \\ \mathcal{V}_n\langle\frac{\partial}{\partial Q}\psi_m|\psi_n\rangle + \langle\psi_m|\frac{\partial\mathcal{H}_{el}(q;Q)}{\partial Q}|\psi_n\rangle + \mathcal{V}_m\langle\psi_m|\frac{\partial}{\partial Q}\psi_n\rangle &= 0 \qquad (2.12)\end{aligned}$$

Electronic eigenfunctions, ψ_m and ψ_n are orthogonal to each other,

$$\langle\psi_m|\psi_n\rangle = 0 \qquad (2.13)$$

Differentiating Eq. (2.13) with respect to Q, we get

$$\begin{aligned} \langle\psi_m|\frac{\partial\psi_n}{\partial Q}\rangle + \langle\frac{\partial\psi_m}{\partial Q}|\psi_n\rangle &= 0 \\ \langle\frac{\partial\psi_m}{\partial Q}|\psi_n\rangle &= -\langle\psi_m|\frac{\partial\psi_n}{\partial Q}\rangle \end{aligned} \tag{2.14}$$

Substituting Eq. ((2.14) in Eq. (2.12), we reach to an equation like this,

$$\begin{aligned} -\mathcal{V}_n\langle\psi_m|\frac{\partial\psi_n}{\partial Q}\rangle + \mathcal{V}_m\langle\psi_m|\frac{\partial\psi_n}{\partial Q}\rangle + \langle\psi_m|\frac{\partial\mathcal{H}_{el}(q;Q)}{\partial Q}|\psi_n\rangle = 0 \\ \langle\psi_m|\frac{\partial\mathcal{H}_{el}(q;Q)}{\partial Q}|\psi_n\rangle + (\mathcal{V}_m - \mathcal{V}_n)\langle\psi_m|\frac{\partial\psi_n}{\partial Q}\rangle = 0 \\ \langle\psi_m|\frac{\partial}{\partial Q}|\psi_n\rangle = \frac{1}{(\mathcal{V}_n - \mathcal{V}_m)}\langle\psi_m|\frac{\partial\mathcal{H}_{el}(q,Q)}{\partial Q}|\psi_n\rangle \end{aligned} \tag{2.15}$$

From Eq. (2.15), $A^{(i)}_{nm}(Q)$ can be expressed as [2, 6, 7]

$$A^{(i)}_{nm}(Q) = \frac{\langle\psi_m(q;Q)|\nabla_i\mathcal{H}_{el}(q;Q)|\psi_n(q;Q)\rangle}{\mathcal{V}_n(Q) - \mathcal{V}_m(Q)}, \tag{2.16}$$

where $\mathcal{H}_{el}$ represents the electronic Hamiltonian for fixed nuclear configuration. When the two surfaces $\mathcal{V}_n(Q)$ and $\mathcal{V}_m(Q)$ become degenerate, the derivative coupling elements of Eq. (2.16) exhibit a singularity. This results discontinuity in both the electronic wavefunction and the derivative of energy at the point of degeneracy and making the adiabatic representation unsuitable for the nuclear dynamics study. The derivative coupling, $A^{(i)}_{nm}(Q)$, becomes extremely large at near-degeneracy or at degeneracy of different electronic PESs eventually breaking down the BO approximation. Typical phenomena associated with a violation of the BO approximation are inelastic atom-atom collisions and the radiationless decay of excited electronic states [7, 8]. To solve this singularity problem in the derivative coupling operator, the adiabatic basis functions are replaced by

smooth, slowly varying functions of nuclear coordinates and correspond to potential energy surfaces which may cross at the avoided crossings of adiabatic PESs. These functions are called as diabatic basis [2, 9–12].

2.1.3 Adiabatic to diabatic Transformation

The concept of diabatic electronic representation was introduced to solve the singularity problem of the adiabatic electronic representation [9–11]. By a suitable unitary transformation the diverging kinetic energy couplings of the adiabatic representation transform to smooth potential energy couplings in a diabatic representation. This results into a diagonal form for the nuclear kinetic energy operator and the coupling between the electronic states is described by the off-diagonal elements of the potential energy operator. In this representation the coupled equations of motion (as compared to Eq. 2.6) is,

$$\left[\mathcal{T}_N(Q) + \mathcal{U}_{nn}(Q)\right] \chi_n(Q) = \sum_{m \neq n} U_{nm}(Q) \chi_m(Q), \tag{2.17}$$

where $\mathcal{U}_{nn}(Q)$ are the diabatic PESs and $\mathcal{U}_{nm}(Q)$ are their coupling elements. The latter are given by

$$\sum_m U_{nm}(Q) = \int dq \phi_n^*(q;Q) \left[\mathcal{T}_{el} + \mathcal{V}(Q)\right] \phi_m(q;Q) \tag{2.18}$$

where $\phi(q;Q)$ represents the diabatic electronic wavefunction constructed from the corresponding adiabatic $\psi(q;Q)$ ones via a suitable unitary transformation,

$$\phi(q;Q) = \mathbf{S}(Q)\ \psi(q;Q), \tag{2.19}$$

$\mathbf{S}(Q)$ is the transformation matrix which reads as

$$\mathbf{S}(Q) = \begin{pmatrix} \cos\theta(Q) & \sin\theta(Q) \\ -\sin\theta(Q) & \cos\theta(Q) \end{pmatrix}. \tag{2.20}$$

The matrix $\mathbf{S}(Q)$ is called the adiabatic-to-diabatic transformation (ADT) matrix and $\theta(Q)$ defines the transformation angle. The required condition for such transformation is that the first-order derivative couplings of Eq. (2.9) vanishes in the new representation for all nuclear coordinates [13, 14] i.e.,

$$\int dq \psi_n^*(q;Q) \frac{\partial}{\partial Q_i} \psi_m(q;Q) = 0. \tag{2.21}$$

This requirement yields the following differential equations for the transformation matrix [13, 15, 16]

$$\frac{\partial \mathbf{S}}{\partial Q_i} + \mathbf{A^{(i)}}\mathbf{S} = 0, \tag{2.22}$$

where the elements of the first-order derivative coupling matrix $\mathbf{A^{(i)}}$ are given by Eq. (2.9). A unique solution of the above equation can be obtained only when starting from a finite subspace of electronic states [14]. Therefore, for polyatomic molecular systems rigorous diabatic electronic states do not exist [14]. Approximate schemes are therefore developed to construct diabatic electronic states [15, 17, 18]. The concept of diabatic electronic basis was introduced quite early in the literature in the context of describing the electron-nuclear coupling in atomic collision processes [9] as well as in molecular spectroscopy [19] . However, construction of the latter for polyatomic molecular systems is a tedious and difficult since it is a problem depending on multi-coordinates rather than a single nuclear coordinate. Therefore, various approximate mathematical schemes have been proposed in the literature [13, 14, 17, 18, 20–23] to accomplish this task.

2.1.4 The model diabatic vibronic Hamiltonian

A diabatic electronic basis is used for all the theoretical studies which are presented in this thesis. The diabatic basis results a diagonal form of nuclear kinetic energy operator and the coupling between the electronic states is described by the off-diagonal elements of the potential energy operator. The PESs are smooth, crossing curves in diabatic basis in contrast to the adiabatic basis where PESs are non crossing and exhibit a discontinuity at the avoided crossing. The vibronic Hamiltonian of the final states of the excited species is constructed in terms of the dimensionless normal coordinates of the electronic ground state of the corresponding (reference) neutral species.

Following the traditional approach [3, 19, 24, 25], normal coordinates [26] are introduced to describe the small amplitude vibrations around the equilibrium geometry of the electronic ground state (we assume here that we are dealing with a closed-shell molecule with a well-define structure). The normal coordinates are defined by

$$Q = L^{-1}\delta R \tag{2.23}$$

where δR is the 3N – 6 (3N – 5 for linear molecules) dimensional vector of internal displacement coordinates (changes of bond lengths and bond angles) for an N atomic molecule and L is the L-matrix of the well-known Wilson FG-matrix method [26]. It is convenient to introduce dimensionless normal coordinates Q_i via the mass-weighted normal coordinates (q_i) which are obtained by diagonalizing the force field, are converted into the dimensionless form [26] by

$$Q_i = (\omega_i/\hbar)^{\frac{1}{2}} q_i, \tag{2.24}$$

where ω_i is the harmonic frequency of the i^{th} vibrational mode. These actually describes the normal displacement coordinates from the equilibrium configuration, $\mathbf{Q} = 0$, of the reference state.

Let us assume that a diabatic basis has been obtained for a given set of vibronically interacting electronic states n and m. In this basis the vibronic matrix Hamiltonian which describes the photoinduced molecular processes is given by [2],

$$\mathcal{H} = (\mathcal{T}_{\mathcal{N}} + \mathcal{V}_0)\mathbf{1}_n + \mathcal{W}(Q). \tag{2.25}$$

In the *harmonic approximation*, which implies the expansion of the unperturbed reference electronic ground state potential energy up to second order in the displacements as well as the approximation of the metric tensor by its value at the equilibrium geometry, the kinetic-energy $\mathcal{T}_{\mathcal{N}}$ and potential-energy $\mathcal{V}_0$ operators of the electronic ground state take the simple form

$$\mathcal{T}_{\mathcal{N}} = -\frac{1}{2}\sum_i \omega_i \left[\frac{\partial^2}{\partial Q_i^2}\right], \tag{2.26}$$

and

$$\mathcal{V}_0 = \frac{1}{2}\sum_i \omega_i Q_i^2, \tag{2.27}$$

respectively. The quantity $\mathbf{1}_n$ is a $(n \times n)$ (where n is the number of final electronic states) unit matrix and $\mathcal{W}$ in Eq. (2.25) describes the change in the electronic energy upon ionization/excitation. This is a $(n \times n)$ non-diagonal matrix.

The matrix elements of the potential matrix $\mathcal{W}(Q)$ is,

$$W_{nm}(Q) = \int dq \phi_n^*(q;Q) H_{el} \phi_m(q;Q). \tag{2.28}$$

The $\phi_n(q;Q)$ are the diabatic wave functions for an electronic state of index n. For a polyatomic molecule, the accurate solution of the matrix Hamiltonian (Eq. 2.25) is very tedious and often impossible. Therefore, an approximate form of the matrix Hamiltonian is commonly considered for which the Schrödinger equation can be accurately solved. The simplest, yet elegant approximation is to expand the potential-energy matrix $\mathcal{W}(Q)$ about a reference nuclear configuration Q_0 and retaining the terms linear in Q for the off-diagonal terms is known as **linear vibronic coupling (LVC)** scheme [2,27]. The linear approximation is often sufficient since the elements of the $\mathcal{W}(Q)$ matrix are, by definition, slowly varying functions of Q. Without any loss of generality it is assumed that the diabatic and adiabatic states are identical at the reference geometry Q_0.

For the interacting electronic states n and m, the elements of the matrix Hamiltonian in the linear approximation are,

$$H_{nn} = \mathcal{T}_{\mathcal{N}} + \mathcal{V}_0(Q) + E_n + \sum_s \kappa_s^{(n)} Q_s. \tag{2.29}$$

$$H_{nm} = H_{nm}(0) + \sum_c \lambda_c^{(n,m)} Q_c. \tag{2.30}$$

The energies E_n which appear in the diagonal of H are constants given by $W_{nn}(Q_0)$. The $\kappa_s^{(n)}$ represent the gradients of the excited state potential functions at the equilibrium geometry of the ground state and are referred to as first-order intra-state electronic-vibrational coupling constants. The $H_{nm}(0)$ is zero if the two interacting electronic states n and m, are transformed according to different irreducible representations. The $\lambda_c^{(n,m)}$ are correspondingly called first-order

interstate coupling constants.

$$k_s^{(n)} = \left.\frac{\partial V_n(Q)}{\partial Q_s}\right|_{Q_0} \tag{2.31}$$

$$\lambda_c^{(n,m)} = \left.\frac{\partial V_{nm}(Q)}{\partial Q_c}\right|_{Q_0} \tag{2.32}$$

The non-vanishing interstate coupling constants λ_c are the product of the irreducible representations of electronic states ϕ_n and ϕ_m, and of the nuclear coordinate Q_c which contains the totally symmetric representation Γ_A , i.e. ,

$$\Gamma_n \times \Gamma_{Q_c} \times \Gamma_m \supset \Gamma_A. \tag{2.33}$$

where Γ_m, Γ_n and Γ_{Q_c} refer to the IREPs of the electronic states m, n and the c^{th} vibrational mode, respectively [2]. The analogous condition for the intrastate coupling constants κ_s^n is

$$\Gamma_n \times \Gamma_{Q_s} \times \Gamma_n \supset \Gamma_A. \tag{2.34}$$

Certainly all totally symmetric modes can couple to the electronic motion which emphasize the important role of these modes in the VC problem. From the above symmetry selection rules (Eqs. 2.33 and 2.34), it can be said that only the totally symmetric modes give rise to nonzero intrastate coupling constants and only nontotally symmetric modes to nonzero interstate coupling constants.

2.1.5 Vibronic Coupling for molecules without degeneracy

Construction of the molecular Hamiltonian is simple and straightforward when there is no degeneracy (i.e electronic states or vibrational modes) in the picture. The Taylor series expansion can be written as follows,

$$\mathcal{W}_{nn}(Q) = W_0(Q) + E_n + \sum_s \kappa_s^{(n)} Q_s + \frac{1}{2}\sum_{s,c} \gamma_{sc}^{(n)} Q_s Q_c + ... \tag{2.35}$$

and

$$\mathcal{W}_{nm}(Q) = W_{nm}(0) + \sum_c \lambda_c^{(nm)} Q_c + ..., \tag{2.36}$$

respectively. The linear intrastate coupling parameter, $\kappa_s^{(n)}$ and interstate coupling parameter, $\lambda_c^{(nm)}$ are same as Eq. 2.31 and 2.32 respectively and the quadratic intrastate coupling parameter, $\gamma_{sc}^{(n)}$ is expressed as

$$\gamma_{sc}^{(n)} = [(\partial^2 W_{nn}/\partial Q_s Q_c)_0] \tag{2.37}$$

Here E_n denotes the vertical excitation/ionization energy of the n^{th} excited electronic state from the reference state. Possible coupling between the states is assessed by the symmetry selection rule which is given in Eq. 2.33. Q_s and Q_c represents the normal coordinates along the totally symmetric and nontotally symmetric vibrational modes, respectively.

2.1.6 Vibronic coupling for molecules with degeneracy

All polyatomic molecules which fall under the non-Abelian point groups (the Abelian point groups are C_n, S_n, C_{2v}, D_2 and D_{2h}) possess degenerate electronic

states and degenerate vibrational modes. When the molecules under observation possess degenerate electronic state and degenerate vibrational modes, the construction of molecular Hamiltonian for the study of VC is not so straight forward because degenerate electronic states are the outstanding examples of the failure of the Born-Oppenheimer adiabatic approximation.

For degenerate states in nonlinear molecules, Jahn and Teller have shown that there always exists a nontotally symmetric vibrational mode that can lift the degeneracy in first order due to VC within the components of the degenerate electronic states [28, 29]. Considering a two-fold degenerate (E) electronic state, the symmetry of the desired vibrational mode for VC should be such that it is contained in the decomposition of the symmetrized product (E^2) . It is then found that in all but seven molecular-point groups (with four-fold principal rotation axis, e.g.,C_{4v}, C_{4h} etc.) degenerate vibrations can be JT active, leading to the $E \times e$ JT effect. It is thus important to solve the multimode JT coupling problem in order to arrive at an understanding of the interactions that actually occur in nonlinear polyatomic molecules. In case of linear molecules such type of VC problem is known as RT coupling of a doubly degenerate electronic state, is discussed in detail in this thesis.

Renner Teller effect

For linear molecule the vibronic coupling within degenerate states (Π, Δ etc.) requires a special treatment, since the lowest order VC terms are at least quadratic [30–32]. The z component of the electronic orbital angular momentum around the molecular axis takes one of the values $\Lambda = 0, 1, 2 \cdots$ in case of linear molecules. The corresponding electronic states are called $\Sigma, \Pi, \Delta \cdots$ states. For all nonzero values of Λ, the electronic state is two-fold degenerate. Since linear molecules

possess a rotational symmetry, the diabatic functions associated with a given value of Λ are subject to the following transformation under the action of C_ϕ

$$C_\phi \Psi_\Lambda = e^{i\Lambda\phi}\Psi_\Lambda, \qquad \Lambda = 0, \pm 1, \pm 2, \cdots \tag{2.38}$$

In the original work of Renner, the VC of the degenerate Π electronic state was considered. Since then, this work has received a significant attention by several researcher [19, 32–36]. According to Eq. 2.33, the bending vibrational mode of π symmetry is RT active. The degenerate bending mode can be described by the cartesian coordinates (Q_x, Q_y) and polar coordinates (ρ, ϕ) as :

$$Q_x = \rho \; cos\chi \tag{2.39}$$

$$Q_y = \rho \; sin\chi \tag{2.40}$$

The transformation properties of $Q_\pm$ under C_ϕ

$$C_\phi Q_\pm = e^{i\Lambda\phi} Q_\pm. \tag{2.41}$$

Here in this section by performing the Taylor series expansion of the electronic part of the Hamiltonian, Eq. 2.25 with respect to $Q_\pm$ and using the symmetry properties Eqs. 2.38 and 2.41, the vibronic model Hamiltonian for the Δ, Π and Δ - Π electronic states is derived along the RT active degenerate π vibrational mode [37].

i) $\Delta - \Pi$ *coupling:*

Linear molecules belong to $D_{\infty h}$ symmetry point group which possess doubly degenerate electronic state like $\Pi, \Delta, \cdots$ etc. From the carbon cluster study it is

seen that linear carbon chains only possess $\sigma_g^+, \sigma_u^+, \pi_g$ and π_u vibrational modes (it is shown in subsection 2.1.7). Due to the lack of δ vibrational modes in linear molecules degenerate Π electronic states are **second order (quadratic) RT active** and Δ electronic states are **fourth order (quartic) RT active** along the π_g and π_u bending vibrational modes. The symmetry selection rules are given below:

$$\Pi_g \otimes \Pi_g \supset \delta_g + \sigma_g^+ + \sigma_g^- \tag{2.42}$$

$$\Pi_u \otimes \Pi_u \supset \delta_g + \sigma_g^+ + \sigma_g^- \tag{2.43}$$

$$\Pi_g \otimes \Pi_u \supset \delta_u + \sigma_u^+ + \sigma_u^- \tag{2.44}$$

$$\Delta_g \otimes \Delta_g \supset \phi_g + \sigma_g^+ + \sigma_g^- \tag{2.45}$$

$$\Delta_u \otimes \Delta_u \supset \phi_g + \sigma_g^+ + \sigma_g^- \tag{2.46}$$

$$\Delta_g \otimes \Delta_u \supset \phi_u + \sigma_u^+ + \sigma_u^- \tag{2.47}$$

Here we are interested to derive the electronic Hamiltonian for the doubly degenerate Δ and Π coupled electronic state. Let ϕ_{Δ_x} and ϕ_{Δ_y} be the two components of the Δ state and ϕ_{Π_x} and ϕ_{Π_y} be the two components of the Π state.
In spherical coordinates the two components of Δ states can be written as

$$\phi_{\Delta_x} = \rho \; cos2\phi \tag{2.48}$$

$$\phi_{\Delta_y} = \rho \; sin2\phi. \tag{2.49}$$

As we know in quantum mechanics a state can be represented only in complex plane, so we will make the functions complex. The X axis is spherical coordinates will be assumed as real part of the function and Y axis is assumed as imaginary part of the function. In complex coordinates it can be written as:

$$\phi_{\Delta_+} = \phi_{\Delta_x} + i\phi_{\Delta_y} = \rho\ e^{i2\phi} \tag{2.50}$$

$$\phi_{\Delta_-} = \phi_{\Delta_x} - i\phi_{\Delta_y} = \rho\ e^{-i2\phi} \tag{2.51}$$

these are known as step-up and step-down state functions in the literature. Similarly, in spherical coordinates the two components of Π states can be written as

$$\phi_{\Pi_x} = \rho\ cos\phi \tag{2.52}$$

$$\phi_{\Pi_y} = \rho\ sin\phi. \tag{2.53}$$

and in complex coordinates the step-up and step-down state functions for Π electronic states can be represented as below:

$$\phi_{\Pi_+} = \phi_{\Pi_x} + i\phi_{\Pi_y} = \rho\ e^{i\phi} \tag{2.54}$$

$$\phi_{\Pi_-} = \phi_{\Pi_x} - i\phi_{\Pi_y} = \rho\ e^{-i\phi} \tag{2.55}$$

The degenerate Δ and Π states can be coupled through the degenerate π_g or π_u vibrational modes. Let us assume that the coupling mode is π_g. Here the Hamiltonian for π_g mode is derived. Similarly the vibrational normal mode which can split the degeneracy of a Δ or Π electronic state are the degenerate π_g or π_u bending modes.

Here the Hamiltonian is derived by considering the π_g vibrational mode and the derivation for π_u vibrational mode will be obvious from π_g derivation.

Lets say Q_x and Q_y are two components of a degenerate π_g vibrational mode. Similar to the state representation, the two components Q_x and Q_y can be ex-

pressed as

$$Q_x = \rho\, cos\phi \;\; (in\ spherical\ coordinates) \tag{2.56}$$

$$Q_y = \rho\, sin\phi \tag{2.57}$$

$$Q_+ = Q_x + iQ_y = \rho\, e^{i\phi} \;\; (in\ complex\ coordinate) \tag{2.58}$$

$$Q_- = Q_x - iQ_y = \rho\, e^{-i\phi} \tag{2.59}$$

Here the multiplication of the angle is taken as ' ϕ'. From the above Eq. 2.38, it is known that for Π electronic state it is 1 and for Δ, it is 2 and so on. These values are similar to the angular moment value. Now some group theoretical analysis is done here to show that these functions are invariant w.r.t symmetry operations (we will make a rotation ' θ' (where ' θ' is small) on these functions), in principle it can be any angle :

For Δ electronic state :

$$C_\theta \phi_{\Delta_+} = C_\theta \rho\, e^{i2\phi} = \rho\, e^{i2(\phi+\theta)} = e^{2i\theta}\phi_{\Delta_+} \tag{2.60}$$

$$C_\theta \phi_{\Delta_-} = C_\theta \rho\, e^{-i2\phi} = \rho\, e^{-i2(\phi+\theta)} = e^{-2i\theta}\phi_{\Delta_-} \tag{2.61}$$

For Π electronic state :

$$C_\theta \phi_{\Pi_+} = C_\theta \rho\, e^{i\phi} = \rho\, e^{i(\phi+\theta)} = e^{i\theta}\phi_{\Pi_+} \tag{2.62}$$

$$C_\theta \phi_{\Pi_-} = C_\theta \rho\, e^{-i\phi} = \rho\, e^{-i(\phi+\theta)} = e^{-i\theta}\phi_{\Pi_-} \tag{2.63}$$

For π_g vibrational mode :

$$C_\theta \; Q_+ = C_\theta \; \rho \; e^{i\phi} = \rho \; e^{i(\phi+\theta)} = e^{i\theta} Q_+ \tag{2.64}$$

$$C_\theta \; Q_- = C_\theta \; \rho \; e^{-i\phi} = \rho \; e^{-i(\phi+\theta)} = e^{-i\theta} Q_- \tag{2.65}$$

Now the $4\times$ 4 electronic hamiltonian for the coupling of Δ and Π electronic states is :

$$H_{el} = \begin{bmatrix} S_{11} & S_{12} & S_{13} & S_{14} \\ S_{21} & S_{22} & S_{23} & S_{24} \\ S_{31} & S_{32} & S_{33} & S_{34} \\ S_{41} & S_{42} & S_{43} & S_{44} \end{bmatrix}$$

Here 1 and 2 are the x and y components of Δ electronic state and 3 and 4 are the x and y components of Π electronic state. We know that electronic Hamiltonian is hermitian in nature , so the above Hamiltonian actually becomes :

$$H_{el} = \begin{bmatrix} S_{11} & S_{12} & S_{13} & S_{14} \\ S_{12}^* & S_{22} & S_{23} & S_{24} \\ S_{13}^* & S_{14}^* & S_{33} & S_{34} \\ S_{23}^* & S_{24}^* & S_{34}^* & S_{44} \end{bmatrix}$$

Now we will evaluate each and every terms of this Hamiltonian. To do that we will expand the electronic Hamiltonian in a Taylor series expansion. By using

the Taylor series expansion the electronic Hamiltonian can be expanded as :

$$\begin{aligned} H_{el} = \quad & W^{(0)} + W^{(1)}Q_+ + W^{(1)}Q_- + W^{(2)}Q_+^2 + W^{(2)}Q_-^2 + W^{(2)}Q_+Q_- + \\ & W^{(3)}Q_+^3 + W^{(3)}Q_+^2Q_- + W^{(3)}Q_+Q_-^2 + W^{(3)}Q_-^3 + W^{(4)}Q_+^4 + \\ & W^{(4)}Q_+^3Q_- + W^{(4)}Q_+^2Q_-^2 + W^{(4)}Q_+Q_-^3 + W^{(4)}Q_-^4 \end{aligned} \tag{2.66}$$

Now this electronic Hamiltonian terms should be invariant w.r.t symmetry (we will operate rotation operator upon each and every terms of this Hamiltonian):

$$\begin{aligned} H_{el} = \quad & W^{(0)} + W^{(1)}e^{i\theta}Q_+ + W^{(1)}e^{-i\theta}Q_- + W^{(2)}e^{2i\theta}Q_+^2 + W^{(2)}e^{-2i\theta}Q_-^2 + \\ & W^{(2)}Q_+Q_- + W^{(3)}e^{3i\theta}Q_+^3 + W^{(3)}e^{i\theta}Q_+^2Q_- + W^{(3)}e^{-i\theta}Q_+Q_-^2 + \\ & W^{(3)}e^{-3i\theta}Q_-^3 + W^{(4)}e^{4i\theta}Q_+^4 + W^{(4)}e^{2i\theta}Q_+^3Q_- + W^{(4)}Q_+^2Q_-^2 + \\ & W^{(4)}e^{-2i\theta}Q_+Q_-^3 + W^{(4)}e^{-4i\theta}Q_-^4 \end{aligned} \tag{2.67}$$

Now, it will be shown that every terms of the above Hamiltonian is invariant w.r.t symmetry :

$$S_{11} =< \phi_{\Delta_+}|H_{el}|\phi_{\Delta_+} >=< e^{2i\theta}\phi_{\Delta_+}|H_{el}|e^{2i\theta}\phi_{\Delta_+} >=< \phi_{\Delta_+}|H_{el}|\phi_{\Delta_+} > \tag{2.68}$$

To make this term symmetry invariant, collect the terms which does not have any $e^{i\theta}$ terms.

$$S_{11} =< \phi_{\Delta_+}|H_{el}|\phi_{\Delta_+} >= W^{(0)} + W^{(2)}Q_+Q_- + W^{(4)}Q_+^2Q_-^2 \tag{2.69}$$

Similarly,

$$S_{22} =< \phi_{\Delta_-}|H_{el}|\phi_{\Delta_-} >= W^{(0)} + W^{(2)}Q_+Q_- + W^{(4)}Q_+^2Q_-^2 \tag{2.70}$$

Now

$$\begin{aligned} S_{12} =< \phi_{\Delta_+}|H_{el}|\phi_{\Delta_-} >= & < e^{2i\theta}\phi_{\Delta_+}|H_{el}|e^{-2i\theta}\phi_{\Delta_-} > \\ & = e^{-4i\theta} < \phi_{\Delta_+}|H_{el}|\phi_{\Delta_-} > \end{aligned} \tag{2.71}$$

To make this term symmetry independent we need to look for the terms with $e^{-4i\theta}$ coefficients (upto quartic terms).

$$S_{12} =< \phi_{\Delta_+}|H_{el}|\phi_{\Delta_-} >= W^{(4)}Q_-^4 \tag{2.72}$$

$$\begin{aligned} S_{33} =< \phi_{\Pi_+}|H_{el}|\phi_{\Pi_+} > \\ =< e^{i\theta}\phi_{\Pi_+}|H_{el}|e^{i\theta}\phi_{\Pi_+} > \\ =< \phi_{\Pi_+}|H_{el}|\phi_{\Pi_+} > \end{aligned} \tag{2.73}$$

To make this term invariant we need to look for the terms with $e^{i\theta}$ coefficients upto quadratic terms.

$$S_{33} = \quad W^{(0)} + W^{(2)}Q_+Q_- \tag{2.74}$$

Similarly,

$$S_{44} = \quad < \phi_{\Pi_-}|H_{el}|\phi_{\Pi_-} >= W^{(0)} + W^{(2)}Q_+Q_- \tag{2.75}$$

Now

$$\begin{aligned} S_{34} = & \quad < \phi_{\Pi_+} | H_{el} | \phi_{\Pi_-} > \\ = & \quad W^{(2)} Q_-^2 \end{aligned} \tag{2.76}$$

$$\begin{aligned} S_{13} = & \quad < \phi_{\Delta_+} | H_{el} | \phi_{\Pi_+} > \\ = & \quad < e^{2i\theta} \phi_{\Delta_+} | H_{el} | e^{i\theta} \phi_{\Pi_+} > \\ = & \quad e^{i\theta} < \phi_{\Delta_+} | H_{el} | \phi_{\Pi_+} > \\ = & \quad W^{(1)} Q_+ \end{aligned} \tag{2.77}$$

$$\begin{aligned} S_{14} = & \quad < \phi_{\Delta_+} | H_{el} | \phi_{\Pi_-} > \\ = & \quad < e^{2i\theta} \phi_{\Delta_+} | H_{el} | e^{-i\theta} \phi_{\Pi_-} > \\ = & \quad e^{-3i\theta} < \phi_{\Delta_+} | H_{el} | \phi_{\Pi_-} > \\ = & \quad 0 \end{aligned} \tag{2.78}$$

$$\begin{aligned} S_{23} = & \quad < \phi_{\Delta_-} | H_{el} | \phi_{\Pi_+} > \\ = & \quad < e^{-2i\theta} \phi_{\Delta_-} | H_{el} | e^{i\theta} \phi_{\Pi_+} > \\ = & \quad e^{3i\theta} < \phi_{\Delta_-} | H_{el} | \phi_{\Pi_+} > \\ = & \quad 0 \end{aligned} \tag{2.79}$$

$$\begin{aligned} S_{24} = & \quad < \phi_{\Delta_-} | H_{el} | \phi_{\Pi_-} > \\ = & \quad < e^{-2i\theta} \phi_{\Delta_-} | H_{el} | e^{-i\theta} \phi_{\Pi_-} > \\ = & \quad e^{i\theta} < \phi_{\Delta_-} | H_{el} | \phi_{\Pi_-} > \\ = & \quad W^{(1)} Q_+ \end{aligned} \tag{2.80}$$

So,

$$S_{11} = \quad S_{22} = W^{(0)} + W^{(2)} Q_+ Q_- + W^{(4)} Q_+^2 Q_-^2 \tag{2.81}$$

$$S_{12} = \quad W^{(4)} Q_-^4 \tag{2.82}$$

$$S_{33} = \quad S_{44} = W^{(0)} + (W_{+-}^{(2)} Q_+ Q_- + W_{-+}^{(2)}) Q_- Q_+ \tag{2.83}$$

$$S_{34} = \quad W^(2) Q_-^2 \tag{2.84}$$

$$S_{13} = \quad W^{(1)} Q_- \tag{2.85}$$

$$S_{24} = \quad W^{(1)} Q_+ \tag{2.86}$$

$$S_{23} = \quad 0 \tag{2.87}$$

$$S_{14} = \quad 0 \tag{2.88}$$

we know the step-up and step-down functions are :

$$Q_+ = Q_x + iQ_y$$

$$Q_- = Q_x - iQ_y$$

putting these values in the above equations we get,

$$S_{11} = \quad S_{22} = W^{(0)} + W^{(2)}(Q_x^2 + Q_y^2) + W^{(4)}(Q_x^2 + Q_y^2)^2 \tag{2.89}$$

$$S_{12} = \quad W^{(4)}[Q_x^4 - 4iQ_x^3Q_y - 6Q_x^2Q_y^2 + 4iQ_xQ_y^3 + Q_y^4] \tag{2.90}$$

$$S_{12}^* = \quad W^{(4)}[Q_x^4 + 4iQ_x^3Q_y - 6Q_x^2Q_y^2 - 4iQ_xQ_y^3 + Q_y^4] \tag{2.91}$$

$$S_{33} = \quad S_{44} = W^{(0)} + W^{(2)}(Q_x^2 + Q_y^2) \tag{2.92}$$

$$S_{34} = \quad W^{(2)}(Q_x^2 - 2iQ_xQ_y - Q_y^2) \tag{2.93}$$

$$S_{34}^* = \quad W^{(2)}(Q_x^2 + 2iQ_xQ_y - Q_y^2) \tag{2.94}$$

$$S_{13} = \quad W^{(1)}(Q_x - iQ_y) \tag{2.95}$$

$$S_{13}^* = \quad W^{(1)}(Q_x + iQ_y) \tag{2.96}$$

$$S_{24} = \quad W^{(1)}(Q_x + iQ_y) \tag{2.97}$$

$$S_{24}^* = \quad W^{(1)}(Q_x - iQ_y) \tag{2.98}$$

So to get the Hamiltonian in real representation, we need to do a unitary transformation with unitary matrix : A matrix U is called unitary matrix when U^{-1} $= U^+$ or $UU^+ =$ I(identity matrix); and we know that $U^+ = (U^*)^T$

$$U = \frac{1}{\sqrt{2}} \begin{bmatrix} 1 & -i & 0 & 0 \\ 1 & i & 0 & 0 \\ 0 & 0 & 1 & -i \\ 0 & 0 & 1 & i \end{bmatrix}$$

$$U^+ = (U*)^T = \frac{1}{\sqrt{2}} \begin{bmatrix} 1 & 1 & 0 & 0 \\ i & -i & 0 & 0 \\ 0 & 0 & 1 & 1 \\ 0 & 0 & i & -i \end{bmatrix}$$

By doing unitary transformation we get the Hamiltonian in real representation :

$$H_{real} = U^{+} H_{el} U \tag{2.99}$$

$$H_{real} = \frac{1}{2}\begin{bmatrix} S_{11}+S_{22}+S_{12}+S_{12}^{*} & -i(S_{11}+S_{12}^{*})+i(S_{12}+S_{22}) & S_{13}+S_{23}+S_{14}+S24 & -i(S_{13}+S_{23})+i(S_{14}+S_{24}) \\ i(S_{11}-S_{12}^{*})+i(S_{12}-S_{22}) & (S_{11}-S_{12}^{*})-(S_{12}-S_{22}) & i(S_{13}-S_{23})+i(S_{14}-S_{24}) & (S_{13}-S_{23})-(S_{14}-S_{24}) \\ S_{13}^{*}+S_{23}^{*}+S_{14}^{*}+S_{24}^{*} & -i(S_{13}^{*}+S_{23}^{*})+i(S_{14}^{*}+S_{24}^{*}) & S_{33}+S_{34}^{*}+S_{34}+S_{44} & -i(S_{33}+S_{34}^{*})+i(S_{34}+S_{44}) \\ i(S_{13}^{*}-S_{23}^{*})+i(S_{14}^{*}-S_{24}^{*}) & (S_{13}^{*}-S_{23}^{*})+(S_{14}^{*}+S_{24}^{*}) & i(S_{33}-S_{34}^{*})+i(S_{34}-S_{44}) & (S_{33}-S_{34}^{*})-(S_{34}-S_{44}) \end{bmatrix}$$

After some algebra the terms can be written as

$$S_{11} = \frac{1}{2}[(W^{(0)}+W^{(2)}(Q_x^2+Q_y^2)+W^{(4)}(Q_x^2+Q_y^2)^2+W^4(Q_x^4-6Q_x^2Q_y^2+Q_y^4))] \tag{2.100}$$

$$(H_{real})_{11} = [E_{\Delta}+g^{(2)}(Q_x^2+Q_y^2)+g^{(4)}(Q_x^2+Q_y^2)^2+\eta^{(4)}(Q_x^4-6Q_x^2Q_y^2+Q_y^4)] \tag{2.101}$$

$$S_{22} = \frac{1}{2}[(W^{(0)}+W^{(2)}(Q_x^2+Q_y^2)+W^{(4)}(Q_x^2+Q_y^2)^2-W^4(Q_x^4-6Q_x^2Q_y^2+Q_y^4))] \tag{2.102}$$

$$(H_{real})_{22} = [E_{\Delta}+g^{(2)}(Q_x^2+Q_y^2)+g^{(4)}(Q_x^2+Q_y^2)^2-\eta^{(4)}(Q_x^4-6Q_x^2Q_y^2+Q_y^4)] \tag{2.103}$$

$$S_{12} = \frac{1}{2}8W^{(4)}(Q_x^3Q_y-Q_xQ_y^3) \tag{2.104}$$

$$(H_{real})_{12} = 4\eta^{(4)}(Q_x^3Q_y-Q_xQ_y^3) \tag{2.105}$$

and

$$S_{33} = \frac{1}{2}[W^{(0)}+W^{(2)}(Q_x^2+Q_y^2)+W^{(2)}(Q_x^2-Q_y^2)] \tag{2.106}$$

$$(H_{real})_{33} = [E_{\Pi}+g^{(2)}(Q_x^2+Q_y^2)+\eta^{(2)}(Q_x^2-Q_y^2)] \tag{2.107}$$

$$S_{44} = \frac{1}{2}[W^{(0)}+W^{(2)}(Q_x^2+Q_y^2)-W^{(2)}(Q_x^2-Q_y^2)] \tag{2.108}$$

$$(H_{real})_{44} = [E_{\Pi}+g^{(2)}(Q_x^2+Q_y^2)-\eta^{2}(Q_x^2-Q_y^2)] \tag{2.109}$$

$$S_{34} = \frac{1}{2}(4W^{(2)}Q_xQ_y) \tag{2.110}$$

$$(H_{real})_{34} = 2\eta^{(2)}Q_xQ_y \tag{2.111}$$

$$S_{13} = \frac{1}{2}(2W^{(1)}Q_x) \tag{2.112}$$

$$(H_{real})_{13} = \lambda Q_x \tag{2.113}$$

$$S_{14} = -\frac{1}{2}(2W^{(1)}Q_y) \tag{2.114}$$

$$(H_{real})_{14} = -\lambda Q_y \tag{2.115}$$

$$S_{24} = \frac{1}{2}(2W^{(1)}Q_x) \tag{2.116}$$

$$(H_{real})_{24} = \lambda Q_x \tag{2.117}$$

$$S_{23} = \frac{1}{2}(2W^{(1)}Q_y) \tag{2.118}$$

$$(H_{real})_{23} = \lambda Q_y \tag{2.119}$$

ii) $\Sigma - \Pi$ *coupling:*

In addition to the VC of the two components of the degenerate Π electronic state, the degenerate bending vibrational mode of π symmetry can couple a doubly degenerate Π electronic state with a nondegenerate Σ electronic state in linear molecules. This coupling is known as $\Sigma - \Pi$ coupling. This coupling mechanism becomes important when a doubly degenerate Π electronic state lies close in energy to a Σ state [38, 40–44, 66]. By considering the diabatic basis states $\Psi_{\pm}$ and

Ψ_0 for the Π and Σ states, respectively, and following the steps described above, the $\Sigma - \Pi$ Hamiltonian is obtained as [37]

$$H_{\Sigma-\Pi} = (T_N + \frac{\omega}{2}Q^2)\mathbf{1_3} + \begin{bmatrix} E_\Pi & 2\eta Q_x Q_y & \lambda Q_x \\ & E_\Pi & \lambda Q_y \\ hc & & E_\Sigma \end{bmatrix}$$

where E_Π and E_Σ are the energies of the Π and Σ electronic states respectively; η represents quadratic RT coupling and λ represents the linear interstate (Σ - Π) coupling.

2.1.7 Lack of δ vibrational mode in Linear molecules :

Here in this section it is proved that linear molecules does not have any δ vibrational mode, because of that degenerate Π_g or Π_u electronic states are second order RT active and Δ_g or Δ_u electronic states are fourth order RT active along π_g or π_u vibrational modes. For that we are taking an example of linear molecule C_3, (C=C=C) whose point group is $D_{\infty h}$. But Molpro or any other quantum chemistry softwares would approximate it to its highest abelian point group (D_{2h}) in this case. Lets' say, the molecule is in YZ plane and the molecular axis is along Z axis. Now, the correlation table of $D_{\infty h}$ - D_{2h} symmetry point group is the following [45]:

$D_{\infty h}$	D_{2h}	vib mode
Σ_g^+	A_g	σ_g^+
Σ_g^-	B_{1g}	σ_g^-
Σ_u^+	B_{1u}	σ_u^+
Σ_u^-	A_u	σ_u^-
Π_g	B_{2g}+B_{3g}	π_g
Π_u	B_{2u}+B_{3u}	π_u
Δ_g	A_g+B_{1g}	δ_g
Δ_u	A_u+B_{1u}	δ_u

Now the reducible representation of C_3 in D_{2h} point group is :

D_{2h}	E	$C_2(z)$	$C_2(y)$	$C_2(x)$	i	$\sigma(xy)$	$\sigma(xz)$	$\sigma(yz)$
Γ_{red}	9	-3	-1	-1	-3	1	3	3

A decomposition of the above reducible to the IREPs of the D_{2h} symmetry point group yields :

$$\eta_{A_g} = \frac{1}{8}[9-3-1-1-3+1+3+3] = 1$$
$$\eta_{A_u} = \frac{1}{8}[9-3-1-1+3-1-3-3] = 0$$
$$\eta_{B_{1g}} = \frac{1}{8}[9-3+1+1-3+1-3-3] = 0$$
$$\eta_{B_{2g}} = \frac{1}{8}[9+3+1-1-3-1-3+3] = 1$$

$$\eta_{B_{3g}} = \frac{1}{8}[9+3+1-1-3-1+3-3] = 1$$
$$\eta_{B_{2u}} = \frac{1}{8}[9+3-1+1+3+1+3-3] = 2$$
$$\eta_{B_{3u}} = \frac{1}{8}[9+3-1+1+3+1-3+3] = 2$$
$$\eta_{B_{1u}} = \frac{1}{8}[9-3+1+1+3-1+3+3] = 2$$

Therefore,

$$\begin{aligned} \Gamma_{total} = & \quad 1A_g + 2B_{1u} + 1B_{2g} + 1B_{3g} + 1B_{2u} + 1B_{3u} \\ = & \quad 1\sigma_g^+ + 2\sigma_u^+ + 1\pi_g + 2\pi_u \end{aligned} \tag{2.120}$$

From the character table D_{2h} point we get,

$$\begin{aligned} \Gamma_{rotational} = & \quad 1B_{2g} + 1B_{3g} + 1B_{1g} \\ = & \quad 1\pi_g + 0 \end{aligned} \tag{2.121}$$

Since, C_n is linear, rotation along z-axis, R_z should be ignored. So, B_{1g} vanishes in the above expression. Now,

$$\Gamma_{translational} = \quad 1B_{2u} + 1B_{3u} + 1B_{1u} = 1\pi_u + 1\sigma_u^+ \tag{2.122}$$

Therefore,

$$\Gamma_{vibrational} = \quad \Gamma_{total} - \Gamma_{rotational} - \Gamma_{translational} = 1\sigma_g^+ + 1\sigma_u^+ + 1\pi_u \tag{2.123}$$

Now, we will extend the above derivation for n odd number of atoms (where, n= 5, ..., 15,17,19,21). The reducible representation for D_{2h} point group for n number of atom is as follows

D_{2h}	E	$C_2(z)$	$C_2(y)$	$C_2(x)$	i	$\sigma(xy)$	$\sigma(xz)$	$\sigma(yz)$
Γ_{red}	3n	-n	-1	-1	-3	1	n	n

Now the components of D_{2h} point group reduces to :

$$\begin{aligned}
\eta_{A_g} = &\quad \frac{1}{8}[3n-n-1-1-3+1+n+n] = \frac{1}{8}[4n-4] = \frac{(n-1)}{2} \\
\eta_{A_u} = &\quad \frac{1}{8}[3n-n-1-1+3-1-n-n] = 0 \\
\eta_{B_{1g}} = &\quad \frac{1}{8}[3n-n+1+1-3+1-n-n] = 0 \\
\eta_{B_{2g}} = &\quad \frac{1}{8}[3n+n+1-1-3-1+n-n] = \frac{1}{8}[4n-4] = \frac{(n-1)}{2} \\
\eta_{B_{3g}} = &\quad \frac{1}{8}[3n+n-1+1-3-1+n+n] = \frac{1}{8}[4n-4] = \frac{(n-1)}{2} \\
\eta_{B_{2u}} = &\quad \frac{1}{8}[3n+n-1+1+3+1+n-n] = \frac{1}{8}[4n+4] = \frac{(n+1)}{2} \\
\eta_{B_{3u}} = &\quad \frac{1}{8}[3n+n-1+1+3+1-n+n] = \frac{1}{8}[4n+4] = \frac{(n+1)}{2} \\
\eta_{B_{1u}} = &\quad \frac{1}{8}[3n-n+1+1+3-1+n+n] = \frac{1}{8}[4n+4] = \frac{(n+1)}{2}
\end{aligned}$$

Now,

$$\begin{aligned}
\Gamma_{total} = &\quad \frac{(n-1)}{2}A_g + \frac{(n+1)}{2}B_{1u} + \frac{(n-1)}{2}(B_{2g}+B_{3g}) + \frac{(n+1)}{2}(B_{2u}+B_{3u}) \\
= &\quad \frac{(n-1)}{2}\sigma_g^+ + \frac{(n+1)}{2}\sigma_u^+ + \frac{(n-1)}{2}\pi_g + \frac{(n+1)}{2}\pi_u
\end{aligned} \tag{2.124}$$

$$\begin{aligned}
\Gamma_{rotational} = &\quad 1B_{2g} + 1B_{3g} + 1B_{1g} \\
= &\quad 1\pi_g + 0
\end{aligned} \tag{2.125}$$

Since, C_n is linear, rotation along z-axis, R_z should be ignored. So, B_{1g} vanishes

from here.

$$\begin{aligned} \Gamma_{translational} = & \quad 1B_{2u} + 1B_{3u} + 1B_{1u} \\ = & \quad 1\pi_u + 1\sigma_u^+ \end{aligned} \tag{2.126}$$

Now,

$$\begin{aligned} \Gamma_{vibrational} = & \quad \Gamma_{total} - \Gamma_{rotational} - \Gamma_{translational} \\ = & \quad \frac{(n-1)}{2}A_g + \frac{(n-1)}{2}B_{1u} + \frac{(n-3)}{2}(B_{2g} + B_{3g}) + \frac{(n-1)}{2}(B_{2u} + B_{3u}) \\ = & \quad \frac{(n-1)}{2}\sigma_g^+ + \frac{(n-1)}{2}\sigma_u^+ + \frac{(n-3)}{2}\pi_g + \frac{(n-1)}{2}\pi_u \end{aligned} \tag{2.127}$$

It proves that linear odd numbered molecules do not have any δ_g or δ_u vibrational modes. That's why the degenerate Π and Δ electronic states are second order and fourth order Renner-Teller(RT) active, respectively through degenerate π_g and π_u vibrational modes.

2.1.8 Adiabatic potential energy surfaces and conical intersections

The concept of adiabatic electronic potential energy surfaces (PESs) is important for the interpretation and understanding of all kinds of phenomena in molecular physics and chemistry. Therefore, we shall consider in some detail of the adiabatic PESs. To start with, let us consider a 2×2 model diabatic Hamiltonian containing N tuning modes (totally symmetric, Q_{si}) and M coupling (non-totally symmetric, Q_{cj}) vibrational modes and is given as

$$H = (T_N + V_0)\mathbf{1} + \begin{bmatrix} E_1 + \sum_{i=1}^{N} \kappa_i^{(1)} Q_{si} & \sum_{j=1}^{M} \lambda_j Q_{cj} \\ \sum_{j=1}^{M} \lambda_j Q_{cj} & E_2 + \sum_{i=1}^{N} \kappa_i^{(2)} Q_{si} \end{bmatrix} \tag{2.128}$$

where,

$$T_N = -\frac{1}{2}\sum_{i=1}^{N} \omega_i (\frac{\partial^2}{\partial Q_{si}^2}) - \frac{1}{2}\sum_{j=1}^{M} \omega_j (\frac{\partial^2}{\partial Q_{cj}^2}) \tag{2.129}$$

$$V_0 = \frac{1}{2}\sum_{i=1}^{N} \omega_i Q_{si}^2 + \frac{1}{2}\sum_{j=1}^{M} \omega_j Q_{cj}^2. \tag{2.130}$$

The quantities κ and λ represents the intrastate and interstate coupling parameters. Here, E_1 and E_2 (assuming $E_1 < E_2$) are ionization or excitation energies of the coupled electronic states at the reference geometry $Q = 0$, where Q represents collectively the set of nuclear coordinates (Q_s, Q_c). T_N is the nuclear kinetic energy operator and V_0 is the potential energy operator. The adiabatic PESs are obtained by diagonalizing the above Hamiltonian in the fixed-nuclei limit, $T_N \to 0$, as follows [2].

$$\mathbf{S}^{\dagger}(H - T_N 1)S = V \tag{2.131}$$

where

$$V = \begin{bmatrix} V_1(Q) & 0 \\ 0 & V_2(Q) \end{bmatrix} \tag{2.132}$$

Here $\mathbf{S}$ is a 2×2 unitary matrix which describes the diabatic to adiabatic transformation. $V_1(Q)$ and $V_2(Q)$ are the adiabatic PESs of Hamiltonian (Eq. 2.128). For detail discussion of the static aspects of the adiabatic PESs, it is convenient to rewrite H of Eq.2.128 in the following general form [2]:

$$H = H_0\mathbf{1} + \begin{bmatrix} -d & c \\ c & d \end{bmatrix} \tag{2.133}$$

where,

$$H = T_N + V_0 + \Sigma + \sigma Q_s \tag{2.134}$$

$$\Sigma = \frac{(E_1 + E_2)}{2} \tag{2.135}$$

$$\Delta = \frac{(E_2 - E_1)}{2} \tag{2.136}$$

$$\sigma_i = \frac{(\kappa_i^{(1)} + \kappa_i^{(2)})}{2} \tag{2.137}$$

$$\delta_i = \frac{(\kappa_i^{(2)} - \kappa_i^{(1)})}{2} \tag{2.138}$$

$$d = \Delta + \sum_{i=1}^{N} \delta_i Q_{si} \tag{2.139}$$

$$c = \sum_{j=1}^{M} \lambda_j Q_{cj} \tag{2.140}$$

The expression of adiabatic potentials within the linear vibronic coupling (LVC) model are then read,

$$V_{1,2}(\mathbf{Q}) = V_0(\mathbf{Q}) + \Sigma + \sum_{i=1}^{N} \sigma_i Q_{si} \mp W \tag{2.141}$$

where

$$W = \sqrt{d^2 + c^2} \tag{2.142}$$

Now the conditions for the occurrence of a CI of the adiabatic PESs of the above

Hamiltonian are simply $d = 0$ and $c = 0$. These conditions define a hypersurface of dimensional $N + M - 2$ and $N + M$ dimensional coordinate space i.e in case of one coupling mode and two tuning modes, for example, we obtain a line of CIs in three dimensional space.

The minimum of the seam of CIs within LVC scheme is given by

$$V_{min}^{(c)} = \Sigma + \frac{(F - D)^2}{2D} - \frac{1}{2}\sum_{i=1}^{N} \sigma^i/\omega_{si} \tag{2.143}$$

The position of the minimum in the space of the tuning mode within LVC scheme is,

$$(Q_{si}^{(c)})_{min} = \frac{(\delta_i/\omega_{gi}(F - D))}{D} - \frac{\sigma_i}{\omega_{si}}, i = 1, \cdots N \tag{2.144}$$

The minimum of the seam of the CIs relative to the minimum of the upper adiabatic PESs is given by

$$V_{min}^{(c)} - (V_2)_{min} = \frac{1}{2D}(\Delta - D - F)^2 \tag{2.145}$$

where

$$D = \sum_{i=1}^{N} \frac{\delta_i^2}{\omega_{si}} \tag{2.146}$$

$$F = \sum_{i=1}^{N} \frac{\delta_i \sigma_i}{\omega_{si}} \tag{2.147}$$

Next we shall examine the CI of two diabatic surfaces ($j = 1, 2$) described by diabatic potentials containing both linear ($\kappa_i^{(j)}$) and quadratic ($\gamma_i^{(j)}$) coupling term (cf. Eq. 2.133) i.e within QVC scheme

$$V_j(\mathbf{Q}) = E_j + \sum_{i=1}^{N} \kappa_i^{(j)} Q_i + [\frac{\omega_i}{2} + \gamma_i^{(j)}] Q_i^2 \tag{2.148}$$

Since $V_1(\mathbf{Q}) = V_2(\mathbf{Q})$ at CI, one immediately obtains the equation of the conical intersection in the $\mathbf{Q}$-space as

$$\Delta + \sum_{i=1}^{N} (\delta_i Q_i + \gamma_i Q_i^2) = 0, \tag{2.149}$$

$\gamma_i = \frac{(g_i^{(2)} - g_i^{(1)})}{2}$. We mention that inclusion of quadratic coupling term in the diabatic potential, as obtained l.h.s of Eq. 2.149 making the hypersurface to differ from a hyperline as encountered in the LVC case.

The energies at the conical intersection seam are given by $V_2(\mathbf{Q})$ or $(V_1(\mathbf{Q}))$, with $\mathbf{Q}$ subjected to the constraint Eq. 2.149. To obtain the minimum of the seam of the conical intersection, one has to consider the the functional $F(\mathbf{Q}) \equiv V_2(\mathbf{Q}) + \mu G(\mathbf{Q})$, where μ is a Lagrange multiplier and $G(\mathbf{Q})$ is a shorthand for the l.h.s of Eq. 2.149. By imposing $\frac{\partial F(\mathbf{Q})}{\partial Q_i} = 0$ one straightforwardly gets [9]

$$Q_i = -\frac{\kappa_i^{(2)} + \mu\delta_i}{\omega_i + 2\gamma_i^{(2)} + 2\mu\gamma_i} \tag{2.150}$$

The insertion of the above expression for Q_i into Eq. 2.149 yields

$$\Delta + \sum_{i=1}^{N} [-\delta_i \frac{\kappa_i^{(2)} + \mu\delta_i}{\omega_i + 2\gamma_i^{(2)} + 2\mu\gamma_i} + \gamma_i (\frac{\kappa_i^{(2)} + \mu\delta_i}{\omega_i + 2\gamma_i^{(2)} + 2\mu\gamma_i})^2] = 0. \tag{2.151}$$

To find the seam minimum, we have to solve the above equation for the Lagrange multiplier μ. Within the LVC model ($\gamma_i = 0$), Eq. 2.151 is linear in μ, possessing therefore exactly one root. Putting this root value in Eq. 2.150, one can get an unique solution of the minimization problem irrespective of the number of the tuning modes. In contrast to this, within QVC model we are lead to the problem of solving an algebraic equation of order 2N+1, where N is the number of tuning

modes possessing nonvanishing quadratic couplings ($\gamma_i \neq 0$). In general, out of the total number 2N+1 of its roots, there are several real roots. To determine the energy E_s of the minimum of the seam of the CI, one has to select thereof that root for μ, which, inserted into Eq.2.149, leads to the smallest value of $V_2(\mathbf{Q})$ $(= E_s)$. To solve the minimization problem along the approach described above, we used the MATHEMATICA package version 5.1. Fortunately, it succeed to find the roots of the highly nonlinear equation 2.151 for fluorophenol molecules where upto 23 tuning modes were accounted for.

2.2 Calculation of excitation spectrum

Lets say, a molecule is initially in the state Ψ_0 , is excited by some operator $\hat{T}$ into a manifold of vibronically coupled electronic state. According to Fermi's golden rule, the spectral intensity of photoexcitation and photoelectron spectrum is calculated which is described by function

$$P(E) = \sum_v \left| \langle \Psi_v^f | \hat{T} | \Psi_0^i \rangle \right|^2 \delta(E - E_v^f + E_0^i), \tag{2.152}$$

where the quantity $\hat{T}$ represents the transition dipole operator that describes the interaction of the electron with the external radiation of energy E during the photoionization process. $|\Psi_0^i\rangle$ is the initial vibronic ground state (reference state) with energy E_0^i and $|\Psi_v^f\rangle$ corresponds to the (final) vibronic state of the photoionized/excited molecule with energy E_v^f. The reference ground electronic state is approximated to be vibronically decoupled from the other states and it is given by

$$|\Psi_0^i\rangle = |\Phi^0\rangle|\chi_0^0\rangle, \tag{2.153}$$

The final vibronic state $|\Psi_v^f\rangle$ in the coupled electronic manifold of n interacting states can be written as

$$|\Psi_v^f\rangle = \sum_n |\Phi^n\rangle|\chi_v^n\rangle, \tag{2.154}$$

where $|\Phi\rangle$ and $|\chi\rangle$ represent the diabatic electronic and vibrational part of the wavefunction, respectively. The superscripts refer to the ground and excited states. With the help of Eqs. (2.153-2.154), the excitation function Eq. (2.152) can be rewritten as

$$P(E) = \sum_v \left| \sum_n \tau^n \langle \chi_v^n | \chi_0^0 \rangle \right|^2 \delta(E - E_v^f + E_0^i), \tag{2.155}$$

where

$$\tau^n = \langle \Phi^n | \hat{T} | \Phi^0 \rangle \tag{2.156}$$

represent the matrix elements of the transition dipole operator of the final electronic state n. In diabatic basis, these elements depends very weakly on nuclear coordinates Q. Hence, in the study of photoinduced processes presented in this thesis, the transition dipole operator elements are considered as constants. This approximation is called as Condon approximation [47].

2.2.1 Time-independent approach

In a time-independent matrix diagonalization quantum mechanical approach the photoinduced electronic spectrum is calculated by solving the eigenvalue equation

i.e. the time-independent vibronic Schrödinger equation,

$$\mathcal{H}|\Psi_n^f\rangle = E_n|\Psi_n^f\rangle, \tag{2.157}$$

It is solved by expanding the vibronic eigenstates $\{|\Psi_n^f\rangle\}$ in the direct product harmonic oscillator basis of the electronic ground state [2]

$$|\Psi_n^f\rangle \;=\; \sum_{\{|K_i\rangle\}} a^n_{K_1,\ldots,K_l}|K_1\rangle|K_2\rangle\ldots|K_l\rangle|\phi_n\rangle \tag{2.158}$$

Here K^{th} level of i^{th} vibrational mode is denoted by $|K_i\rangle$. $|\phi_m\rangle$ is the electronic wavefunction. For each vibrational mode, the oscillator basis is suitably truncated in the numerical calculations. In practice, the maximum level of excitation for each mode is estimated from the convergence behavior of the spectral envelope. The Hamiltonian matrix expressed in a direct product Harmonic oscillator basis is highly sparse and is tri-diagonalized by the Lanczos algorithm [48]. The diagonal elements of the resulting eigenvalue matrix give the position of the vibronic lines and the relative intensities are obtained from the squared first components of the Lanczos eigenvectors [2, 12]. These calculations are simplified by employing the generalized Condon approximation in a diabatic electronic basis [47], that is, the matrix elements of $\hat{T}$ in the diabatic electronic basis are treated to be independent of nuclear coordinates and have the equal modulus. To reflect the inherent broadening of the experimental vibronic spectrum, the stick vibronic lines obtained from the matrix diagonalization calculations are usually convoluted [2] with a Lorentzian line shape function

$$L(E) \;=\; \frac{1}{\pi}\;\frac{\frac{\Gamma}{2}}{E^2+(\frac{\Gamma}{2})^2}\;\;, \tag{2.159}$$

with a FWHM Γ.

2.2.2 Time-dependent approach

In a time-dependent picture, the Fourier transform representation of the Dirac delta function, $\delta(x) = \frac{1}{2\pi}\int_{-\infty}^{+\infty} e^{ixt/\hbar}$, is used in the Fermi's golden rule equation, Eq. (2.152) to calculate spectral intensity. The resulting expression for the spectral intensity then rearranges to the Fourier transform of the time autocorrelation function of the wave packet,

$$P(E) \approx 2Re \int_0^{\infty} e^{iEt/\hbar} \langle \Psi_i(0)|\tau^{\dagger} e^{-i\mathcal{H}t/\hbar}\tau|\Psi_i(0)\rangle dt, \tag{2.160}$$

$$\approx 2Re \int_0^{\infty} e^{iEt/\hbar}\ C_i(t)\ dt. \tag{2.161}$$

In Eq. (2.160) the elements of the transition dipole matrix $\tau^{\dagger}$ is given by, $\tau^f = \langle \phi^f|\hat{T}|\phi^i\rangle$. The quantity $C_f(t) = \langle \Psi_f(0)|\Psi_f(t)\rangle$, is the time autocorrelation function of the WP initially prepared on the f^{th} electronic state and, $\Psi_f(t) = e^{-i\mathcal{H}t/\hbar}\ \Psi_f(0)$. In the time-dependent calculations, the time autocorrelation function is damped with a suitable time-dependent function before Fourier transformation. The usual choice has been a function of type

$$f(t) \ = \ exp[-t/\tau_r] \ , \tag{2.162}$$

where τ_r represents the relaxation time. Multiplying $C(t)$ with $f(t)$ and then Fourier transforming it is equivalent to convoluting the spectrum with a Lorentzian line shape function (cf., Eq. (2.159)) of FWHM, $\Gamma = 2/\tau_r$.

2.2.3 Propagation of wave packet by MCTDH algorithm

The matrix diagonalization approach becomes computationally impracticable with increase in the electronic and nuclear degrees of freedom. Therefore, for large molecules and with complex vibronic coupling mechanism this method often becomes unachievable. The WP propagation approach within the MCTDH scheme has emerged as a very promising alternative tool for such situation [49–52]. This is a grid based method which utilizes DVR combined with fast Fourier transformation and powerful integration schemes. The efficient multiset ansatz of this scheme allows for an effective combination of vibrational degrees of freedom and thereby reduces the dimensionality problem. In this approach the wavefunction for a nonadiabatic system is expressed as [50–52]

$$\Psi(Q_1,...,Q_f,t) = \Psi(R_1,...,R_p,t) \tag{2.163}$$

$$= \sum_{\alpha=1}^{\sigma}\sum_{j_1=1}^{n_1^{(\alpha)}}...\sum_{j_p=1}^{n_p^{(\alpha)}} A^{(\alpha)}_{j_1,...,j_p}(t)\prod_{k=1}^{p}\varphi_{jk}^{(\alpha,k)}(R_k,t)|\alpha\rangle, \tag{2.164}$$

Where, R_1,..., R_p are the coordinates of p particles formed by combining vibrational degrees of freedom, α is the electronic state index and $\varphi_{jk}^{(\alpha,k)}$ are the n_k SPFs for each degree of freedom k associated with the electronic state α. Employing a variational principle, the solution of the time-dependent Schrödinger equation is described by the time-evolution of the expansion coefficients $A^{(\alpha)}_{j_1,...,j_p}$. In this scheme all multi-dimensional quantities are expressed in terms of one-dimensional ones employing the idea of mean-field or Hartree approach. This provides the efficiency of the method by keeping the size of the basis optimally small. Furthermore, multi-dimensional SPFs are designed by appropriately choosing the set of system coordinates so as to reduce the number of particles and hence the com-

putational overheads. The operational principles, successes and shortcomings of this schemes are detailed in the literature [50–52]. The Heidelberg MCTDH package [49] is employed to propagate WPs in the numerical simulations for present molecules. The spectral intensity is finally calculated using Eq. (2.160) from the time-evolved WP. Here we provide a brief overview on the memory requirement for the MCTDH method. The memory required by standard method is proportional to N^f, where N is the total number of grid points or primitive basis functions and f is the total number of degrees of freedom. In contrast, memory needed by the MCTDH method scales as

$$memory \quad \sim \quad fnN + n^f \tag{2.165}$$

where, n represent the SPFs. The memory requirements can however reduced if SPFs are used that describe a set of degrees of freedom, termed as *multimode* SPFs. By combining d degrees of freedom together to form a set of $p{=}f/d$ particles, the memory requirement changes to

$$memory \quad \sim \quad f\tilde{n}N^d + \tilde{n}^f \tag{2.166}$$

where $\tilde{n}$ is the number of multimode functions needed for the new particles. If only single-mode functions are used i.e. $d{=}1$, the memory requirement, Eq. (2.166), is dominated by n^f. By combining degrees of freedom together this number can be reduced, but at the expense of longer product grids required to describe the multimode SPFs.

References

[1] M. Born and R. Oppenheimer, Ann. Phys. 84, 457 (1927).

[2] H. Köppel, W. Domcke, and L. S. Cederbaum, Adv. Chem. Phys. 57, 59 (1984).

[3] G. Fisher, *Vibronic coupling*, Academic press, London (1984).

[4] B. H. Lengsfield and D. R. Yarkony, Adv. Chem. Phys. 82, 1 (1992).

[5] C. J. Ballhausen and A. E. Hansen, Ann. Rev. Phys. Chem. 23, 15 (1972).

[6] H. Köppel, L.S. Cederbaum, and S. Mahapatra, *Theory of the JahnTeller Effect*, in *Handbook of high-resolution spectroscopy*, John Wiley & Sons, (2011).

[7] S. Mahapatra, Acc. Chem. Res. 42, 1004 (2009).

[8] M. Baer, *Beyond Born-Oppenheimer: electronic non-adiabatic coupling terms and conical intersections*, John Wiley and Sons, (2006).

[9] W. Lichten, Phys. Rev. 131, 229 (1963).

[10] F. T. Smith, Phys. Rev. 179, 111 (1969).

[11] T. F. O'Malley, Adv. At. Mol. Phys. 7, 223 (1971).

[12] H. Köppel and W. Domcke: in *Encyclopedia of computational chemistry* edited by P. v. R. Schleyer, Wiley, New York (1998), p 3166.

[13] M. Baer, Chem. Phys. Lett. 35, 112 (1975).

[14] C. A. Mead, D. G. Truhlar, J. Chem. Phys. 77, 6090 (1982).

[15] V. Sidis, Adv. Chem. Phys. 82, 73 (1992).

[16] M. Baer, Chem. Phys. 15, 49 (1976).

[17] T. Pacher, L. S. Cederbaum and H. Köppel, Adv. Chem. Phys. 84, 293 (1993).

[18] A. Thiel and H. Köppel, J. Chem. Phys. 110, 9371 (1999).

[19] H. C. Longuet-Higgins, Proc. Roy. Soc. London, Ser. A, 344, 147 (1975).

[20] R. K. Preston and J. C. Tully, J. Chem. Phys. 54, 4297 (1971).

[21] G. Hirsch, P. J. Bruna, R. J. Buenker, and S. D. Peyerimhoff, Chem. Phys. 45, 335 (1980)

[22] H. J. Werner and W. Meyer, J. Chem. Phys. 74, 5802 (1981).

[23] H. Köppel, J. Gronki, and S. Mahapatra, J. Chem. Phys. 115, 23771 (2001)

[24] The Dynamical Jahn-Teller Effect in Localized Systems, edited by Y. E.Perlin and M. Wagner (North-Holland, Amsterdam, 1984).

[25] I. B. Bersuker and V. Z. Polinger, Vibronic Interactions in Molecules and-Crystals (Springer-Verlag, Berlin, 1989).

[26] E. B. Wilson Jr., J. C. Decius, and P. C. Cross, *Molecular vibrations*, McGraw-Hill, New York (1955).

[27] L. S. Cederbaum and W. Domcke, Adv. Chem. Phys. 36, 205 (1977).

[28] H. A. Jahn and E. Teller, Proc. R. Soc. London, Ser. A 161, 220 (1937).

[29] H. A. Jahn, Proc. R. Soc. London, Ser. A 164, 117 (1938).

[30] R. Renner, Z. Phys. 92, 172 (1934).

[31] J. M. Brown, F. Jrgensen, Adv. Chem. Phys. 52, 117 (1983).

[32] J. A. Pople, H. C. Longuet-Higgins, Mol. Phys. 1, 372 (1958).

[33] T. Barrow, R. N. Dixon, G. Duxbury, Mol. Phys. 27, 1217 (1974).

[34] M. Peric, C. M. Marian, S. D. Peyerimhoff, J. Mol. Spectrosc. 166, 406 (1994).

[35] M. Peric, C. M. Marian, S. D. Peyerimhoff, J. Chem. Phys. 114, 6086 (2001).

[36] M. Peric, M. Mladenovic, K. Tomic, C. M. Marian, J. Chem. Phys. 118, 4444 (2003).

[37] H. Köppel, W. Domcke, L. S. Cederbaum, J. Chem. Phys. 74, 2945 (1981).

[38] P. S. H. Bolman, J. M. Brown, A. Carrington, I. Kopp, D. A. Ramsay, Proc. R. Soc. London, Ser. A 343, 17 (1975).

[39] R. N. Dixon, D. A. Ramsay, Can. J. Phys. 46, 2619 (1968).

[40] D. C. Frost, S. T. Lee, C. A. McDowell, Chem. Phys. Lett. 23, 472 (1973).

[41] H. Köppel, L. S. Cederbaum, W. Domcke, W. von Niessen, Chem. Phys. 37, 303 (1979).

[42] P. M. Dehmer, J. L. Dehmer, W. A. Chupka, J. Chem. Phys. 73, 126 (1980).

[43] A. Mebel, M. Baer, S. H. Lin, J. Chem. Phys. 112, 10703 (2000).

[44] R. Tarroni, S. Carter, J. Chem. Phys. 119, 12878 (2003).

[45] G. Herzberg, *Molecular Spectra and Molecular structure*, Vol. III, page number- 576, Van Nostrand Reinhold Company, New York (1966).

[46] E. Gindensperger, I. Bâldea, J. Franz and H. Kppel, Chem. Phys. 338, 207 (2007).

[47] W. Domcke, H. Köppel, and L. S. Cederbaum, Mol. Phys. 43, 851 (1981).

[48] J. Cullum and R. Willoughby, *Lanczos algorithms for large symmetric eigenvalue problems*, Birkhäuser, Boston (1985), Vols. I and II.

[49] G. A. Worth, M. H. Beck, A. Jäckle, and H. -D. Meyer, *The MCTDH Package*, Version 8.2, (2000), University of Heidelberg, Heidelberg, Germany. H. -D. Meyer, Version 8.3 (2002), Version 8.4 (2007). See http://mctdh.uni-hd.de.

[50] H. -D. Meyer, U. Manthe, and L. S. Cederbaum, Chem. Phys. Lett. 165, 73 (1990).

[51] U. Manthe, H. -D. Meyer, and L. S. Cederbaum, J. Chem. Phys. 97, 3199 (1992).

[52] M. H. Beck, A. Jäckle, G. A. Worth, and H. -D. Meyer, Phys. Rep. 324, 1 (2000).

Chapter 3

Electronic spectroscopy of carbon clusters (C_{2n+1}, n=7-10). I. Quantum Chemistry.

Extensive ab initio quantum chemistry calculations are carried out to establish the electronic potential energy surfaces and their coupling surfaces for carbon clusters containing odd number of carbon atoms (C_{2n+1}, n=7-10). A vibronic coupling model is established to carry out nuclear dynamics calculations from first principles. The latter are reported in chapter 4. The mentioned clusters possess linear cumulenic chain structure at the equilibrium minimum of their electronic ground state and an excited state of $^1\Sigma_u^+$ term is found to be extremely bright optically in the visible region of the electromagnetic spectrum. The oscillator strength of this state linearly increases with an increase of the chain length. There are states belonging to Π_g, Π_u, Δ_g and Δ_u terms, in the immediate vicinity of the $^1\Sigma_u^+$ state, which are optically dark but can gain intensity through vibronic coupling with this bright state. Such a coupling scheme is developed in this chapter. The Hamil-

tonian is constructed in a diabatic electronic basis in terms of the dimensionless normal coordinates of the vibrational modes of the cluster. Both Renner-Teller and pseudo-Renner-Teller type of couplings are included in the Hamiltonian. The theoretical results are discussed in relation to the experimental findings.

3.1 Introduction

The electronic structure and absorption spectroscopy of neutral carbon clusters received renewed attention in the literature because of their apparent importance in the spectroscopy of interstellar medium [1,2]. The first spectroscopic detection of C_3 in comets in 1881 triggered curiosity among the stellar as well as laboratory spectroscopists to identify neutral carbon clusters as carrier of diffuse interstellar bands (DIBs) [3]. Douglas in a seminal paper suggested that the carbon chains C_n, where n may lie in the range 5-15 could show spectroscopic features consistent with DIBs [4]. The diffuse structure of these bands is attributed to a short lifetime of excited electronic states of the carrier molecules [5].

Following the above development, many experimental and computational studies were carried out on anionic, neutral and cationic bare carbon clusters [6–10]. In this context two reviews, covering the rich history of carbon clusters, by Weltner [11] and Orden [12] are noteworthy. Smaller carbon clusters were predicted to have linear equilibrium geometry with a cumulenic (:C=C=C=C:) type of bonding with nearly equal bond lengths. Linear chains with odd number of carbon atoms were predicted to have $^1\Sigma_g^+$ electronic ground term in contrast to a $^3\Sigma_g^-$ electronic ground term for the cluster chains with even number of carbon atoms. Clusters larger than C_{10} were proposed to have ring structures as well, because of the reduction of ring strain and added stability due to extra C−C bond. However,

the cyclic clusters are reported to be difficult to detect and characterize spectroscopically [11, 12]. Therefore, the linear clusters are discussed in majority of the experiments [28, 29]. The clusters, C_{2n+1}, (n=7-10), also have linear cumulenic equilibrium structure [15].

Energetically low-lying electronic states of C_{15}, C_{17}, C_{19} and C_{21} clusters studied here belong to $^1\Sigma$, $^1\Pi$ or a $^1\Delta$ terms. About twelve excited electronic states are found to exist to within 4 eV energy. While a Σ state is nondegenerate, the Π and Δ states are doubly degenerate. The degeneracy of the latter states split upon distortion (from equilibrium) along bending vibrational modes of the cluster and can give rise to Renner-Teller (RT) effect. In addition, the RT split components may also undergo symmetry allowed coupling with the nondegenerate ($^1\Sigma$) or another RT split component state, giving rise to a pseudo-Renner-Teller (PRT) type of interaction (equivalent to pseudo-Jahn-Teller interaction in nonlinear systems) of the electronic states. The $^1\Sigma_u^+$ electronic state is the optically bright state in all the clusters studied here. It's oscillator strength scales linearly (cf. Fig. 3.1) with the cluster chain length. Several optically dark non-degenerate and degenerate electronic states appear to within 1.0 eV energy range of this $^1\Sigma_u^+$ state. Therefore, elucidation of the coupling mechanism of the latter state is important in order to understand its detailed vibronic structure. Such studies are not available in the literature so far. The present effort is aimed to fulfil this task.

While detailed *ab initio* electronic structure calculations are carried out to establish the coupling mechanism and construct a vibronic Hamiltonian in this chapter, the nuclear dynamics calculations are carried out in chapter 4. The results are compared with the available experimental findings.

3.2 Electronic structure calculations

The ground vibrational level of the electronic ground state (S_0 $^1\Sigma_g^+$) of C_{2n+1} (n=7-10) is taken as the reference state to investigate $^1\Sigma_u^+$ photoabsorption spectroscopy of these clusters. The equilibrium geometry of the reference state is optimized by the Becke-3-parameter (exchange), Lee, Yang, and Parr (B3LYP) density functional method using the correlation consistent polarized valence double - ζ (cc-pVDZ) basis set of Dunning [16]. The Gaussian-09 suite of program [17] is used for the optimization calculations. The optimized equilibrium geometry yields an average C=C bond length of ~ 1.30 A^0 in agreement with the literature data [18]. Harmonic frequency (ω_k) of vibrational modes and their dimensionless normal displacement coordinates (Q_k) are calculated by diagonalizing the kinematic and force constant matrices of the reference equilibrium geometry, given in Table 3.3. Symmetry analysis of the normal modes of linear clusters with odd number of carbon atoms, C_{2n+1} (say, 2n+1=N), yields (N-1) nondegenerate (σ) and (N-2) degenerate (π) vibrations. They decompose into the following irreducible representations (IREPs) of the $D_{\infty h}$ symmetry point group as shown in chapter 2 (Sec. 2.1.7).

$$\Gamma \;=\; ((N-1)/2)\sigma_g^+ \oplus ((N-1)/2)\sigma_u^+ \oplus ((N-3)/2)\pi_g \oplus ((N-1)/2)\pi_u. \tag{3.1}$$

The analysis also reveals that these linear molecules do not contain vibrations with higher angular momentum like δ, ϕ etc. The vertical excitation energies (VEEs) of the electronic states of C_{15}, C_{17}, C_{19} and C_{21} are calculated along the dimensionless normal coordinates of all vibrational modes. The calculations are carried out using EOM-CCSD method implemented in the MOLPRO suite of programs [19] and cc-pVDZ basis set. In MOLPRO, the calculations are performed

in D_{2h} symmetry. The D_{2h} - $D_{\infty h}$ correlation table (which is given in Chapter 2, sec. 2.1.7) is utilized to derive electronic terms and symmetry representation of vibrational modes. The VEEs calculated at the equilibrium geometry of the reference ground state of energetically low-lying (to within 4 eV relative to reference equilibrium energy) electronic states are given in Table. 3.1. Along with the VEEs the oscillator strengths values are also given in the table. It can be seen that the $^1\Sigma_u^+$ is the only optically bright state in these clusters. The oscillator strength of this state for clusters containing odd number of C atoms from C_5 to C_{21} is plotted as a function of the chain length in Fig. 3.1. It can be seen from this figure that the oscillator strength increases linearly with increasing chain length.

VEEs are calculated over a range of displacement of normal coordinates (-5.00 $\leq$ Q $\leq$ 5.00) of the vibrational modes. These energies plus the energy of the reference state define the adiabatic energies of the excited electronic states of the clusters. From Table. 3.1, it can be seen that the electronic states of the clusters studied here have Σ, Π and Δ terms. All of them have $^1\Sigma_g^+$ electronic ground term. The energy of the target $^1\Sigma_u^+$ state is lowered with increasing chain length. This state is energetically very close to its neighboring states (cf. Table 3.1) and vibronic coupling is expected to play important role in the nuclear dynamics on this state. The Π and Δ electronic states are orbitally degenerate at the $D_{\infty h}$ symmetry configuration. This degeneracy is split upon bending the linear cluster chain and gives rise to Renner-Teller (RT) effect. The RT split component states may undergo PRT type of coupling with the non-degenerate $^1\Sigma_u^+$ state. Using elementary symmetry rule the following coupling scheme can be derived from the character table of $D_{\infty h}$ symmetry point group.

Table 3.1: Vertical excitation energy (VEE in eV) and oscillator strength (f) of energetically low-lying excited singlet electronic states of neutral carbon clusters C_{15}, C_{17}, C_{19} and C_{21}. * indicates the states which are considered for nuclear dynamics study.

State	VEE	f	State	VEE	f
C_{15}			C_{17}		
$S_5^*\ ^1\Pi_g$	3.1082	0.00	$S_5^*\ ^1\Sigma_u^+$	2.951	14.81
$S_6^*\ ^1\Pi_u$	3.1097	0.01	$S_6\ ^1\Sigma_u^-$	3.060	0.00
$S_7^*\ ^1\Sigma_u^+$	3.2730	12.97	$S_7^*\ ^1\Pi_u$	3.087	0.01
$S_8\ ^1\Sigma_u^-$	3.4325	0.00	$S_8^*\ ^1\Pi_g$	3.089	0.00
$S_9\ ^1\Sigma_g^-$	3.4485	0.00	$S_9^*\ ^1\Delta_u$	3.132	0.00
$S_{10}^*\ ^1\Delta_g$	3.4801	0.00	$S_{10}\ ^1\Sigma_g^-$	3.163	0.00
$S_{11}^*\ ^1\Delta_u$	3.5149	0.00	$S_{11}^*\ ^1\Delta_g$	3.199	0.00
$S_{12}^*\ ^1\Sigma_g^+$	3.6133	0.00	$S_{12}^*\ ^1\Sigma_g^+$	3.346	0.00
C_{19}			C_{21}		
$S_5^*\ ^1\Sigma_u^+$	2.6783	16.55	$S_5^*\ ^1\Sigma_u^+$	2.444	18.19
$S_6\ ^1\Sigma_u^-$	2.7528	0.00	$S_6\ ^1\Sigma_u^-$	2.494	0.00
$S_7^*\ ^1\Delta_u$	2.8144	0.01	$S_7^*\ ^1\Delta_u$	2.546	0.00
$S_8\ ^1\Sigma_g^-$	2.9284	0.00	$S_8\ ^1\Sigma_g^-$	2.732	0.00
$S_9^*\ ^1\Delta_g$	2.9676	0.00	$S_9^*\ ^1\Delta_g$	2.773	0.00
$S_{10}^*\ ^1\Pi_g$	3.0712	0.01	$S_{10}^*\ ^1\Sigma_g^+$	2.939	0.00
$S_{11}^*\ ^1\Pi_u$	3.0723	0.00	$S_{11}^*\ ^1\Pi_u$	3.0595	0.01
$S_{12}^*\ ^1\Sigma_g^+$	3.1252	0.00	$S_{12}^*\ ^1\Pi_g$	3.0604	0.00

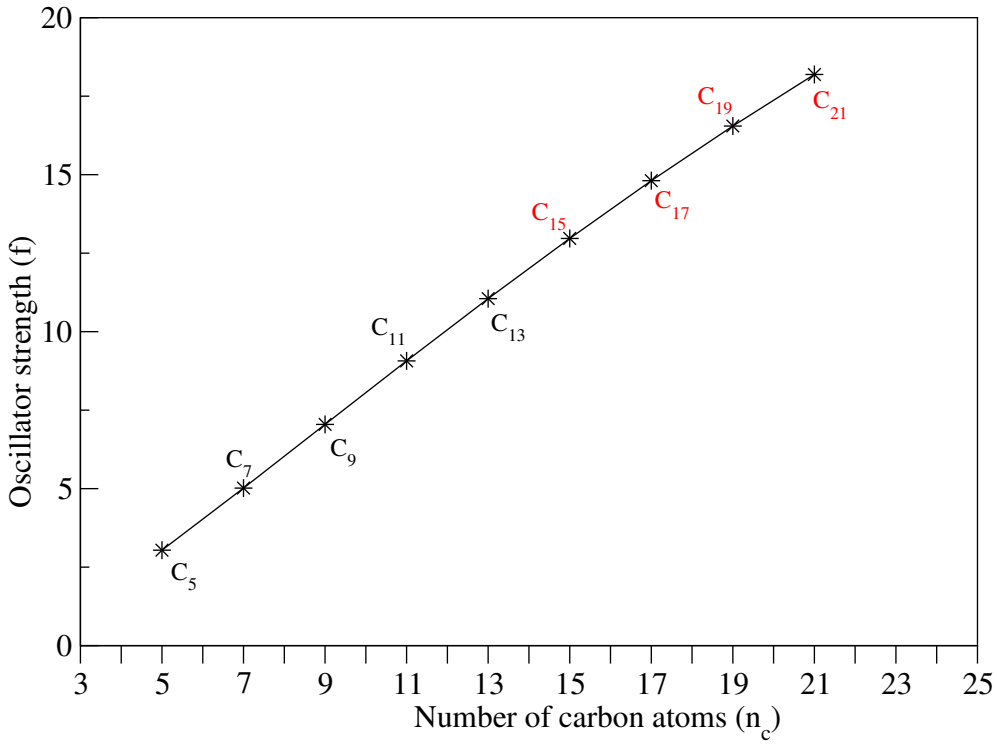

Figure 3.1: Oscillator strength (f) of linear carbon chains with odd number of carbon atoms as a function of the number of carbon atoms. The points are obtained from *ab initio* quantum chemistry calculations by EOM-CCSD method with a cc-pVDZ basis set and the solid line represent a linear fit to the *ab initio* data given by, f= -2.53 + 1.13 n_c.

The first-order coupling between electronic states i and j through vibrational mode k is governed by the symmetry rule: $\Gamma_i \otimes \Gamma_k \otimes \Gamma_j \supset \sigma_g^+$ [20]. The symbol Γ represents the IREPs. The symbol σ_g^+ is the IREP of totally symmetric vibrational mode of linear molecule. According to this rule the latter vibrational modes are active within a given electronic states ($i = j$). Now for the degenerate Π and Δ states the symmetrized direct products transform according to : $(\Pi_g)^2 = (\Pi_u)^2 = \sigma_g^+ + \delta_g$ and $(\Delta_g)^2 = (\Delta_u)^2 = \sigma_g^+ + \gamma_g$. While the totally symmetric σ_g^+ vibrational modes can not lift orbital degeneracy, the modes of δ_g and γ_g symmetry can lift the same in first order of the Π and Δ states, respectively. The lack of vibrational modes of δ_g and γ_g symmetry in linear molecules make the first-order RT coupling vanish in those states. However, $(\pi_g)^2 = (\pi_u)^2 \supset \delta_g$ and $(\pi_g)^4 = (\pi_u)^4 \supset \gamma_g$, therefore, the π_g and π_u modes can be RT active in the Π and Δ states in second-order and fourth-order, respectively. The RT split components of the Π and Δ states can undergo PRT type of coupling according to :

$$\Pi_g \otimes \Pi_u = \delta_u + \sigma_u^- + \sigma_u^+; \tag{3.2a}$$

$$\Pi_{g/u} \otimes \Delta_{g/u} = \pi_g + \phi_g; \tag{3.2b}$$

$$\Pi_{g/u} \otimes \Delta_{u/g} = \pi_u + \phi_u; \tag{3.2c}$$

$$\Delta_g \otimes \Delta_u = \gamma_u + \sigma_u^- + \sigma_u^+. \tag{3.2d}$$

The nondegenerate Σ state can undergo coupling with the neighboring Σ or Π states according to :

$$\Sigma_u^+ \otimes \Sigma_g^+ = \sigma_u^+; \tag{3.3a}$$

$$\Sigma_u^+ \otimes \Pi_{g/u} = \pi_{u/g} \tag{3.3b}$$

$$\Sigma_g^+ \otimes \Pi_{g/u} = \pi_{g/u} \tag{3.3c}$$

3.3 The Vibronic Hamiltonian

It can be seen from Table 3.1 that in the immediate neighborhood of $^1\Sigma_u^+$ states, there are many states of Σ, Π and Δ symmetry. Consideration of all states listed in Table II in the dynamics (treated in chapter 4) is computationally impracticable. We therefore selected the states marked with an asterisk in Table 3.1 and developed a vibronic Hamiltonian in the following. It can be seen from Table 3.1 that in addition to the $^1\Sigma_u^+$ state, $^1\Pi_g$, $^1\Pi_u$, $^1\Sigma_g^+$, $^1\Delta_g$ and $^1\Delta_u$ state one each is considered. These states are energetically closest to the $^1\Sigma_u^+$ state. With the aid of the symmetry rules discussed in the previous section and standard vibronic coupling theory the following vibronic Hamiltonian can be derived in a diabatic electronic basis

$$\mathcal{H} = \mathcal{H}_0 \mathbf{1_{10}} + \Delta\mathcal{H}, \tag{3.4}$$

where, $\mathcal{H}_0 = \mathcal{T}_N + \mathcal{V}_0$, with

$$\mathcal{T}_N = -\frac{1}{2} \sum_{k \in \sigma_g^+,\, \sigma_u^+} \omega_k \frac{\partial^2}{\partial Q_k^2} - \frac{1}{2} \sum_{k \in \pi_g,\, \pi_u} \omega_k \left(\frac{\partial^2}{\partial Q_{kx}^2} + \frac{\partial^2}{\partial Q_{ky}^2} \right),$$

and

$$\mathcal{V}_0 \;=\; \frac{1}{2}\sum_{k\,\in\,\sigma_g^+,\,\sigma_u^+}\omega_k Q_k^2 + \frac{1}{2}\sum_{k\,\in\,\pi_g,\,\pi_u}\omega_k\left(Q_{kx}^2+Q_{ky}^2\right),$$

is the unperturbed harmonic Hamiltonian of the reference electronic ground state. $\mathbf{1_{10}}$ is a 10×10 unit matrix. The components of doubly degenerate vibrational modes and electronic states are labelled with x and y, respectively. The quantity $\Delta\mathcal{H}$ defines the change in electronic energy upon excitation. This is a 10×10 matrix Hamiltonian in the diabatic electronic basis which can be symbolically represented as

$$\Delta\mathcal{H} = \begin{bmatrix} H_1 & H_{12} & H_{13} & H_{14} & H_{15} & H_{16} & H_{17} & H_{18} & H_{19} & H_{110} \\ & H_2 & H_{23} & H_{24} & H_{25} & H_{26} & H_{27} & H_{28} & H_{29} & H_{210} \\ & & H_3 & H_{34} & H_{35} & H_{36} & H_{37} & H_{38} & H_{39} & H_{310} \\ & & & H_4 & H_{45} & H_{46} & H_{47} & H_{48} & H_{49} & H_{410} \\ & & & & H_5 & H_{56} & H_{57} & H_{58} & H_{59} & H_{510} \\ & & & & & H_6 & H_{67} & H_{68} & H_{69} & H_{610} \\ & & & & & & H_7 & H_{78} & H_{79} & H_{710} \\ & & h.c & & & & & H_8 & H_{8,9} & H_{8,10} \\ & & & & & & & & H_9 & H_{910} \\ & & & & & & & & & H_{10}. \end{bmatrix} \tag{3.5}$$

In the above equation the states are identified with the index 1 to 10 as ${}^1\Sigma_u^+$, ${}^1\Pi_{gx}$, ${}^1\Pi_{gy}$, ${}^1\Pi_{ux}$, ${}^1\Pi_{uy}$, ${}^1\Sigma_g^+$, ${}^1\Delta_{gx}$, ${}^1\Delta_{gy}$, ${}^1\Delta_{ux}$ and ${}^1\Delta_{uy}$, respectively. The elements of this Hamiltonian matrix are expanded in a Taylor series around the reference equilibrium configuration in the following way:

$$\begin{aligned}\Delta\mathcal{H}_i =& \mathcal{E}_i^0 + \sum_{k\,\in\,\sigma_g^+} \kappa_k^i Q_k + \sum_{k\,\in\,\sigma_g^+,\ \sigma_u^+} \gamma_k^i Q_k^2 + \sum_{k\,\in\,\pi_g,\ \pi_u} \gamma_k^i (Q_{kx}^2 + Q_{ky}^2) + \sum_{k\,\in\,\pi_g,\ \pi_u} \rho_k^i (Q_{kx}^2 + Q_{ky}^2)^2 \\ &\pm \sum_{k\,\in\,\pi_g,\ \pi_u} \eta_k^{i,j} (Q_{kx}^2 - Q_{ky}^2) \pm \sum_{k\,\in\,\pi_g,\ \pi_u} \beta_k^{i,j} (Q_{kx}^4 - Q_{ky}^4) \pm \sum_{k\,\in\,\pi_g,\ \pi_u} \xi_k^{i,j} (Q_{kx}^4 - 6Q_{kx}^2 Q_{ky}^2 + Q_{ky}^4).\end{aligned} \tag{3.6}$$

In the above ε_i^0 defines the VEE, κ_k^i first-order and γ_k^i and ρ_k^i second-order and fourth order intrastate coupling along mode k of the i^{th} electronic state, respectively. The + and - sign of the last two terms of Eq. 3.6 applies to the x and y component of the degenerate state, respectively. The quantities, $\eta_k^{i,j}$ and $\beta_k^{i,j}$ are the quadratic and quartic RT coupling parameters within the Π states, respectively and the quartic RT coupling parameters within the Δ states are define as $\xi_k^{i,j}$. The various off-diagonal terms of the Hamiltonian (Eq. 3.5) representing RT and PRT couplings are listed in Table 3.2.

Table 3.2: Various offdiagonal terms of the Hamiltonian (Eq. 3.5) representing RT and PRT couplings.

	$H_1\ ^1\Sigma_u^+$	$H_2\ ^1\Pi_{gx}$	$H_3\ ^1\Pi_{gy}$	$H_4\ ^1\Pi_{ux}$	$H_5\ ^1\Pi_{uy}$	$H_6\ ^1\Sigma_g^+ gx$	$H_7\ ^1\Delta gx$	$H_8\ ^1\Delta gy$	$H_9\ ^1\Delta ux$	$H_{10}\ ^1\Delta uy$
$H_1\ ^1\Sigma_u^+$		$\sum_{k\in\pi_u} \lambda_k^{1,2} Q_{kx}$	$\sum_{k\in\pi_u} \lambda_k^{1,3} Q_{ky}$ $\sum_{k\in\pi_g,\ \pi_u} 2\eta_k^{(2,3)}(Q_{kx}Q_{ky}) +$ $\sum_{k\in\pi_g,\ \pi_u} 2\beta_k^{(2,3)}(Q_{kx}^3 Q_{ky} + Q_{kx}Q_{ky}^3)$	$\sum_{k\in\pi_g} \lambda_k^{1,4} Q_{kx}$ $\sum_{k\in\sigma_u^+} \lambda_k^{2,4} Q_k$	$\sum_{k\in\pi_g} \lambda_k^{1,5} Q_{ky}$ - $\sum_{k\in\sigma_u^+} \lambda_k^{3,5} Q_k$ $\sum_{k\in\pi_g,\ \pi_u} 2\eta_k^{(4,5)}(Q_{kx}Q_{ky}) +$ $\sum_{k\in\pi_g,\ \pi_u} 2\beta_k^{(4,5)}(Q_{kx}^3 Q_{ky} + Q_{kx}Q_{ky}^3)$	$\sum_{k\in\sigma_u^+} \lambda_k^{1,6} Q_k$ $\sum_{k\in\pi_g} \lambda_k^{2,6} Q_{kx}$ $\sum_{k\in\sigma_g^+} \lambda_k^{3,6} Q_{ky}$ $\sum_{k\in\pi_u} \lambda_k^{4,6} Q_{kx}$ $\sum_{k\in\pi_u} \lambda_k^{5,6} Q_{ky}$	-	-	-	-
$H_2\ ^1\Pi_{gx}$						$\sum_{k\in\pi_g} \lambda_k^{2,7} Q_{kx}$	$\sum_{k\in\pi_g} \lambda_k^{3,7} Q_{ky}$	$-\sum_{k\in\pi_g} \lambda_k^{2,8} Q_{ky}$	$\sum_{k\in\pi_u} \lambda_k^{2,9} Q_{kx}$	$-\sum_{k\in\pi_u} \lambda_k^{2,10} Q_{ky}$
$H_3\ ^1\Pi_{gy}$				-		$\sum_{k\in\pi_g} \lambda_k^{3,7} Q_{ky}$	$\sum_{k\in\pi_g} \lambda_k^{3,8} Q_{kx}$	$\sum_{k\in\pi_u} \lambda_k^{3,9} Q_{ky}$	$\sum_{k\in\pi_u} \lambda_k^{3,10} Q_{kx}$	
$H_4\ ^1\Pi_{ux}$						$\sum_{k\in\pi_u} \lambda_k^{4,6} Q_{kx}$	$\sum_{k\in\pi_u} \lambda_k^{4,7} Q_{kx}$	$-\sum_{k\in\pi_u} \lambda_k^{4,8} Q_{ky}$	$\sum_{k\in\pi_g} \lambda_k^{4,9} Q_{kx}$	$-\sum_{k\in\pi_g} \lambda_k^{4,10} Q_{ky}$
$H_5\ ^1\Pi_{uy}$	h.c					$\sum_{k\in\pi_u} \lambda_k^{5,6} Q_{ky}$	$\sum_{k\in\pi_u} \lambda_k^{5,7} Q_{ky}$	$\sum_{k\in\pi_u} \lambda_k^{5,8} Q_{kx}$	$\sum_{k\in\pi_g} \lambda_k^{5,9} Q_{ky}$	$\sum_{k\in\pi_g} \lambda_k^{5,10} Q_{kx}$
$H_6\ ^1\Sigma_g^+$							-	-	-	-
$H_7\ ^1\Delta gx$								$\sum_{k\in\pi_g,\ \pi_u} 4\xi_k^{(7,8)}(Q_{kx}^3 Q_{ky} - Q_{kx}Q_{ky}^3)$	$\sum_{k\in\sigma_u^+} \lambda_k^{7,9} Q_k$	-
$H_8\ ^1\Delta gy$									-	$\sum_{k\in\sigma_u^+} \lambda_k^{8,10} Q_k$
$H_9\ ^1\Delta ux$										$\sum_{k\in\pi_g,\ \pi_u} 4\xi_k^{(9,10)}(Q_{kx}^3 Q_{ky} - Q_{kx}Q_{ky}^3)$
$H_{10}\ ^1\Delta uy$										

In the above table, $\lambda_k^{i,j}$, defines the linear PRT coupling parameter between states i and j along the vibrational mode k. The quadratic and quartic RT coupling parameters within the Π states are given by $\eta_k^{i,j}$ and $\beta_k^{i,j}$ along the vibrational mode k and within the Δ electronic states the quartic RT coupling parameters are given by $\xi_k^{i,j}$ along vibrational mode k. A rigorous derivation of this vibronic Hamiltonian is presented in Chapter-2. All the coupling parameters defined above are estimated from the calculated adiabatic electronic energies along a given vibrational mode. Non-linear least squares fit of the adiabatic energies to the adiabatic form of the diabatic Hamiltonian Eq. 3.5 along each vibrational mode is carried out for this purpose. The complete list of parameters for all four clusters are given in Tables 3.4, 3.5, 3.6, 3.7, 3.8, 3.9, 3.10 and 3.11. A close look at the parameters given in these tables reveal that the lowest frequency, σ_g^+ vibrational modes (ν_7 in C_{15}, ν_8 in C_{17}, ν_9 in C_{19} and ν_{10} in C_{21}) possess large excitation strength in Σ and Δ states. The vibrational modes, ν_1 - ν_5 on the other hand are condon active within the Π states. The excitation strength of these modes is nearly same in both the $^1\Pi_g$ and $^1\Pi_u$ states of all four clusters. This is because these states are quasi-degenerate which give rise to same κ and γ values.

Table 3.3: Harmonic frequency (in ev and cm^{-1}) and symmetry of the vibrational modes of C_{2n+1}, (n=7-10).

C_{15}				C_{17}				C_{19}				C_{21}			
Symmetry	Mode	Frequency		Symmetry	Mode	Frequency		Symmetry	Mode	Frequency		Symmetry	Mode	Frequency	
	k	ev	cm^{-1}		k	ev	cm^{-1}		k	ev	cm^{-1}		k	ev	cm^{-1}
σ_g^+	ν_1	0.2780	2243	σ_g^+	ν_1	0.2798	2257	σ_g^+	ν_1	0.2799	2258	σ_g^+	ν_1	0.2790	2250
	ν_2	0.2748	2216		ν_2	0.2706	2182		ν_2	0.2721	2195		ν_2	0.2759	2225
	ν_3	0.2549	2055		ν_3	0.2648	2136		ν_3	0.2651	2138		ν_3	0.2615	2109
	ν_4	0.2175	1755		ν_4	0.2387	1925		ν_4	0.2503	2018		ν_4	0.2587	2087
	ν_5	0.1622	1308		ν_5	0.1954	1576		ν_5	0.2207	1780		ν_5	0.2376	1916
	ν_6	0.1014	817		ν_6	0.1452	1171		ν_6	0.1778	1434		ν_6	0.2026	1634
	ν_7	0.0349	281		ν_7	0.0902	727		ν_7	0.1313	1059		ν_7	0.1630	1314
σ_u^+	ν_8	0.2802	2260		ν_8	0.0308	249		ν_8	0.0811	654		ν_8	0.1198	967
	ν_9	0.2687	2167	σ_u^+	ν_9	0.2787	2248		ν_9	0.0276	222		ν_9	0.0737	594
	ν_{10}	0.2481	2001		ν_{10}	0.2743	2213	σ_u^+	ν_{10}	0.2782	2244		ν_{10}	0.0250	202
	ν_{11}	0.2386	1924		ν_{11}	0.2528	2039		ν_{11}	0.2754	2222	σ_u^+	ν_{11}	0.2792	2252
	ν_{12}	0.1903	1534		ν_{12}	0.2395	1932		ν_{12}	0.2623	2116		ν_{12}	0.2731	2202
	ν_{13}	0.1325	1069		ν_{13}	0.2191	1767		ν_{13}	0.2388	1926		ν_{13}	0.2686	2166
	ν_{14}	0.0688	555		ν_{14}	0.1709	1378		ν_{14}	0.2317	1869		ν_{14}	0.2488	2007
π_g	ν_{15}	0.0943	760		ν_{15}	0.1182	954		ν_{15}	0.1993	1608		ν_{15}	0.2258	1812
	ν_{16}	0.0735	593		ν_{16}	0.0610	492		ν_{16}	0.1550	1251		ν_{16}	0.2212	1784
	ν_{17}	0.0569	459	π_g	ν_{17}	0.0986	795		ν_{17}	0.1067	860		ν_{17}	0.1832	1478
	ν_{18}	0.0341	275		ν_{18}	0.0787	634		ν_{18}	0.0547	441		ν_{18}	0.1418	1143
	ν_{19}	0.0190	154		ν_{19}	0.0627	506	π_g	ν_{19}	0.1029	830		ν_{19}	0.0971	783
	ν_{20}	0.0064	51		ν_{21}	0.0403	325		ν_{20}	0.0834	673		ν_{20}	0.0496	400
π_u	ν_{21}	0.1063	857		ν_{21}	0.0289	233		ν_{21}	0.0674	543	π_g	ν_{21}	0.1074	866
	ν_{22}	0.0838	676		ν_{22}	0.0154	124		ν_{22}	0.0548	442		ν_{22}	0.0877	708
	ν_{23}	0.0648	523		ν_{23}	0.0051	41		ν_{23}	0.0362	292		ν_{23}	0.0717	578
	ν_{24}	0.0397	321	π_u	ν_{24}	0.1112	897		ν_{24}	0.0243	196		ν_{24}	0.0597	482
	ν_{25}	0.0268	216		ν_{25}	0.0884	713		ν_{25}	0.0126	101		ν_{25}	0.0411	331
	ν_{26}	0.0121	97		ν_{26}	0.0699	564		ν_{26}	0.0041	33		ν_{26}	0.0319	257
	ν_{27}	0.0023	19		ν_{27}	0.0557	449	π_u	ν_{27}	0.1163	938		ν_{27}	0.0205	166
					ν_{28}	0.0353	284		ν_{28}	0.0927	748		ν_{28}	0.0104	84
					ν_{29}	0.0220	177		ν_{29}	0.0747	602		ν_{29}	0.0034	27
					ν_{30}	0.0097	78		ν_{30}	0.0610	492	π_u	ν_{30}	0.1212	978
					ν_{31}	0.0019	15		ν_{31}	0.0407	328		ν_{31}	0.0968	781
									ν_{32}	0.0306	247		ν_{32}	0.0792	639
									ν_{33}	0.0181	146		ν_{33}	0.0654	528
									ν_{34}	0.0078	63		ν_{34}	0.0541	436
									ν_{35}	0.0015	12		ν_{35}	0.0369	298
													ν_{36}	0.0262	212
													ν_{37}	0.0152	122
													ν_{38}	0.0065	52
													ν_{39}	0.0012	10

Table 3.4: *Ab initio* calculated linear and quadratic coupling parameters for the $^1\Sigma_u^+$, $^1\Pi_g$, $^1\Pi_u$, $^1\Sigma_g^+$, $^1\Delta_g$ and $^1\Delta_u$ electronic states of C_{15} cluster. All data are given in the eV unit unless otherwise stated.

Mode	κ_k^i i=1	γ_k^i	κ_k^i or $\eta_k^{i,j}$ [$\beta_k^{i,j}$] i=2,3	γ_k^i [ρ_k^i]	κ_k^i or $\eta_k^{i,j}$ [$\beta_k^{i,j}$] i=4,5	γ_k^i [ρ_k^i]	κ_k^i i=6	γ_k^i	κ_k^i or $\xi_k^{i,j}$ i=7,8	γ_k^i [ρ_k^i]	κ_k^i or $\xi_k^{i,j}$ i=9,10	γ_k^i [ρ_k^i]
	$^1\Sigma_u^+$		$^1\Pi_g$		$^1\Pi_u$		$^1\Sigma_g^+$		$^1\Delta_g$		$^1\Delta_u$	
ν_1*	-0.0063(0.00)	-0.0065	0.0948(0.06)	-0.0053	0.0947(0.06)	-0.0053	-0.0174(0.00)	-0.0011	0.0203(0.00)	-0.0125	0.0456(0.01)	-0.0073
ν_2*	0.0385(0.01)	-0.0173	0.2329(0.36)	-0.0171	0.2327(0.36)	-0.0171	-0.0144(0.00)	-0.0191	-0.1008(0.07)	0.0089	0.0581(0.02)	-0.0045
ν_3*	0.0026(0.00)	-0.0018	0.1523(0.18)	-0.0056	0.1521(0.18)	-0.0056	-0.0277(0.01)	-0.0023	-0.0342(0.01)	-0.0040	-0.0327(0.01)	-0.0042
ν_4*	0.0017(0.00)	-0.0014	-0.0856(0.08)	-0.0019	-0.0854(0.08)	-0.0019	0.0190(0.00)	-0.0010	0.0191(0.00)	-0.0018	0.0265(0.01)	-0.0027
ν_5*	-0.0044(0.00)	-0.0009	0.0483(0.04)	-0.0003	0.0480(0.04)	-0.0003	-0.0156(0.00)	-0.0007	-0.0140(0.00)	-0.0009	-0.0379(0.03)	-0.0018
ν_6	-0.0077(0.00)	-0.0006	0.0171(0.01)	0.0001	0.0170(0.01)	0.0001	-0.0189(0.02)	-0.0002	-0.0117(0.01)	-0.0004	-0.0303(0.04)	-0.0004
ν_7*	-0.0273(0.31)	0.0001	-0.0026(0.00)	0.0001	-0.0026(0.00)	0.0001	-0.0221(0.20)	0.0001	-0.0265(0.29)	0.0001	-0.0340(0.47)	0.0001
ν_8*		-0.0090	-	-0.0074	-	-0.0074		-0.0037		-0.0097	-	-0.0097
ν_9*		-0.0058	-	-0.0061	-	-0.0063		-0.0080		-0.0052	-	-0.0108
ν_{10}		-0.1209	-	0.0038	-	-0.0834		-0.0181		-0.0269	-	-0.0579
ν_{11}*		-0.0256	-	0.0014	-	-0.0178		0.0093		-0.0047	-	-0.0087
ν_{12}*		-0.0014	-	-0.0001	-	-0.0013		-0.0008		-0.0013	-	-0.0023
ν_{13}		-0.0007	-	0.0004	-	0.0004		-0.0007		-0.0005	-	-0.0011
ν_{14}		-0.0010	-	0.0002	-	0.0000		0.0003		-0.0003	-	-0.0005
ν_{15}		-0.0024	-0.0043	-0.0036	-0.0036	-0.0041 [0.0001]		-0.0027	-0.0003	-0.0030 [0.0001]	-0.0002	-0.0034 [0.0001]
ν_{16}*		-0.0028	-0.0046	-0.0032	-0.0035	-0.0038		-0.0032	-0.0002	-0.0042	-0.0001	-0.0045 [0.0001]
ν_{17}*		-0.0037	-0.0039	-0.0032	-0.0038	-0.0037		-0.0038	-0.0001	-0.0046 [-0.0001]	0.0000	-0.0048 [0.0001]
ν_{18}		-0.0013	0.0004	0.0134 [-0.0001]	-0.0002[0.0002]	0.0163 [-0.0002]		-0.0009	0.0000	-0.0033	0.0000	-0.0024
ν_{19}		-0.0022	-0.0001	-0.0102	-0.0001	0.0107		-0.0030	0.0000	-0.0036	0.0000	-0.0047
ν_{20}		-0.0027	-0.0002	0.0064	-0.0002	0.0064		-0.0036	0.0000	-0.0040	0.0000	-0.0055
ν_{21}		-0.0032	-0.0040	-0.0023	-0.0040	-0.0025		-0.0019	-0.0002	-0.0026	-0.0001	-0.0034 [0.0001]
ν_{22}*		-0.0023	-0.0040	-0.0048	-0.0042	-0.0036		-0.0029	-0.0003	-0.0032 [0.0001]	-0.0001	-0.0043 [0.0001]
ν_{23}*		-0.0032	-0.0038	-0.0037	-0.0038	-0.0026		-0.0040	-0.0002	-0.0055	0.0000	-0.0044 [0.0002]
ν_{24}		-0.0030	-0.0021	0.0080 [-0.0001]	-0.0019	0.0087		0.0018	-0.0001	-0.0001	0.0000	-0.0028
ν_{25}		-0.0018	-0.0009	0.0130 [-0.0001]	-0.0006	0.0135		-0.0029	0.0000	-0.0037	0.0000	-0.0020
ν_{26}		-0.0024	-0.0003	0.0082	-0.0003	0.0083		-0.0033	0.0000	-0.0037	0.0000	-0.0050
ν_{27}		-0.0035	-0.0001	0.0050	-0.0001	0.0049		-0.0045	0.0000	-0.0047	0.0000	-0.0066

Table 3.5: Interstate coupling parameters (in eV) of the vibronic Hamiltonian of Eq. 3.3 defined in table 3.2 between electronic states of C_{15} cluster estimated from the *ab initio* electronic structure results (see text for details).

Symm	Mode	$\lambda_k^{2,4}/\lambda_k^{3,5}$	$\lambda_k^{1,6}$	$\lambda_k^{7,9}/\lambda_k^{8,10}$										
σ_u^+	ν_8	0.1437(0.13)	0.0309(0.01)	0.1449(0.13)										
	ν_9	0.1225(0.10)	-	0.0189(0.00)										
	ν_{10}	0.1750(0.25)	0.2107(0.36)	0.0732(0.04)										
	ν_{11}	0.1663(0.24)	0.0842(0.06)	0.0193(0.00)										
	ν_{12}	0.0662(0.06)	0.0095(0.00)	-										
	ν_{13}	0.0342(0.03)	-	-										
	ν_{14}	0.0060(0.00)	0.0150(0.02)	-										
Symm	Mode	$\lambda_k^{1,4}$	$\lambda_k^{1,5}$	$\lambda_k^{2,7}$	$\lambda_k^{2,8}$	$\lambda_k^{3,7}$	$\lambda_k^{3,8}$	$\lambda_k^{4,9}$	$\lambda_k^{4,10}$	$\lambda_k^{5,9}$	$\lambda_k^{5,10}$	$\lambda_k^{2,6}$	$\lambda_k^{3,6}$	
π_g	ν_{15}	0.0237(0.03)	0.0105(0.01)	0.0280(0.04)	0.0339(0.06)	-	-	0.0307(0.05)	0.0340(0.06)	-	-	0.0356(0.07)	-	
	ν_{16}	0.0206(0.04)	-	0.0212(0.04)	0.0266(0.07)	-	-	0.0238(0.05)	0.0272(0.07)	-	-	0.0310(0.09)	-	
	ν_{17}	0.0179(0.05)	-	0.0197(0.06)	0.0219(0.07)	-	-	0.0229(0.08)	0.0243(0.09)	-	-	0.0255(0.10)	-	
	ν_{18}	-	-	-	-	-	-	-	-	-	-	-	-	
	ν_{19}	-	-	-	-	-	-	-	-	-	-	-	-	
	ν_{20}	-	-	-	-	-	-	-	-	-	-	-	-	
Symm	Mode	$\lambda_k^{1,2}$	$\lambda_k^{1,3}$	$\lambda_k^{2,9}$	$\lambda_k^{2,10}$	$\lambda_k^{3,9}$	$\lambda_k^{3,10}$	$\lambda_k^{4,7}$	$\lambda_k^{4,8}$	$\lambda_k^{5,7}$	$\lambda_k^{5,8}$	$\lambda_k^{4,6}$	$\lambda_k^{5,6}$	
π_u	ν_{21}	0.0182(0.01)	-	0.0240(0.03)	0.0272(0.02)	-	-	0.0265(0.03)	0.0315(0.04)	-	-	0.0357(0.06)	0.0020(0.00)	
	ν_{22}	0.0247(0.04)	0.0034(0.00)	0.0295(0.06)	0.0326(0.08)	-	-	0.0261(0.05)	0.0321(0.07)	-	-	0.0347(0.09)		
	ν_{23}	0.0193(0.04)	-	0.0267(0.08)	0.0267(0.08)	-	-	0.0085(0.01)	0.0154(0.03)	-	-	0.0220(0.06)		
	ν_{24}	-	-	-	-	-	-	-	-	-	-	-		
	ν_{25}	-	-	-	-	-	-	-	-	-	-	-		
	ν_{26}	-	-	-	-	-	-	-	-	-	-	-		
	ν_{27}	-	-	-	-	-	-	-	-	-	-	-		

Table 3.6: *Ab initio* calculated linear and quadratic coupling parameters for the $^1\Sigma_u^+$, $^1\Pi_g$, $^1\Pi_u$, $^1\Sigma_g^+$, $^1\Delta_g$ and $^1\Delta_u$ electronic states of C_{17} cluster. All data are given in the eV unit unless otherwise stated.

Mode	κ_k^i i=1	γ_k^i	κ_k^i or $\eta_k^{i,j}$ $[\beta_k^{i,j}]$ i=2,3	γ_k^i $[\rho_k^i]$	κ_k^i or $\eta_k^{i,j}$ $[\beta_k^{i,j}]$ i=4,5	γ_k^i $[\rho_k^i]$	κ_k^i i=6	γ_k^i	κ_k^i or $\xi_k^{i,j}$ i=7,8	γ_k^i $[\rho_k^i]$	κ_k^i or $\xi_k^{i,j}$ i=9,10	γ_k^i $[\rho_k^i]$
	$^1\Sigma_u^+$			$^1\Pi_g$		$^1\Pi_u$		$^1\Sigma_g^+$		$^1\Delta_g$		$^1\Delta_u$
ν_1*	-0.0012 (0.00)	-0.0051	-0.1401 (0.13)	-0.0057	-0.1402 (0.13)	-0.0057	0.0147 (0.00)	-0.0028	-0.0017(0.00)	-0.0165	-0.0436(0.01)	-0.0126
ν_2*	-0.0364 (0.01)	-0.0147	-0.1680 (0.19)	-0.0168	-0.1679 (0.19)	-0.0168	0.0056 (0.00)	-0.0196	0.0794(0.04)	0.0075	-0.0453(0.01)	0.0003
ν_3*	0.0112 (0.00)	-0.0037	0.1887 (0.25)	-0.0069	0.1886 (0.25)	-0.0069	-0.0238 (0.00)	-0.0037	-0.0486(0.02)	-0.0027	-0.0147(0.00)	-0.0061
ν_4*	0.0004 (0.00)	-0.0009	0.1176 (0.12)	-0.0044	0.1178 (0.12)	-0.0045	-0.0182 (0.00)	-0.0015	-0.0210(0.00)	-0.0021	-0.0225(0.00)	-0.0024
ν_5*	0.0020 (0.00)	-0.0009	-0.0625 (0.05)	-0.0007	-0.0627 (0.05)	-0.0007	-0.0121 (0.00)	-0.0007	0.0119(0.00)	-0.0009	0.0192(0.00)	-0.0016
ν_6	-0.0040 (0.00)	-0.0006	0.0372 (0.03)	-0.0001	0.0373 (0.03)	-0.0001	-0.0110 (0.00)	-0.0005	-0.0099(0.00)	-0.0006	-0.0230(0.01)	-0.0009
ν_7	-0.0065 (0.00)	-0.0004	0.0113 (0.01)	0.0001	0.0113 (0.01)	0.0001	0.0143 (0.01)	-0.0001	-0.0085(0.00)	-0.0003	-0.0235(0.03)	-0.0002
ν_8*	-0.0227 (0.27)	0.0000	-0.0026 (0.00)	0.0000	-0.0025 (0.00)	0.0000	-0.0180 (0.17)	0.0001	-0.0217(0.25)	0.0001	-0.0273(0.39)	0.0001
ν_9*	-	-0.0084	-	-0.0074	-	-0.0073	-	-0.0039		-0.0097		-0.0093
ν_{10}*	-	-0.0027		-0.0060	-	-0.0060	-	-0.0082		-0.0093		-0.0093
ν_{11}*	-	-0.0096	-	-0.0068	-	-0.0068	-	-0.0093		-0.0094		-0.0058
ν_{12}	-	-0.1381	-	-0.1076	-	0.0096	-	-0.0437		-0.0798		-0.0176
ν_{13}*	-	-0.0037	-	-0.0039	-	-0.0003	-	-0.0001		-0.0022		-0.0022
ν_{14}	-	-0.0008	-	-0.0002	-	-0.0045	-	-0.0006		-0.0021		-0.0009
ν_{15}	-	-0.0005	-	-0.0001	-	0.0003	-	-0.0004		-0.0005		-0.0005
ν_{16}	-	-0.0007		-0.0001		0.0003		0.0002		-0.0004		-0.0002
ν_{17}	-	-0.0026	-0.0034	-0.0034 [0.0001]	-0.0038[0.0002]	-0.0042	-	-0.0021	-0.0002	-0.0023	-0.0002	-0.0009 [0.0002]
ν_{18}	-	-0.0037	-0.0036	-0.0035	-0.0045[0.0003]	-0.0058	-	-0.0024	-0.0002	-0.0030 [0.0001]	-0.0003	0.0017
ν_{19}	-	-0.0039	-0.0034	-0.0026	-0.0039[0.0002]	-0.0044	-	-0.0035	-0.0001	-0.0047	-0.0003	-0.0006 [0.0002]
ν_{20}	-	-0.0041	-0.0018	0.0071	-0.0003	0.0049 [-0.0005]	-	0.0021	0.0000	0.0008	-0.0001	0.0014 [0.0004]
ν_{21}	-	-0.0023	-0.0005[-0.0001]	0.0154 [-0.0009]	-0.0005	0.0077 [-0.0007]	-	-0.0018	0.0000	-0.0027 [0.0001]	0.0000	0.0043 [0.0006]
ν_{22}*	-	-0.0020	-0.0003	0.0076	-0.0002	0.0083 [-0.0009]	-	-0.0022	0.0000	-0.0028	0.0000	-0.0034 [0.0004]
ν_{23}*	-	-0.0022	-0.0001	0.0049	-0.0001	0.0051	-	-0.0027	0.0000	-0.0030	0.0000	-0.0044
ν_{24}	-	-0.0026	-0.0035	-0.0033	-0.0035	-0.0021 [0.0001]	-	-0.0015	-0.0002	-0.0023 [0.0001]	-0.0001	-0.0024 [0.0001]
ν_{25}	-	-0.0031	-0.0043[0.0003]	-0.0061	-0.0035	-0.0036	-	-0.0023	-0.0003	-0.0024 [0.0001]	-0.0003	0.0008
ν_{26}	-	-0.0040	-0.0042[0.0003]	-0.0054	-0.0036	-0.0026	-	-0.0028	-0.0002	-0.0037	-0.0003	0.0009
ν_{27}	-	-0.0034	-0.0043[0.0002]	-0.0039 [-0.0001]	-0.0039	-0.0028	-	-0.0034	-0.0001	-0.0042	-0.0002	-0.0021 [0.0001]
ν_{28}	-	-0.0024	-0.0017	0.0157 [-0.0009]	-0.0003	0.0068 [-0.0007]	-	-0.0003	0.0000	-0.0020 [0.0001]	0.0001	0.0064 [0.0005]
ν_{29}	-	-0.0021	0.0002[-0.0002]	0.0114 [-0.0005]	-0.0002	0.0075 [-0.0008]	-	-0.0020	0.0000	-0.0027	0.0000	-0.0022 [0.0007]
ν_{30}*	-	-0.0020	0.0002	0.0067 [-0.0002]	-0.0001	0.0069	-	-0.0025	0.0000	-0.0028	0.0000	-0.0040 [0.0002]
ν_{31}*	-	-0.0027	0.0001	0.0037	0.0001	0.0037		-0.0032	0.0000	-0.0034	0.0000	-0.0049

Table 3.7: Interstate coupling parameters (in eV) of the vibronic Hamiltonian of Eq. 3.3 defined in table 3.2 between electronic states of C_{17} cluster estimated from the *ab initio* electronic structure results (see text for details).

Symm	Mode	$\lambda_k^{2,4}/\lambda_k^{3,5}$	$\lambda_k^{1,6}$	$\lambda_k^{7,9}/\lambda_k^{8,10}$											
σ_u^+	ν_9	0.1157(0.09)	0.0299(0.01)	0.1439(0.13)											
	ν_{10}	0.1577(0.17)	-	0.0370(0.01)											
	ν_{11}	0.0892(0.06)	-	0.0112(0.00)											
	ν_{12}	0.2188(0.42)	0.1912(0.32)	-											
	ν_{13}	0.0938(0.09)	0.0272(0.01)	-											
	ν_{14}	0.0516(0.05)	-	0.0073(0.00)											
	ν_{15}	0.0252(0.02)	-	0.0047(0.00)											
	ν_{16}	0.0032(0.00)	0.0140(0.03)	-											
Symm	Mode	$\lambda_k^{1,4}$	$\lambda_k^{1,5}$	$\lambda_k^{2,7}$	$\lambda_k^{2,8}$	$\lambda_k^{3,7}$	$\lambda_k^{3,8}$	$\lambda_k^{4,9}$	$\lambda_k^{4,10}$	$\lambda_k^{5,9}$	$\lambda_k^{5,10}$	$\lambda_k^{2,6}$	$\lambda_k^{3,6}$		
π_g	ν_{17}	-	0.0104(0.01)	0.0168(0.01)	0.0192(0.02)	-	-	0.0132(0.01)	0.0157(0.01)	-	-	0.0264(0.04)	0.0118(0.01)		
	ν_{18}	-	0.0139(0.02)	0.0151(0.02)	0.0174(0.02)	-	-	0.0163(0.02)	0.0198(0.03)	-	-	0.0248(0.05)			
	ν_{19}	-	0.0156(0.03)	0.0080(0.01)	0.0101(0.01)	-	-	0.0131(0.02)	0.0159(0.03)	-	-	0.0169(0.04)			
	ν_{20}	0.0246(0.19)	0.0251(0.19)	-	-	-	-	-	-	-	-	-			
	ν_{21}	0.0252(0.38)	0.0272(0.44)	-	-	-	-	-	-	-	-	-			
	ν_{22}	0.0233(1.15)	0.0234(1.15)	-	-	-	-	-	-	-	-	-			
	ν_{23}	0.0233(10.44)	0.0235(10.61)	-	-	-	-	-	-	-	-	-			
Symm	Mode	$\lambda_k^{1,2}$	$\lambda_k^{1,3}$	$\lambda_k^{2,9}$	$\lambda_k^{2,10}$	$\lambda_k^{3,9}$	$\lambda_k^{3,10}$	$\lambda_k^{4,7}$	$\lambda_k^{4,8}$	$\lambda_k^{5,7}$	$\lambda_k^{5,8}$	$\lambda_k^{4,6}$	$\lambda_k^{5,6}$		
π_u	ν_{24}	0.0125(0.01)	0.0134(0.01)	0.0104(0.00)	0.0112(0.01)	-	-	0.0140(0.01)	0.0150(0.01)	-	-	0.0233(0.02)	-		
	ν_{25}	-	0.0115(0.01)	0.0161(0.02)	0.0192(0.02)	-	-	0.0160(0.02)	0.0186(0.02)	-	-	0.0255(0.04)	-		
	ν_{26}	-	0.0139(0.02)	0.0154(0.02)	0.0189(0.04)	-	-	0.0113(0.01)	0.0137(0.02)	-	-	0.0203(0.04)	-		
	ν_{27}	-	0.0157(0.04)	0.0116(0.02)	0.0136(0.03)	-	-	0.0113(0.02)	0.0125(0.03)	-	-	0.0184(0.05)	-		
	ν_{28}	0.0311(0.39)	0.0350(0.49)	-	-	-	-	-	-	-	-	-	-		
	ν_{29}	0.0284(0.83)	0.0299(0.92)	-	-	-	-	-	-	-	-	-	0.1845(35.16)		
	ν_{30}	0.0246(3.22)	0.0241(3.08)	-	-	-	-	-	-	-	-	-	0.1632(141.54)		
	ν_{31}	0.0216(64.62)	0.0214(63.43)	-	-	-	-	-	-	-	-	-			

Table 3.8: *Ab initio* calculated linear and quadratic coupling parameters for the $^1\Sigma_u^+$, $^1\Pi_g$, $^1\Pi_u$, $^1\Sigma_g^+$, $^1\Delta_g$ and $^1\Delta_u$ electronic states of C_{19} cluster. All data are given in the eV unit unless otherwise stated.

Mode	κ_k^i i=1	γ_k^i	κ_k^i or $\eta_k^{i,j}$ $[\beta_k^{i,j}]$ i=2,3	γ_k^i $[\rho_k^i]$	κ_k^i or $\eta_k^{i,j}$ $[\beta_k^{i,j}]$ i=4,5	γ_k^i $[\rho_k^i]$	κ_k^i i=6	γ_k^i	κ_k^i or $\xi_k^{i,j}$ i=7,8	γ_k^i $[\rho_k^i]$	κ_k^i or $\xi_k^{i,j}$ i=9,10	γ_k^i $[\rho_k^i]$
	$^1\Sigma_u^+$		$^1\Pi_g$		$^1\Pi_u$		$^1\Sigma_g^+$		$^1\Delta_g$		$^1\Delta_u$	
ν_1*	-0.0030(0.00)	-0.0048	-0.1450(0.13)	-0.0061	-0.1450(0.13)	-0.0061	0.0106(0.00)	-0.0035	-0.0014(0.00)	-0.0182	-0.0396(0.01)	-0.0139
ν_2*	0.0065(0.00)	-0.0025	-0.0979(0.06)	-0.0046	-0.0979(0.06)	-0.0046	0.0108(0.00)	-0.0042	-0.0056(0.00)	-0.0053	0.0252(0.00)	-0.0031
ν_3*	0.0364(0.01)	-0.0149	0.2191(0.34)	-0.0204	0.2189(0.34)	-0.0204	-0.0050(0.00)	-0.0242	-0.0805(0.05)	-0.0076	0.0344(0.01)	-0.0020
ν_4*	0.0026(0.00)	-0.0012	0.1423(0.16)	-0.0048	0.1424(0.16)	-0.0047	-0.0165(0.00)	-0.0016	-0.0241(0.00)	-0.0022	-0.0173(0.00)	-0.0026
ν_5*	-0.0007(0.00)	-0.0010	0.0796(0.07)	-0.0017	0.0797(0.07)	-0.0017	-0.0107(0.00)	-0.0006	-0.0117(0.00)	-0.0011	-0.0153(0.00)	-0.0016
ν_6	-0.0022(0.00)	-0.0006	0.0504(0.04)	-0.0004	0.0506(0.04)	-0.0004	-0.0087(0.00)	-0.0005	-0.0084(0.00)	-0.0007	-0.0150(0.00)	-0.0014
ν_7	-0.0036(0.00)	-0.0004	0.0288(0.02)	0.0000	0.0289(0.02)	0.0000	-0.0082(0.00)	-0.0003	-0.0074(0.00)	-0.0004	-0.0240(0.02)	-0.0006
ν_8	-0.0056(0.00)	-0.0003	0.0073(0.00)	0.0001	0.0073(0.00)	0.0001	-0.0112(0.01)	-0.0001	-0.0063(0.00)	-0.0002	-0.0188(0.03)	-0.0001
ν_9*	-0.0193(0.24)	0.0000	-0.0025(0.00)	0.0000	-0.0024(0.00)	0.0000	-0.0150(0.15)	0.0000	-0.0181(0.22)	0.0000	-0.0224(0.33)	0.0001
ν_{10}	-	-0.0048		-0.0039		-0.0039	-	-0.0029		-0.0080	-	-0.0080
ν_{11}*	-	-0.0057		-0.0102		-0.0100	-	-0.0093	-	-0.0151	-	-0.0119
ν_{12}*	-	-0.0017		-0.0045		-0.0045	-	-0.0051	-	-0.0047	-	-0.0047
ν_{13}	-	-0.0219		-0.0095		-0.0095	-	-0.0200	-	-0.0217	-	-0.0013
ν_{14}	-	-0.1618		-0.1232		0.0146	-	-0.0724	-	-0.1455	-	0.0563
ν_{15}	-	-0.0013		0.0018		0.0002	-	-0.0006	-	-0.0012	-	-0.0012
ν_{16}*	-	-0.0005		-0.0002		-0.0002		-0.0004	-	-0.0011	-	-0.0007
ν_{17}*	-	-0.0004		0.0000		0.0002	-	-0.0003	-	-0.0003	-	-0.0003
ν_{18}	-	-0.0005		0.0001		0.0001	-	0.0001	-	-0.0005	-	0.0001
ν_{19}	-	-0.0019	-0.0030	-0.0025	-0.0029	-0.0024 [0.0001]	-	-0.0016	-0.0001	-0.0020 [0.0001]	-0.0001	-0.0026 [0.0001]
ν_{20}	-	-0.0022	-0.0035	-0.0030	-0.0033	-0.0019	-	-0.0016	-0.0001	-0.0027 [0.0001]	-0.0001	-0.0043 [0.0001]
ν_{21}	-	-0.0028	-0.0035	-0.0022	-0.0032	-0.0011	-	-0.0022	-0.0001	-0.0035	0.0000	-0.0046
ν_{22}	-	-0.0024	-0.0044	-0.0025	-0.0043	-0.0021	-	-0.0030	-0.0001	-0.0040	0.0000	-0.0036
ν_{23}	-	-0.0020	0.0003[-0.0004]	0.0126 [-0.0005]	-0.0016	0.0123		0.0001	0.0000	-0.0015	0.0000	-0.0027
ν_{24}	-	-0.0018	0.0011[-0.0004]	0.0108 [-0.0005]	-0.0003	0.0102	-	-0.0010	0.0000	-0.0021	0.0000	-0.0035
ν_{25}*	-	-0.0017	0.0006[-0.0002]	0.0078 [-0.0003]	-0.0002	0.0067	-	-0.0017	0.0000	-0.0021	0.0000	-0.0031
ν_{26}*	-	-0.0019	-0.0002	0.0045	-0.0002	0.0044	-	-0.0022	0.0000	-0.0024	0.0000	-0.0037
ν_{27}	-	-0.0021	-0.0037	-0.0014	-0.0037	-0.0017	-	-0.0012	-0.0001	-0.0020	-0.0001	-0.0023 [0.0001]
ν_{28}	-	-0.0019	-0.0030	-0.0026	-0.0039	-0.0031 [0.0001]	-	-0.0016	-0.0002	-0.0021 [0.0001]	-0.0001	-0.0038 [0.0001]
ν_{29}	-	-0.0026	-0.0030	-0.0016	-0.0041	-0.0022	-	-0.0018	-0.0001	-0.0033 [0.0001]	-0.0001	-0.0045 [0.0001]
ν_{30}		-0.0027	-0.0028	-0.0016	-0.0033	-0.0022	-	-0.0029	-0.0001	-0.0043 [-0.0001]	-0.0001	-0.0038 [0.0001]
ν_{31}	-	-0.0035	-0.0001	0.0050	0.0002	0.0078 [-0.0001]		0.0033	0.0000	0.0009	0.0000	-0.0027
ν_{32}	-	-0.0019	0.0007[-0.0005]	0.0124 [-0.0006]	-0.0005	0.0123		-0.0017	0.0000	-0.0021	0.0000	-0.0020
ν_{33}	-	-0.0017	0.0011[-0.0003]	0.0095 [-0.0004]	-0.0001	0.0080		-0.0014	0.0000	-0.0021	0.0000	-0.0032
ν_{34}*	-	-0.0017	0.0003	0.0063 [-0.0002]	-0.0001	0.0055		-0.0019	0.0000	-0.0022	0.0000	-0.0032
ν_{35}*	-	-0.0024	0.0001	0.0034	-0.0001	0.0034		-0.0026	0.0000	-0.0029	0.0000	-0.0042

Table 3.9: Interstate coupling parameters (in eV) of the vibronic Hamiltonian of Eq. 3.3 defined in table 3.2 between electronic states of C_{19} cluster estimated from the *ab initio* electronic structure results (see text for details).

Symm	Mode	$\lambda_k^{2,4}/\lambda_k^{3,5}$	$\lambda_k^{1,6}$	$\lambda_k^{7,9}/\lambda_k^{8,10}$										
σ_u^+	ν_{10}	0.0579(0.02)	0.0207(0.00)	0.0585(0.02)										
	ν_{11}	0.1816(0.22)	-	0.1359(0.12)										
	ν_{12}	0.1257(0.11)	-	0.0185(0.00)										
	ν_{13}	0.0414(0.02)	-	-										
	ν_{14}	0.2202(0.45)	0.1482(0.20)	-										
	ν_{15}	0.0650(0.05)	0.0131(0.00)	0.0060(0.00)										
	ν_{16}	0.0409(0.35)	0.0052(0.00)	0.0080(0.00)										
	ν_{17}	0.0186(0.06)	0.0045(0.00)	0.0039(0.00)										
	ν_{18}	0.0014(0.00)	0.0126(0.03)	-										
Symm	Mode	$\lambda_k^{1,4}$	$\lambda_k^{1,5}$	$\lambda_k^{2,7}$	$\lambda_k^{2,8}$	$\lambda_k^{3,7}$	$\lambda_k^{3,8}$	$\lambda_k^{4,9}$	$\lambda_k^{4,10}$	$\lambda_k^{5,9}$	$\lambda_k^{5,10}$	$\lambda_k^{2,6}$	$\lambda_k^{3,6}$	
π_g	ν_{19}	-	0.0213(0.02)	-	0.0124(0.01)	-	0.0102(0.00)	-	0.0205(0.02)	-	0.0185(0.02)	0.0117(0.01)	0.0057(0.00)	
	ν_{20}	-	0.0259(0.05)	-	0.0146(0.02)	-	0.0130(0.01)	-	0.0280(0.06)	-	0.0271(0.05)	0.0128(0.01)	-	
	ν_{21}	-	0.0321(0.11)	-	0.0180(0.04)	-	0.0170(0.03)	-	0.0307(0.10)	-	0.0302(0.10)	0.0105(0.01)	-	
	ν_{22}	-	0.0300(0.15)	-	0.0187(0.06)	-	0.0171(0.05)	-	0.0274(0.13)	-	0.0269(0.12)	0.0098(0.02)	-	
	ν_{23}	0.0517(1.02)	0.0576(1.27)	0.0253(0.24)	0.0289(0.32)	0.0253(0.24)	0.0288(0.32)	0.0436(0.73)	0.0484(0.89)	0.0436(0.73)	0.0483(0.89)	-	-	
	ν_{24}	0.0488(2.02)	0.0501(2.12)	0.0244(0.50)	0.0265(0.59)	0.0244(0.50)	0.0265(0.59)	0.0428(1.55)	0.0438(1.62)	0.0428(1.55)	0.0438(1.62)	-	-	
	ν_{25}	0.0403(5.11)	0.0416(5.45)	0.0217(1.48)	0.0226(1.61)	0.0217(1.48)	0.0226(1.61)	0.0360(4.08)	0.0370(4.31)	0.0360(4.08)	0.0370(4.31)	-	-	
	ν_{26}	0.0350(36.44)	0.0357(37.91)	0.0195(11.31)	0.0199(11.78)	0.0195(11.31)	0.0199(11.78)	0.0328(32.0)	0.0332(32.7)	0.0328(32.0)	0.0332(32.7)	-	-	
Symm	Mode	$\lambda_k^{1,2}$	$\lambda_k^{1,3}$	$\lambda_k^{2,9}$	$\lambda_k^{2,10}$	$\lambda_k^{3,9}$	$\lambda_k^{3,10}$	$\lambda_k^{4,7}$	$\lambda_k^{4,8}$	$\lambda_k^{5,7}$	$\lambda_k^{5,8}$	$\lambda_k^{4,6}$	$\lambda_k^{5,6}$	
π_u	ν_{27}	-	0.0263(0.03)	-	0.0243(0.02)	-	0.0229(0.02)	-	0.0138(0.01)	-	0.0139(0.01)	0.0121(0.01)	0.0046(0.00)	
	ν_{28}	-	0.0179(0.02)	-	0.0243(0.03)	-	0.0227(0.03)	-	0.0125(0.01)	-	0.0099(0.01)	0.0131(0.01)	0.0036(0.00)	
	ν_{29}	-	0.0294(0.08)	-	0.0292(0.08)	-	0.0285(0.07)	-	0.0175(0.03)	-	0.0165(0.02)	0.0120(0.01)		
	ν_{30}	-	0.0297(0.12)	-	0.0271(0.10)	-	0.0263(0.10)	-	0.0191(0.05)	-	0.0183(0.05)	0.0080(0.01)		
	ν_{31}	0.0423(0.54)	0.0447(0.60)	0.0325(0.32)	0.0345(0.36)	0.0325(0.32)	0.0345(0.36)	0.0192(0.11)	0.0180(0.10)	0.0180(0.10)	0.0178(0.10)	-		
	ν_{32}	0.0484(1.25)	0.0537(1.54)	0.0396(0.84)	0.0441(1.04)	0.0393(0.82)	0.0440(1.04)	0.0291(0.45)	0.0302(0.49)	0.0291(0.45)	0.0302(0.49)	-		
	ν_{33}	0.0424(2.74)	0.0447(3.05)	0.0374(2.13)	0.0392(2.34)	0.0374(2.13)	0.0392(2.34)	0.0240(0.88)	0.0247(0.93)	0.0240(0.88)	0.0247(0.93)	-		
	ν_{34}	0.0369(11.19)	0.0381(11.92)	0.0336(9.28)	0.0345(9.78)	0.0336(9.28)	0.0345(9.78)	0.0208(3.56)	0.0213(3.72)	0.0208(3.56)	0.0213(3.72)	-		
	ν_{35}	0.0336(250.0)	0.0338(253.9)	0.0317(223.0)	0.0318(223.0)	0.0316(223.0)	0.0318(223.0)	0.0188(78.5)	0.0190(80.0)	0.0187(78.5)	0.0190(80.0)	-		

Table 3.10: *Ab initio* calculated linear and quadratic coupling parameters for the $^1\Sigma_u^+$, $^1\Pi_g$, $^1\Pi_u$, $^1\Sigma_g^+$, $^1\Delta_g$ and $^1\Delta_u$ electronic states of C_{21} cluster. All data are given in the eV unit unless otherwise stated.

Mode	κ_k^i i=1	γ_k^i	κ_k^i or $\eta_k^{i,j}$ $[\beta_k^{i,j}]$ i=2,3	γ_k^i $[\rho_k^i]$	κ_k^i or $\eta_k^{i,j}$ $[\beta_k^{i,j}]$ i=4,5	γ_k^i $[\rho_k^i]$	κ_k^i i=6	γ_k^i	κ_k^i or $\xi_k^{i,j}$ i=7,8	γ_k^i $[\rho_k^i]$	κ_k^i or $\xi_k^{i,j}$ i=9,10	γ_k^i $[\rho_k^i]$
	$^1\Sigma_u^+$		$^1\Pi_g$		$^1\Pi_u$		$^1\Sigma_g^+$		$^1\Delta_g$		$^1\Delta_u$	
ν_1*	0.0035(0.00)	-0.0045	0.1352(0.12)	-0.0063	0.1352(0.12)	-0.0063	-0.0064(0.00)	-0.0039	0.0017(0.00)	-0.0203	0.0369(0.01)	-0.0143
ν_2*	0.0010(0.00)	-0.0021	-0.1348(0.12)	-0.0046	-0.1348(0.12)	-0.0046	0.0105(0.00)	-0.0033	0.0028(0.00)	-0.0060	0.0144(0.00)	-0.0146
ν_3	-0.0272(0.01)	-0.0078	-0.0706(0.04)	-0.0142	-0.0705(0.04)	-0.0142	-0.0047(0.00)	-0.0159	0.0494(0.02)	-0.0001	-0.0273(0.01)	-0.0004
ν_4*	0.0254(0.00)	-0.0080	0.2298(0.39)	-0.0149	0.2298(0.39)	-0.0148	-0.0106(0.00)	-0.0142	-0.0642(0.03)	0.0006	0.0051(0.00)	-0.0028
ν_5*	0.0080(0.00)	-0.0007	0.1108(0.11)	-0.0037	0.1108(0.11)	-0.0037	-0.0110(0.00)	-0.0011	-0.0147(0.00)	-0.0014	-0.0142(0.00)	-0.0017
ν_6*	0.0011(0.00)	-0.0007	-0.0597(0.04)	-0.0007	-0.0596(0.04)	-0.0008	0.0072(0.00)	-0.0005	-0.0076(0.00)	-0.0008	0.0114(0.00)	-0.0011
ν_7	-0.0021(0.00)	-0.0005	0.0414(0.03)	-0.0002	0.0415(0.03)	-0.0002	-0.0067(0.00)	-0.0004	-0.0063(0.00)	-0.0005	-0.0121(0.00)	-0.0009
ν_8	-0.0032(0.00)	-0.0003	0.0223(0.02)	0.0000	0.0224(0.02)	0.0001	-0.0063(0.00)	-0.0002	-0.0056(0.00)	-0.0003	-0.0198(0.01)	-0.0004
ν_9	-0.0049(0.00)	-0.0002	0.0045(0.00)	0.0001	0.0045(0.00)	0.0001	-0.0091(0.01)	-0.0001	-0.0049(0.00)	-0.0001	-0.0154(0.02)	-0.0001
ν_{10}*	-0.0166(0.22)	0.0000	-0.0023(0.00)	-0.0000	-0.0023(0.00)	0.0000	-0.0128(0.13)	0.0000	-0.0155(0.19)	0.0000	-0.0188(0.28)	0.0001
ν_{11}	-	-0.0034		-0.0041		-0.0041	-	-0.0038		-0.0107		-0.0073
ν_{12}*	-	-0.0060		-0.0101		-0.0101		-0.0087		-0.0102		-0.0104
ν_{13}*	-	-0.0016		-0.0052		-0.0052		-0.0043		-0.0059		-0.0059
ν_{14}*	-	-0.0014		-0.0023		-0.0023	-	-0.0058		-0.0051		-0.0021
ν_{15}*		-0.1417		0.0003		0.0003		-0.1216		-0.1526		0.0334
ν_{16}*		-0.0267		0.0073		0.0073		-0.0205		-0.0236		0.0004
ν_{17}		-0.0007		0.0001		0.0001		-0.0005		-0.0010		-0.0010
ν_{18}		-0.0004		0.0003		0.0003		-0.0003		-0.0007		-0.0007
ν_{19}		-0.0003		0.0002		0.0002		-0.0002		-0.0002		-0.0002
ν_{20}		-0.0004		0.0001		0.0001		0.0000		-0.0002		-0.0002
ν_{21}		-0.0016	-0.0023[-0.0002]	-0.0024 [0.0001]	-0.0024[-0.0002]	-0.0021		-0.0014	-0.0001	-0.0016 [0.0001]	-0.0001	-0.0019 [0.0001]
ν_{22}		-0.0017	-0.0027	-0.0032	-0.0032	-0.0025		-0.0021	-0.0001	-0.0019 [0.0001]	-0.0001	-0.0032 [0.0001]
ν_{23}		-0.0022	-0.0023[-0.0002]	-0.0022	-0.0026[-0.0002]	-0.0016		-0.0024	-0.0001	-0.0028	-0.0001	-0.0035 [0.0001]
ν_{24}		-0.0022	-0.0021[-0.0002]	-0.0021	-0.0023[-0.0002]	-0.0018		-0.0030	-	-0.0039	-0.0001	-0.0029
ν_{25}		-0.0031	-0.0012[0.0001]	0.0052	-0.0012[0.0001]	0.0054		0.0020	-	0.0013	-	-0.0021
ν_{26}		-0.0016	-0.0001	0.0118	-0.0002	0.0107		-0.0011	-	-0.0015	-	-0.0014
ν_{27}		-0.0015	-0.0002	0.0080	-0.0001	0.0077		-0.0013	-	-0.0016	-	-0.0026
ν_{28}*		-0.0014	-0.0002	0.0056	0.0001	0.0055		-0.0015	-	-0.0017	-	-0.0026
ν_{29}*		-0.0016	0.0001	0.0039	-0.0001	0.0039		-0.0018	-	-0.0020	-	-0.0031
ν_{30}		-0.0018	-0.0040[-0.0002]	-0.0015	-0.0040[-0.0002]	-0.0012		-0.0012	-	-0.0017 [0.0001]	-0.0001	-0.0018 [0.0001]
ν_{31}		-0.0016	-0.0030	-0.0028 [0.0001]	-0.0028	-0.0028		-0.0018	-0.0001	-0.0016 [0.0001]	-0.0001	-0.0028 [0.0001]
ν_{32}		-0.0020	-0.0024[-0.0002]	-0.0022	-0.0020	-0.0025		-0.0022	-0.0001	-0.0024 [0.0001]	-	-0.0033 [0.0001]
ν_{33}		-0.0023	-0.0024[-0.0002]	-0.0016	-0.0022	-0.0019		-0.0026	-0.0001	-0.0032	-	-0.0037
ν_{34}		-0.0019	-0.0052[-0.0001]	-0.0022	-0.0051	-0.0023		-0.0026	-	-0.0037	-	-0.0029
ν_{35}		-0.0018	-0.0013	0.0110	-0.0016	0.0106		0.0000	-	-0.0009	-	-0.0020
ν_{36}		-0.0016	-0.0003	0.0096	-0.0005	0.0093		-0.0012	-	-0.0016	-	-0.0028
ν_{37}		-0.0014	-0.0002	0.0066	-0.0003	0.0065		-0.0014	-	-0.0016	-	-0.0025
ν_{38}*		-0.0014	-0.0001	0.0046	-0.0001	0.0047		-0.0016	-	-0.0018	-	-0.0027
ν_{39}*		-0.0020	0.0001	0.0030	0.0001	0.0030		-0.0022	-	-0.0024	-	-0.0035

Table 3.11: Interstate coupling parameters (in eV) of the vibronic Hamiltonian of Eq. 3.3 defined in table 3.2 between electronic states of C_{21} cluster estimated from the *ab initio* electronic structure results (see text for details).

Symm	Mode	$\lambda_k^{2,4}/\lambda_k^{3,5}$	$\lambda_k^{1,6}$	$\lambda_k^{7,9}/\lambda_k^{8,10}$										
σ_u^+	ν_{11}	0.1053(0.07)	-	0.0038(0.00)										
	ν_{12}	0.1171(0.09)	-	0.1383(0.13)										
	ν_{13}	0.1642(0.19)	-	0.0557(0.02)										
	ν_{14}	0.1065(0.09)	-	-										
	ν_{15}	0.1667(0.27)	-	-										
	ν_{16}	0.1249(0.16)	-	-										
	ν_{17}	0.0526(0.04)	0.0065(0.00)	0.0078(0.00)										
	ν_{18}	0.0329(0.03)	0.0041(0.00)	0.0072(0.00)										
	ν_{19}	0.0138(0.01)	-	-										
	ν_{20}	0.0003(0.00)	0.0095(0.02)	-										
Symm	Mode	$\lambda_k^{1,4}$	$\lambda_k^{1,5}$	$\lambda_k^{2,7}$	$\lambda_k^{2,8}$	$\lambda_k^{3,7}$	$\lambda_k^{3,8}$	$\lambda_k^{4,9}$	$\lambda_k^{4,10}$	$\lambda_k^{5,9}$	$\lambda_k^{5,10}$	$\lambda_k^{2,6}$	$\lambda_k^{3,6}$	
π_g	ν_{21}	-	0.0224(0.02)	-	0.0154(0.01)	-	0.0139(0.01)	-	0.0286(0.04)	-	0.0260(0.03)	-	-	
	ν_{22}	-	0.0224(0.03)	-	0.0149(0.01)	-	0.0113(0.01)	-	0.0318(0.07)	-	0.0298(0.06)	-	0.0095(0.00)	
	ν_{23}	-	0.0359(0.13)	-	0.0242(0.06)	-	0.0232(0.05)	-	0.0386(0.14)	-	0.0376(0.14)	-	0.0151(0.02)	
	ν_{24}	-	0.0345(0.17)	-	0.0282(0.11)	-	0.0273(0.10)	-	0.0346(0.17)	-	0.0336(0.15)	-	0.0172(0.04)	
	ν_{25}	0.0490(0.71)	0.0539(0.86)	0.0209(0.13)	0.0266(0.21)	0.0209(0.13)	0.0258(0.20)	0.0417(0.51)	0.0465(0.64)	0.0417(0.51)	0.0464(0.64)	0.0121(0.04)	0.0162(0.08)	
	ν_{26}	0.0618(1.88)	0.0632(1.96)	0.0442(0.96)	0.0450(1.00)	0.0442(0.96)	0.0449(1.00)	0.0563(1.56)	0.0575(1.62)	0.0562(1.56)	0.0574(1.62)	0.0295(0.43)	0.0301(0.45)	
	ν_{27}	0.0532(3.37)	0.0540(3.47)	0.0373(1.65)	0.0379(1.71)	0.0373(1.65)	0.0379(1.71)	0.0517(3.18)	0.0524(3.27)	0.0517(3.18)	0.0524(3.27)	0.0246(0.72)	0.0250(0.74)	
	ν_{28}	0.0457(9.65)	0.0466(10.04)	0.0326(4.91)	0.0333(5.13)	0.0326(4.91)	0.0333(5.13)	0.0454(9.53)	0.0462(9.87)	0.0454(9.53)	0.0462(9.87)	0.0213(2.10)	0.0217(2.18)	
	ν_{29}	0.0404(70.56)	0.0412(73.42)	0.0290(36.38)	0.0295(37.64)	0.0290(36.38)	0.0295(37.64)	0.0423(77.39)	0.0429(79.60)	0.0423(77.39)	0.0429(79.60)	0.0189(15.45)	0.0193(16.11)	
Symm	Mode	$\lambda_k^{1,2}$	$\lambda_k^{1,3}$	$\lambda_k^{2,9}$	$\lambda_k^{2,10}$	$\lambda_k^{3,9}$	$\lambda_k^{3,10}$	$\lambda_k^{4,7}$	$\lambda_k^{4,8}$	$\lambda_k^{5,7}$	$\lambda_k^{5,8}$	$\lambda_k^{4,6}$	$\lambda_k^{5,6}$	
π_u	ν_{30}	-	0.0340(0.04)	-	0.0312(0.03)	-	0.0296(0.03)	-	0.0250(0.02)	-	0.0233(0.02)	-	0.0124(0.01)	
	ν_{31}	-	0.0215(0.02)	-	0.0260(0.04)	-	0.0235(0.03)	-	0.0152(0.01)	-	0.0099(0.01)	-	-	
	ν_{32}	-	0.0306(0.07)	-	0.0357(0.10)	-	0.0342(0.09)	-	0.0212(0.04)	-	0.0197(0.03)	-	0.0135(0.01)	
	ν_{33}	-	0.0359(0.15)	-	0.0385(0.17)	-	0.0378(0.17)	-	0.0262(0.08)	-	0.0255(0.08)	-	0.0163(0.03)	
	ν_{34}	-	0.0389(0.26)	-	0.0390(0.26)	-	0.0386(0.25)	-	0.0272(0.13)	-	0.0269(0.12)	-	0.0199(0.07)	
	ν_{35}	0.0598(1.32)	0.0663(1.61)	0.0558(1.14)	0.0617(1.40)	0.0558(1.14)	0.0617(1.40)	0.0384(0.54)	0.0445(0.73)	0.0384(0.54)	0.0444(0.72)	0.0243(0.22)	0.0287(0.30)	
	ν_{36}	0.0584(2.48)	0.0600(2.62)	0.0567(2.34)	0.0581(2.46)	0.0566(2.34)	0.0581(2.46)	0.0394(1.13)	0.0410(1.22)	0.0394(1.13)	0.0410(1.22)	0.0260(0.49)	0.0272(0.54)	
	ν_{37}	0.0492(5.24)	0.0507(5.56)	0.0483(5.05)	0.0496(5.32)	0.0483(5.05)	0.0496(5.32)	0.0344(2.56)	0.0354(2.71)	0.0343(2.56)	0.0354(2.71)	0.0223(1.08)	0.0231(1.15)	
	ν_{38}	0.0428(21.68)	0.0434(22.29)	0.0436(22.49)	0.0441(23.02)	0.0436(22.49)	0.0441(23.02)	0.0306(11.09)	0.0312(11.52)	0.0303(11.09)	0.0310(11.37)	0.0198(4.64)	0.0203(4.88)	
	ν_{39}	0.0389(525.42)	0.0389(525.42)	0.0410(583.68)	0.0410(583.68)	0.0410(583.68)	0.0410(583.68)	0.0279(270.28)	0.0280(272.22)	0.0279(270.28)	0.0280(272.22)	0.0180(112.50)	0.0181(113.75)	

3.4 Results and Discussion

3.4.1 Adiabatic potential energy surfaces

In this section we examine the topography of the adiabatic PESs of ten (including degeneracy) excited singlet electronic states (as discussed above) obtained by diagonalizing the electronic Hamiltonian of the diabatic model developed above. One dimensional cuts of the potential energy hypersurfaces of C_{2n+1}, (where, n=7-10) are plotted along the given totally symmetric (σ_g^+) and RT active (π_g and π_u) vibrational modes keeping others at their equilibrium values at, $\mathbf{Q}$=0, are shown in Figs. 3.2, 3.3, 3.4, 3.5, 3.6, 3.7, 3.8, 3.9, 3.10, 3.11, 3.12 and 3.13. In the figure the solid curves represent the adiabatic potential energy functions obtained from the model developed in Sec 3.2 and the points superimposed on them are obtained from *ab initio* quantum chemical calculations discussed in Sec. 3.2. It can be seen from the figures that the *ab initio* energies are very well reproduced by the model. The energetic minimum of the seam of various CIs and the minimum of the upper adiabatic electronic states are estimated with a QVC(quadratic vibronic coupling) model. The resulting data are collected in Table 3.12. The diagonal entries in this table are the energy at the minimum of a state. Whereas, the off-diagonal entries represent the minimum of the seam of CIs.

The probable impact of this energetics is explained below in detail for all the four clusters:

In case of C_{15}, $^1\Sigma_u^+$ electronic state is vertically above the $^1\Pi_g$ and $^1\Pi_u$ and below $^1\Delta_g$, $^1\Delta_u$ and $^1\Sigma_g^+$ states. $^1\Pi_g$ and $^1\Pi_u$ states intersect with $^1\Sigma_u^+$ state at a large distance ($\approx$ 3 (Q)). $^1\Pi_g$ and $^1\Pi_u$ states can form low energy conical inter-

section with $^1\Sigma_u^+$ state along the normal coordinates of the symmetric stretching modes ν_1 (2243 cm^{-1}) and ν_4 (1755 cm^{-1}). $^1\Pi_g$ and $^1\Pi_u$ electronic states are quasi-degenerate at their equilibrium minimum (cf. Fig. 3.2). Vertically these states are separated by only $\sim$ 0.002 eV (cf. Table 3.1). The minimum of $^1\Pi_g$ - $^1\Pi_u$ intersections occurs at $\sim$ 1.82 eV above the minimum of the upper adiabatic $^1\Pi_u$ electronic state. From Table 3.5 it can be seen that interstate coupling between these states is moderately strong along the anti-symmetric stretch, ν_{10} (2001 cm^{-1}) and ν_{11} (1924 cm^{-1}) vibrational modes of σ_u^+ symmetry. Similarly, the minimum of the $^1\Sigma_u^+$ state is only $\sim$0.04 eV lower in energy than the minimum of the $^1\Sigma_u^+$ - $^1\Pi_g$ and $^1\Sigma_u^+$ - $^1\Pi_u$ PRT intersection minimum. This would leads to a ultrafast nonradiative decay of the excited electronic state. Strong interstate coupling between these states is caused by the π_u and π_g vibrational modes (cf. Table 3.5). Hence, it is expected that the absorption bands of $^1\Pi_g$, $^1\Pi_u$ and $^1\Sigma_u^+$ will be perturbed significantly by the $^1\Pi_g$ - $^1\Sigma_u^+$ and $^1\Pi_u$ - $^1\Sigma_u^+$ interstate couplings. Similarly, the minimum of $^1\Pi_g$ - $^1\Sigma_g^+$ and $^1\Pi_u$ - $^1\Sigma_g^+$ CIs occurs $\sim$ 0.12 eV above the minimum of $^1\Sigma_g^+$ electronic state. The interstate coupling between them is weak. The $^1\Sigma_u^+$ - $^1\Sigma_g^+$ intersection minimum occurs at much higher energy $\sim$ 2.7 eV above the $^1\Sigma_u^+$ minimum. This separation is relatively high when compared to the remaining energetic positions discussed above. However, the strong coupling between $^1\Sigma_u^+$ - $^1\Sigma_g^+$ along ν_{10} (2001 cm^{-1}) (anti-symmetric stretch) makes the nonadiabatic interactions stronger in these coupled electronic states. It can be seen from the Fig 3.2 that along the coordinates of ν_2 (2216 cm^{-1}) and ν_3 (2055 cm^{-1}) symmetric stretch vibrational modes low energy crossing among $^1\Sigma_u^+$ - $^1\Pi_g$ - $^1\Pi_u$ - $^1\Delta_g$ - $^1\Delta_u$ - $^1\Sigma_g^+$ states develop. $^1\Pi_g$ - $^1\Delta_g$ and $^1\Pi_u$ - $^1\Delta_g$ intersection minimum occurs at $\sim$ 0.03 eV above the $^1\Delta_g$ state minimum and $^1\Pi_g$ - $^1\Delta_u$ and $^1\Pi_u$ - $^1\Delta_u$ minimum occurs at $\sim$ 0.14 eV above the $^1\Delta_g$ state minimum. $^1\Delta_g$ -

$^1\Delta_u$ intersection minimum is degenerate with the $^1\Delta_u$ state minimum, shows a strong coupling along the anti-symmetric stretch vibration, ν_8 (2260 cm^{-1}).

In case of C_{17}, optically bright $^1\Sigma_u^+$ electronic state is vertically below the $^1\Pi_g$, $^1\Pi_u$, $^1\Delta_g$, $^1\Delta_u$ and $^1\Sigma_g^+$ states. The minimum of this state occurs close to the minimum of the seams of intersection with the $^1\Pi_g$ and $^1\Pi_u$ states and $^1\Pi_g$ and $^1\Pi_u$ electronic states are quasi-degenerate and have approximately same equilibrium minimum (cf. Fig. 3.2 and Table 3.12). From Table 3.7 it can be seen that interstate coupling between these states is moderately strong along the anti-symmetric stretch, ν_{12} (1932 cm^{-1}) vibrational mode of σ_u^+ symmetry. The $^1\Sigma_u^+$ - $^1\Pi_g$ and $^1\Sigma_u^+$ - $^1\Pi_u$ intersection minimum occurs $\sim$ 0.08 eV and $\sim$ 0.09 eV above the minimum of the $^1\Pi_g$ and $^1\Pi_u$ states, respectively. Interstate coupling between $^1\Sigma_u^+$ - $^1\Pi_g$, and $^1\Sigma_u^+$ - $^1\Pi_u$ states is very strong along the low frequency π_u nag π_g bending vibrational modes (cf. Table 3.7). It can be seen from Fig. 3.5 that along the symmetric stretch vibrational modes, ν_1 (2257 cm^{-1}), ν_2 (2182 cm^{-1}), ν_3 (2136 cm^{-1}) and ν_4 (1925 cm^{-1}) low energy crossing among $^1\Sigma_u^+$ - $^1\Pi_g$ - $^1\Pi_u$ - $^1\Delta_g$ - $^1\Delta_u$ - $^1\Sigma_g^+$ states develop. The $^1\Sigma_u^+$ - $^1\Sigma_g^+$ intersection minimum occurs at much higher energy, $\sim$ 3 eV above the $^1\Sigma_u^+$ minimum. This separation is relatively large when compared to the remaining energetic positions discussed above. However, strong coupling between $^1\Sigma_u^+$ - $^1\Sigma_g^+$ along ν_{12} (1932 cm^{-1}) mode makes the nonadiabatic interactions stronger in these coupled electronic states. The minimum of the $^1\Delta_u$ state is degenerate with the minimum of the seam of its intersections with the $^1\Pi_g$ and $^1\Pi_u$ states. Similarly, the equilibrium minimum of the $^1\Delta_g$ state is quasi-degenerate with the minimum of its seam of intersections with the $^1\Pi_g$ state. The minimum of $^1\Delta_u$ - $^1\Delta_g$ conical intersections occur at $\sim$ 0.01 eV above the minimum of $^1\Delta_g$ state. It shows a strong coupling along

the anti-symmetric stretch, ν_9 (2248 cm^{-1}) vibrational mode of σ_u^+ symmetry (cf. Table 3.7).

In case of C_{19}, the $^1\Sigma_u^+$ electronic state is vertically below the $^1\Pi_g$, $^1\Pi_u$, $^1\Delta_g$, $^1\Delta_u$ and $^1\Sigma_g^+$ electronic states. The $^1\Pi_g$ and $^1\Pi_u$ electronic states are quasi-degenerate and their equilibrium minimum occurs at nearly same location. The minimum of $^1\Pi_g$ - $^1\Pi_u$ intersections is $\sim$ 0.43 eV above the minimum of the $^1\Pi_u$ electronic state and these are strongly coupled along the anti-symmetric stretch vibrational modes, ν_{11} (2222 cm^{-1}), ν_{14} (1869 cm^{-1}), and ν_{16} (1251 cm^{-1}) (cf. Table 3.9) of σ_u^+ symmetry. The minimum of $^1\Sigma_u^+$ - $^1\Pi_g$ and $^1\Sigma_u^+$ - $^1\Pi_u$ intersections is energetically very close to the minimum of the $^1\Pi_g$ and $^1\Pi_u$ states. These intersections are just $\sim$ 0.17 eV above the minimum of the $^1\Sigma_u^+$ state. The interstate coupling between these states are strong along the low frequency π_g and π_u vibrational modes (cf. Table 3.9). The minimum of $^1\Sigma_u^+$ - $^1\Sigma_g^+$ conical intersections occurs at much higher energy, $\sim$ 2.6 eV above the equilibrium minimum of the $^1\Sigma_g^+$ state. These states are fairly strongly coupled by the anti-symmetric stretch ν_{14} (1869 cm^{-1}) vibrational mode of σ_u^+ symmetry. The $^1\Delta_g$ - $^1\Delta_u$ intersection minimum occurs at $\sim$ 0.15 eV above the $^1\Delta_u$ minimum, coupled through the anti-symmetric stretch, ν_{11} (2222 cm^{-1}) vibrational mode of σ_u^+ symmetry. It can be seen from the Fig. 3.8 that along the symmetric stretch coordinates of ν_3 (2138 cm^{-1}) and ν_4 (2018 cm^{-1}) vibrational modes low energy crossing among $^1\Sigma_u^+$ - $^1\Pi_g$ - $^1\Pi_u$ - $^1\Delta_g$ - $^1\Delta_u$ - $^1\Sigma_g^+$ states develop. From Table 3.9, it is seen that the interstate coupling between the $^1\Delta_{g/u}$ - $^1\Pi_{g/u}$ state is very strong along the low frequency vibrational modes of π_g and π_u symmetry. The $^1\Delta_u$ - $^1\Pi_g$ and $^1\Delta_g$ - $^1\Pi_g$ intersection minimum is $\sim$ 0.04 and $\sim$ 0.15 eV above the $^1\Pi_g$ minimum. Similarly, $^1\Delta_u$ - $^1\Pi_g$ and $^1\Delta_g$ - $^1\Pi_u$ intersection minimum is $\sim$ 0.15 above the $^1\Pi_u$

minimum.

In case of C_{21}, the $^1\Sigma_u^+$ electronic state is vertically below the $^1\Pi_g$, $^1\Pi_u$, $^1\Delta_g$, $^1\Delta_u$ and $^1\Sigma_g^+$ states. The $^1\Pi_g$ and $^1\Pi_u$ electronic states are quasi-degenerate and have the equilibrium minimum located nearly at the same place (cf. Table 3.12 and Fig. 3.11). The minimum of the $^1\Pi_u$-$^1\Pi_g$ intersections occurs $\sim$ 0.30 eV above the minimum of the $^1\Pi_g$ electronic state. These states are strongly coupled along the anti-symmetric stretch, ν_{13} (2166 cm^{-1}), ν_{15} (1821 cm^{-1}), and ν_{16} (1784 cm^{-1}) (cf. Table 3.11) vibrational modes of σ_u^+ symmetry. The $^1\Sigma_u^+$-$^1\Pi_g$ and $^1\Sigma_u^+$-$^1\Pi_u$ intersection minimum are close to the minimum of the $^1\Pi_g$ and $^1\Pi_u$ state, with an energy gap of $\sim$ 0.01 and $\sim$ 0.03 eV, respectively. These intersections occur $\sim$ 0.41 eV above the minimum $^1\Sigma_u^+$ state. The interstate coupling between these states are strong along the low frequency π_g and π_u bending vibrational modes. The $^1\Sigma_u^+$ -$^1\Sigma_g^+$ conical intersection minimum occurs at much higher energy at $\sim$ 3.8 eV above the minimum of the $^1\Sigma_g^+$ state. The coupling is also weak between these states (cf. Table 3.11). The $^1\Delta_u$ and $^1\Delta_g$ intersection minimum occurs at $\sim$ 0.39 eV above the minimum of the $^1\Delta_g$ state. They are coupled through the anti-symmetric stretch, ν_{12} (2202 cm^{-1}) vibrational mode of σ_u^+ symmetry. It can be seen from the Fig 3.11 that along the symmetric stretch vibrational mode of ν_1 (2250 cm^{-1}) and ν_4 (2087 cm^{-1}) low energy crossing among $^1\Sigma_u^+$-$^1\Pi_g$-$^1\Pi_u$-$^1\Delta_g$-$^1\Delta_u$-$^1\Sigma_g^+$ states develop. From Table 3.11, it can be seen that interstate coupling between the $^1\Delta_{g/u}$-$^1\Pi_{g/u}$ state is very strong along the low frequency vibrational modes of π_g and π_u symmetry. The $^1\Delta_u$ -$^1\Pi_u$ and $^1\Delta_g$ -$^1\Pi_u$ intersection minimum is $\sim$ 0.02 eV lower and $\sim$ 0.04 eV above the minimum of the $^1\Pi_u$ state. Likewise, $^1\Delta_u$ -$^1\Pi_g$ intersection minimum is degenerate with the $^1\Pi_g$ state minimum whereas $^1\Delta_g$ -$^1\Pi_g$ intersection minimum is $\sim$ 0.06 eV above

the $^1\Pi_g$ state minimum.

Implications of these stationary points on the potential energy hypersurfaces on the nuclear dynamics is studied and discussed in chapter-4.

Table 3.12: Estimated equilibrium minimum (diagonal entries) and minimum of the seam of various intersection seams (off-diagonal entries) of the electronic states of C_{15}, C_{17}, C_{19} and C_{21} within a quadratic coupling model. All quantities are given in eV.

C_{15}							C_{17}						
	$^1\Pi_g$	$^1\Pi_u$	$^1\Sigma_u^+$	$^1\Delta_g$	$^1\Delta_u$	$^1\Sigma_g^+$		$^1\Sigma_u^+$	$^1\Pi_u$	$^1\Pi_g$	$^1\Delta_u$	$^1\Delta_g$	$^1\Sigma_g^+$
$^1\Pi_g$	2.91	4.73	3.30	3.48	3.62	3.77	$^1\Sigma_u^+$	2.94	2.96	2.96	-	-	6.21
$^1\Pi_u$	-	2.91	3.30	3.48	3.62	3.77	$^1\Pi_u$	-	2.87	3.99	3.11	3.27	3.37
$^1\Sigma_u^+$	-	-	3.26	-	-	5.97	$^1\Pi_g$	-	-	2.88	3.11	3.17	3.37
$^1\Delta_g$	-	-	-	3.45	3.48	-	$^1\Delta_u$	-	-	-	3.11	3.18	-
$^1\Delta_u$	-	-	-	-	3.48	-	$^1\Delta_g$	-	-	-	-	3.17	-
$^1\Sigma_g^+$	-	-	-	-	-	3.60	$^1\Sigma_g^+$	-	-	-	-	-	3.34
C_{19}							C_{21}						
	$^1\Sigma_u^+$	$^1\Delta_u$	$^1\Delta_g$	$^1\Pi_g$	$^1\Pi_u$	$^1\Sigma_g^+$		$^1\Sigma_u^+$	$^1\Delta_u$	$^1\Delta_g$	$^1\Sigma_g^+$	$^1\Pi_u$	$^1\Pi_g$
$^1\Sigma_u^+$	2.67	-	-	2.84	2.84	5.72	$^1\Sigma_u^+$	2.44	-	-	6.73	2.85	2.85
$^1\Delta_u$	-	2.79	3.10	2.88	2.89	-	$^1\Delta_u$	-	2.53	3.14	-	2.82	2.82
$^1\Delta_g$	-	-	2.95	2.99	2.99	-	$^1\Delta_g$	-	-	2.75	-	2.88	2.88
$^1\Pi_g$	-	-	-	2.84	3.27	3.12	$^1\Sigma_g^+$	-	-	-	2.93	2.96	2.96
$^1\Pi_u$	-	-	-	-	2.84	3.12	$^1\Pi_u$	-	-	-	-	2.84	3.12
$^1\Sigma_g^+$	-	-	-	-	-	3.12	$^1\Pi_g$	-	-	-	-	-	2.82

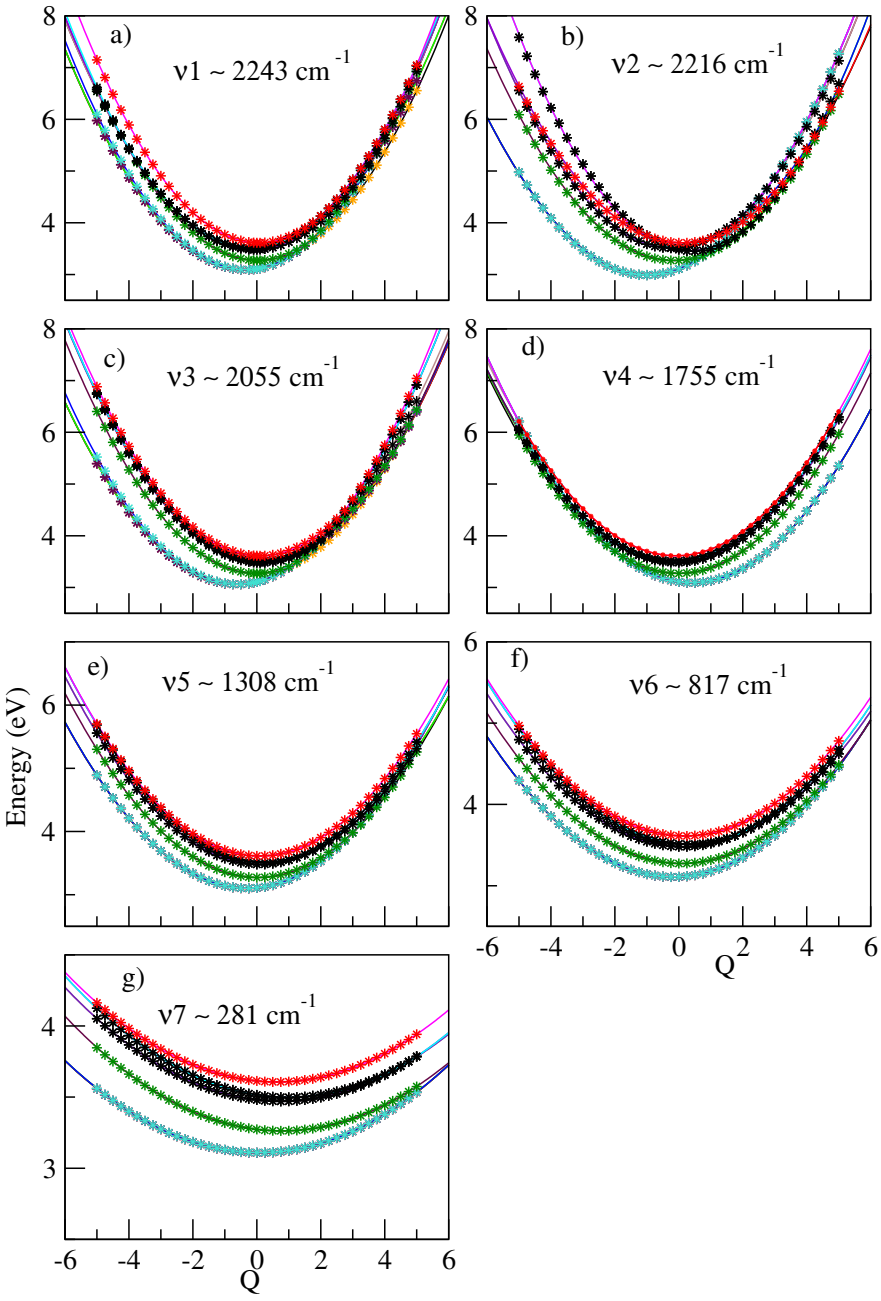

Figure 3.2: Adiabatic potential energies of the low-lying excited singlet electronic states, $^1\Pi_g$, $^1\Pi_u$, $^1\Sigma_u^+$, $^1\Delta_g$, $^1\Delta_u$ and $^1\Sigma_g^+$ of C_{15} along the normal coordinates of totally symmetric vibrational modes (σ_g^+). The potential energies obtained from the present vibronic model are shown by the solid lines and the computed *ab initio* energies are shown by the asterisk.

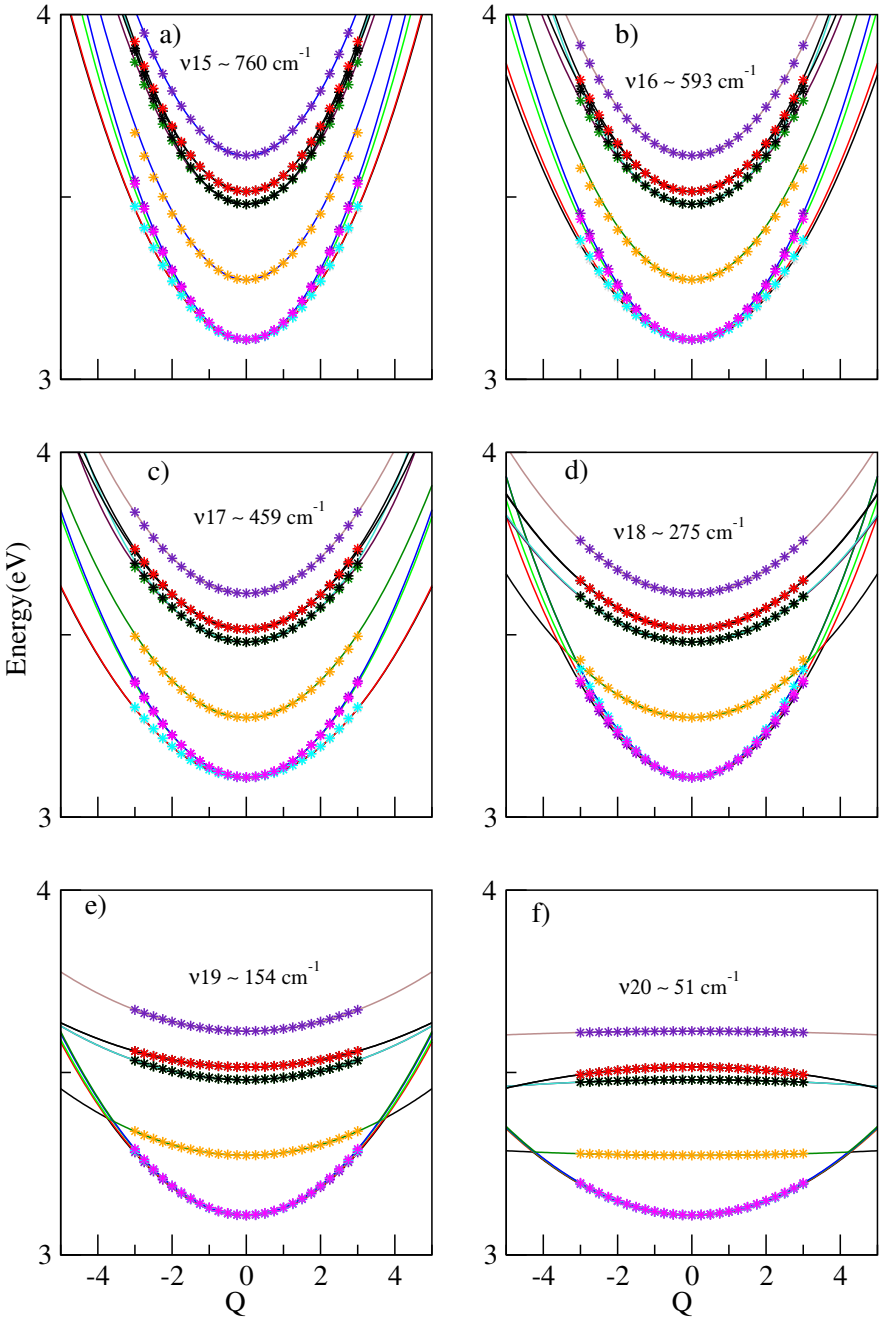

Figure 3.3: Adiabatic potential energies of the low-lying excited singlet electronic states, $^1\Pi_g$, $^1\Pi_u$, $^1\Sigma_u^+$, $^1\Delta_g$, $^1\Delta_u$ and $^1\Sigma_g^+$ of C_{15}, along the normal coordinates of RT active vibrational modes (π_g). The potential energies obtained from the present vibronic model are shown by the solid lines and the computed *ab initio* energies are shown by the asterisk.

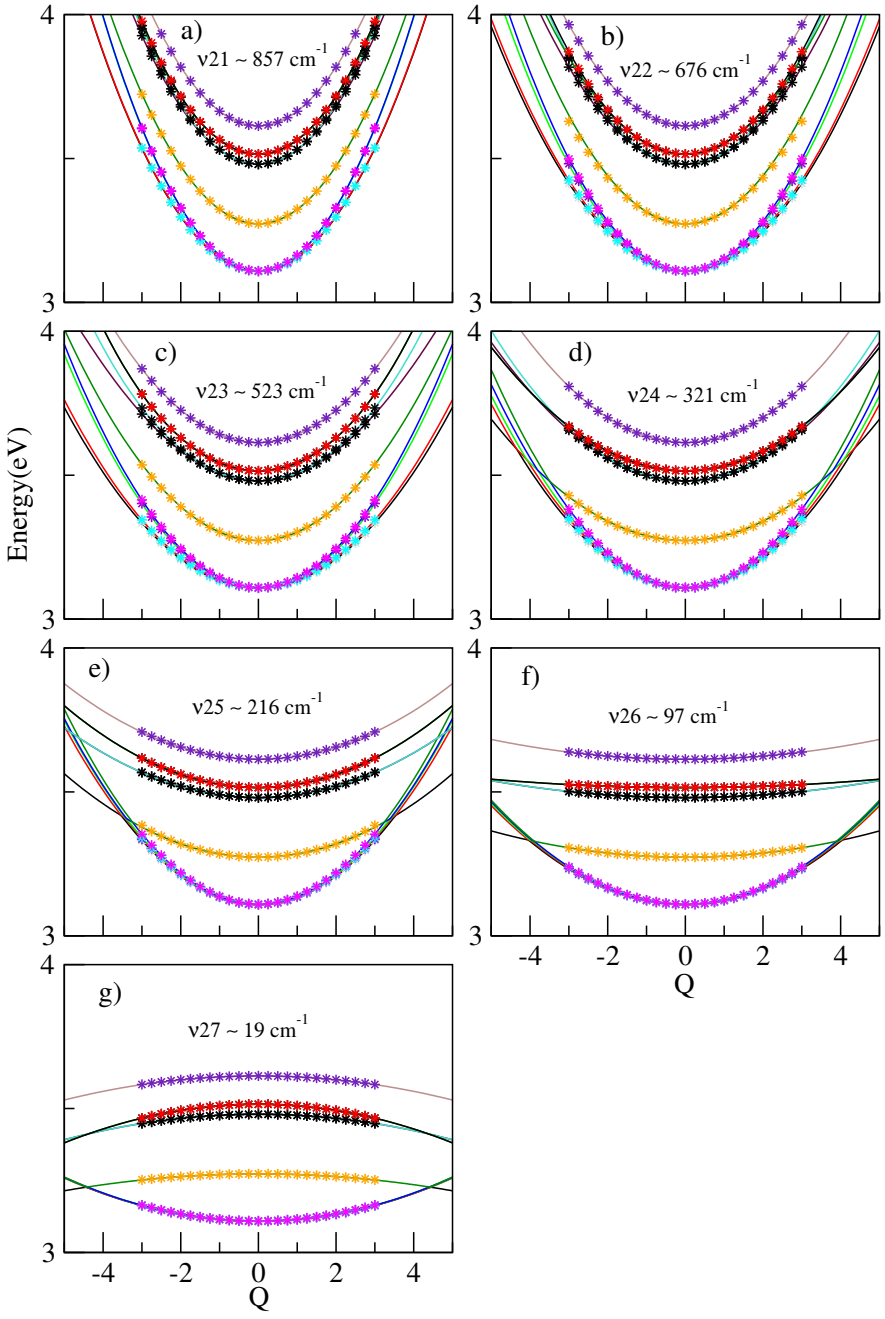

Figure 3.4: Adiabatic potential energies of the low-lying excited singlet electronic states, $^1\Pi_g$, $^1\Pi_u$, $^1\Sigma_u^+$, $^1\Delta_g$, $^1\Delta_u$ and $^1\Sigma_g^+$ of C_{15}, along the normal coordinates of RT active vibrational modes (π_u) . The potential energies obtained from the present vibronic model are shown by the solid lines and the computed *ab initio* energies are shown by the asterisk.

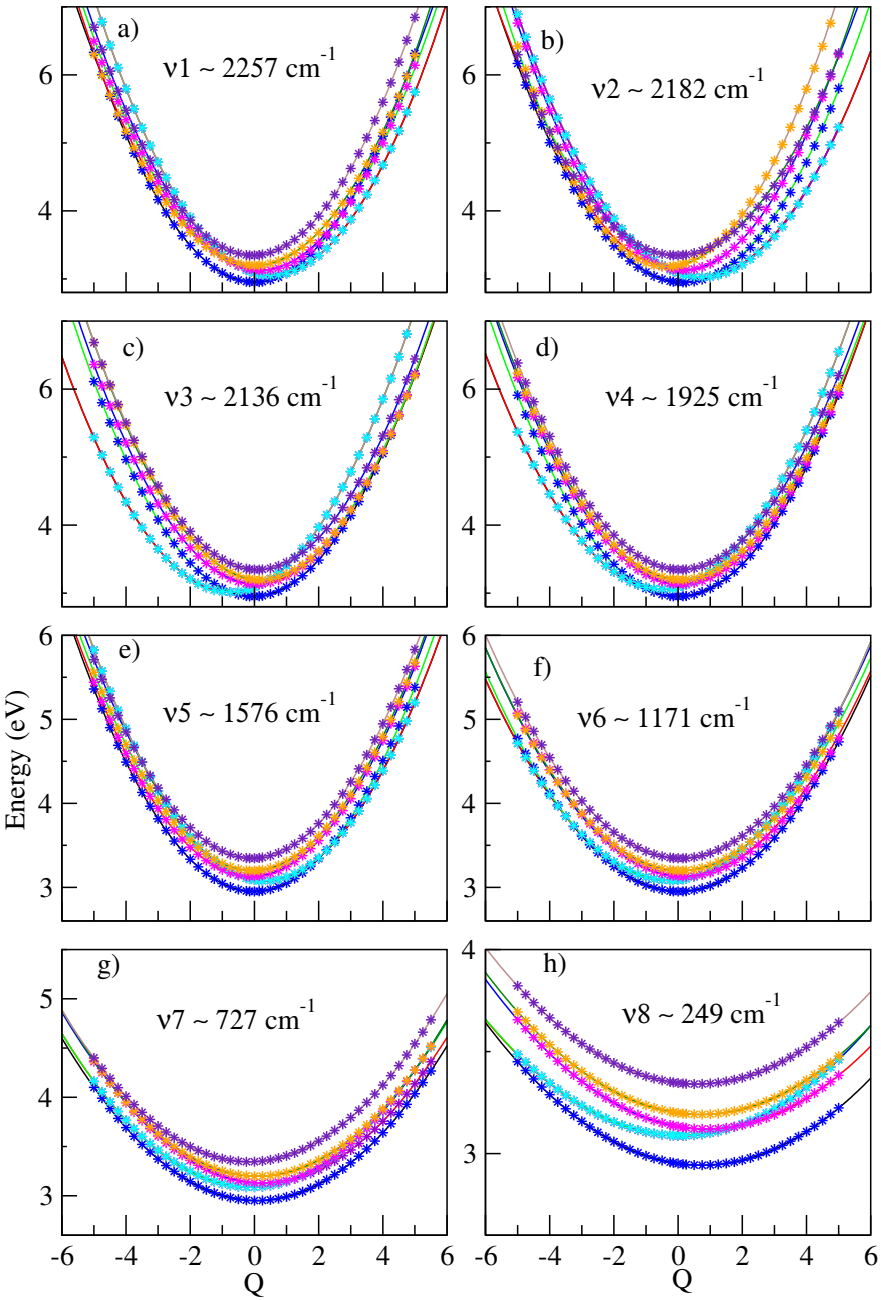

Figure 3.5: Adiabatic potential energies of the low-lying excited singlet electronic states, $^1\Sigma_u^+$, $^1\Pi_u$, $^1\Pi_g$, $^1\Delta_u$, $^1\Delta_g$ and $^1\Sigma_g^+$ of C_{17}, along the normal coordinates of totally symmetric vibrational modes (σ_g^+). The potential energies obtained from the present vibronic model are shown by the solid lines and the computed *ab initio* energies are shown by the asterisk.

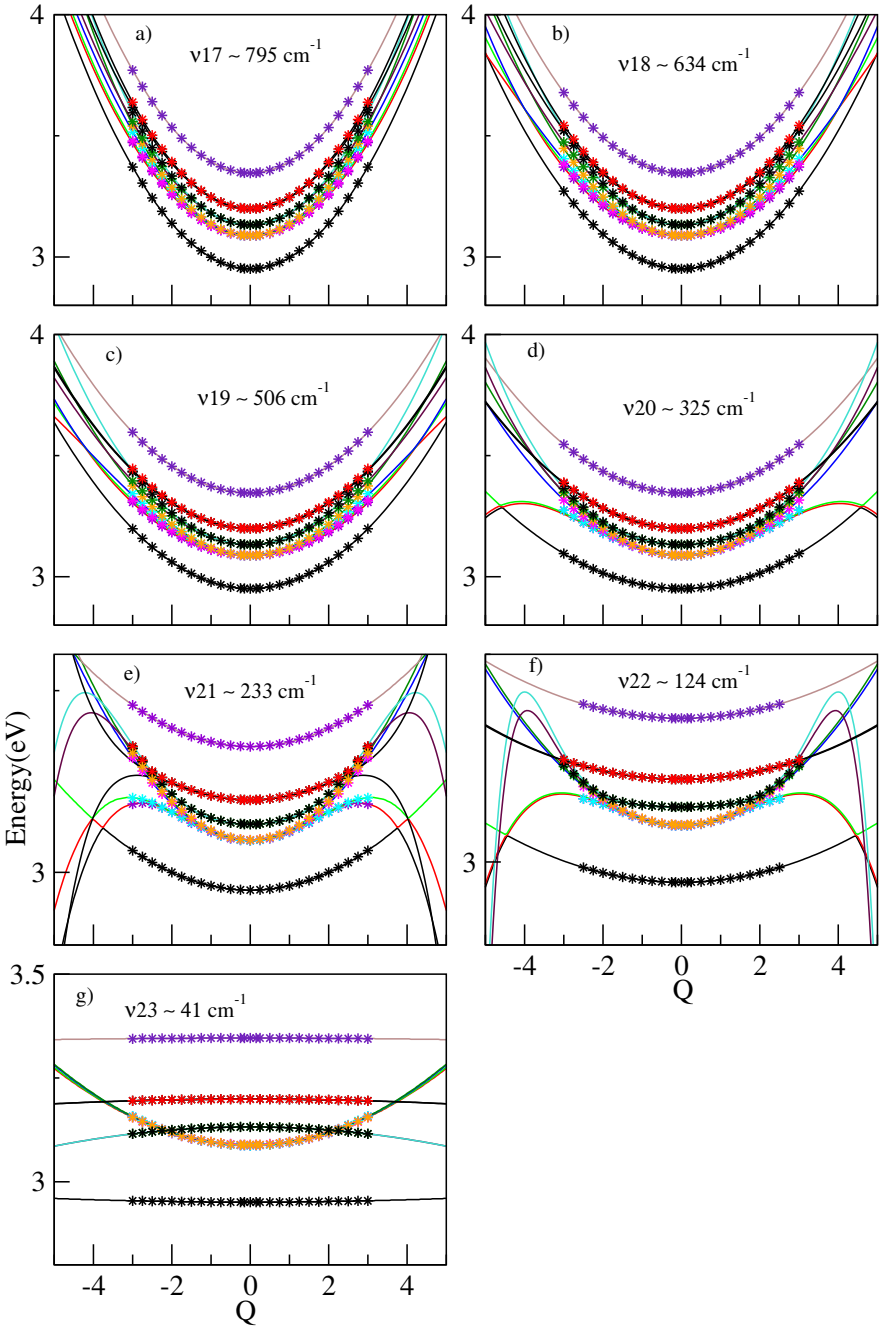

Figure 3.6: Adiabatic potential energies of the low-lying excited singlet electronic states, $^1\Sigma_u^+$, $^1\Pi_u$, $^1\Pi_g$, $^1\Delta_u$, $^1\Delta_g$ and $^1\Sigma_g^+$ of C_{17}, along the normal coordinates of RT active vibrational modes (π_g). The potential energies obtained from the present vibronic model are shown by the solid lines and the computed *ab initio* energies are shown by the asterisk.

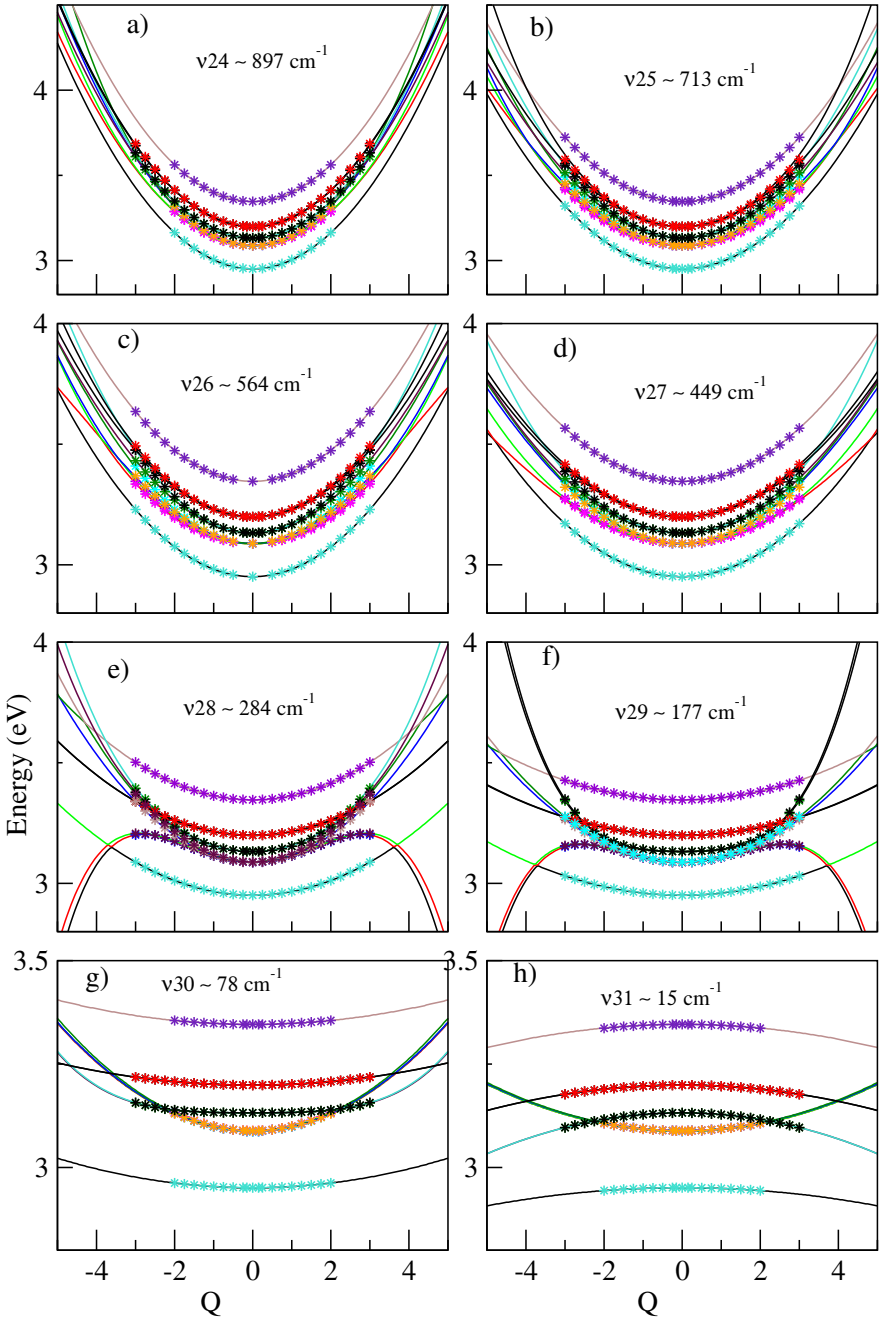

Figure 3.7: Adiabatic potential energies of the low-lying excited singlet electronic states, $^1\Sigma_u^+$, $^1\Pi_u$, $^1\Pi_g$, $^1\Delta_u$, $^1\Delta_g$ and $^1\Sigma_g^+$ of C_{17}, along the normal coordinates of RT active vibrational modes (π_u). The potential energies obtained from the present vibronic model are shown by the solid lines and the computed *ab initio* energies are shown by the asterisk.

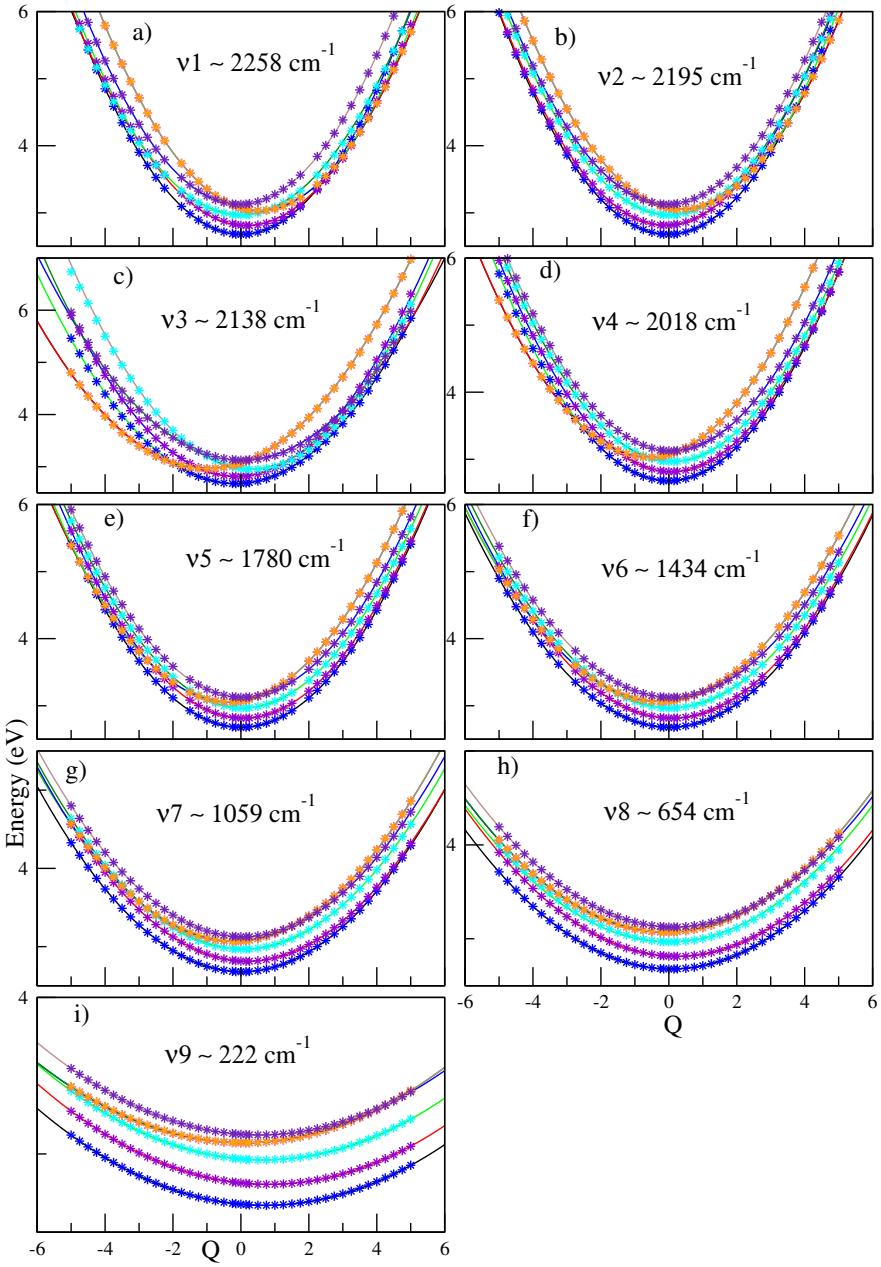

Figure 3.8: Adiabatic potential energies of the low-lying excited singlet electronic states, $^1\Sigma_u^+$, $^1\Delta_u$, $^1\Delta_g$, $^1\Pi_g$, $^1\Pi_u$ and $^1\Sigma_g^+$ of C_{19}, along the normal coordinates of totally symmetric vibrational modes (σ_g^+). The potential energies obtained from the present vibronic model are shown by the solid lines and the computed *ab initio* energies are shown by the asterisk.

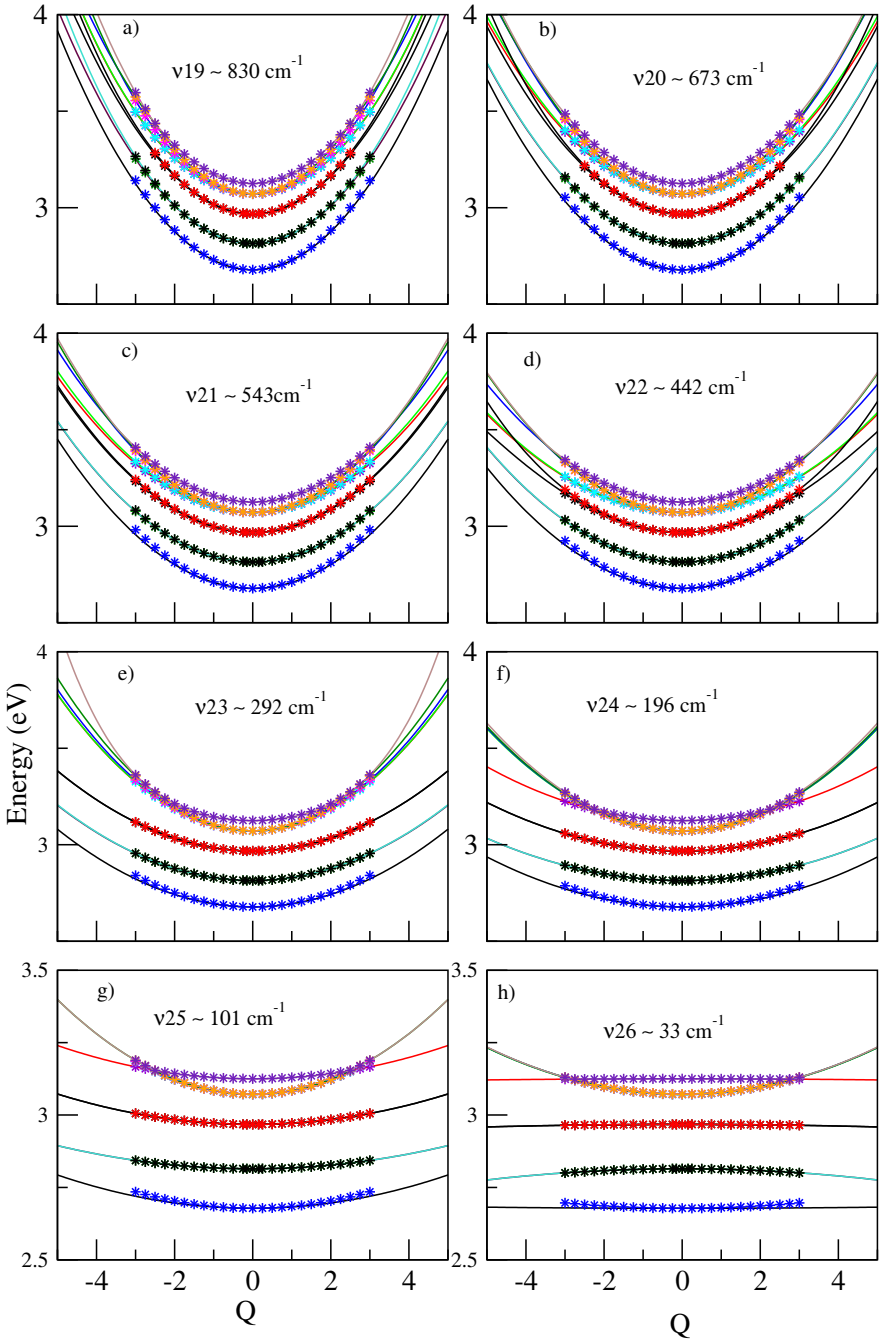

Figure 3.9: Adiabatic potential energies of the low-lying excited singlet electronic states, $^1\Sigma_u^+$, $^1\Delta_u$, $^1\Delta_g$, $^1\Pi_g$, $^1\Pi_u$ and $^1\Sigma_g^+$ of C_{19}, along the normal coordinates of RT active vibrational modes (π_g). The potential energies obtained from the present vibronic model are shown by the solid lines and the computed *ab initio* energies are shown by the asterisk.

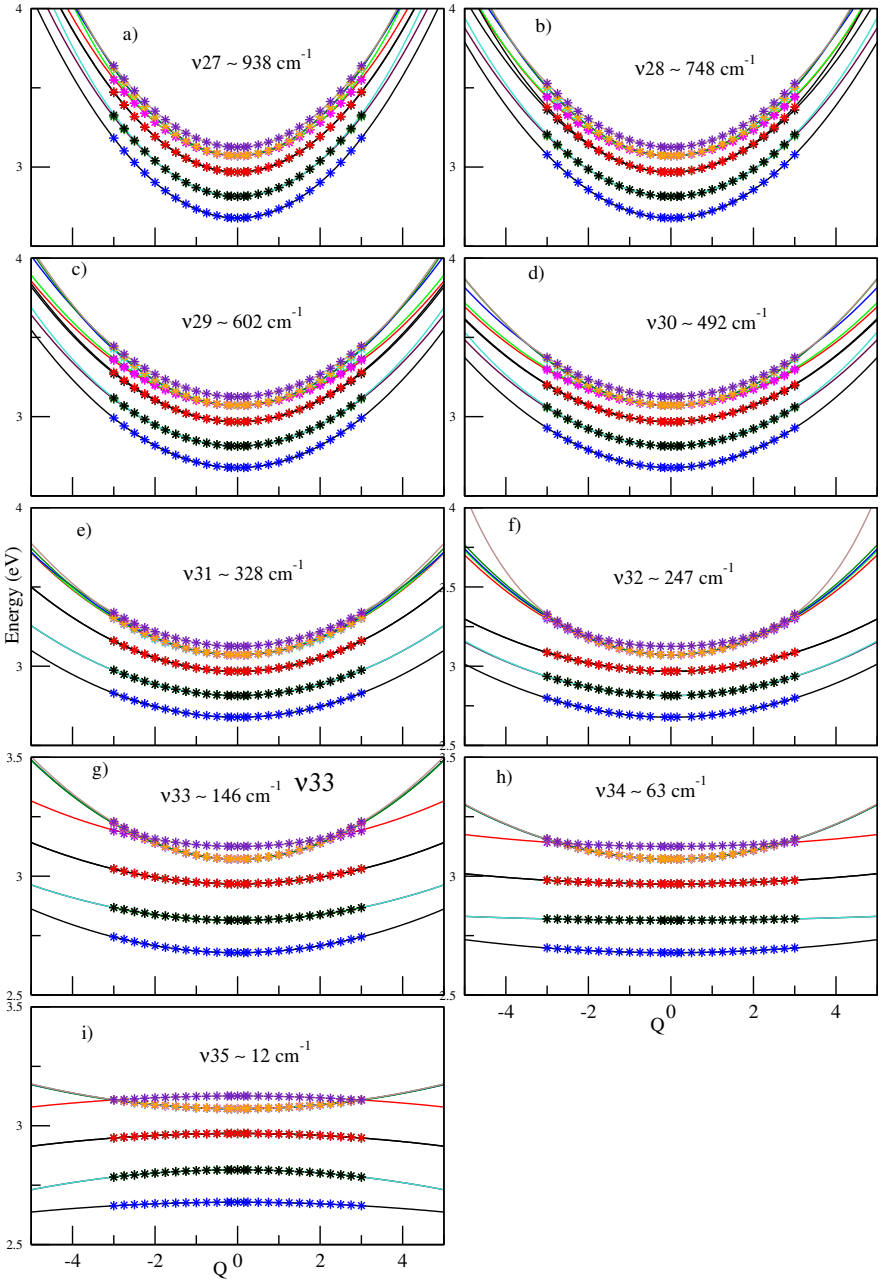

Figure 3.10: Adiabatic potential energies of the low-lying excited singlet electronic states, $^1\Sigma_u^+$, $^1\Delta_u$, $^1\Delta_g$, $^1\Pi_g$, $^1\Pi_u$ and $^1\Sigma_g^+$ of C_{19}, along the normal coordinates of RT active vibrational modes (π_u). The potential energies obtained from the present vibronic model are shown by the solid lines and the computed *ab initio* energies are shown by the asterisk.

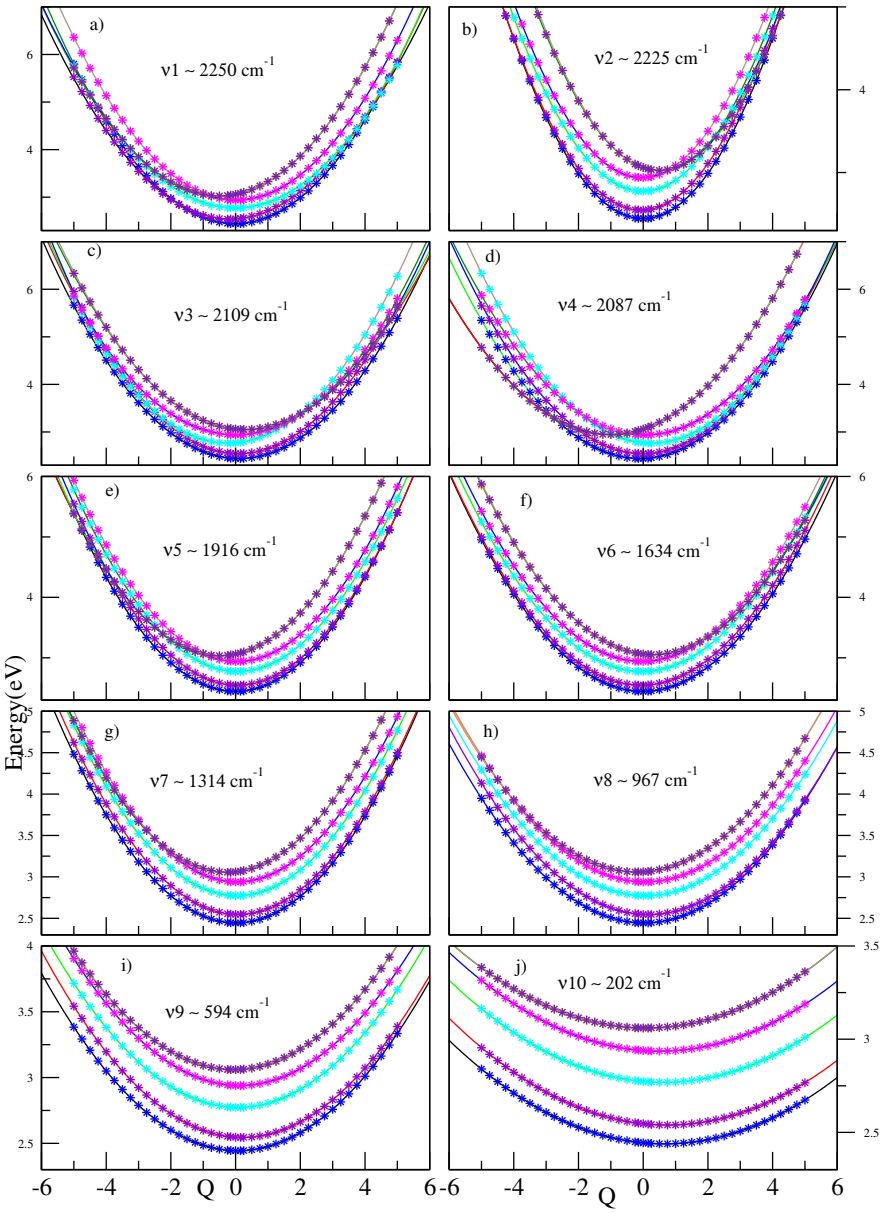

Figure 3.11: Adiabatic potential energies of the low-lying excited singlet electronic states, $^1\Sigma_u^+$, $^1\Delta_u$, $^1\Delta_g$, $^1\Sigma_g^+$, $^1\Pi_u$ and $^1\Pi_g$ of C_{21}, along the normal coordinates of totally symmetric vibrational modes (σ_g^+). The potential energies obtained from the present vibronic model are shown by the solid lines and the computed *ab initio* energies are shown by the asterisk.

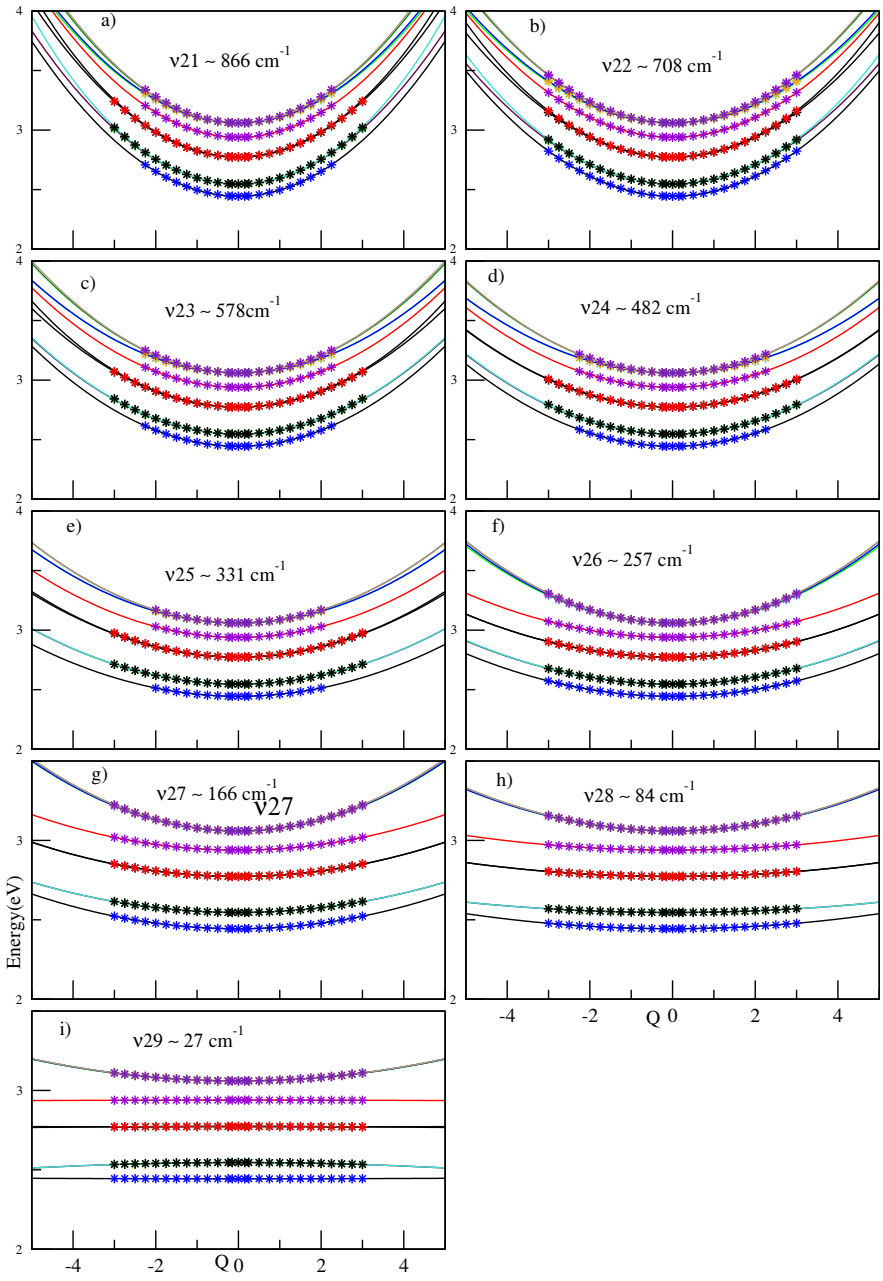

Figure 3.12: Adiabatic potential energies of the low-lying excited singlet electronic states, $^1\Sigma_u^+$, $^1\Delta_u$, $^1\Delta_g$, $^1\Sigma_g^+$, $^1\Pi_u$ and $^1\Pi_g$ of C_{21}, along the normal coordinates of RT active vibrational modes (π_g). The potential energies obtained from the present vibronic model are shown by the solid lines and the computed *ab initio* energies are shown by the asterisk.

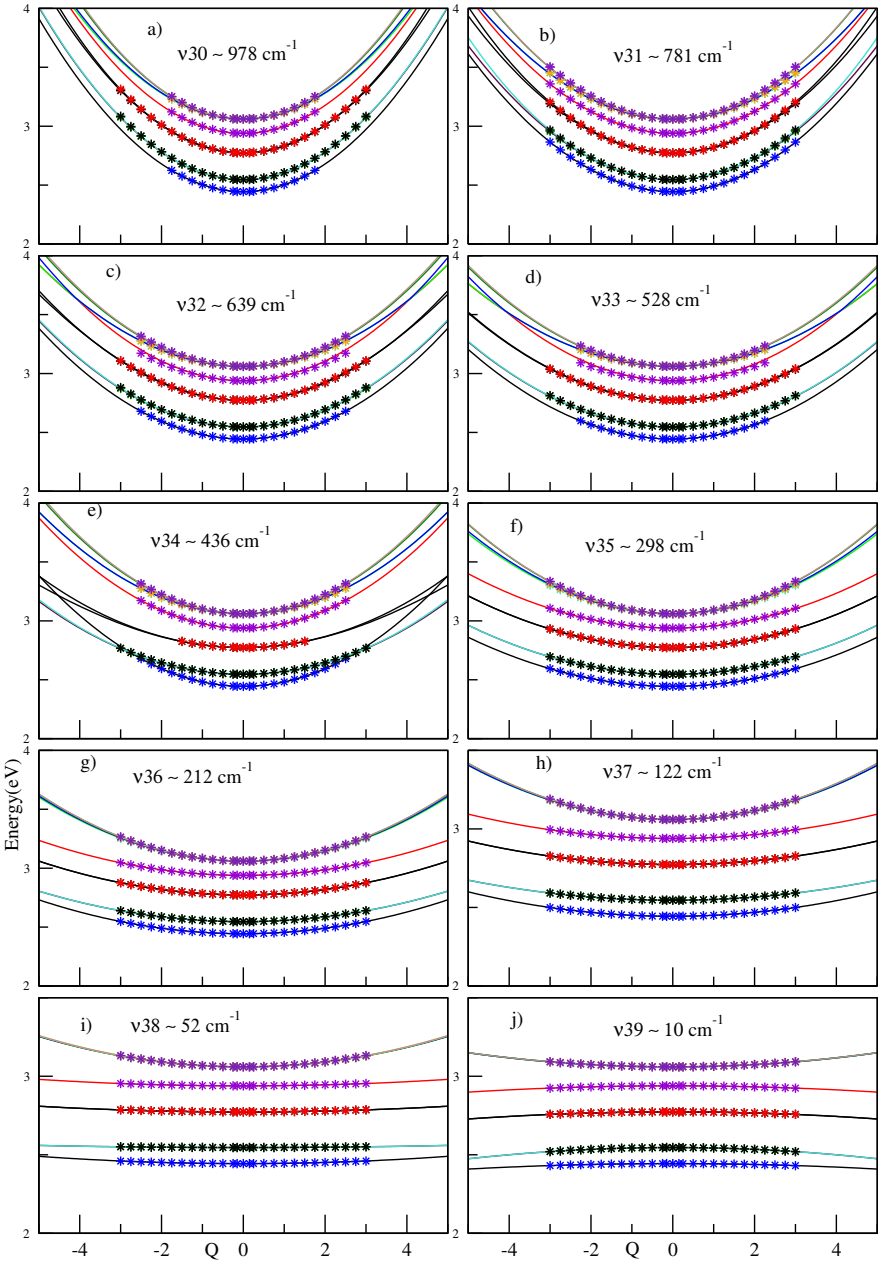

Figure 3.13: Adiabatic potential energies of the low-lying excited singlet electronic states, $^1\Sigma_u^+$, $^1\Delta_u$, $^1\Delta_g$, $^1\Sigma_g^+$, $^1\Pi_u$ and $^1\Pi_g$ of C_{21}, along the normal coordinates of RT active vibrational modes (π_u). The potential energies obtained from the present vibronic model are shown by the solid lines and the computed *ab initio* energies are shown by the asterisk.

3.5 Summarizing Remarks

The structures and energetics of the ten (including degeneracy) energetically closely lying electronic states (viz. $^1\Sigma_u^+$, $^1\Pi_g$, $^1\Pi_u$, $^1\Sigma_g^+$, $^1\Delta_g$ and $^1\Delta_u$) of neutral linear carbon clusters, C_{2n+1}, (n=7-10) have been investigated here as a prerequisite for the dynamics study (presented in chapter 4) to examine the photoabsorption spectrum of the corresponding clusters. The electronic energies are calculated by the EOM-CCSD method along the normal coordinate of the vibrational modes. The clusters, C_{2n+1}, (n=7-10), have linear cumulenic equilibrium structure [15] with the $^1\Sigma_g^+$ ground electronic term symbol. For all the clusters it is seen that $^1\Sigma_u^+$ electronic state is optically bright with a very high oscillator strength. A model diabatic Hamiltonian is constructed by taking 10 electronic states, which are in the immediate vicinity of the $^1\Sigma_u^+$ state, to study the nuclear dynamics. All intrastate and interstate coupling parameters are extracted for all the states of all four molecules with the aid of rigorous *ab initio* calculations. One dimensional potential energy curves are calculated along σ_g^+, π_g and π_u vibrational modes of all four clusters. The stationary points, viz., the energetic minimum of the seam of intersections among various electronic states of carbon clusters, C_{2n+1}, (n=7-10) and the equilibrium minimum of the respective states are discussed. With the aid of the calculated electronic energies *ab initio* , model vibronic Hamiltonians are constructed in terms of normal coordinates of vibrational modes and employing a diabatic electronic basis. The expected implications of these energetics of various curve crossing on the nuclear dynamics of

linear carbon clusters, C_{2n+1}, (n=7-10) electronic states is discussed in chapter-4.

References

[1] T. P. Snow and B. J. McCall, Annu. Rev. Astron. Astrophys **44**, 367 (2006).

[2] H. W. Kroto, Int. Rev. Phys. Chem. **1** (3), 309-376 (1981).

[3] W. Huggins, Proc. R. Soc. Landon **33**, 1 (1982); G. Herzberg, Astophys. J. **96**, 314 (1942).

[4] A. E. Douglas. Nature **269** 130 (1997).

[5] W. H. Smith, T. P. Snow and D. G. York, Astrophys. J. **218**, 124 (1977).

[6] J. P. Maier Chem. Soc. Rev. **17**, 45, (1988).

[7] J. P. Maier Chem. Soc. Rev. **26**, 21, (1997).

[8] J. P. Maier J. Phys. Chem. A **102** 3462 (1998).

[9] E. B. Jochnowitz and J. P. Maier, Annu. Rev. Phys. Chem. **59**, 519 (2008).

[10] C. A. Rice and J. P. Maier, J. Phys. Chem. A **117**, 5559 (2013).

[11] W. Weltner, Jr. and R. J. van Zee, Chem. Rev. **89**, 1713 (1989).

[12] A. V. Orden and R. J. Saykally, Chem. Rev. **98**, 2313 (1998).

[13] D. Forney, P. Freivogel, M. Grutter, and J. P. Maier, J. Chem. Phys. **104**, 4954 (1996);

[14] M. Wyss, M. Grutter and J. P. Maier, Chem. Phys. Lett. **304**, 35 (1999);

[15] S. Yang, M. Kertesz, J. Phys. Chem. A **112**, 146 (2008).

[16] T. H. Dunning, Jr., J. Chem. Phys. **90**, 1007 (1989).

[17] M. J. Frisch, *et al.* Gaussian 03, Revision B. 05, Gaussian, Inc., Pittsburgh, PA, 2003.

[18] J. M. L. Martin, J. E. Yazal and J-P Francois, Chem. Phys. Lett. **252**, 9, (1996).

[19] H. -J. Werner, P. J. Knowles, R. D. Amos, A. Bernhardsson, and others, MOLPRO-2002, a package of ab initio programs; Universitat Stuttgart: Stuttgart, Germany; University of Birmingham:Birmingham, United Kingdom, 2002.

[20] H. Köppel, W. Domcke and L. S. Cederbaum, *Adv. Chem. Phys.* **57**, 59 (1984).

Chapter 4

Electronic spectroscopy of carbon clusters (C_{2n+1}, n=7-10). II. Quantum Dynamics

Photoabsorption spectroscopy of neutral carbon clusters, C_{2n+1}, (n=7-10) is theoretically studied in this chapter. The model vibronic Hamiltonian developed through extensive ab initio quantum chemistry calculation in chapter 3 is employed in the first principles nuclear dynamics calculations. While the precise location of vibronic lines and progression of vibrational modes within a given electronic band is derived from time-independent quantum mechanical calculations, the broadband spectral envelopes and nonradiative decay rate of electronic states are calculated by propagating wave packets in a time-dependent quantum mechanical framework. A detailed investigation of vibronic interactions among Σ, Π and Δ electronic states and their impact on the vibronic structure of each state is carried out. The theoretical results are found to be in good accord with the experiment.

4.1 Introduction

The nuclear dynamics of long chain carbon clusters (C_{2n+1}, n=7-10) is studied in this chapter. In polyatomic systems crossing of various electronic states leading to CIs [1, 2] often control the nuclear motion primarily on the participating electronic states and contribute to their overall band structures and time-dependent properties. The most critical consequence of CIs of electronic PESs is a breakdown of the adiabatic BO theoretical formalism [3, 4]. In such circumstances it is necessary to go beyond and examine nuclear motion concurrently with the electronic motion [1, 5–7]. In such circumstances ideally one needs to undertake a full quantum mechanical treatment of the nuclear dynamics including most of the relevant electronic and nuclear degrees of freedom.

The photoabsorption spectrum of C_{2n+1} (n=7-10) studied here has been experimentally recorded by Maier and co-workers [29]. They observed the $^1\Sigma_u^+ \longleftarrow {}^1\Sigma_g^+$ absorption band of C_{15}, C_{17}, C_{19} and C_{21} at 419 nm, 460 nm, 503 nm and 544 nm respectively, in the neon matrix environment at 5 K using the approach that combines mass selection with matrix isolation spectroscopy. In the theoretical study detailed below, we attempt to identify and assign the specific vibrational modes that contribute to a given spectral envelope predominantly. The neutral and anions of bare carbon chains are studied with various spectroscopic techniques ranging from pulsed and continuous-wave cavity ringdown (CRD), resonant-two-color-two-photon ionization (R2C2PI), laser induced fluorescence (LIF), trapped ion photofragmentation, and electron photodetachment processes during the past decades [8–12]. It followed from the study of Maier *et al.* that bare carbon chains C_n upto n=12 can not be carrier for diffuse interstellar bands (DIBs). The following criteria were proposed by the authors for a species to have, to be a potential DIB carrier: "(a) absorptions in the 400-800 nm range, (b) oscillator strength f

values in the 1-10 range, and (c) an excited electronic-state lifetime longer than a few picoseconds so that intramolecular broadening would still be compatible with the typical half-widths of the narrower DIBs (i.e., a few wave numbers)" [11].

The longer chains with an odd number of carbon atoms of the length 15, 17, 19 and 21 are expected to satisfy the first two criteria because their transitions are in the 400-800 nm range and the f value of the optically bright state $^1\Sigma_u^+$ scales with the chain length. It remains to be seen by doing nuclear dynamics study, whether the excited electronic state $^1\Sigma_u^+$ has a lifetime longer than a few picoseconds to satisfy the third condition listed above. So far there is no experimental evidence appeared on the presence of other electronic states in the vicinity of $^1\Sigma_u^+$ state. It follows from the results of chapter 3 that energetically close lying degenerate electronic states exist in the neighborhood of $^1\Sigma_u^+$ state. Therefore, examination of impact of nonadiabatic interactions is essential to understand the spectral broadening and estimate the decay rate of the $^1\Sigma_u^+$ state.

For linear systems Renner-Teller effect [15] represents one of the most crucial factor for the violation of the validity of the BO approximation. It originates from the splitting of the degeneracy of Π, Δ etc. states of linear molecule upon bending. At small distortions from linearity, the two split component electronic states, lie close to each other, which gives rise to coupling between electronic states through suitable vibrational modes. It is also necessary to consider the spin-orbit coupling in addition to electron-nuclear coupling. This is because majority of the electronic states involved in such vibronic couplings are open-shell systems with non-zero spin, and that the magnitude of the spin-orbit splitting/shifting of the energy levels is (at least in molecules involving only relatively light atoms) usually

comparable in magnitude to that caused by the vibronic coupling. Linear odd numbered bare carbon clusters (C_{2n+1}, n=7-10) which are investigated here are all closed shell systems, and spin-orbit coupling is not taken into consideration.
It was discussed in the literature that the RT effect is the driving force behind bending instability of linear molecules in degenerate states [13]. Upon bending the molecule, an additional dipole moment is set up in the molecular plane which lifts the electronic degeneracy. The split component of the electronic states may undergo symmetry allowed coupling with the neighboring electronic states and can give rise to PRT (Pseudo Renner Teller) effect [14] (in nonlinear molecule this is termed as PJT, Pseudo Jahn Teller effect).
The RT effect in triatomic molecules is extensively studied theoretically by perturbative treatment of the Hamiltonian when expanded in a Taylor series around the linear configuration [15–18]. While there are plethora of studies on the triatomic RT effect, studies on linear polyatomic molecules with atoms more than three, are very less. The situation concerning the RT effect in larger linear molecules is quite different. In this case the theory is much more complicated than in triatomics. Firstly there are several bending modes involved and secondly, the asymmetric form of the electronic wave functions, corresponding to small distortion from linearity, is not determined by symmetry as in triatomic molecules. To the best of our knowledge carbon chains of upto 6 atom length were theoretically studied by including the RT [19, 20] effect. However perturbation theory is known to fail in strong coupling case and when the interacting states are very closely spaced. The quasi-diabatic model proposed by Köppel *et al.* to avoid the perturbative treatment of the RT [2, 21] intersections seems to be more general. In this study we exercised this model as discussed in chapter 3.

4.2 Results and Discussion

In this section the complete broad band spectral envelopes of the electronic states of carbon clusters, $C_{2n+1}, (n = 7 - 10)$ are presented and discussed. These broad band envelopes are calculated by propagating WPs using the MCTDH program modules [22–25] and considering the complete Hamiltonian developed in Chapter 3. The *ab initio* electronic structure parameters reported therein are used. The theoretical results are compared with the available experimental results [26–29]. Subsequently, each of the broad spectral envelope is critically examined at higher energy resolution. In this case the precise location of the vibronic levels is calculated and assigned by a time-independent matrix diagonalization approach employing the Lanczos algorithm [30]. In order to confirm the assignments, vibronic wave functions are calculated by the block-improved Lanczos method using the MCTDH program modules [31, 32]. The resolved band structures are also compared with resolved experimental results whenever available. Importantly, this exercise enabled us to identify the excitations of the vibrational modes underlying the broad experimental bands and to assess the impact of electronic nonadiabatic effects on their overall structure. Finally, the nonradiative decay of excited electronic states is examined and discussed.

4.2.1 Electronic Absorption spectrum

Vibronic energy levels of the $^1\Pi_g$, $^1\Pi_u$, $^1\Sigma_u^+$, $^1\Delta_g$, $^1\Delta_u$ and $^1\Sigma_g^+$ electronic states of C_{2n+1} where, n=7-10 are shown and discussed here. To start with, we construct various reduced dimensional models and examine the vibrational energy levels of each of these electronic states by excluding the PRT coupling with their neighbors. These results help us to understand the role of various vibrational modes

and electronic states in the complex vibronic structures of these clusters. The calculations are carried out including the relevant symmetric vibrational modes only. The numerical details of the calculations, in terms of vibrational modes and dimension of the secular matrix are given in Table 4.1. The final calculation of nuclear dynamics is, however, carried out by including all relevant couplings of the Hamiltonian and propagating wave packets using the MCTDH suite of programs to elucidate the nonadiabatic coupling effects on the spectral envelopes. The theoretical results are compared with the available experimental absorption spectrum of C_{2n+1}, where n=7-10 [26–29].

4.2.1.1 Uncoupled spectra of $^1\Sigma_u^+$ state

The vibronic energy eigenvalues of the $^1\Sigma_u^+$ electronic states are obtained by diagonalizing the Hamiltonian matrix using the Lanczos algorithm [30] and are shown as the stick lines in Figs. 4.1a, 4.2a, 4.3a and 4.4a. For C_{15} chain the envelopes are obtained by convoluting these stick lines with a Lorentzian function of 10 meV FWHM. Further details of the calculations are given in Table 4.1. The vibrational structure of the $^1\Sigma_u^+$ electronic state in absence of coupling with its neighboring states and the experimental recording of Ref [28, 29] in neon matrix is shown in Fig. 4.1. It can be seen in comparison that the theoretical results are in very good agreement with the experimental band structure of the $^1\Sigma_u^+$ state. From the data given in Table 3.4 of Chapter-3, the excitation of vibrational modes ν_2 and ν_7 can be expected in this band. The excitation of the ν_7 modes is stronger than that of ν_2. Line spacings of ~ 2072 and ~ 282 cm^{-1} corresponding to the frequency of these modes, respectively, are extracted from the theoretical spectrum. In addition to energetic location and excitation strength

analyses, the assignment of the peaks is confirmed through a thorough analysis of the nodal pattern of their eigenvectors. These eigenvectors are calculated by a block improved Lanczos method as implemented in the MCTDH program module. To illustrate it we present in Fig. 4.5 a few representative eigenvectors only. In these figures the wavefunction probability density is plotted in a suitable reduced dimensional normal coordinate plane. In panel a and b the wavefunction of the fundamental of ν_2 (2072 cm^{-1}) and ν_7 (282 cm^{-1}) is shown, respectively. It can be seen from these plots that the wavefunctions acquire a node along the respective normal coordinate. In panel c and d the first and second overtone of ν_7 at 565 cm^{-1} and 847 cm^{-1}, respectively revealing two and three nodes along the respective coordinate is shown. The wavefunction for the combination peaks $\nu_2 + \nu_7$ (2354 cm^{-1}) is shown in panel e. It can be seen that the latter wavefunctions show one quantum excitation along both the modes forming the pair.

For C_{17} chain the envelopes are obtained by convoluting the stick line spectrum with a Lorentzian function of 10 meV FWHM. Further details of the calculations are given in Table 4.1. For C_{17} chain the vibrational structure of the $^1\Sigma_u^+$ electronic state in absence of coupling with its neighboring states and the experimental recording of Ref [28, 29] in neon matrix is shown in Fig. 4.2a. It can be seen in comparison that the theoretical results are in very good agreement with the experimental band structure of the $^1\Sigma_u^+$ state. From the data given in Table 3.6 of Chapter-3, the excitation of vibrational modes ν_2 and ν_8 can be expected in this band. The excitation of the ν_8 modes is stronger than that of ν_2. Line spacings of $\sim$ 2061 and $\sim$ 248 cm^{-1} corresponding to the frequency of these modes, respectively, are extracted from the theoretical spectrum. As in case of C_{17} the eigenvectors of the fundamental of ν_2 (2061 cm^{-1}) and ν_8 (248 cm^{-1}) are shown,

respectively, in panel a and b of Fig. 4.6. It can be seen from these plots that the wavefunctions acquire a node along the respective normal coordinate. In panel c, d and e of Fig. 4.6 the first, second and third overtone of ν_8 occurring at 497 cm^{-1}, 745 cm^{-1} and 994 cm^{-1}, respectively revealing two, three and four nodes along the respective coordinate is shown.

For C_{19} chain the envelope is obtained by convoluting the stick line with a Lorentzian function of 5 meV FWHM. Further details of the calculations are given in Table 4.1. For C_{19} chain the vibrational structure of the $^1\Sigma_u^+$ electronic state in absence of coupling with its neighboring states and the experimental recording of Ref. [28, 29] in neon matrix is shown in Fig. 4.3a. It can be seen in comparison that the theoretical results are in very good agreement with the experimental band structure of the $^1\Sigma_u^+$ state. From the data given in Table 3.8 of Chapter-3, the excitation of vibrational modes ν_3 and ν_9 can be expected in this band. The excitation of the ν_9 mode is stronger than that of ν_3. Line spacings of $\sim$ 2014 and $\sim$ 223 cm^{-1} corresponding to the frequency of these modes, respectively, are extracted from the theoretical spectrum. As before the eigenvectors of the fundamental of ν_3 (2015 cm^{-1}), ν_9 (223 cm^{-1}), the first (445 cm^{-1}), second (668 cm^{-1}) and third (891 cm^{-1}) overtone of ν_9 and the combination peaks ν_3 + ν_9 (2238 cm^{-1}) are shown in Fig. 4.7 (a-f), respectively.

For C_{21} chain the envelope is obtained by convoluting these stick line with a Lorentzian function of 10 meV FWHM . Further details of the calculations are given in Table 4.1. For C_{21} chain the vibrational structure of the $^1\Sigma_u^+$ electronic state in absence of coupling with its neighboring states and the experimental recording of Ref [28, 29] in neon matrix is shown in Fig. 4.4a. It can be seen in

comparison that the theoretical results are in very good agreement with the experimental band structure of the $^1\Sigma_u^+$ state. From the data given in Table 3.10 of Chapter-3, the excitation of vibrational modes ν_4 and ν_{10} can be expected in this band. The excitation of the ν_{10} modes is stronger than that of ν_4. Line spacings of ~ 2021 and ~ 202 cm^{-1} corresponding to the frequency of these modes, respectively, are extracted from the theoretical spectrum. As before the eigenvectors of the fundamental of ν_4 (2021 cm^{-1}), ν_{10} (202 cm^{-1}), the first (403 cm^{-1}), second (605 cm^{-1}) and third (807 cm^{-1}) overtone of ν_{10} and the combination peaks ν_4 + ν_{10} (2223 cm^{-1}) are shown in Fig. 4.8 (a-f), respectively.

The above discussion revealed that there are only two symmetric vibrational modes which form the primary progression in the vibronic structure of the $^1\Sigma_u^+$ electronic band of all the clusters.

4.2.1.2 Uncoupled spectra of $^1\Delta_g$, $^1\Delta_u$ and $^1\Sigma_g^+$ electronic states

The stick vibronic energy eigenvalues and their convoluted spectra of $^1\Delta_g$, $^1\Delta_u$ and $^1\Sigma_g^+$ electronic states of C_{15} are obtained by diagonalizing the Hamiltonian matrix using the Lanczos algorithm [30] and are shown in the panel a, b and c of Figs. 4.9. The numerical details of the calculations are given in Table 4.1. In all these states the lowest frequency totally symmetric vibrational modes (ν_7, 282 cm^{-1}) forms dominant the progression.

Similarly, the stick vibronic energy eigenvalues and their convoluted spectra of $^1\Delta_u$, $^1\Delta_g$ and $^1\Sigma_g^+$ electronic states of C_{17} are obtained by diagonalizing the Hamiltonian matrix using the Lanczos algorithm [30] and are shown in the panel d, e and f of Figs. 4.9. The numerical details of the calculations are given in Table 4.1. The lowest frequency totally symmetric vibrational mode (ν_8, 249 cm^{-1})

forms the dominant progression in this case.

The stick vibronic energy eigenvalues and their convoluted spectra of $^1\Delta_u$, $^1\Delta_g$ and $^1\Sigma_g^+$ electronic states of C_{19} are obtained by diagonalizing the Hamiltonian matrix using the Lanczos algorithm [30] and are shown in the panel a, b and c of Figs. 4.10. The numerical details of the calculations are given in Table 4.1. The lowest frequency totally symmetric vibrational mode (ν_9, 223 cm^{-1}) forms the dominant progression in this case.

The stick vibronic energy eigenvalues and their convoluted spectra of $^1\Delta_u$, $^1\Delta_g$ and $^1\Sigma_g^+$ electronic states of C_{21} are obtained by diagonalizing the Hamiltonian matrix using the Lanczos algorithm [30] and are shown in the panel d, e and f of Figs. 4.10. The numerical details of the calculations are given in Table 4.1. The lowest frequency totally symmetric vibrational modes (ν_{10}, 202 cm^{-1}) form dominant progression in this case.

4.2.1.3 Uncoupled spectra of $^1\Pi_g$ and $^1\Pi_u$ electronic states : Renner Teller effect.

The Π electronic states are Renner Teller active in fourth order along the π_g and π_u vibrational modes. The RT splitting is small (see. Figs. 3.3, 3.4, 3.6, 3.7, 3.9, 3.10, 3.12 and 3.13 of chapter 3).

Π_g and Π_u electronic states are quasi degenerate. The theoretical stick line spectrum of each $\Pi_{g/u}$ electronic state (shown in panel a) is calculated with the vibronic model Hamiltonian, developed in chapter 3 and all relevant totally symmetric vibrational modes are included. A Lorentzian line shape function of 10 meV (in case of C_{19}, it is 5meV) full width at the half maximum (FWHM) is used to convolute the stick line spectrum in each case and to generate the respective

spectral envelope. In absence of any intermode coupling terms, the Hamiltonian for the degenerate Π states are separable in terms of the σ_g^+, π_g and π_u modes. Therefore, the partial spectra calculated with the totally symmetric and degenerate vibrational modes separately, can be convoluted to get the composite vibronic structure of the electronic states. The spectrum of the $\Pi_{g/u}$ states of C_{15}, C_{17}, C_{19} and C_{21} obtained by including the σ_g^+ modes only is shown in Figs. 4.11 (a) and (d), 4.12 (a) and (d), 4.13 (a) and (d) and 4.14 (a) and (d), respectively.
In the $\Pi_{g/u}$ state of C_{15}, excitation of ν_1, ν_2, ν_3, ν_4 and ν_5 modes is strong. The fundamentals of ν_1, ν_2, ν_3, ν_4 and ν_5 vibrations are 2199 cm^{-1}, 2074 cm^{-1}, 2010 cm^{-1}, 1739 cm^{-1} and 1306 cm^{-1} spaced, respectively.
In the $\Pi_{g/u}$ state of C_{17}, excitation of ν_1, ν_2, ν_3, ν_4, ν_5 and ν_6 are strong. The fundamentals of these modes are 2210 cm^{-1}, 2042 cm^{-1}, 2079 cm^{-1}, 1889 cm^{-1} 1571 cm^{-1} and 1170 cm^{-1} spaced, respectively.
In the $\Pi_{g/u}$ state of C_{19}, excitation of ν_1, ν_2, ν_3, ν_4, ν_5 and ν_6 are strong. The fundamentals of these modes are 2208 cm^{-1}, 2157 cm^{-1}, 1967 cm^{-1}, 1981 cm^{-1}, 1766 cm^{-1} and 1431 cm^{-1} spaced, respectively.
In the $\Pi_{g/u}$ state of C_{21}, excitation of ν_1, ν_2, ν_3, ν_4, ν_5, ν_6 and ν_7 are strong. The fundamentals of these modes are 2199 cm^{-1}, 2188 cm^{-1}, 2031 cm^{-1}, 1964 cm^{-1}, 1866 cm^{-1}, 1628 cm^{-1} and 1313 cm^{-1} spaced, respectively.

The partial spectra of C_{15}, C_{17}, C_{19} and C_{21} calculated with the degenerate RT modes (π_g and π_u) are shown in Figs. 4.11 (b) and (e), 4.12 (b) and (e), 4.13 (b) and (e) and 4.14 (b) and (e) respectively.
The composite spectrum obtained by convoluting the symmetric and degenerate mode is shown in panel (c) and (f) of this figure. The spectra presented in panel (b) and (e) reflects a weak contribution of RT coupling in the vibronic structure

of $\Pi_{g/u}$ states. As a result, the overall spectral envelop (panel (c) and (f)) appears to be very similar and close to that shown in panel (a) and (d) of the above mentioned figures.

In all the clusters Δ electronic states are also Renner Teller active in fourth order along the π_g and π_u vibrational modes. But the splitting between the two components is very small when distorted along the degenerate vibrational modes. It can be expected that Renner-Teller coupling will have a negligible effect in the vibronic structure of $\Delta_{g/u}$ states. It can also be seen from Figs. 3.3, 3.4, 3.6, 3.7, 3.9, 3.10, 3.12 and 3.13 of chapter 3 that splitting between the two components of the degenerate electronic states are very small.

4.2.1.4 Effect of Σ - Π - Δ electronic states on $^1\Sigma_u^+$ electronic state:

So far PRT coupling between various electronic states is not considered in various calculations. On inclusion of this coupling, the separation of the Hamiltonian in terms of the symmetric and degenerate vibrational modes for the degenerate electronic states as explored above is not possible. $^1\Pi_g$, $^1\Pi_u$ and $^1\Sigma_g^+$ electronic states coupled with $^1\Sigma_u^+$ electronic state due to the availability of π_u, π_g and σ_g^+ vibrational modes, respectively.

The $^1\Delta_g$ and $^1\Delta_u$ electronic states are energetically very close to the $^1\Sigma_u^+$ state. But $^1\Delta$ - $^1\Sigma_u^+$ coupling is not possible due to the lack of δ vibrational modes in linear carbon chains. The transition to the $^1\Delta$ electronic states from the ground state (of $^1\Sigma_g^+$ symmetry) is optically dark but these states can gain intensity via Pseudo-Renner-Teller type of coupling with the optically allowed Π electronic states.

It is therefore necessary to follow the nuclear dynamics simultaneously on ten coupled electronic states ($^1\Sigma_u^+$ - $^1\Pi_g$ - $^1\Pi_u$ - $^1\Sigma_g^+$ - $^1\Delta_g$ - $^1\Delta_u$ coupled calculation) including all relevant vibrational degrees of freedom. Computationally, it becomes difficult to simulate the nuclear dynamics quantum mechanically by the matrix diagonalization approach employed above. We therefore resort to the MCTDH algorithm [22–25], and propagate WPs on ten coupled electronic states including all vibrational degrees of freedom. Even with MCTDH, simulations with 40 of C_{15} or 46 of C_{17} or 52 of C_{19} or 58 of C_{21} vibrational modes is not possible. By looking at the coupling strength of the vibrational modes of C_{2n+1}, where n=7-10 in Tables 3.4 and 3.5; 3.6 and 3.7; 3.8 and 3.9; and 3.10 and 3.11 of chapter 3,respectively, it is clear that, not all the vibrational modes are important in the nuclear dynamics simulations. We selected eighteen vibrational modes (including x and y components of the degenerate vibrational modes) on the basis of the coupling strength. The eighteen vibrational degrees of freedom are grouped into four particles. The combination scheme of the vibrational modes of C_{2n+1}, where n=7-10 is given in Table 4.2 along with the sizes of the primitive and SPF bases. The parameters of C_{15}, C_{17}, C_{19} and C_{21} are documented in Table 4.2, are optimally chosen to ensure the numerical convergence of the vibronic bands shown in Fig. 4.1(b), 4.2(b), 4.3(b), 4.4(b). The WP in each calculation is propagated for 400 fs. Fig. 4.15 displays the present theoretical diabatic electronic population diagram of C_{2n+1} where n=7-10 in the energy range ∼3-6 eV.

The theoretical results of Fig. 4.15 are obtained by including the coupling among the states. Ten WP propagations in the coupled $^1\Pi_g$ - $^1\Pi_u$ - $^1\Sigma_u^+$ - $^1\Sigma_g^+$ - $^1\Delta_g$ - $^1\Delta_u$ electronic manifold are carried out by initially preparing the WP separately on each of the component state of this manifold. Here, WP propagation of $^1\Sigma_u^+$ electronic state of C_{2n+1}, where n=7-10 is presented. For C_{15}, C_{17} and

C_{21} the resulting time autocorrelation function is damped with an exponential function $e^{\frac{-t}{\tau}}$ with τ=66 fs (which corresponds to a 10 meV FWHM Lorentzian function) before Fourier transformation to generate the spectral envelopes, while for C_{19} damping factor is 132 fs (which corresponds to a 5 meV FWHM Lorentzian function).

It is seen from the Figs. 4.1 (b), 4.2 (b), 4.3 (b) and 4.4 (b) that Σ - Π - Δ coupling does not significantly perturb the spectrum of $^1\Sigma_u^+$ electronic state but it has a very strong effect on the diabatic state population calculations which reduces the lifetime of $^1\Sigma_u^+$ electronic state drastically, particularly in case of C_{15} and C_{17} (see. Fig. 4.15).

4.2.2 Internal conversion dynamics

As stated in the introduction, the lifetime of the $^1\Sigma_u^+$ excited electronic state of C_{2n+1}, where n=7-10 is calculated. To be a good carrier for DIBs, the nonradiative decay of the diabatic population of $^1\Sigma_u^+$ electronic state is expected be around 70-200 fs [12]. Here in this section, we present the time-dependence of the diabatic electronic populations in the coupled manifold $^1\Sigma_u^+$ - $^1\Pi_g$ - $^1\Pi_u$ - $^1\Sigma_g^+$ - $^1\Delta_g$ - $^1\Delta_u$ electronic states. It would have been more realistic to calculate the adiabatic electronic populations. Such calculations could not be done because of huge computational overheads.

The diabatic electronic populations are calculated for an initial transition to each of the above electronic states separately. The results are shown in Figs. 4.15, 4.16, 4.17, 4.18 and 4.19. Interesting observations of C_{15}, C_{17}, C_{19} and C_{21} on the dynamical mechanism can be obtained from these population curves in

conjunction with the coupling parameters given in Table 3.4 and 3.5; 3.6 and 3.7; 3.8 and 3.9; and 3.10 and 3.11 respectively and the stationary points on the PESs detailed in Section 3.4.1 and Table 3.12.

For C_{15} carbon chain the population dynamics of the WP initially prepared on the $^1\Sigma_u^+$ is shown in panel a of Fig. 4.15. In this case the electronic diabatic population of $^1\Sigma_u^+$ state flows to the $^1\Pi_g$ and $^1\Pi_u$ electronic states only. The depletion of the $^1\Sigma_u^+$ electronic state population relates to a decay rate of $\sim$ 76 fs. It is already stated that while the PRT coupling between $^1\Pi_g$ and $^1\Sigma_u^+$ states is strong, the PRT coupling between $^1\Pi_u$ and $^1\Sigma_u^+$ electronic states is weak. The minimum of $^1\Pi_g$- $^1\Sigma_u^+$ and $^1\Pi_u$- $^1\Sigma_u^+$ intersections is $\sim$ 0.04 eV above the minimum of $^1\Sigma_u^+$ electronic state. Hence the population of the $^1\Sigma_u^+$ state is expected to transfer to $^1\Pi_g$ state. The $^1\Pi_g$ state is in-turn strongly coupled to the $^1\Pi_u$ state via σ_u^+ modes. A population transfer to $^1\Pi_u$ state from $^1\Sigma_u^+$ state can also be seen from the figure 4.15.

For C_{17} carbon chain the population dynamics of the WP initially prepared on the $^1\Sigma_u^+$ is shown in panel b of Fig. 4.15. In this case the electronic diabatic population of $^1\Sigma_u^+$ state also flows to the $^1\Pi_u$ and $^1\Pi_g$ electronic states. The decay rate of the $^1\Sigma_u^+$ electronic state is estimated to be $\sim$ 64 fs. A similar mechanism as stated for C_{15} operates in this case. The minimum of $^1\Pi_g$- $^1\Sigma_u^+$ and $^1\Pi_u$- $^1\Sigma_u^+$ intersections is $\sim$ 0.02 eV above the minimum of $^1\Sigma_u^+$ electronic state in this case.

For the C_{19} carbon chain the population dynamics of the WP initially prepared on the $^1\Sigma_u^+$ state is shown in panel c of Fig. 4.15. In this case the electronic population transfer to the $^1\Pi_g$ and $^1\Pi_u$ electronic states is much less. The decay rate of the $^1\Sigma_u^+$ electronic state is estimated to be $\sim$ 189 fs.

For the C_{21} carbon chain the population dynamics of the WP initially prepared

on the $^1\Sigma_u^+$ is shown in panel d of Fig. 4.15. Analogous to C_{19}, in this case also rate of population transfer to the $^1\Pi_u$ and $^1\Pi_g$ electronic states is much slower. The decay rate of the $^1\Sigma_u^+$ electronic state is estimated to be $\sim$ 337 fs.

From Fig. 4.16, 4.17, 4.18 and 4.19 it is seen that degenerate electronic state $\Pi_{g/u}$ and $\Delta_{g/u}$ exchange its population with the degenerate $\Pi_{u/g}$, $\Delta_{g/u}$ and $^1\Sigma_u^+$ electronic state. So, it can be said that PRT effect dominates over RT effect in all four clusters.

Table 4.1: The number of HO basis functions along with the totally symmetric vibrational modes and the dimension of the secular matrix used in the calculation of the uncoupled stick vibronic spectra shown in various figures noted below.

	Vibrational modes	No. of HO basis	Dimension of secular matrix	Figure(s)
C_{15}				
$^1\Sigma_u^+$	ν_1, ν_2,ν_3,ν_4,ν_5,ν_6,ν_7	4,6,4,4,4,4,10	61440	4.1(a)
$^1\Pi_g$	ν_1, ν_2,ν_3,ν_4,ν_5,ν_6,ν_7	7,16,10,8,6,5,4	1075200	4.11(a)
$^1\Pi_u$	ν_1, ν_2,ν_3,ν_4,ν_5,ν_6,ν_7	7,16,10,8,6,5,4	1075200	4.11(d)
$^1\Delta_g$	ν_1, ν_2,ν_3,ν_4,ν_5,ν_6,ν_7	6,9,6,6,6,7,15	1224720	4.9(a)
$^1\Delta_u$	ν_1, ν_2,ν_3,ν_4,ν_5,ν_6,ν_7	6,9,6,6,6,7,15	1224720	4.9(b)
$^1\Sigma_g^+$	ν_1, ν_2,ν_3,ν_4,ν_5,ν_6,ν_7	4,4,6,4,4,7,10	107520	4.9(c)
C_{17}				
$^1\Sigma_u^+$	ν_1, ν_2,ν_3,ν_4,ν_5,ν_6,ν_8	4,6,4,4,4,4,14	86016	4.2(a)
$^1\Pi_u$	ν_1, ν_2,ν_3,ν_4,ν_5,ν_6,ν_8	8,10,14,8,4,4,4	573440	4.12(a)
$^1\Pi_g$	ν_1, ν_2,ν_3,ν_4,ν_5,ν_6,ν_8	8,10,14,8,4,4,4	573440	4.12(d)
$^1\Delta_u$	ν_1, ν_2,ν_3,ν_4,ν_5,ν_6,ν_8	7,9,8,6,6,7,9,12	13716864	4.9(d)
$^1\Delta_u$	ν_1, ν_2,ν_3,ν_4,ν_5,ν_6,ν_8	7,9,8,6,6,7,9,12	13716864	4.9(e)
$^1\Sigma_g^+$	ν_1, ν_2,ν_3,ν_4,ν_5,ν_6,ν_8	4,4,4,4,4,4,10	40960	4.9(f)
C_{19}				
$^1\Sigma_u^+$	ν_1, ν_2,ν_3,ν_4,ν_5,ν_6,ν_9	4,4,6,4,4,4,14	86016	4.3(a)
$^1\Delta_u$	ν_1, ν_3, ν_7, ν_8,ν_9	6,10,6,8,14	40320	4.10(a)
$^1\Delta_g$	ν_1, ν_3, ν_7, ν_8,ν_9	6,10,6,8,14	40320	4.10(b)
$^1\Pi_g$	ν_1, ν_2,ν_3,ν_4,ν_5,ν_6,ν_9	8,6,14,10,7,5,4	940800	4.13(a)
$^1\Pi_u$	ν_1, ν_2,ν_3,ν_4,ν_5,ν_6,ν_9	8,6,14,10,7,5,4	940800	4.13(d)
$^1\Sigma_g^+$	ν_1, ν_2,ν_3,ν_4,ν_5,ν_6,ν_9	4,4,4,4,4,4,14	229376	4.10(c)
C_{21}				
$^1\Sigma_u^+$	ν_1, ν_2,ν_3,ν_4,ν_5,ν_6,ν_7,ν_{10}	4,4,6,4,4,4,4,14	344064	4.4(a)
$^1\Delta_u$	ν_1, ν_2,ν_3,ν_4,ν_5,ν_6,ν_7,ν_{10}	8,6,8,8,6,6,6,12	7962624	4.10(d)
$^1\Delta_g$	ν_1, ν_2,ν_3,ν_4,ν_5,ν_6,ν_7,ν_{10}	8,6,8,8,6,6,6,12	7962624	4.10(e)
$^1\Sigma_g^+$	ν_1, ν_2,ν_3,ν_4,ν_5,ν_6,ν_7,ν_{10}	4,4,4,4,4,4,4,14	229376	4.10(f)
$^1\Pi_u$	ν_1, ν_2,ν_3,ν_4,ν_5,ν_6,ν_7,ν_{10}	8,8,6,14,10,6,5,4	6451200	4.14(a)
$^1\Pi_g$	ν_1, ν_2,ν_3,ν_4,ν_5,ν_6,ν_7,ν_{10}	8,8,6,14,10,6,5,4	6451200	4.14(d)

Table 4.2: Normal mode combination, sizes of the primitive and the single particle bases used in the WP propagation within the MCTDH framework on the ten coupled electronic manifold using the complete vibronic Hamiltonian of Eq. (3.5). First column denotes the vibrational DOF which are combined to particles. Second column gives the number of primitive basis functions for each DOF. Third column gives the number of SPFs for the electronic state in the $^1\Sigma_u^+$ - $^1\Pi_g$ - $^1\Pi_u$ - $^1\Sigma_g^+$ - $^1\Delta_g$ - $^1\Delta_u$ coupled calculations.

Normal modes	Primitive Basis	SPF Basis	Figures
ν_2,ν_7,ν_{23x},ν_{23y}	(10,12,10,10)	[9,9,9,9,9,9,9,9,9,9]	4.1 (b)
ν_3,ν_{11},ν_{17x},ν_{17y}	(9,9,9,9)	[8,8,8,8,8,8,8,8,8,8]	
ν_1,ν_4,ν_8,ν_9,ν_{22x},ν_{22y}	(8,8,8,8,8,8)	[7,7,7,7,7,7,7,7,7,7]	
ν_5,ν_{12},ν_{16x},ν_{16y}	(6,7,7,7)	[6,6,6,6,6,6,6,6,6,6]	
ν_3,ν_8,ν_{31x},ν_{31y}	(10,12,11,11)	[12,12,12,12,12,12,12,12,12,12]	4.2 (b)
ν_2,ν_{10},ν_{23x},ν_{23y}	(9,9,10,10)	[10,10,10,10,10,10,10,10,10,10]	
ν_1,ν_4,ν_9,ν_{30x},ν_{30y}	(8,8,8,9,9)	[9,9,9,9,9,9,9,9,9,9]	
ν_5,ν_{11},ν_{13},ν_{22x},ν_{22y}	(6,6,7,8,8)	[8,8,8,8,8,8,8,8,8,8]	
ν_3,ν_9,ν_{35x},ν_{35y}	(12,12,10,10)	[9,9,9,9,9,9,9,9,9,9]	4.3 (b)
ν_{16},ν_{26x},ν_{26y}	(9,9,9)	[8,8,8,8,8,8,8,8,8,8]	
ν_1,ν_4,ν_{11},ν_{12},ν_{34x},ν_{34y}	(9,9,8,6,8,8)	[7,7,7,7,7,7,7,7,7,7]	
ν_2,ν_5,ν_{17},ν_{25x},ν_{25y}	(7,7,5,7,7)	[6,6,6,6,6,6,6,6,6,6]	
ν_4,ν_{10},ν_{39x},ν_{39y}	(10,10,10,10)	[9,9,9,9,9,9,9,9,9,9]	4.4 (b)
ν_{13},ν_{16},ν_{29x},ν_{29y}	(8,8,9,9)	[8,8,8,8,8,8,8,8,8,8]	
ν_1,ν_2,ν_5,ν_{12},ν_{38x},ν_{38y}	(9,9,9,7,8,8)	[7,7,7,7,7,7,7,7,7,7]	
ν_6,ν_{14},ν_{28x},ν_{28y}	(7,6,7,7)	[6,6,6,6,6,6,6,6,6,6]	

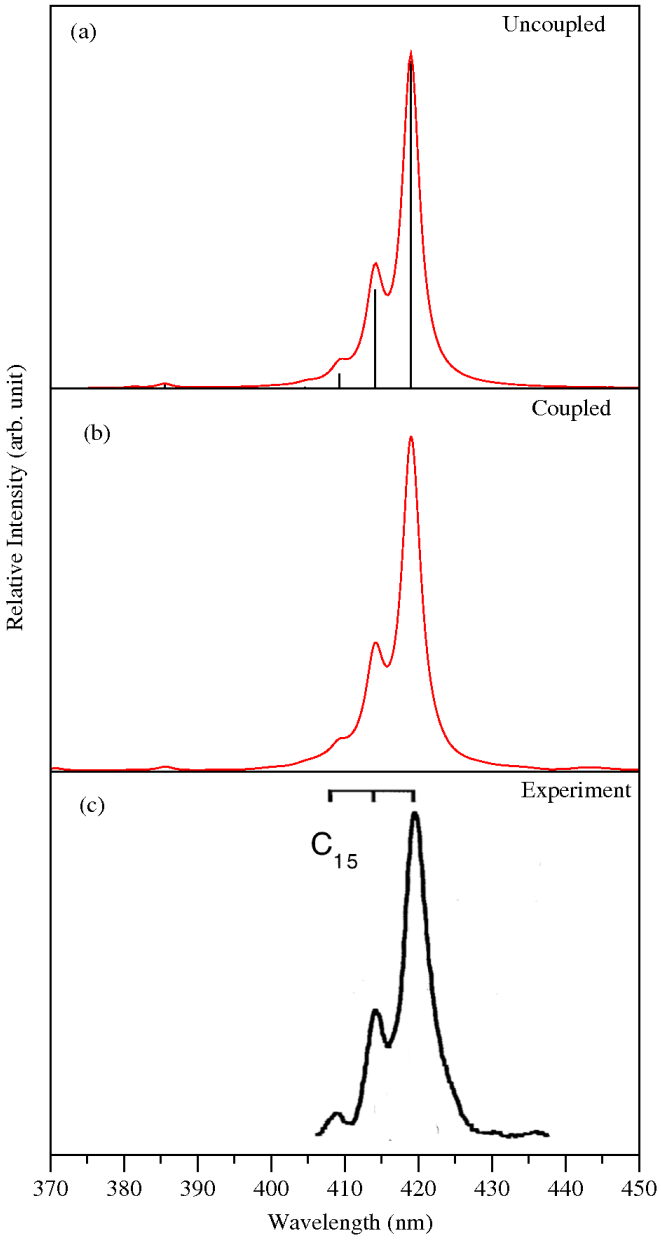

Figure 4.1: The stick vibronic spectrum and the convoluted envelope of the $^1\Sigma_u^+$ electronic state of C_{15} calculated with the σ_g^+ vibrational modes plotted in panel a. The absorption bands of the $^1\Sigma_u^+$ electronic state of C_{15} obtained from the coupled state dynamics study (see text for details). The intensity in arbitrary units is plotted as a function of wavelength in panel b. The experimental spectrum reproduced from Ref. [28] and shown in panel b.

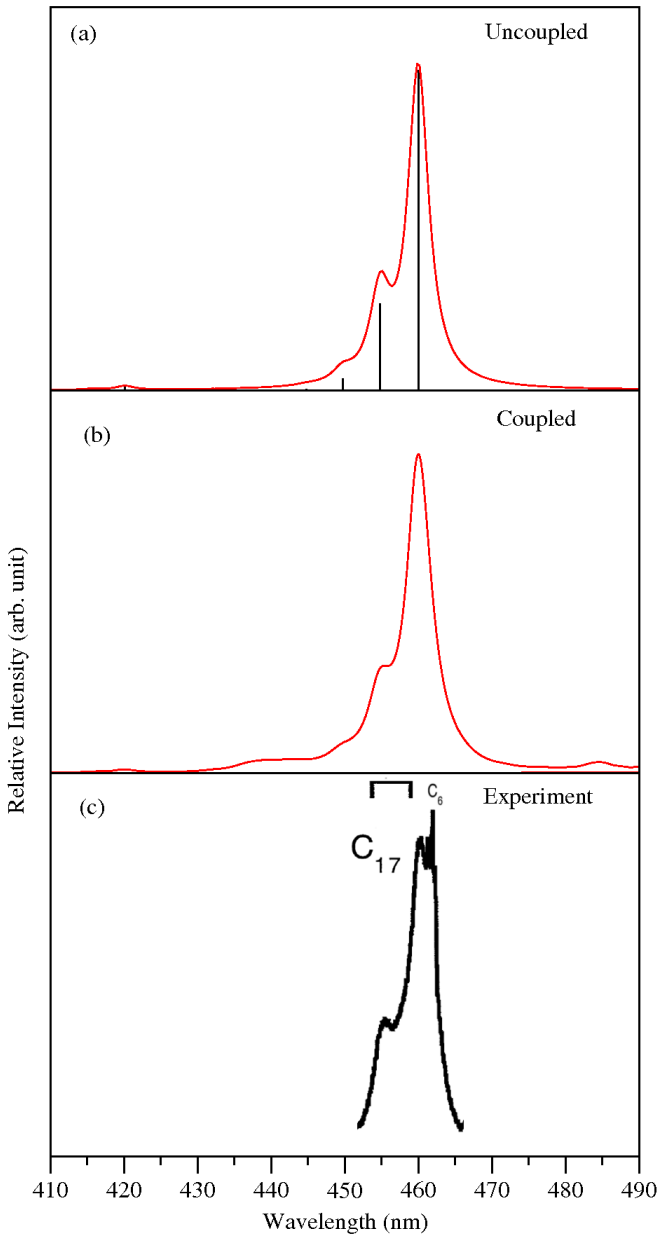

Figure 4.2: The stick vibronic spectrum and the convoluted envelope of the $^1\Sigma_u^+$ electronic state of C_{17} calculated with the σ_g^+ vibrational modes plotted in panel a. The absorption bands of the $^1\Sigma_u^+$ electronic state of C_{17} obtained from the coupled state dynamics study (see text for details). The intensity in arbitrary units is plotted as a function of wavelength in panel b. The experimental spectrum reproduced from Ref. [28] and shown in panel c.

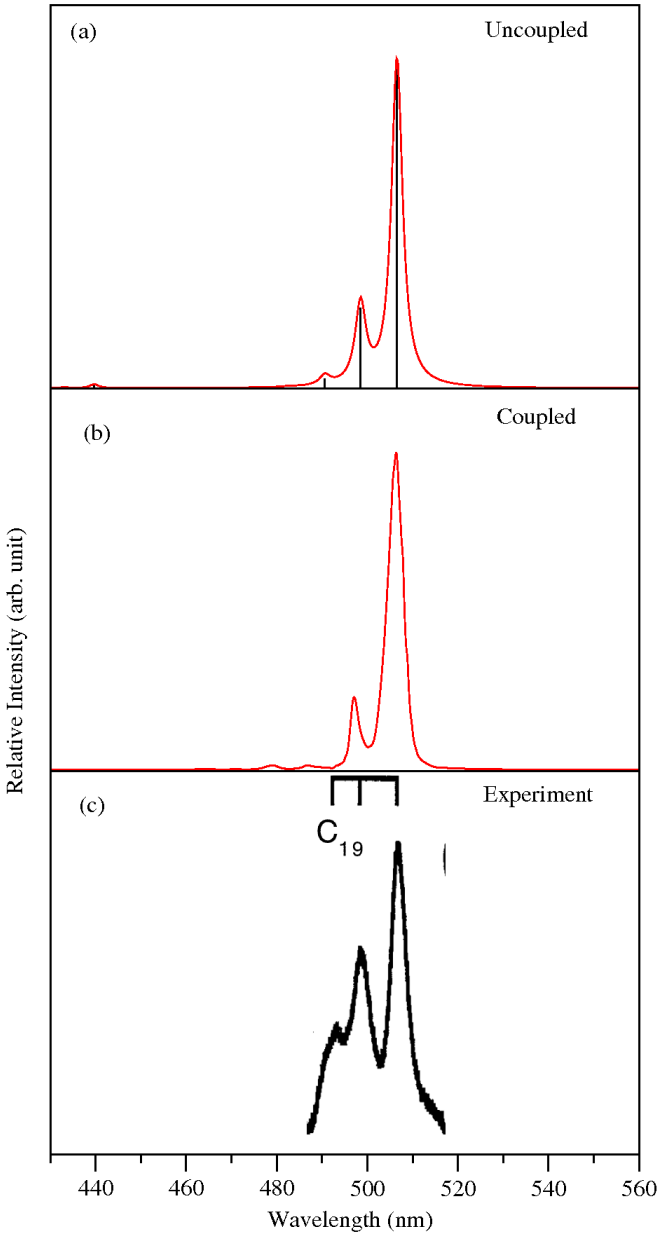

Figure 4.3: The stick vibronic spectrum and the convoluted envelope of the $^1\Sigma_u^+$ electronic state of C_{19} calculated with the σ_g^+ vibrational modes plotted in panel a. The absorption bands of the $^1\Sigma_u^+$ electronic state of C_{19} obtained from the coupled state dynamics study (see text for details). The intensity in arbitrary units is plotted as a function of wavelength in panel b. The experimental spectrum reproduced from Ref. [28] and shown in panel c.

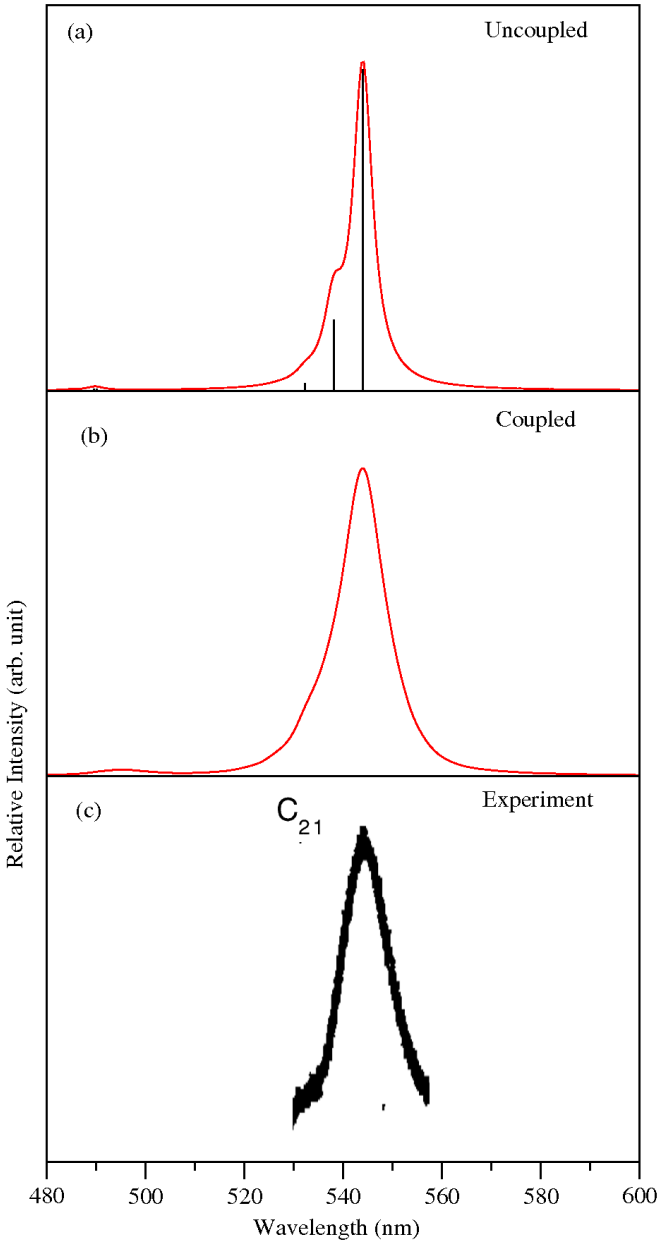

Figure 4.4: The stick vibronic spectrum and the convoluted envelope of the $^1\Sigma_u^+$ electronic state of C_{21} calculated with the σ_g^+ vibrational modes plotted in panel a. The absorption bands of the $^1\Sigma_u^+$ electronic state of C_{21} obtained from the coupled state dynamics study (see text for details). The intensity in arbitrary units is plotted as a function of wavelength in panel c. The experimental spectrum reproduced from Ref. [28] and shown in panel c.

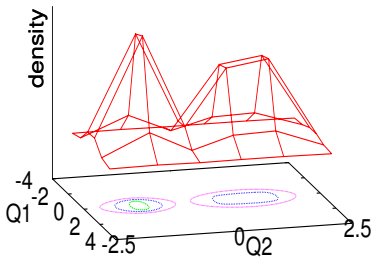

(a)

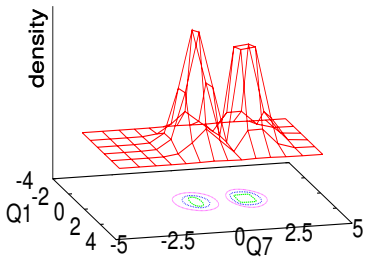

(b)

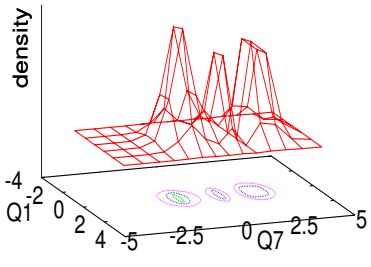

(c)

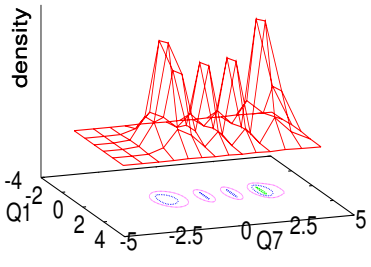

(d)

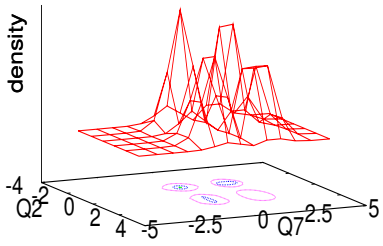

(e)

Figure 4.5: Reduced density plots of the vibronic wavefunctions of the fundamental of ν_2 and ν_7 (panels a-b, respectively) and first and second of ν_2 (panels c-d, respectively) excited in the $^1\Sigma_u^+$ state spectrum of C_{15}. The wavefunction in panels e represents the combination peak of $\nu_2 + \nu_7$.

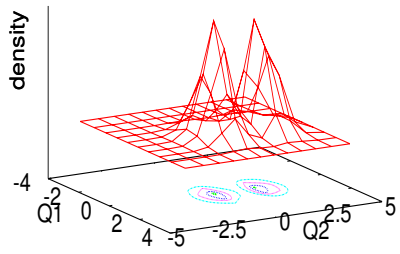

(a)

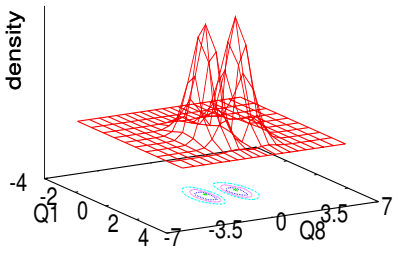

(b)

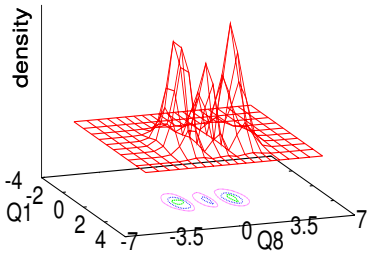

(c)

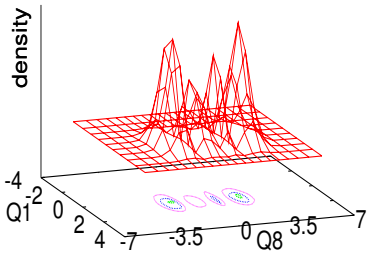

(d)

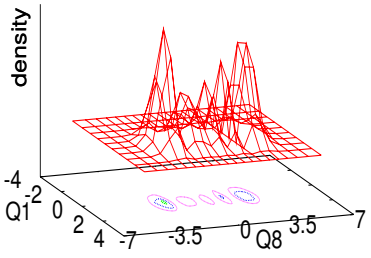

(e)

Figure 4.6: Reduced density plots of the vibronic wavefunctions of the fundamental of ν_2 and ν_8 (panels a-b, respectively) and first, second and third overtone of ν_8 (panels c-e, respectively) excited in the $^1\Sigma_u^+$ state spectrum of C_{17}.

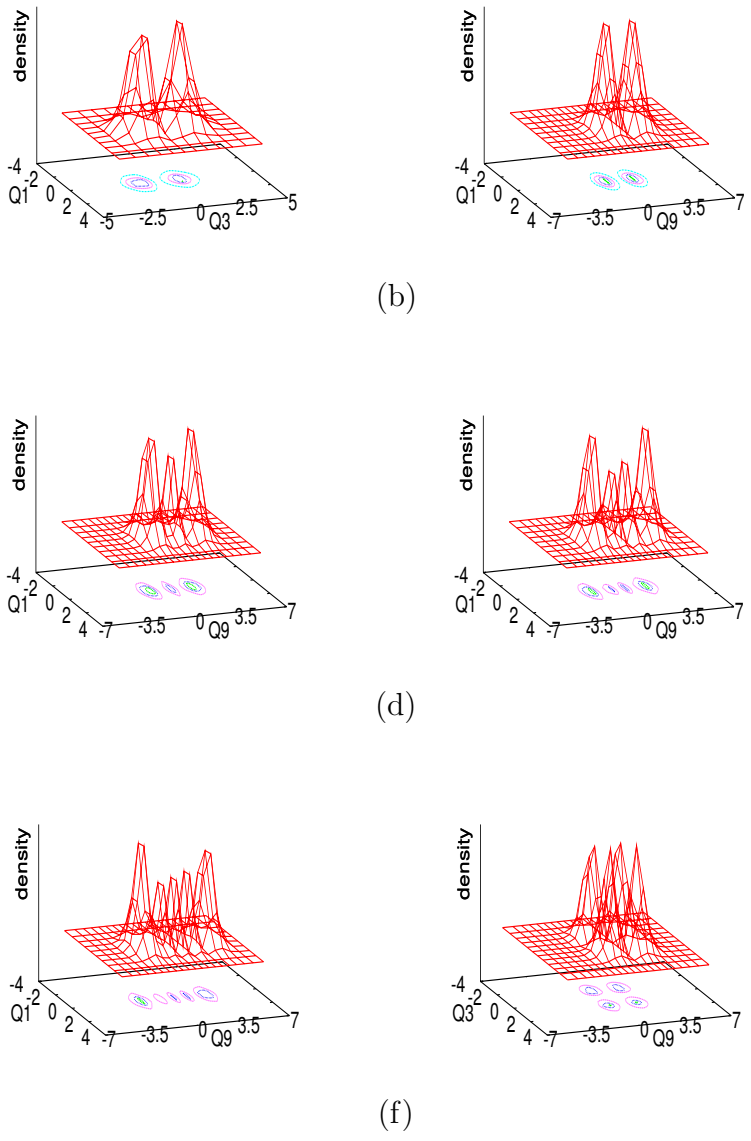

Figure 4.7: Reduced density plots of the vibronic wavefunctions of the fundamental of ν_3 and ν_9, (panels a-b, respectively) and first, second and third overtone of ν_9 (panels c-e, respectively) excited in the $^1\Sigma_u^+$ state spectrum of C_{19}. The wavefunction in panels f represents the combination peak of $\nu_3 + \nu_9$.

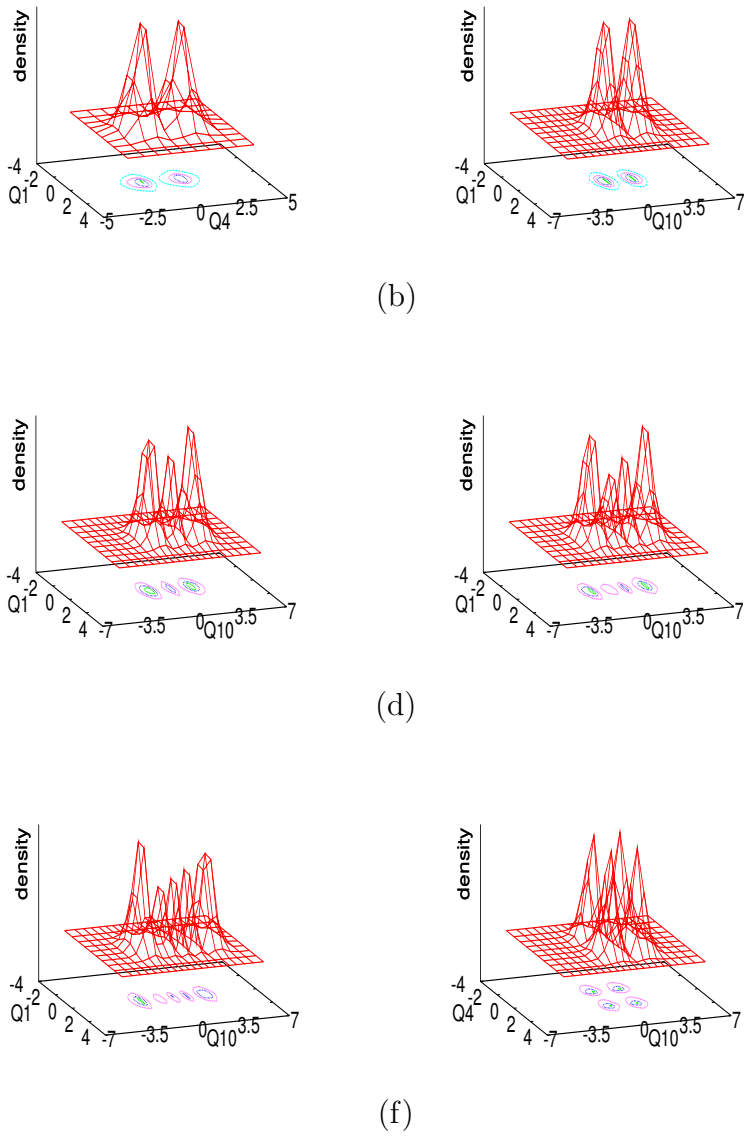

Figure 4.8: Reduced density plots of the vibronic wavefunctions of the fundamental of ν_4 and ν_{10} (panels a-b, respectively) and first, second and third overtone of ν_{10} (panels c-e, respectively) excited in the $^1\Sigma_u^+$ state spectrum of C_{21}. The wavefunction in panel f represents the combination peak of $\nu_4 + \nu_{10}$, respectively.

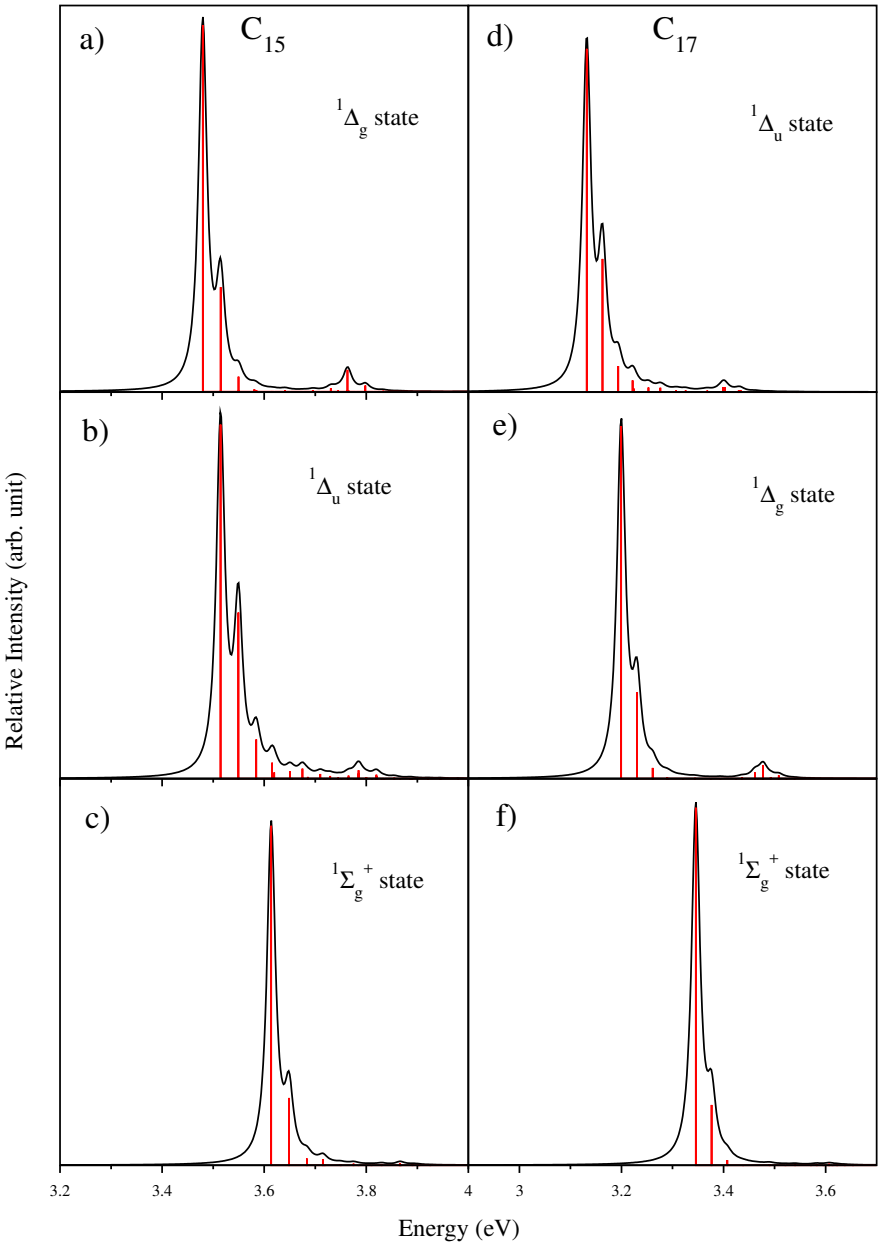

Figure 4.9: The stick vibronic spectrum and the convoluted envelope of the $^1\Delta_g$, $^1\Delta_u$ and $^1\Sigma_g^+$, electronic state of C_{15} (panel a-c, respectively) and $^1\Delta_u$, $^1\Delta_g$ and $^1\Sigma_g^+$, electronic state of C_{17} (panel d-f, respectively) calculated with the σ_g^+ vibrational modes are plotted.

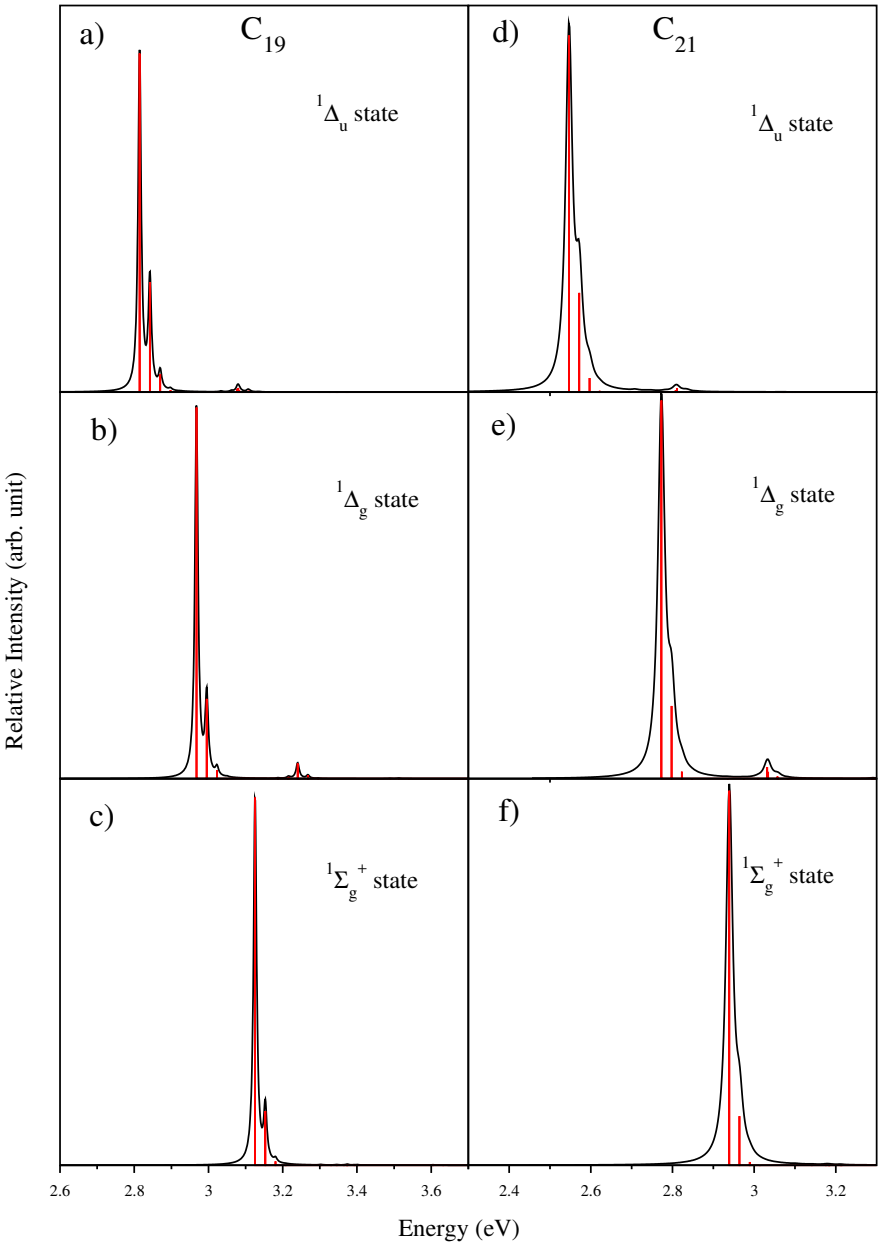

Figure 4.10: The stick vibronic spectrum and the convoluted envelope of the $^1\Delta_u$, $^1\Delta_g$ and $^1\Sigma_g^+$, electronic state of C_{19} (panel a-c, respectively) and $^1\Delta_u$, $^1\Delta_g$ and $^1\Sigma_g^+$, electronic state of C_{21} (panel d-f, respectively) calculated with the σ_g^+ vibrational modes are plotted.

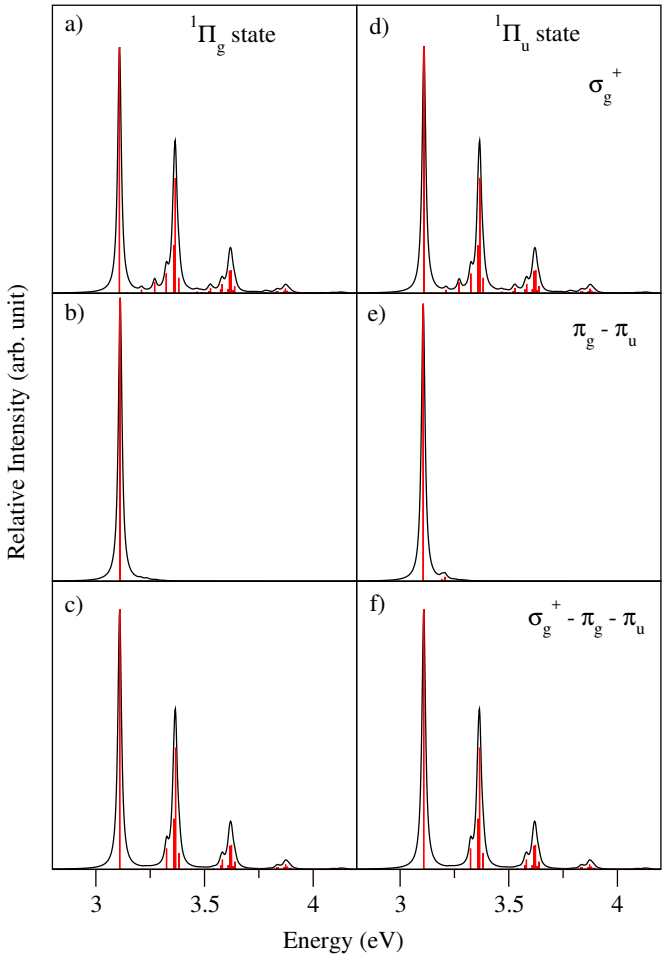

Figure 4.11: Vibrational energy level spectrum of the uncoupled Π_g and Π_u electronic states of C_{15} computed with (a) totally symmetric vibrational modes (σ_g^+) and (b) degenerate vibrational modes (π_g and π_u). The convoluted spectra of symmetric and degenerate vibrational modes are shown in panel c.

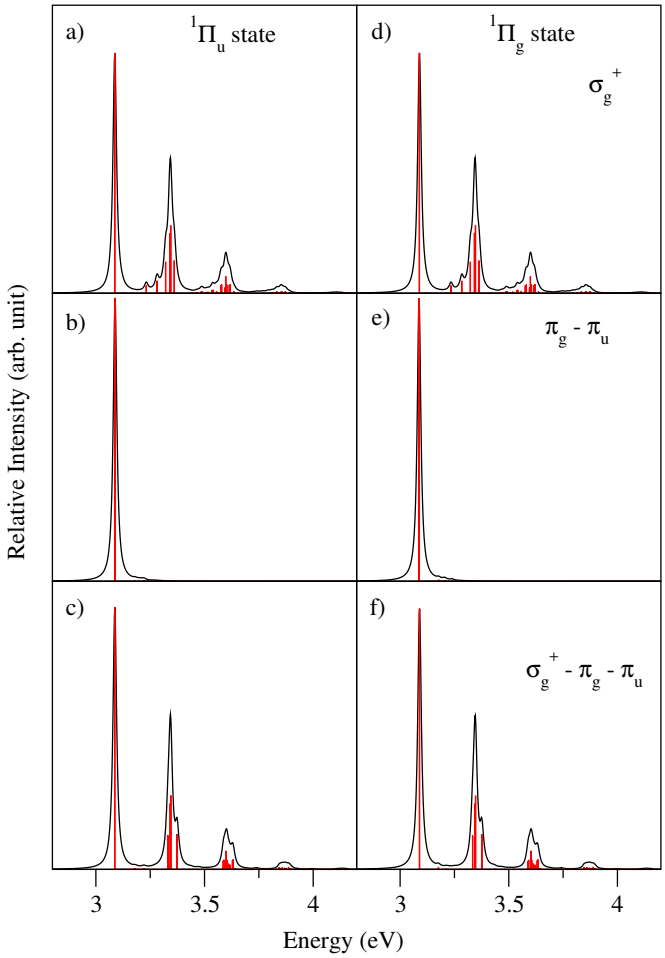

Figure 4.12: Vibrational energy level spectrum of the uncoupled Π_g and Π_u electronic states of C_{17} computed with (a) totally symmetric vibrational modes (σ_g^+) and (b) degenerate vibrational modes (π_g and π_u). The convoluted spectra of symmetric and degenerate vibrational modes are shown in panel c.

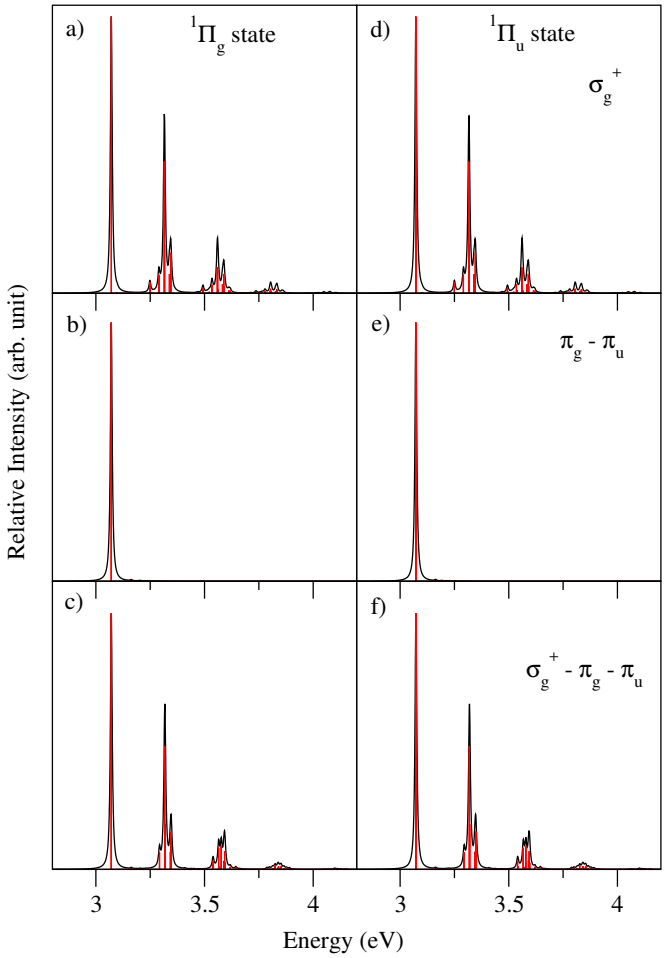

Figure 4.13: Vibrational energy level spectrum of the uncoupled Π_g and Π_u electronic states of C_{19} computed with (a) totally symmetric vibrational modes (σ_g^+) and (b) degenerate vibrational modes (π_g and π_u). The convoluted spectra of symmetric and degenerate vibrational modes are shown in panel c.

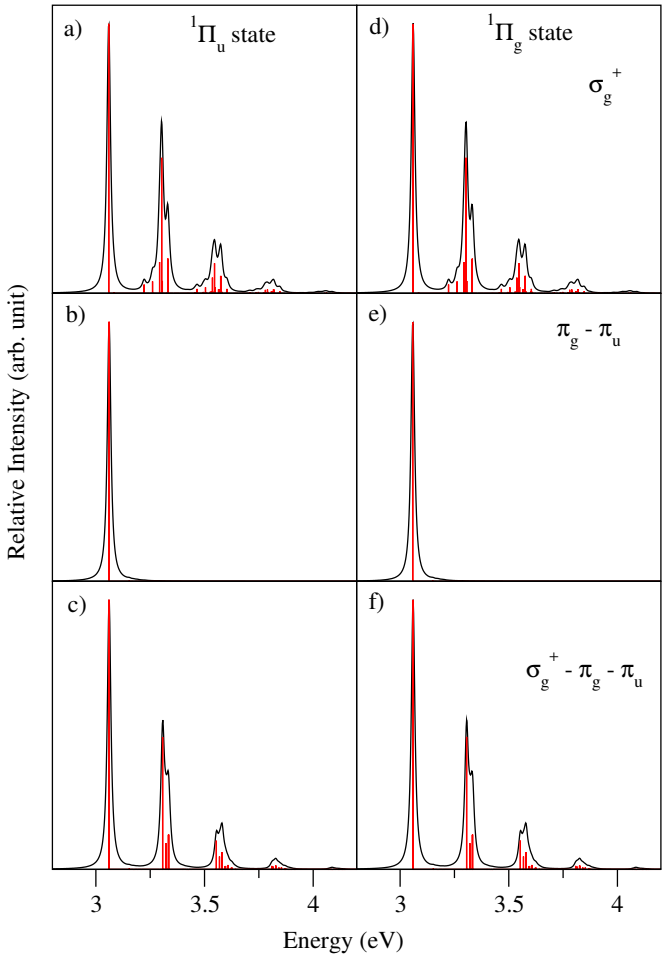

Figure 4.14: Vibrational energy level spectrum of the uncoupled Π_g and Π_u electronic states of C_{21} computed with (a) totally symmetric vibrational modes (σ_g^+) and (b) degenerate vibrational modes (π_g and π_u). The convoluted spectra of symmetric and degenerate vibrational modes are shown in panel c.

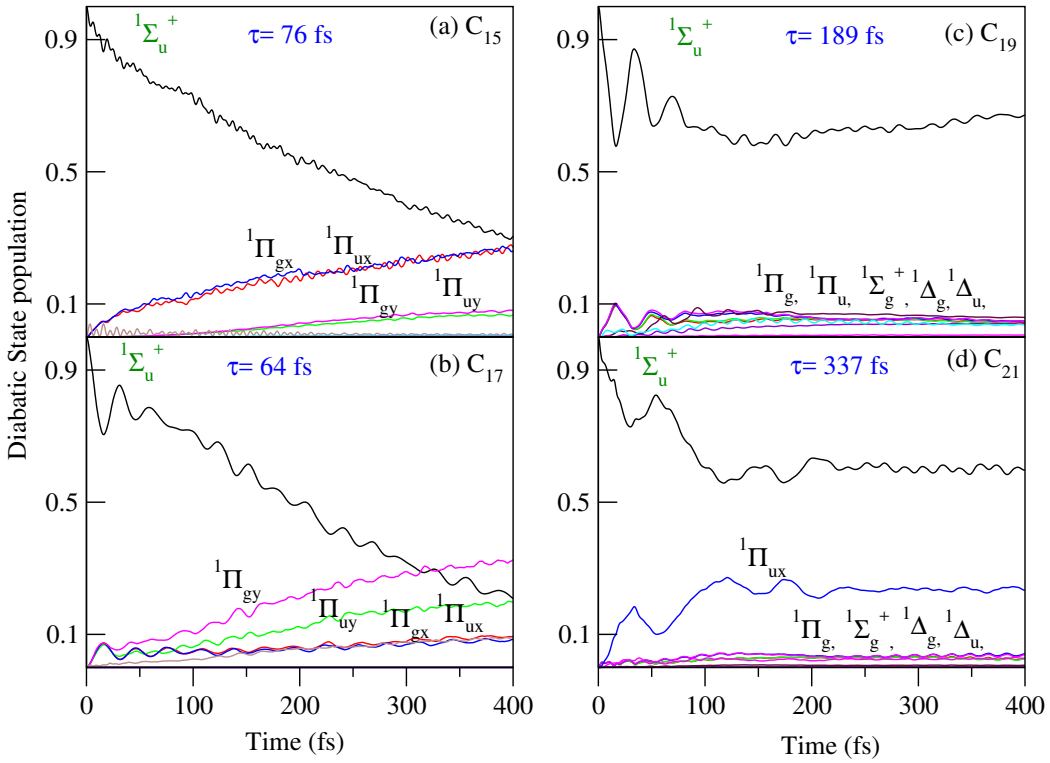

Figure 4.15: The time-dependence of diabatic electronic populations in the $^1\Pi_g$, $^1\Pi_u$, $^1\Sigma_u^+$, $^1\Sigma_g^+$, $^1\Delta_g$ and $^1\Delta_u$, coupled states nuclear dynamics of C_{2n+1} (n=7-10). The results obtained by initially locating the WP on the $^1\Sigma_u^+$ electronic states of C_{15}, C_{17}, C_{19} and C_{21} carbon chains are shown in panels a, b, c and d , respectively.

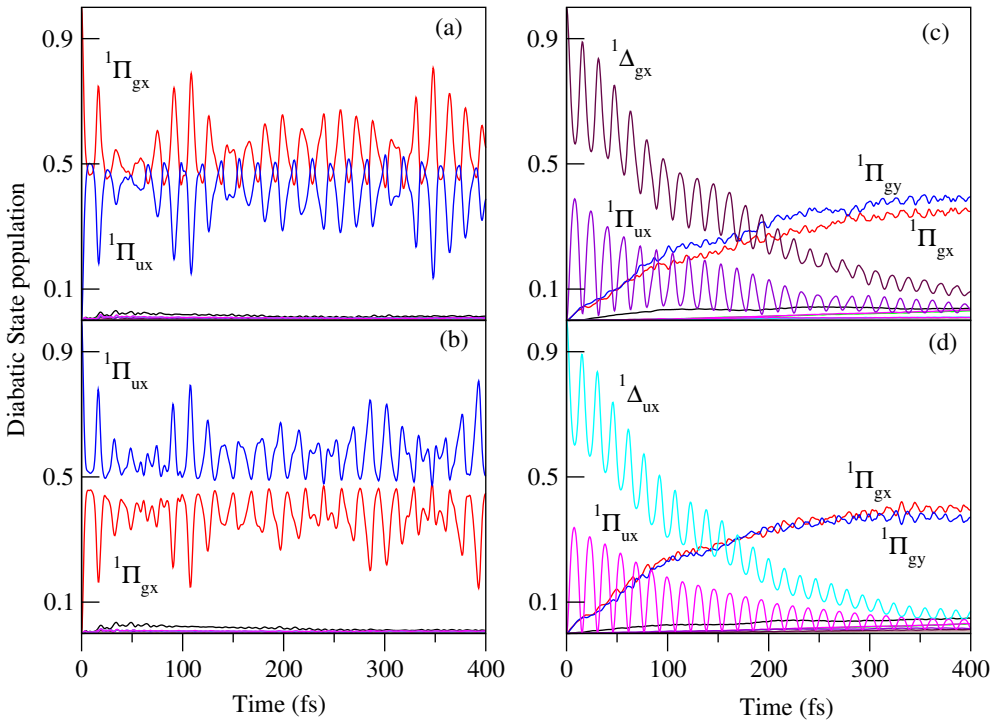

Figure 4.16: The time-dependence of diabatic electronic populations in the $^1\Sigma_u^+$ - $^1\Pi_g$ - $^1\Pi_u$ - $^1\Sigma_g^+$ - $^1\Delta_g$ - $^1\Delta_u$ coupled states nuclear dynamics of C_{2n+1} (n=7-10). The results obtained by initially locating the WP on the $^1\Pi_{gx}$, $^1\Pi_{ux}$, $^1\Delta_{gx}$ and $^1\Delta_{ux}$ electronic states of C_{15} are shown in panels a, b, c and d, respectively.

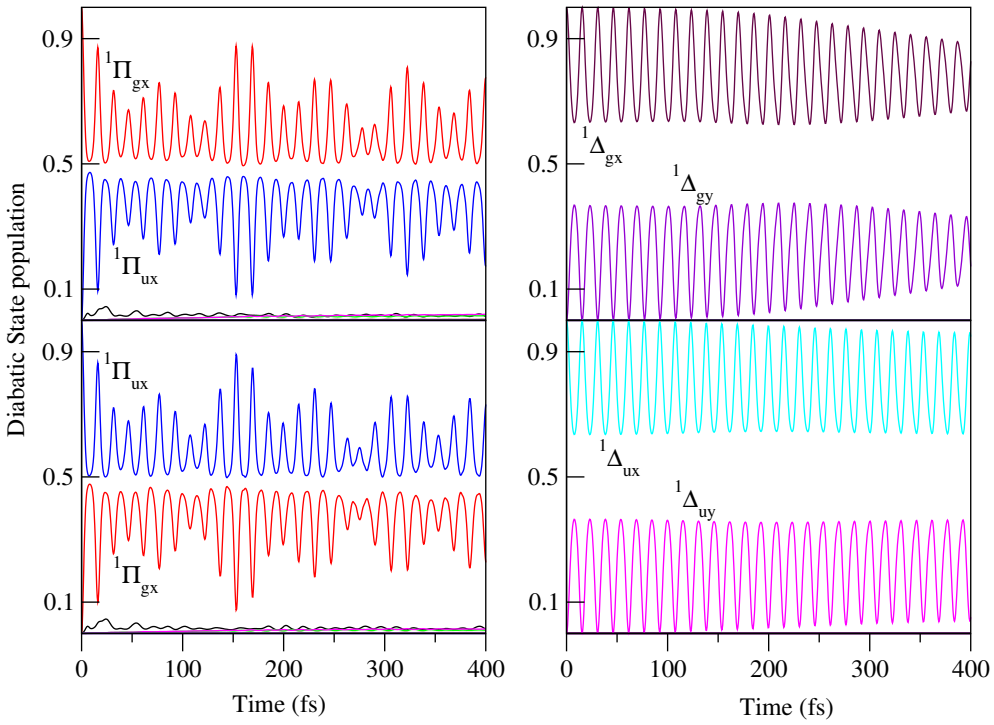

Figure 4.17: The time-dependence of diabatic electronic populations in the $^1\Sigma_u^+$ - $^1\Pi_g$ - $^1\Pi_u$ - $^1\Sigma_g^+$ - $^1\Delta_g$ - $^1\Delta_u$ coupled states nuclear dynamics of C_{2n+1} (n=7-10). The results obtained by initially locating the WP on the $^1\Pi_{gx}$, $^1\Pi_{ux}$, $^1\Delta_{gx}$ and $^1\Delta_{ux}$ electronic states of C_{17} are shown in panels a, b, c and d, respectively.

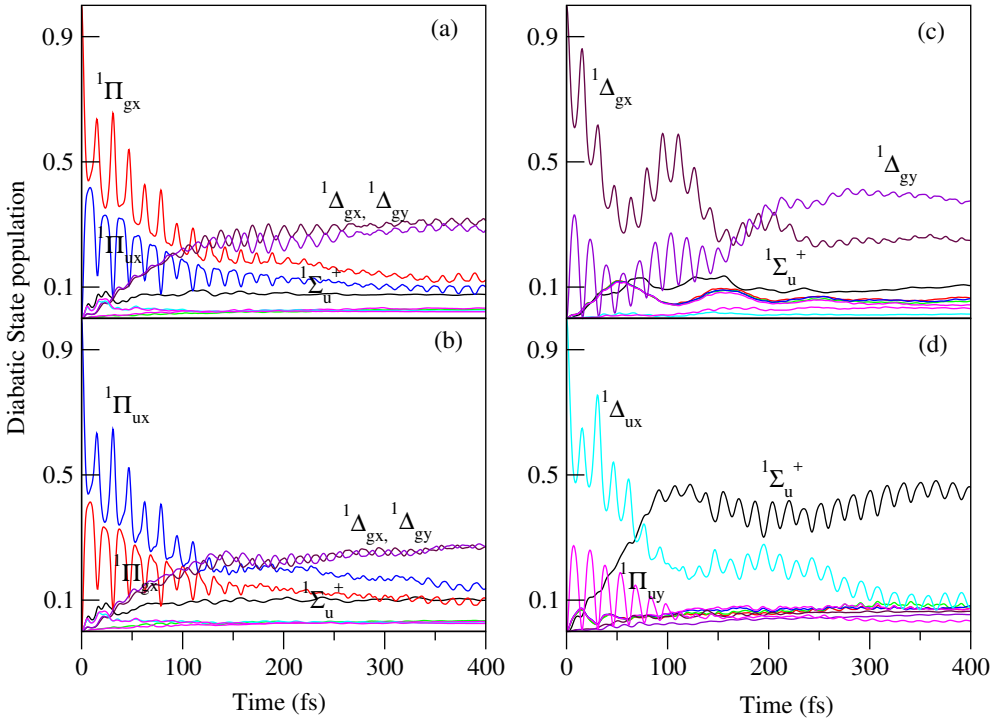

Figure 4.18: The time-dependence of diabatic electronic populations in the $^1\Sigma_u^+$ - $^1\Pi_g$ - $^1\Pi_u$ - $^1\Sigma_g^+$ - $^1\Delta_g$ - $^1\Delta_u$ coupled states nuclear dynamics of C_{2n+1} (n=7-10). The results obtained by initially locating the WP on the $^1\Pi_{gx}$, $^1\Pi_{ux}$, $^1\Delta_{gx}$ and $^1\Delta_{ux}$ electronic states of $_{C19}$ are shown in panels a, b, c and d, respectively.

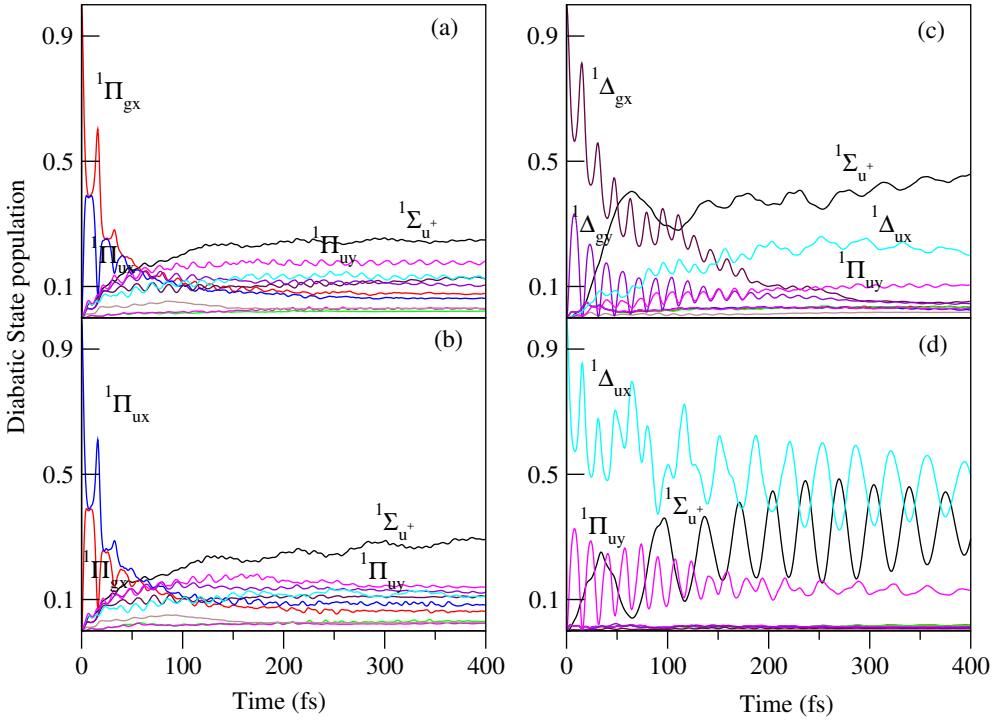

Figure 4.19: The time-dependence of diabatic electronic populations in the $^1\Sigma_u^+$ - $^1\Pi_g$ - $^1\Pi_u$ - $^1\Sigma_g^+$ - $^1\Delta_g$ - $^1\Delta_u$ coupled states nuclear dynamics of C_{2n+1} (n=7-10). The results obtained by initially locating the WP on the $^1\Pi_{gx}$, $^1\Pi_{ux}$, $^1\Delta_{gx}$ and $^1\Delta_{ux}$ electronic states of C_{21} are shown in panels a, b, c and d, respectively.

4.3 Summary

A detailed theoretical account of the multimode RT and PRT interactions in excited electronic states of linear C_{2n+1}, (n=7-10) cluster is presented in this chapter. The primary goal of this study is to estimate the lifetime of a strongly absorbing optically bright $^1\Sigma_u^+$ state of these clusters towards an assessment of their potentiality as carrier of DIBs. The vibronic Hamiltonian is constructed in a diabatic electronic basis, including the RT coupling within the degenerate $^1\Pi_g$, $^1\Pi_u$, $^1\Delta_g$ and $^1\Delta_u$ electronic states and the PRT couplings of these RT split states with the nondegenerate $^1\Sigma_u^+$ and $^1\Sigma_g^+$ electronic states (and among themselves)

of C_{2n+1}, where n=7-10. The coupling parameters of the vibronic Hamiltonian are determined by calculating the adiabatic PESs of the $^1\Pi_g$, $^1\Pi_u$, $^1\Delta_g$, $^1\Delta_u$, $^1\Sigma_u^+$ and $^1\Sigma_g^+$ electronic states along each of the 40 of C_{15}, 46 of C_{17}, 52 of C_{19} and 58 of C_{21} vibrational modes. First principles nuclear dynamics calculations are carried out both via time-independent and time-dependent quantum mechanical methods to simulate the nonadiabatic nuclear motion on the coupled manifold of these electronic states. The theoretical results are found to be in good accord with the available experimental results. The final theoretical calculations using the full Hamiltonian of Eq. 3.5 can only be carried out by propagating WPs employing the MCTDH algorithm . A careful examination of various theoretical results enabled us to arrive at the following conclusions. The RT effect in the $^1\Pi_g$ and $^1\Pi_u$ electronic states of C_{2n+1}, where n=7-10 is very weak. The PRT coupling between the $^1\Pi_g$ and $^1\Pi_u$ dominates the RT coupling. Due to the clustering of the four excited states within $\sim$ 1.0 eV, the nonradiative processes are found to be dominanting in predicting the vibronic structure and the transfer of diabatic electronic population among these states. The initial decay of the diabatic population of $^1\Sigma_u^+$ is estimated to be $\sim$76 fs for C_{15}, $\sim$64 fs for C_{17}, $\sim$189 fs for C_{19} and $\sim$337 fs for C_{21} which lie in the much anticipated range of $\sim$70-200 fs [11,12] for the potential carrier of DIBs.

References

[1] Conical Intersections: Electronic Structure, Dynamics and Spectroscopy, edited by W. Domcke, D. R. Yarkony, and H. Köppel (World Scientific, Singapore, 2004).

[2] H. Köppel, W. Domcke and L. S. Cederbaum, *Adv. Chem. Phys.* **57**, 59 (1984).

[3] M. Born and R. Oppenheimer, Ann. Phys. **84**, 457 (1927).

[4] M. Born and K. Huang, The Dynamical Theory of Crystal Lattices, (Oxford University Press, Oxford, U.K., 1954).

[5] R. Englman, The Jahn-Teller Effect, (Wiley, New York, 1972).

[6] M. Baer, Beyond Born-Oppenheimer:electronic non-adiabatic coupling terms and conical intersections, (John Wiley and Sons, 2006).

[7] S. Mahapatra, Acc. Chem. Res. **42**, 1004 (2009).

[8] J. P. Maier Chem. Soc. Rev. **17**, 45, (1988).

[9] J. P. Maier Chem. Soc. Rev. **26**, 21, (1997).

[10] J. P. Maier J. Phys. Chem. A **102** 3462 (1998).

[11] E. B. Jochnowitz and J. P. Maier, Annu. Rev. Phys. Chem. **59**, 519 (2008).

[12] C. A. Rice and J. P. Maier, J. Phys. Chem. A **117**, 5559 (2013).

[13] I. B. Bersuker, *The Jahn-Teller effect*, (Cambridge University Press, Cambridge (U.K), 2006).

[14] P. Garcia-Fernandez and I. B. Bersuker, Int, Jou, Quant, Chem, **112**, 3025 (2012).

[15] R. Renner, Z. Physik **92**, 172 (1934).

[16] J. A. Pople, Mol. Phys.**3**, 16, (1960).

[17] A. J. Merer and D. N. Travis, Can. J. Phys. **43**, 1795 (1965).

[18] J. A. Pople and H. C. Louguet-Higgins, Mol. Phys. **1**, 372 (1958).

[19] M. Perić, M. Petković and S. Jerosimić, Chem. Phys. **343**, 141 (2008).

[20] M. Perić, R. Ranković and S. Jerosimić, Chem. Phys. **344**, 35 (2008)

[21] H. Köppel, W. Domcke and L. S. Cederbaum, J. Chem. Phys. **74**, 2945 (1991).

[22] G. A. Worth, M. H. Beck, A. Jäckle, and H. -D. Meyer, The MCTDH Package, Version 8.2, (2000), University of Heidelberg, Heidelberg, Germany. H. -D. Meyer, Version 8.3 (2002), Version 8.4 (2007). See http://mctdh.uni-hd.de.

[23] H. -D. Meyer, U. Manthe, and L. S. Cederbaum, Chem. Phys. Lett. **165**, 73 (1990).

[24] U. Manthe, H. -D. Meyer, and L. S. Cederbaum, J. Chem. Phys. **97**, 3199 (1992).

[25] M. H. Beck, A. Jäckle, G. A. Worth, and H. -D. Meyer, Phys. Rep. **324**, 1 (2000).

[26] J. M. L. Martin, J. E. Yazal and J-P Francois, Chem. Phys. Lett. **252**, 9, (1996).

[27] Botschwina, P, Phys. Chem. A. **111**, 7431, (2007).

[28] D. Forney, P. Freivogel, M. Grutter, and J. P. Maier, J. Chem. Phys. **104**, 4954 (1996);

[29] M. Wyss, M. Grutter and J. P. Maier, Chem. Phys. Lett. **304**, 35 (1999);

[30] J. Cullum and R. Willoughby, Lanczos Algorithms for Large Symmetric Eigenvalue Problems (Birkhäuser, Boston, 1985, Vols. I and II).

[31] Meng. Q.; Meyer. H. -D. MCTDH Study on Vibrational States of the CO/Cu(100) System. *J. Chem. Phys.* **2013**, *139*, 164709-14.

[32] Peláez. D.; Sadri. K.; Meyer. H. -D. Full-dimensional MCTDH/MGPF Study of the Ground and Lowest Lying Vibrational States of the Bihydroxide $H_3O_2^-$ Complex. *Spectrochimica Acta Part A: Molecular and Biomolecular Spectroscopy.* **2014**, *119*, 42-51.

Chapter 5

Vibronic coupling in the $\widetilde{X}^2\Pi_g$ - $\widetilde{A}^2\Pi_u$ band system of diacetylene radical cation

In this chapter vibronic interactions in the two energetically lowest degenerate electronic states ($\widetilde{X}^2\Pi_g$ - $\widetilde{A}^2\Pi_u$) of diacetylene radical cation ($C_4H_2{}^+$) are theoretically examined. The spectroscopy of these two electronic states of $C_4H_2{}^+$ has been a subject of considerable interest and measured in laboratory by various groups. Inspired by numerous experimental data, we attempt here a detailed investigation of vibronic interactions within and between the degenerate electronic states and their impact on the vibronic structure of each state. A vibronic coupling model is constructed in a diabatic electronic basis and with the aid of ab initio *quantum chemistry calculations. The vibronic structures of the electronic states are calculated by time-independent and time-dependent quantum mechanical methods. The progression of vibrational modes in the vibronic band is identified, assigned and discussed in relation to the literature data. The nonradiative*

internal conversion dynamics is also examined and discussed.

5.1 Introduction

The $\widetilde{A}^2\Pi_u$ - $\widetilde{X}^2\Pi_g$ band system of diacetylene radical cation ($C_4H_2^{\cdot\,+}$) is a subject of intense research since 1950. The common visible bands of organic vapors observed by Schüler and Reinebeck [1] and labelled as "T" spectrum was assigned to this band system by Callomon [2]. Since then several high resolution experiments carried out attempting to confirm the presence of $C_4H_2^{\cdot\,+}$ in the interstellar medium as a carrier of 506.9 nm diffuse interstellar band (DIB). Recent gas phase experimental studies of both Motylewski *et al.* [3] and Krelowski *et al.* [4] apparently confirmed the 506.9 nm DIB is due to $\widetilde{A}^2\Pi_u \leftarrow \widetilde{X}^2\Pi_g$ transition in $C_4H_2^{\cdot\,+}$. However, the most recent gas phase absorption measurements of Maier *et al.* [5] disagree with this assignment both in terms of absorption wavelength and the band shape and association of 506.9 nm DIB with $C_4H_2^{\cdot\,+}$ was proposed to be unlikely. Apart from these, $C_4H_2^{\cdot\,+}$ also proposed to play crucial role in the formation of larger polycyclic aromatic hydrocarbons in the interstellar medium [6–8] and have relevance in plasma chemistry.

The structure and spectroscopy of $C_4H_2^{\cdot\,+}$ was studied by several research groups over the past decades [9–11]. Photoelectron spectrum of C_4H_2 was measured by Baker *et al.* [12]. Theoretical and experimental ionization energies have been reported and their possible implication in the redox chemistry of planetary atmosphere was discussed [13]. Very recent study of Gronowski *et al.* [14] reveals that the linear isomer of diacetylene is the most stable structure [14]. In addition to matrix isolation Spectroscopy studies [15–20], gas phase laboratory [3, 19] and stellar spectroscopy studies [4, 5] were also carried out on $C_4H_2^{\cdot\,+}$. The vibronic

progressions in the $\widetilde{X}$ and $\widetilde{A}$ bands have been reported. In the $\widetilde{X}$ band excitation of fundamental of C ≡ C symmetric stretch (ν_2) and first overtone of C – H asymmetric stretch (ν_4) vibrational modes with energy separation of $\sim$ 2121 and $\sim$ 5405 cm^{-1}, respectively, was reported by Baker *et al.* [12]. In the $\widetilde{A}$ band, progression of the fundamental of central C – C stretch (ν_3) vibrational mode at $\sim$ 887 cm^{-1} was reported by the same authors. Callomon *et al.* reported excitation of four vibrational modes and their combinations in the $\widetilde{A}$ band [2]. Peak spacings of $\sim$ 861, $\sim$ 971, $\sim$ 2177 and $\sim$ 3137 cm^{-1} were assigned to ν_3, $2\nu_7$, ν_2 and ν_1 vibrational modes, respectively. Bondybey *et al.* [18] reported $\sim$ 3143, $\sim$ 2177 and $\sim$ 865 cm^{-1} progressions in the $\widetilde{X}$ band and assigned them to the fundamental of ν_1, ν_2 and ν_3 vibrations, respectively. In addition, the progression of $\sim$ 973 cm^{-1} was assigned to the overtone of ν_7 vibration [18]. The corresponding progressions in the $\widetilde{A}$ band were reported at $\sim$ 2821, $\sim$ 2002, $\sim$ 807 and $\sim$ 864 cm^{-1}, respectively, in that order by these authors. The excitation of degenerate vibrational modes in the $\widetilde{A}^2\Pi_u$ - $\widetilde{X}^2\Pi_g$ band system was also reported by various other groups [3, 19, 21, 22].

The linear $C_4H_2^{\cdot+}$ radical cation belongs to the $D_{\infty h}$ symmetry point group at its equilibrium configuration. This linear system is prone to the bending instability and the degeneracy of the Π electronic states would split upon distortion along the bending vibrational modes and would exhibit Renner-Teller (RT) activity. Apart from a few computational studies on the electronic structure of the $\widetilde{X}^2\Pi_g$ and $\widetilde{A}^2\Pi_u$ states of $C_4H_2^{\cdot+}$, a rigorous dynamics study including RT coupling and coupling between the Π states to elucidate the detailed vibronic structures has not been carried out so far. The present effort is aimed towards this endeavor. In order to accomplish the proposed goal, the potential energy surfaces of the coupled $\widetilde{X}^2\Pi_g$ and $\widetilde{A}^2\Pi_u$ electronic states are constructed with the aid of vibronic

coupling theory and *ab initio* quantum chemistry calculations. Employing these potential energy surfaces nuclear dynamics calculations are carried out by time-independent and time-dependent quantum mechanical methods. Theoretically calculated vibronic band structures of the $\widetilde{X}^2\Pi_g$ and $\widetilde{A}^2\Pi_u$ states are compared with the experiment. The progression in the vibronic bands are assigned and compared with the literature data. The effect of RT and $\widetilde{X}$-$\widetilde{A}$ coupling on the vibronic dynamics is examined and discussed.

5.2 The Vibronic Hamiltonian

In this section we construct a Hamiltonian describing vibronic interactions in the Π_g and Π_u electronic states of $C_4H_2^{\cdot +}$. The Hamiltonian is constructed in terms of the dimensionless normal displacement coordinates of the vibrational modes of the electronic ground state of neutral C_4H_2 [23, 24]. Standard vibronic coupling theory in a diabatic electronic representation and elementary symmetry rules are utilized for the purpose. The C_4H_2 molecule possesses $D_{\infty h}$ point group symmetry at the equilibrium minimum of its electronic ground state. Its 13 vibrational modes transform according to,

$$\Gamma_{vib} \;=\; 3\sigma_g^+ \oplus 2\sigma_u^+ \oplus 2\pi_g \oplus 2\pi_u, \tag{5.1}$$

irreducible representations (IREPs) of $D_{\infty h}$ symmetry point group. The activity of vibrational modes in the electronic states j and k is governed by the symmetry rule, $\Gamma_j \otimes \Gamma_k \supset \Gamma_{vib}$. The symmetrized direct product of Π_g and Π_u states in the $D_{\infty h}$ point group reads

$$\Pi_g \otimes \Pi_g = \delta_g + \sigma_g^+ = \Pi_u \otimes \Pi_u$$

The totally symmetric σ_g^+ vibrational modes can not split the degeneracy of either Π_g or Π_u electronic states. These modes are condon active within these electronic states. The δ_g vibrational modes can split the orbital degeneracy of the Π state in first order. Because of lack of vibrational modes of δ_g symmetry in a linear molecule, the first order coupling between the components of doubly degenerate Π state vanishes. However, $(\pi_g)^2 = (\pi_u)^2 \supset \delta_g$, and therefore, the π_g or π_u modes can couple them in second-order. This gives rise to RT coupling and a splitting of the Π degeneracy. The components of the split Π_g or Π_u states can also undergo coupling according to

$$\Pi_g \otimes \Pi_u \;\; = \;\; \delta_u + \sigma_u^+ + \sigma_u^- .$$

Considering the symmetry rules given above the following vibronic Hamiltonian is derived,

$$\mathcal{H} \;\; = \;\; (\mathcal{T}_N + \mathcal{V}_0)\mathbf{1_4} + \begin{pmatrix} W_{\tilde{X}x} & W_{\tilde{X}x-\tilde{X}y} & W_{\tilde{X}x-\tilde{A}x} & 0 \\ & W_{\tilde{X}y} & 0 & W_{\tilde{X}y-\tilde{A}y} \\ & & W_{\tilde{A}x} & W_{\tilde{A}x-\tilde{A}y} \\ h.c & & & W_{\tilde{A}y} \end{pmatrix} . \qquad (5.2)$$

In the above, $\mathcal{H}_0 = \mathcal{T}_N + \mathcal{V}_0$, represents the Hamiltonian (assumed to be harmonic) of the reference electronic ground (S_0) state of C_4H_2 with

$$\mathcal{T}_N = -\frac{1}{2} \sum_{i \,\in\, \sigma_g^+,\, \sigma_u^+} \omega_i \frac{\partial^2}{\partial Q_i^2} - \frac{1}{2} \sum_{i \,\in\, \pi_g,\, \pi_u} \omega_i \left(\frac{\partial^2}{\partial Q_{ix}^2} + \frac{\partial^2}{\partial Q_{iy}^2} \right), \qquad (5.3)$$

and

$$\mathcal{V}_0 = \frac{1}{2} \sum_{i \in \sigma_g^+,\, \sigma_u^+} \omega_i Q_i^2 + \frac{1}{2} \sum_{i \in \pi_g,\, \pi_u} \omega_i \left(Q_{ix}^2 + Q_{iy}^2 \right). \tag{5.4}$$

The quantity $\mathbf{1_4}$ is a 4×4 diagonal unit matrix. The matrix Hamiltonian (with elements W) in Eq. 5.2 represents the diabatic energies of the given electronic states of the radical cation (diagonal elements) and their coupling energies (off-diagonal elements). The elements of this matrix are expanded in a standard Taylor series around the reference equilibrium geometry at, $\mathbf{Q} = \mathbf{0}$, in the following way [23]

$$\begin{aligned} W_{jx/jy} \;=\; & E_0^j + \sum_{i \in \sigma_g^+} \kappa_i^j Q_i + \sum_{i \in \sigma_g^+,\, \sigma_u^+} \gamma_i^j Q_i^2 + \sum_{i \in \pi_g,\, \pi_u} [\gamma_i^j (Q_{ix}^2 + Q_{iy}^2)] + \\ & \sum_{i \in \pi_g,\, \pi_u} [\xi_i^j (Q_{ix}^2 + Q_{iy}^2)^2] \qquad \pm \sum_{i \in \pi_g,\, \pi_u} \eta_i^j (Q_{ix}^2 - Q_{iy}^2) \pm \sum_{i \in \pi_g,\, \pi_u} \delta_i^j (Q_{ix}^4 - Q_{iy}^4);\; j \in \tilde{X}, \tilde{A} \end{aligned} \tag{5.5}$$

$$W_{jx-jy} \;=\; \sum_{i \in \pi_g,\, \pi_u} 2\eta_i^j (Q_{ix} Q_{iy}) + 2\delta_i^j (Q_{ix}^3 Q_{iy} - Q_{ix} Q_{iy}^3) \;;\; j \in \widetilde{X}, \widetilde{A} \tag{5.6}$$

$$W_{jx-kx/jy-ky} \;=\; \sum_{i \in \sigma_u^+} \lambda_i^{j-k} Q_i \;;\; j \in \widetilde{X} \; and \; k \in \widetilde{A} \tag{5.7}$$

In the above equations the quantity $E_0{}^j$ represents the vertical ionization energy (VIE) of the j^{th} electronic state. The two components of the degenerate states and modes are labeled with x/y throughout this study. The quantities κ_i^j, η_i^j and δ_i^j represent linear intrastate, quadratic and quartic RT coupling parameters for the symmetric (σ_g^+) and degenerate (π_g, π_u) vibrational modes, respectively, for the j^{th} electronic state. The first-order coupling parameter of the i^{th} vibrational mode between the electronic states j and k is given by λ_i^{j-k} (this is like pseudo-Jahn-Teller coupling of Jahn-Teller split component electronic states) and

γ_i^j and ξ_i^j are the second-order and fourth-order intrastate coupling parameters respectively, of the i^{th} vibrational mode for the j^{th} electronic state. The summations run over the normal modes of vibration of symmetry specified in the index. The + and - sign applicable to the x and y components of the degenerate state, respectively. We note that the relative sign of various elements of the diabatic electronic Hamiltonian matrix is determined by checking its invariance with respect to various symmetry operations, correlating to the D_{6h} symmetry point group and following similar works on benzene and cyclopropane radical cations [25–27].

5.2.1 Electronic structure calculations

The molecular geometry of C_4H_2 in the electronic ground state is optimized within the second-order Møller-Plesset perturbation (MP2) level of theory employing Dunning's augmented polarized valence triple-zeta basis set (aug-cc-pVTZ) [28] using Gaussian 03 suite of programs [29]. The equilibrium geometry converged to $D_{\infty h}$ symmetry point group. The equilibrium geometry parameters are given in Table 5.1. Harmonic vibrational frequency (ω_i) and mass-weighted normal displacement coordinate of vibrational modes are calculated at the optimized molecular geometry. The normal coordinates are multiplied by $\sqrt{\omega}_i$ (in atomic units) to transform them to their dimensionless form (Q_i) [24]. In this definition equilibrium geometry of C_4H_2 occurs at $\mathbf{Q}$=0. The calculated harmonic frequency of 13 vibrational modes (including degeneracy), their symmetry and description along with the available literature data are given in Table 5.1. The vertical ionization energies (VIEs) of C_4H_2 along each relevant vibrational mode for various nuclear geometries, $Q_i = \pm$ 0.10 and $\pm$ 0.25 to $\pm$ 4.0 with a spacing of 0.25, are computed with the equation-of-motion coupled-cluster singles and

doubles (EOM-CCSD) method using aug-cc-pVTZ basis set. The EOM-CCSD calculations are performed using CFOUR suite of programs [30]. The calculated *ab initio* energies are fitted to the adiabatic counterpart of the diabatic electronic Hamiltonian of Eq. 1 by a least squares procedure to estimate the parameters of the Hamiltonian defined in Sec. 5.2. The coupling parameters (defined above) and VIEs estimated from the present electronic structure data are presented in Tables 5.2 and 5.3, respectively.

Table 5.1: Symmetry and harmonic frequency (in cm^{-1}) of vibrational modes of the ground electronic state of C_4H_2. The experimental results represent fundamental frequencies.

Symm.	Mode	MP2/aug-cc-pVTZ	CCSD(T)/cc-pVQZ [39]	Ref. [40]†	Expt. [41]	Description
σ_g^+	ν_1	3475	3457	3489	3332	C-H symmetric stretch
	ν_2	2185	2235	2222	2189	C≡C symmetric stretch
	ν_3	897	892	885	872	C-C symmetric stretch
σ_u^+	ν_4	3475	3458	3490	3333	C-H asymmetric stretch
	ν_5	2001	2057	2050	2019	C≡C asymmetric stretch
π_g	ν_6	608	632	638	626	C-H bend
	ν_7	448	481	490	483	C-C bend
π_u	ν_8	619	634	641	628	C-H bend
	ν_9	219	220	223	220	C-C bend

Table 5.2: Linear (κ_i and λ_i^{X-A}), quadratic (γ_i and η_i) and quartic (ξ_i and δ_i) coupling constants of the Hamiltonian [*cf.*, Eqs.(2-7)]for the $\widetilde{X}^2\Pi_g$ and $\widetilde{A}^2\Pi_u$ electronic states of $C_4H_2^{\cdot+}$. Dimensionless excitation strengths are given in the square brackets. All quantities are given in the eV unit.

Symmetry	Mode Freq	κ_i or η_i (δ_i)	γ_i (ξ_i)	κ_i or η_i (δ_i)	γ_i (ξ_i)	λ_i^{X-A}
		$\widetilde{X}^2\Pi_g$		$\widetilde{A}^2\Pi_u$		
σ_g^+	ν_1 0.4309	-0.0136 [0.0005]	0.0011	-0.0203 [0.0011]	0.0007	-
	ν_2 0.2710	-0.2393 [0.3899]	0.0052	-0.0646 [0.0284]	0.0049	-
	ν_3 0.1112	0.0396 [0.0634]	-0.0015	-0.1373 [0.7623]	0.0045	-
σ_u^+	ν_4 0.4309	-	0.0006	-	0.0010	0.0234 [0.0014]
	ν_5 0.2481	-	-0.0041	-	0.0176	0.1737 [0.2451]
π_g	ν_6 0.0754	-0.0045 (0.0001)	-0.0009 (0.0000)	0.0027 (0.0000)	-0.0036 (0.0000)	-
	ν_7 0.0556	-0.0044 (0.0000)	0.0026 (0.0000)	-0.0025 (0.0000)	-0.0129 (0.0000)	-
π_u	ν_8 0.0768	-0.0079 (0.0001)	0.0025 (0.0001)	0.0037 (0.0000)	-0.0037 (0.0000)	-
	ν_9 0.0271	-0.0004 (0.0000)	-0.0210 (0.0001)	-0.0005 (0.0000)	-0.0189 (0.0000)	-

Table 5.3: Vertical ionization energies (in eV) of the $\widetilde{X}$ and $\widetilde{A}$ states of $C_4H_2^{\cdot+}$.

States	EOM-CCSD(aug-cc-pVTZ)	Ref. [12]	Ref. [13]
$\widetilde{X}^2\Pi_g$	10.33	10.17	10.03
$\widetilde{A}^2\Pi_u$	12.94	12.62	-

5.3 Nuclear dynamics

The vibronic spectrum of the $\widetilde{X}$ and $\widetilde{A}$ electronic states of $C_4H_2{}^+$ is examined in this study. The spectral intensity as a function of final state energy is calculated using Fermi's golden rule,

$$I(E) \;=\; \sum_{v} \left| \langle \Psi_v^{\alpha} | \hat{T} | \Psi_0^{i} \rangle \right|^2 \delta(E - E_v^{\alpha} + E_0^{i}). \tag{5.8}$$

Here, $|\Psi_0^i\rangle$ represents the wavefunction of the initial vibronic ground state of C_4H_2 (with energy E_0^i), and $|\Psi_v^\alpha\rangle$ is the wavefunction of the final (α) vibronic state with energy E_v^α. The quantity $\hat{T}$ defines the transition dipole operator. The vibronic ground (reference) state is expressed as

$$|\Psi_0^i\rangle \;=\; |\Phi_0^0\rangle|\mathbf{0}\rangle \tag{5.9}$$

where $|\Phi_0^0\rangle$ and $|\mathbf{0}\rangle$ represent the electronic and vibrational components of the initial wavefunction, respectively. Within the harmonic approximation the vibrational component ($|\mathbf{0}\rangle$) is taken as the direct product of the harmonic oscillator functions along the vibrational modes.

In the time-independent framework, $I(E)$ is calculated by a matrix diagonalization method. The Hamiltonian matrix, represented in a direct product basis of diabatic electronic state and one-dimensional harmonic oscillator eigenfunctions of the reference Hamiltonian ($\mathcal{T}_N + \mathcal{V}_0$), is diagonalized by using the Lanczos algorithm [31, 32]. The exact location of the vibronic energy levels and their relative intensities are the eigenvalues and the squared first components of the Lanczos eigenvectors, respectively [23, 33, 34]. The spectral envelope can be obtained within the time-dependent framework by Fourier transform of the time

autocorrelation function of a wave packet (WP) evolving on the final electronic state as

$$P(E) \approx 2Re \int_0^\infty e^{iEt/\hbar} \langle \Psi^\alpha(0) | \boldsymbol{\tau}^\dagger \; e^{-i\mathcal{H}t/\hbar} \; \boldsymbol{\tau} | \Psi^\alpha(0) \rangle dt, \tag{5.10}$$

$$\approx 2Re \int_0^\infty e^{iEt/\hbar} \; C^\alpha(t) \; dt. \tag{5.11}$$

Here, $C^\alpha(t) = \langle \Psi^\alpha(t=0) | \Psi^\alpha(t) \rangle$ represents the time autocorrelation function of the WP initially prepared on the α^{th} electronic state of $C_4H_2^{\cdot +}$. The initial WP at $t = 0$, i.e., $|\Psi_0^i>$, is vertically promoted to the final state α, $|\Psi_0^\alpha>$, and its time-evolution is described by, $\Psi^\alpha(t) = e^{-i\mathcal{H}t/\hbar}\Psi^\alpha(0)$. The quantity $\boldsymbol{\tau}$ represents the transition dipole matrix: $\boldsymbol{\tau}^\dagger = (\tau^X, \tau^A)$, where $\tau^\alpha = \langle \Phi^\alpha | \hat{T} | \Phi^0 \rangle$. Within the generalized Condon approximation in a diabatic electronic basis, the matrix elements of $\hat{T}$ are set to be independent of the nuclear coordinates and are treated as constant [34]. Finally, the composite spectrum is calculated by combining the partial spectra obtained by propagating WP on each of the electronic states. The WP propagation calculations are carried out within the framework of multi-configuration time-dependent Hartree (MCTDH) method [35–37]. The multiset formalism of this method allows to combine several vibrational degrees of freedom (DOF) into a "particle" (p). With such a combination the MCTDH wavefunction can be expressed as

$$\Psi(q_1, ..., q_p, t) \;\; = \;\; \sum_{j_1=1}^{n_1} ... \sum_{j_p=1}^{n_p} A_{j_1,...,j_p}(t) \prod_{k=1}^{p} \varphi_{j_k}^{(k)}(q_k, t). \tag{5.12}$$

Here, $q_k = (Q_i, Q_j, ..)$ is the set of DOF combined together in a single particle

and $A_{j_1,\ldots,j_p}$ denote the MCTDH expansion coefficients. The time-dependent basis functions, $\varphi_{jk}^{(k)}$, are the single-particle functions (SPFs) and n_k is the number of SPFs used to describe the motion of the k^{th} DOF. The MCTDH equations of motion are solved by representing SPFs in a primitive time-independent basis. A harmonic oscillator discrete variable representation (DVR) is used for the primitive basis. All time-dependent WP calculations are carried out using the Heidelberg MCTDH suite of program modules [35–37].

5.4 Results and discussion

5.4.1 Adiabatic potential energy surface : RT and $\widetilde{X}$ - $\widetilde{A}$ conical intersections

In this section we examine the topography of the adiabatic PESs of the degenerate ground and first excited doublet electronic states of $C_4H_2^{\cdot+}$ obtained by diagonalizing the diabatic electronic Hamiltonian (Eq.2). According to the symmetry selection rules given in Sec.5.2, the totally symmetric vibrational modes ν_1-ν_3 of C_4H_2 cannot split the degeneracy of the $\widetilde{X}^2\Pi_g$ and $\widetilde{A}^2\Pi_u$ electronic states. One dimensional view graphs of the multidimensional PESs of $C_4H_2^{\cdot+}$ along a given totally symmetric (σ_g^+) vibrational mode, keeping others at their equilibrium values are shown in Fig. 5.1. The RT effect splits the degeneracy of $\widetilde{X}$ and $\widetilde{A}$ electronic states when the molecule is distorted along π_g (ν_6-ν_7) and π_u (ν_8-ν_9) vibrational modes. The potential energy curves along the x component of π_g and π_u modes and are plotted in Figs. 5.2(a-b) and Figs. 5.2(c-d), respectively. In these plots the adiabatic electronic energies calculated *ab initio* and those obtained from the present vibronic model are shown by points and solid

lines, respectively. It can be seen from Figs. 5.1 and 5.2 that the computed *ab initio* energies compare very well to those obtained from the vibronic coupling model. It can be seen from Fig. 5.2 that the RT splitting of electronic degeneracy is small and the quartic RT coupling terms of the Hamiltonian are very small (Table. 5.2), it makes some minor contribution in the energies in Fig. 5.2(d). The relevant stationary points of the PESs viz., the energetic minimum ($V^{(c)}_{min}$) of the seam of $\widetilde{X}$-$\widetilde{A}$ conical interactions and the energetic minimum (V_{min}) of the electronic states are calculated. The energetic minimum of $\widetilde{X}$ and $\widetilde{A}$ states occurs at $\sim$ 10.23 and $\sim$ 12.85 eV, respectively, and the $\widetilde{X}$-$\widetilde{A}$ seam minimum occurs at a very high energy. Therefore the coupling of the $\widetilde{X}$ and $\widetilde{A}$ states is expected to have negligible role in the nuclear dynamics.

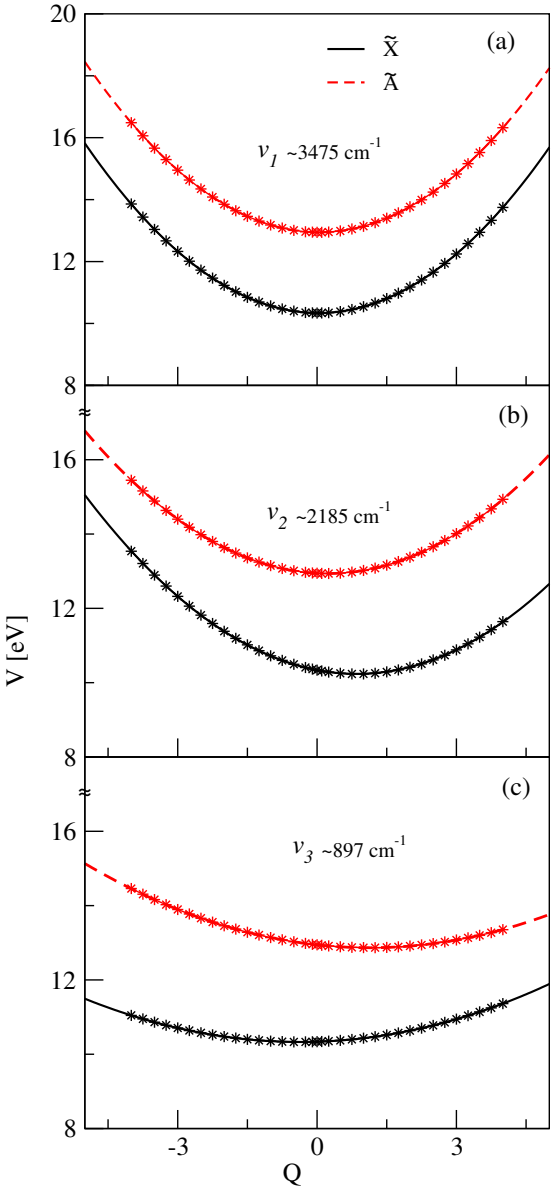

Figure 5.1: Adiabatic potential energies of the $\widetilde{X}$ and $\widetilde{A}$ electronic states of $C_4H_2^+$ along the totally symmetric vibrational modes (ν_1-ν_3). The energies obtained from the present vibronic model and computed *ab initio* energies are shown by lines and points, respectively.

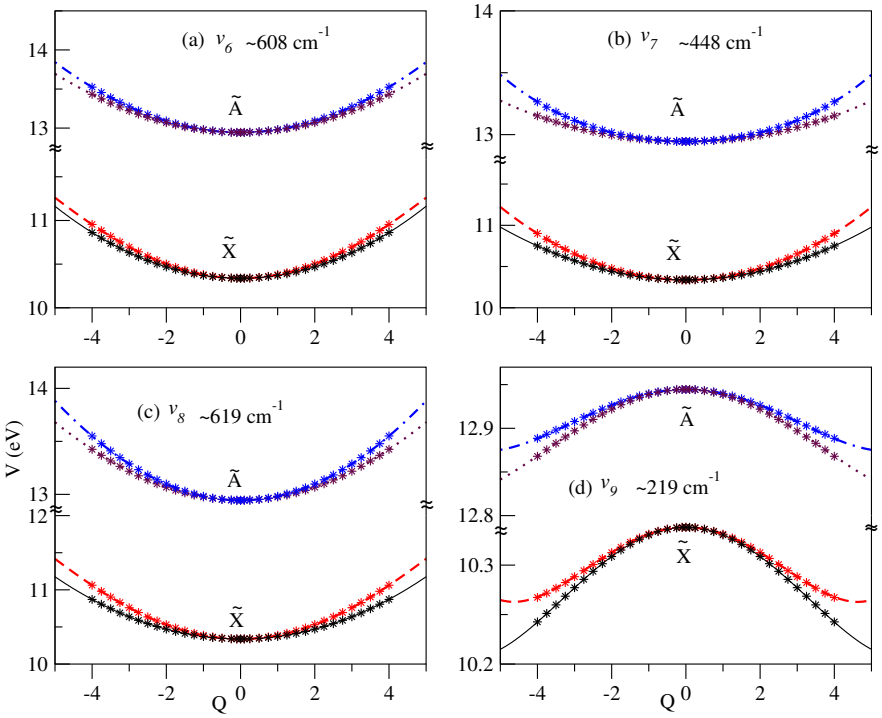

Figure 5.2: Same as in Fig. 5.1, along degenerate π_g (ν_6-ν_7) and π_u (ν_8-ν_9) vibrational modes.

5.4.2 Vibronic band structure of the $\widetilde{X}$ and $\widetilde{A}$ states of $C_4H_2^{\cdot\,+}$

5.4.2.1 Uncoupled state spectrum and Renner-Teller effect

In order to demonstrate the effect of nonadiabatic coupling (both RT and $\widetilde{X}$-$\widetilde{A}$) on the vibronic structure of the photoionization bands of C_4H_2, we first examine the vibrational energy level structure of the uncoupled $\widetilde{X}$, and $\widetilde{A}$ states of $C_4H_2^{\cdot\,+}$. The coupling between the states is included subsequently and the final results are compared with the experiment and discussed. The uncoupled state spectra

Table 5.4: Number of Harmonic oscillator (HO) basis functions for vibrational modes, the dimension of the secular matrix and the number of Lanczos iterations used to calculate the converged theoretical stick spectra of $\widetilde{X}$ and $\widetilde{A}$ states of $C_4H_2^{\cdot+}$shown in various figures.

Vibrational modes(HO basis functions)	Dimension of the matrix	Lanczos iterations	Figure(s)
ν_1, ν_2, ν_3 (4,8,10)	320	10000	panel a of 5.3
ν_{6x}, ν_{6y}, ν_{7x}, ν_{7y}, ν_{8x}, ν_{8y}, ν_{9x}, ν_{9y} (4,4,6,6,6,6,4,4)	331776	10000	panel b of 5.3
ν_1, ν_2, ν_3, ν_{6x}, ν_{6y},ν_{7x}, ν_{7y}, ν_{8x}, ν_{8y}, ν_{9x}, ν_{9y} (3,6,8,4,4,4,4,4,4,4,4)	9437184	10000	panel c of 5.3

shown in Fig. 5.3 are calculated by the time-independent matrix diagonalization approach as discussed in Sec. 5.3. The vibrational basis used in each calculation is given in Table 5.4. The theoretical stick line spectrum of each electronic state (shown in panel a of Fig. 5.3) is calculated with the vibronic Hamiltonian of Eq. 1 and including all three totally symmetric vibrational modes ν_1-ν_3. A Lorentzian line shape function of 20 meV full width at the half maximum (FWHM) is used to convolute the stick line spectrum in each case and to generate the respective spectral envelope. In a situation without $\widetilde{X}$-$\widetilde{A}$ coupling and in absence of any intermode coupling terms, the Hamiltonian for the degenerate $\widetilde{X}^2\Pi_g$ and $\widetilde{A}^2\Pi_u$ states are separable in terms of the σ_g^+, π_g and π_u modes. Therefore, the partial spectra calculated with the totally symmetric and degenerate vibrational modes separately, can be convoluted to get the composite vibronic structure of the electronic states. The spectrum of the $\widetilde{X}$ and $\widetilde{A}$ states obtained by including the σ_g^+ (ν_1-ν_3) modes only is shown in Fig. 5.3(a). In the $\widetilde{X}$ state, excitation of ν_1, ν_2 and ν_3 modes is weak, strong and moderate, respectively. The fundamentals of ν_1, ν_2, and ν_3 vibrations are $\sim$ 3484, $\sim$ 2227 and $\sim$ 885 cm^{-1} spaced, respectively, from the origin peak of the $\widetilde{X}$ band. The $\widetilde{X}^2\Pi_g$ state of $C_4H_2^{\cdot+}$ originates from ionization of an electron from an antibonding (along ν_2) molecular orbital of C_4H_2. The vibrational frequency of ν_2 therefore increases in the $\widetilde{X}$ state of

$C_4H_2^+$ as compared to the same in the ground state of C_4H_2. Since the coupling strength of the ν_2 mode is particularly strong [Table. 5.2], this mode forms an extended progression in the $\widetilde{X}$ state spectrum, the same trend can be observed for the ν_3 mode in the $\widetilde{A}$ state. Peak spacing of ~ 3481, ~ 2225 and ~ 932 cm^{-1} due to the fundamental of ν_1, ν_2 and ν_3 vibrational modes, respectively, is found in the $\widetilde{A}$ state spectrum. In this state the coupling strength [*cf.*, Table. 5.2] of ν_1, ν_2 and ν_3 vibrational modes is weak, moderate and strong, respectively, in that order.

The partial spectra calculated with the degenerate RT modes (π_g and π_u) are shown in panel b of Fig. 5.3. The composite spectrum obtained by convoluting the symmetric and degenerate mode spectra of $\widetilde{X}$ and $\widetilde{A}$ states presented in panel a and panel b of Fig. 5.3 is shown in panel c of this figure. The spectra presented in panel b of Fig. 5.3 reflects a weak contribution of RT coupling in the vibronic structure of $\widetilde{X}$ and $\widetilde{A}$ states. As a result, the overall spectral envelop (panel c of Fig. 5.3) appears to be very similar and close to that shown in panel a of Fig. 5.3. The weak RT coupling within each of these states however, has some effects on the spectral broadening and possibly excitation of additional vibrational modes as the line structure within each spectral peak in panel c suggests. To this end some of the spectral progressions reported in experiments are compared with our theoretical findings. Excitation of the ν_2 vibrational mode in the $\widetilde{X}$ band is reported by Baker *et al.* [12]. From Table 5.2 it can be seen that this mode has the strongest excitation strength compared to all other symmetric modes in the $\widetilde{X}$ state. Our theoretical analysis reveals that the fundamental of ν_2 appears at ~ 2227 cm^{-1} as compared to its value ~ 2121 cm^{-1} reported in the experiment of Baker *et al.* [12]. Bondybey *et al.* also identified the fundamental of ν_1, ν_2, ν_3 modes and the overtone of ν_7 vibrational mode at ~ 3143, ~ 2177, $\sim$

865 and $\sim$ 973 cm^{-1}, respectively. These results are in good accord with the progressions found in the present study at $\sim$ 3484, $\sim$ 2227, $\sim$ 885 and $\sim$ 842 cm^{-1}, respectively, in that order. In order to confirm the assignments, vibronic wavefunctions are calculated by the block-improved-relaxation method using the MCTDH program modules [44, 61, 62]. The wavefunctions corresponding to $\sim$ 3484, $\sim$ 2227, $\sim$ 885 and $\sim$ 842, $\sim$ 1295, $\sim$ 1442 and $\sim$ 3112 cm^{-1} lines are plotted in a given coordinate space and presented in Fig. 5.4(a-g), respectively. It can be seen from these plots that the panels a, b and c reveal one mode along ν_1, ν_2 and ν_3 respectively and confirms the fundamentals along these modes. The plot in panel d, e and f confirms the two quantum excitation along ν_7, ν_6 and ν_8, respectively. The wavefunctions of panel g, on the otherhand, reveals one quantum excitation each along ν_2 and ν_3 and hence represents a combination peak.

In the $\widetilde{A}$ state major progressions are formed by ν_1, ν_2, ν_3 and the overtone of ν_7, ν_6 and ν_8 vibrational modes. Many groups identified progressions in the $\widetilde{A}$ state and assigned to the corresponding vibrational modes. A comparative account of all these results along with the present findings is given in Table 5.5.

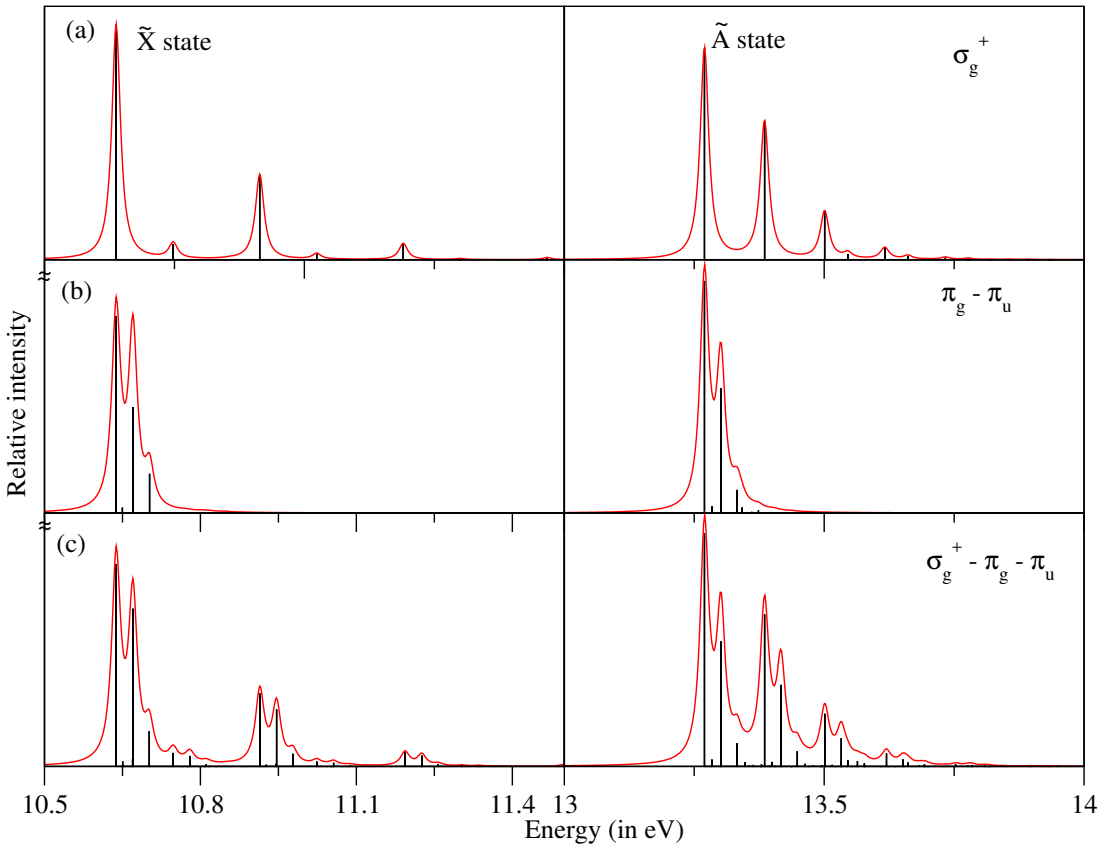

Figure 5.3: Vibrational energy level spectrum of the uncoupled $\widetilde{X}$ and $\widetilde{A}$ electronic states of $C_4H_2^{\cdot\,+}$ computed with (a) totally symmetric vibrational modes (σ_g^+) and (b) degenerate vibrational modes (π_g and π_u). The convoluted spectra of symmetric and degenerate vibrational modes are shown in panel c.

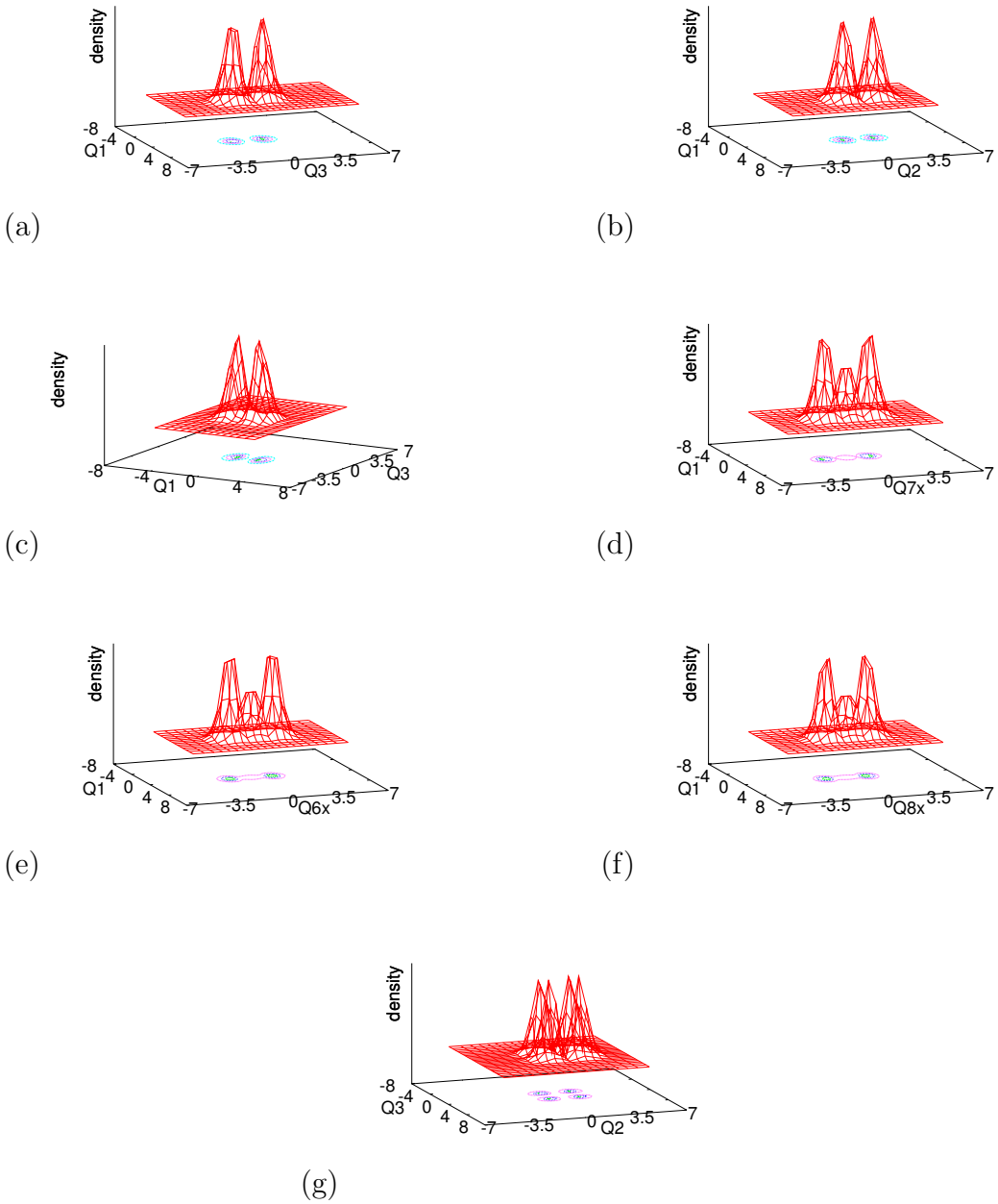

Figure 5.4: Reduced density plots of the vibronic wavefunctions of the fundamental of ν_1, ν_2 and ν_3 (panel a, b and c, respectively) and first overtone of ν_7, ν_6 and ν_8 (panel d, e and f, respectively) excited in the $\widetilde{X}$ state spectrum of $C_4H_2^{\cdot+}$. The wavefunction in panel g represent the combination peak $\nu_2 + \nu_3$.

5.4.2.2 $\widetilde{X}$ - $\widetilde{A}$ Coupled state spectrum and time-dependent dynamics

The symmetry rule (stated in Sec.5.2) allows the coupling of $\widetilde{X}$ and $\widetilde{A}$ states in first-order through the vibrational modes of σ_u^+ symmetry. It can be seen from Table. 5.2 that the vibrational modes ν_4 and ν_5 have nonzero first order coupling. It is mentioned in sec. 5.4.1 that energetic minimum of the seam of conical interactions of $\widetilde{X}$ and $\widetilde{A}$ states occurs at much higher energy and $\widetilde{X}$-$\widetilde{A}$ coupling is, therefore, not expected to affect the nuclear dynamics on these states. In order to confirm, we carried out $\widetilde{X}$-$\widetilde{A}$ coupled states nuclear dynamics calculations. In the coupled states situation the separability of the Hamiltonian (as discussed in the previous section) in terms of symmetric and degenerate vibrational modes is no longer valid. We, therefore, carried out full dimensional calculations with two degenerate coupled electronic states including all thirteen vibrational degrees of freedom. The dynamics calculations are carried out by propagating WPs employing the MCTDH program modules. [60] Four different calculations are carried out by initially preparing the WP on each components of the Π states separately. The vibrational basis functions used in the calculations are given in Table 5.6. The WP is propagated for 200 fs in the coupled manifold of electronic states and the time autocorrelation function, diabatic and adiabatic electronic populations are recorded during the propagation. The time autocorrelation functions obtained from four different calculations are combined, damped with an exponential function, $e^{(-t/\tau_r)}$ (with $\tau_r = 66$ fs) and Fourier transformed to generate the spectral envelopes of the electronic states. The numerical details of converged MCTDH calculations are given in Table 5.4.

The resulting theoretical spectral envelopes are shown in panel a of Fig. 5.5 along with the experimental results of Ref. [16] in panel b. It can be seen that the theoretical results compare very well with the experiment. When compared

with the theoretical results presented in Fig. 5.3(c), it can be seen that the $\widetilde{X}$-$\widetilde{A}$ intersection has negligible effects on the vibronic band structure of both the states. On the other hand, the RT effect is weak but it causes spectral broadening by increasing the vibronic line density as can be seen from Fig. 5.3(c). The origin line of the $\widetilde{A}^2\Pi_u$ band occurs close to the reported DIB at 506.9 nm. From the results presented in Fig. 5.5, the position of the origin line of the $\widetilde{A}$ state relative to the origin line of the $\widetilde{X}$ state is estimated at 471 nm. A more meaningful comparison requires a study of the absorption spectrum of $C_4H_2^{\cdot\,+}$.

The time-dependence of electronic population in the $\widetilde{X}$-$\widetilde{A}$ coupled states dynamics is shown in Fig. 5.6. The diabatic (panel a) and adiabatic (panel b) electron populations are shown in this figure for an initial excitation of the WP to one component of the diabatic $\widetilde{A}$ state. While the diabatic population of the initially prepared state starts from 1.0, its adiabatic counterpart has a population of $\sim$0.5 at $t = 0$. It can be seen from both the panels of Fig.5.6 that the WP does not move to the $\widetilde{X}$ state during the entire course of the dynamics. The RT coupling drives the WP motion back and forth between the RT split component states only. The population dynamics retains all the features noted above when the WP initially prepared on one component of the $\widetilde{X}$ state. In this case the WP does not move to the $\widetilde{A}$ state. It therefore emerges that the $\widetilde{X}$ - $\widetilde{A}$ coupling has insignificant role on the dynamics of both the states. The RT coupling is weak, however, has noticeable effect on the vibronic dynamics of both $\widetilde{X}$ and $\widetilde{A}$ state of diacetylene radical cation.

Table 5.5: A comparative account on the vibrational progressions in the $\widetilde{A}^2\Pi_u$ electronic state of diacetylene radical cation. The numbers represent the frequency of the vibrational mode in cm^{-1}.

Mode	Present results	Ref. [2]	Ref. [21]	Ref [19]	Ref. [18]
ν_1	3481	3137	3158	-	2821
ν_2	2225	2177	2096	1961	2002
ν_3	932	861	987	806	807
$2\nu_6$	1154	-	-	-	-
$2\nu_7$	757	971	-	862	861
$2\nu_8$	1172	-	-	-	-

Table 5.6: Normal mode combinations, sizes of the primitive and the single particle basis used in the wave packet propagation within the MCTDH framework in the four coupled ($\widetilde{X}-\widetilde{A}$) electronic manifold using the complete vibronic Hamiltonian of Eq.(2 to 7). First column denotes the vibrational degrees of freedom (DOF) which are combined to particles. Second column gives the number of primitive basis functions for each DOF. Third column gives the number of single particle functions (SPFs) for each electronic state.

Normal modes	Primitive Basis	SPF Basis
ν_1, ν_4, ν_{6y}, ν_{8x}, ν_{9y}	(4,4,6,6)	[12,12,8,12]
ν_2, ν_5, ν_{7x}, ν_{8y}	(8,8,6,6)	[12,10,8,10]
ν_3, ν_{6x}, ν_{7y}, ν_{9x}	(10,6,6,6)	[8,12,10,10]

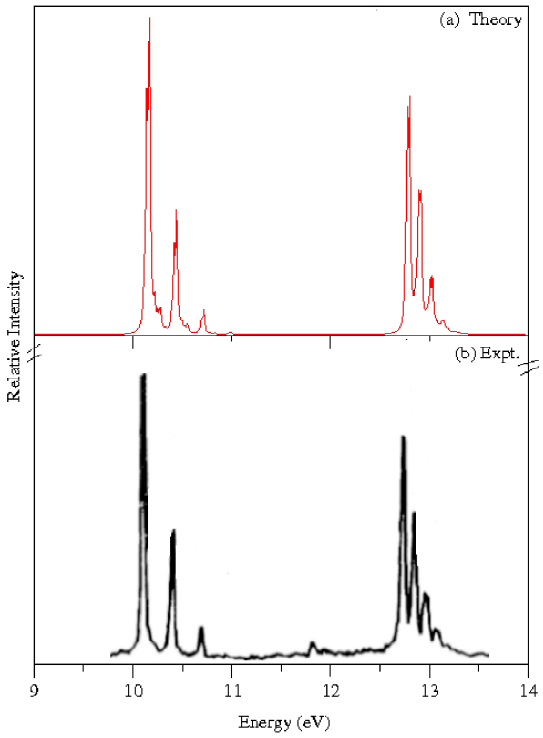

Figure 5.5: Vibronic band structure of the $\widetilde{X}$-$\widetilde{A}$ coupled electronic states of $C_4H_2^{\cdot\,+}$. Relative intensity (in arbitrary units) is plotted as a function of the energy of the vibronic states of $C_4H_2^{\cdot\,+}$. The present theoretical results are shown in panel a and the experimental results of Ref. [12] are reproduced in panel b.

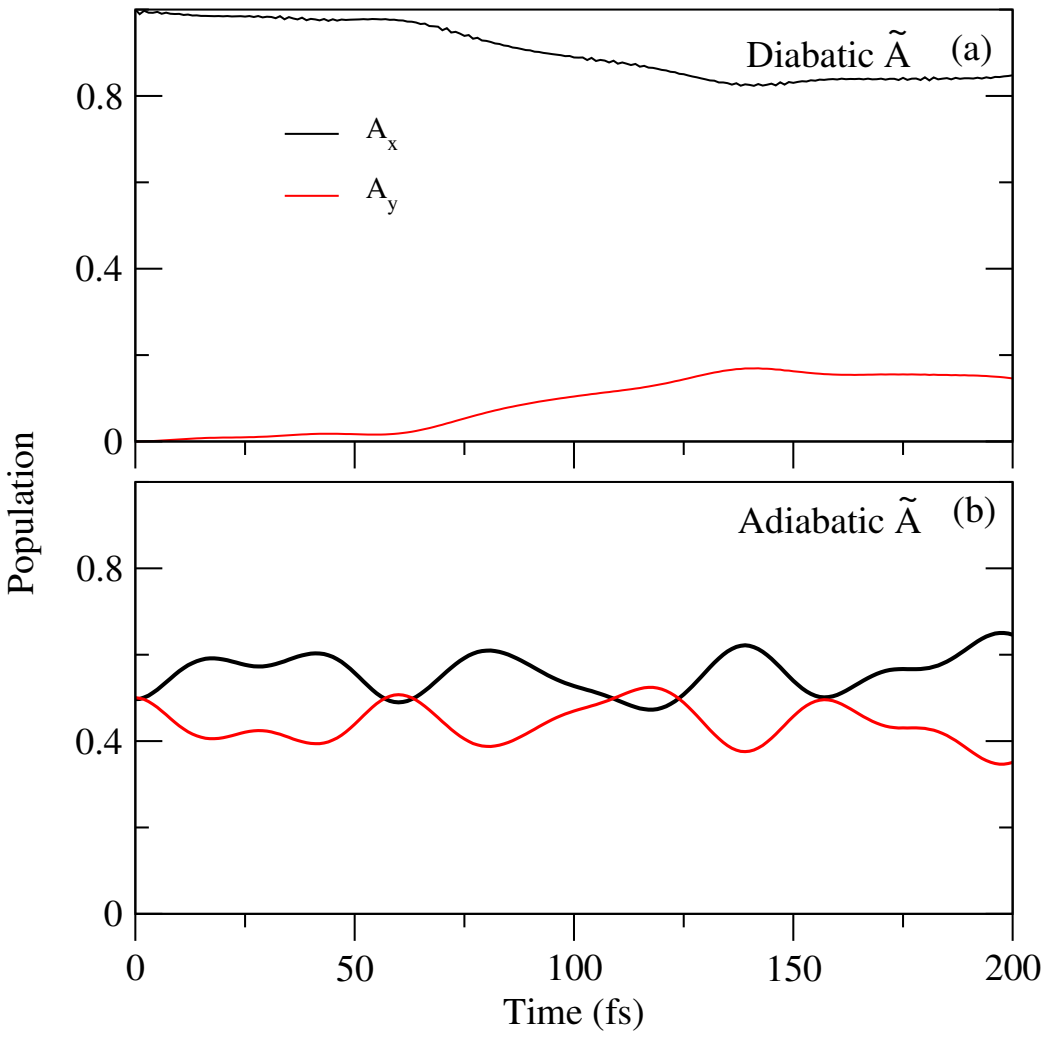

Figure 5.6: Time dependence of diabatic (panel a) and adiabatic (panel b) electron populations in the $\widetilde{X}$-$\widetilde{A}$ coupled states nuclear dynamics of $C_4H_2^{\cdot+}$. The initial (at t=0) WP is located on one of the components of the diabatic $\widetilde{A}$ state.

5.5 Summary

The $\widetilde{X}^2\Pi_g$ and $\widetilde{A}^2\Pi_u$ band system of diacetylene radical cation is theoretically investigated with the aid of *ab initio* quantum chemistry calculations, vibronic coupling theory and time-independent and time-dependent quantum dynamics methods. Both the RT coupling within the $\widetilde{X}$ and $\widetilde{A}$ states and also the coupling between them are considered and the impact of these couplings on the vibronic dynamics of each electronic state is carefully examined. The vibronic band structure of both the $\widetilde{X}$ and $\widetilde{A}$ states are calculated and compared with the available experimental results. The progression of vibrational modes in each electronic states is identified and discussed in relation to the literature results.It is established that the RT coupling within each $\widetilde{X}$ and $\widetilde{A}$ state is weak. However, this coupling triggers the excitation of degenerate vibrational modes within each electronic states. The pseudo-Jahn-Teller type of $\widetilde{X}$ - $\widetilde{A}$ coupling through the vibrational modes of σ_u^+ symmetry has, in particular, no effect on the dynamics.

References

[1] H. Schüler and L. Reinebeck, Über Neue Spektren in der Glimmentladung Mit Naphthalindampf. *Z. Naturforsch.* **1951**, *6a*, 271-275 ; Über ein Spektrum im Sichtbaren beobachtet bei Acetylen, thylen und aromatischen Moleklen **1952**, *7a*, 285-259.

[2] Callomon, J. H. An Emission Spectrum of the Diacetylene Ion, A Study

of Schüler "T" Spectrum Under High Resolution *Can. J. Phys.* **1956**, *34*, 1046-1074.

[3] Motylewski, T.; Linnartz, H.; Vaizert, O.; Maier, J. P.; Galazutdinov, G. A.; Musaev, F. A.; Krelowski, J.; Walker, G. A. H.; Bohlender, D. A. Gas-Phase Electronic Spectra of Carbon-Chain Radicals Compared With Diffuse Interstellar Band Observations. *Astrophys. J.* **2000**, *531*, 312-320.

[4] Krelowski, J.; Beletsky, Y.; Galazutdinov, G. A.; Kolos, R.; Gronowski, M.; Locurto, G. Evidence for Diacetylene Cation as the Carrier of a Diffuse Interstellar Band. *Astrophys. J.* **2010**, *714*, L64-L67.

[5] Maier, J. P.; Chakrabarty, S.; Mazzotti, F. J.; Rice, C. A.; Dietsche, R.; Walker, G. A. H.;Bohlender, D. A.; Assignment of 5069 A^0 Diffuse Interstellar Band to HC4H+: Disagreement With Laboratory Absorption Band *Astrophys. J.* **2011**, *729*, L20(4pp).

[6] Maier, J. P.; Walker, G. A. H.; Bohlender, D. A.; On The Possible Role of Carbon Chains as Carriers of Diffuse Interstellar Bands *Astrophys. J.* **2004** *602*, 286-290.

[7] Douglas, A. E. Origin of Diffuse Interstellar Lines. *Nature* **1977**, *269*, 130-132.

[8] Henning, T.; Salama, F. Carbon in the Universe. *Science* **1998**, *282*, 2204-2210.

[9] Heger, M. L. The Spectra of Certain Class B Stars in the Regions 5360A6680A and 3280A3380A. *Lick. Obs. Bull.* **1921** *10*, 146-147.

[10] Hobbs, L. M.; York, D. G.; Snow, T. P.; Oka, T.; Thorburn, J. A.; Bishof, M.; Friedman, S. D.; McCall, B. J.; B. Rachford, B.; Sonnentrucker, P.; Welty D. E. A Catalog of Diffuse Interstellar Bands in the Spectrum of HD 204827 *Astrophys. J.* **2008** *680*, 1256-1270.

[11] Hobbs, L. M.; York, D. G.; Thorburn, J. A.; Snow, T. P.; Bishof, M.; S.D. Friedman, S. D.; McCall, B. J.; Oka, T.; Rachford, B.; Sonnentrucker, P.; Welty, D. E.; Studies of the Diffuse Interstellar Bands. III. HD 183143 *Astrophys. J.* **2009** *705*, 32-45.

[12] Baker, C.; Turner, D. W. Photoelectron Spectra of Acetylene, Diacetylene, and their Deutero-derivatives *Chemical Communications* **1967**, 797-799.

[13] Kaiser, R. I.; Sun, B. J.; Lin, H. M.; Chang, A. H. H.; Mebel, A. M.; Kostko, O. An experimental and Theoretical Study on the ionization Energies of Polyyenes (H(CC)nH; n = 19). *Astrophys. J.* **2010**, *719*, 1884-1889.

[14] Gronowski, M.; Kolos, R.; Krelowski, J. A Theoretical Study on Structure And Spectroscopy of $C_4H_2^+$ isomers. *Chem. Phys. Lett.* **2013**, *582*, 56-59.

[15] Fulara, J.; Grütter, M.; Maier, J. P. Higher Excited Electronic Transitions of Polyacetylene Cations $HC_{2n}H^+$ n = 2-7 in Neon Matrixes. *J. Phys. Chem. A* **2007** *111*, 11831-11836.

[16] Allan, M.; Kloster-Jensen, E.; Maier, J. P. Emission Spectra of the Radical Cation of Diacetylene ($\widetilde{A}^2\Pi_u \rightarrow \widetilde{X}^2\Pi_g$), Triacetylene ($\widetilde{A}^2\Pi_g \rightarrow \widetilde{X}^2\Pi_u$), and Tetraacetylene ($\widetilde{A}^2\Pi_u \rightarrow \widetilde{X}^2\Pi_g$, 0_0^0, and the Lifetimes of Some Vibronic Level of the $\widetilde{A}$ States. *Chem. Phys.* **1976**, *7*, 11-18.

[17] Bally, T.; Tang, W.; Jungen, M. The Electronic Structure of the Radical Cations of Butadiene, Vinylacetylene and Diacetylene: Similarities and DifferencesChem. *Phys. Lett.* **1992**, *190*, 453-459.

[18] Bondybey, V. L.; English, J. H. Electronic Spectrum of the Diacetylene Radical Cation in Solid Rare Gases. *J. Chem. Phys.* **1979**, *71*, 777-782.

[19] Schmidt, T. W.; Pino, T.; van Wijngaarden, J.; Tikhomirow, K.; Guthe, F.; J. P Maier, J. P. Electronic Photodissociation Spectra of the $Ar_nC_4H_2^+$ (n= 1 4) Weakly Bound Cationic Complexes. *J. Mol. Spectrosc.* **2003**, *222*, 86-92.

[20] Freivogel, P.; Fulara, J.; Lessen, D.; Forney, D.; Maier, J. P. Absorption Spectra of Conjugated Hydrocarbon Cation Chains in Neon Matrices. *Chem. Phys.* **1994**, *189*, 335-341.

[21] Smith, W. L. The Absorption Spectrum of Diacetylene in The Vacuum Ultraviolet. *Proc. R. Soc. A.* **1967**, *300*, 519-533.

[22] Baker, C.; Turner, D. W. High Resolution Molecular Photoelectron Spectroscopy. III. Acetylenes and Aza-acetylenest. *Proc. R. Soc. A.* **1968**, *308*, 19-37.

[23] Köppel. H.; Domcke. W.; Cederbaum. L. S. Multimode Molecular Dynamics Beyond the Born-Oppenheimer Approximation. *Adv. Chem. Phys.* **1984**, *57* , 59-246.

[24] E.B. Wilson Jr., E. B.; Decius, J. C.; Cross, P. C. *Molecular vibrations* (McGraw-Hill, New York, **1955**).

[25] Döscher, M.; Köppel, H.; Szalay, P. Multistate Vibronic Interactions in the Benzene Radical Cation. I. Electronic Structure Calculations. *J. Chem. Phys.* **2002** *117*, 2645-2656.

[26] Venkatesan, T. S.; Meyer, H. -D.; Köppel, H.; Cederbaum, L. S.; Mahapatra, S. Multimode JahnTeller and Pseudo-JahnTeller Interactions in the Cyclopropane Radical Cation: Complex Vibronic Spectra and Nonradiative Decay Dynamics. *J. Phys. Chem. A* **2007**, *111*, 1746-1761.

[27] Mondal, T.; Reddy, S. R.; Mahapatra, S. Photophysics of Fluorinated benzene. III. Hexafluorobenzene *J. Chem. Phys.* **2012**, *137*, 054311-054317.

[28] Dunning. T. H. Jr. Gaussian Basis Sets for Use in Correlated Molecular Calculations. I. The Atoms Boron Through Neon and Hydrogen. *J. Chem. Phys.* **1989**, *90*, 1007-1023.

[29] Frisch, M. J.; Trucks, G. W.; Schlegel H. B. *et al.* , GAUSSIAN 03, Revision B. 05, Gaussian, Inc., Pittsburgh PA, **2003**.

[30] CFOUR, a quantum chemical program package written by Stanton, JF.; Gauss, J.; Harding, M. E.; Szalay, P. G.; with contributions from Auer, A. A.; Bartlett, R. J.; Benedikt, U.; Berger, C.; Bernholdt, D. E.; Bomble, Y. J.; Cheng, L.; Christiansen, O.; Heckert, M.; Heun, O.; Huber, C.; Jagau,T-C.; Jonsson, D.; Jusélius, J.; Klein, K.; Lauderdale, W. J.; Matthews, D. A.; Metzroth, T.; Mck, L. A.; Ó Neill, D. P.; Price, D. R.; Prochnow, E.; Puzzarini, C.; Ruud, K.; Schiffmann, F.; Schwalbach, W.; Simmons, C.; Stopkowicz, S.; Tajti, A.; Vzquez, J.; Wang, F.; Watts, J. D. and the integral packages MOLECULE (Almlf, J.; Taylor, P. R.), PROPS (Taylor, P. R), ABACUS (Helgaker, T.; Aa. Jensen, H. J.; Jør-gensen, P.; Olsen, J.), and

ECP routines by Mitin, A. V.; van Wllen, C. For the current version, see http://www.cfour.de

[31] Lanczos. C. An Iteration Method for the Solution of the Eigenvalue Problem of Linear Differential and Integral Operators. *J. Res. Nat. Bur. Stand.* **1950**, *45*, 255-282.

[32] Cullum. J.; Willoughby. R. Lanczos Algorithms for Large Symmetric Eigenvalue Problems (Birkhäuser, Boston, **1985**), Vols. I and II.

[33] Domcke. W.; Köppel. H. *Encyclopedia of Computational Chemistry-Theoretical and Physical chemistry*, edited by H.F.Schacfer. III. (*Wiley.* New York, **1998**).

[34] Domcke. W.; Köppel. H.; Cederbaum. L. S. Spectroscopic Effects of Conical Intersections of Molecular Potential Energy Surfaces. *Mol. Phys.* **1981**, *43*, 851-875.

[35] Meyer. H. -D.; Manthe. U.; Cederbaum. L. S. The Multi-Configurational Time-dependent Hartree Approach. *Chem. Phys. Lett.* **1990**, *165*, 73-78.

[36] Manthe. U.;, Meyer. H. -D.; Cederbaum. L. S. Wave-packet Dynamics Within the Multiconfiguration Hartree Framework: General Aspects and Application to NOCl. *J. Chem. Phys.* **1992**, *97*, 3199-3213.

[37] Beck. M. H.; Jäckle. A.; Worth. G. A.; Meyer. H. -D. The Multiconfiguration Time-dependent Hartree (MCTDH) Method: a Highly Efficient Algorithm for Propagating Wavepackets. *Phys. Rep.* **2000**, *324*, 1-105.

[38] Worth. G. A.; Beck. M. H.; Jäckle. A.; Meyer. H. -D. The mctdh package, Version 8.4, (2007), University of Heidelberg, Heidelberg, Geramny. See: http://mctdh.uni-hd.de.

[39] S. Thorwirth, S.; Harding, M. E.; Muders, D.; Gauss, J. The Empirical Equilibrium Structure of Diacetylene. *J. Mol. Spectrosc.* **2008**, *251*, 220-223.

[40] Williams, G. A.; Macdonald, J. N. An ab initio and Experimental Study of the Harmonic Force Field of Diacetylene. *J. Mol. Struct.* **1994** *320*, 217-225.

[41] G. Guelachvili, A.M. Craig, and D.A. Ramsay, High-Resolution Fourier Studies of Diacetylene in the Regions of the ν_4 and ν_5 Fundamentals. *J. Mol. Spectrosc.* **1984**, *105*, 156-192.

[42] Meng. Q.; Meyer. H. -D. MCTDH Study on Vibrational States of the CO/Cu(100) System. *J. Chem. Phys.* **2013**, *139*, 164709-14.

[43] Peláez. D.; Sadri. K.; Meyer. H. -D. Full-dimensional MCTDH/MGPF Study of the Ground and Lowest Lying Vibrational States of the Bihydroxide $H_3O_2^-$ Complex. *Spectrochimica Acta Part A: Molecular and Biomolecular Spectroscopy.* **2014**, *119*, 42-51.

[44] Sarkar, R.; Mahapatra, S. Vibronic Dynamics of Electronic Ground State of $CH_2F_2^+$ and Its Deuterated Isotopomer*J. Phys. Chem. A.* **2016**, *120*, 3504 (2016).

Chapter 6

Photophysics of phenol and pentafluorophenol

Multimode vibronic coupling of the energetically low-lying electronic states of phenol and pentafluorophenol is investigated in this chapter. First principles nuclear dynamics calculations are carried out to elucidate the optical absorption spectrum of both the molecules. This is motivated by the recent experimental measurements [Karmakar et. al, J. Chem. Phys. 142, 184303 (2015)] on these systems. Diabatic vibronic coupling models are developed with the aid of adiabatic electronic energies calculated ab initio *by the equation of motion coupled cluster quantum chemistry method. Nuclear dynamics study on the constructed electronic states is carried out both by the time-independent and time-dependent quantum mechanical methods. It is found that the nature of low-energy $\pi\sigma^*$ transition changes, and in pentafluorophenol the energy of the first two $^1\pi\sigma^*$ states is lowered by about half an eV (vertically, relative to those in phenol) and they become energetically close to the optically bright first excited $^1\pi\pi^*$ (S_1) state. This results into strong vibronic coupling and multiple multi-state conical intersections among*

the $\pi\pi^*$ and $\pi\sigma^*$ electronic states of pentafluorophenol. The impact of associated nonadiabatic effects on the vibronic structure and dynamics of the $^1\pi\pi^*$ state is examined at length. The structured vibronic band of phenol becomes structureless in pentafluorophenol. The theoretical results are found to be in good accord with the experimental finding both at high and low energy resolution.

6.1 Introduction

Vibronic coupling (VC) is an ubiquitous mechanism that plays crucial role in the dynamics of electronically excited polyatomic molecules [1, 2]. The mixing of nuclear and electronic degrees of freedom causes a breakdown of the Born-Oppenheimer approximation [3]. As a result the nuclei moves concurrently on multiple electronic states and generally lead to conical intersections (CIs) among them [1, 2, 4–8]. Such intersections drive the nuclear motion on an ultrafast time scale and give rise to nonradiative decay of electronic states and complex molecular electronic spectrum. In recent years the $\pi\sigma^*$ photophysics/chemistry of fluorinated aromatic organic hydrocarbons and heterocyclic compounds received much attention in the literature from both theoretical and experimental view points [9–18].

For aromatic chromophores, important excited states are mainly of optically bright $\pi\pi^*$ type. Existence of low-lying $\pi\sigma^*$ and $n\pi^*$ type of excited states in addition, bring about new features in the spectroscopy and dynamics and has attracted significant attention in the recent past [19–29]. From a number of studies it emerged that aromatic molecules can have different kind of low-lying $\pi\sigma^*$ states if the hydrogen atoms linked to the carbon atoms of the aromatic ring are

replaced by the fluorine atoms. Such fluorine atom substitutions in the aromatic ring lead to a stabilization of the σ type of orbitals and it is referred to as "perfluoro effect" in the literature [18]. Furthermore, owing to an energy lowering it is possible for the optically dark $\pi\sigma^*$ state to gain intensity through vibronic mixing with an optically bright $\pi\pi^*$ state. This happens to be the case in the present study, wherein we find strong vibronic coupling with an optically bright state enables one to probe the optically dark states in the experimental recording [30].

It was observed that the structured absorption spectrum of benzene becomes structureless with increasing fluorine substitution [16–18]. In the recent past this subject is extensively studied by developing sophisticated theoretical models [1, 11–13]. It emerged from these studies that $\pi\sigma^*$ [C-F (σ^*)] state comes down in energy and mixes with first excited $\pi\pi^*$ state and the extent of mixing increases with increasing number of substituted F atom. Such theoretical models could account for the lack of vibronic structure of the absorption bands, large Stoke's shift of fluorescence spectra, low quantum yield of fluorescence and also short lifetimes of excited electronic states [18, 29, 31–33].

Phenol is the chromophoric unit of several biomolecules, amino acids like tyrosine and nucleic acid bases. Photophysical measurements on phenol have been carried out by several groups in the gas phase as well as in different medium [34–38]. Fast internal conversion of UV excited phenol to the electronic ground state has been connected to the photostability of our ecosystem [22, 23, 28, 35, 39–42]. The investigations were mostly focused on the relaxation dynamics and the photoacid character of phenol upon the UV excitation to the low-lying electronic states [22, 39, 43]. The interaction between the low-lying optically bright $^1\pi\pi^*$

and nearby dark $^1\pi\sigma^*$ (which is dissociative along the O-H stretching coordinate) electronic states, was the subject of major interest [21,43–49]. Such $\pi\sigma^*$ states are found to play key role in the relaxation dynamics and also in other photophysical properties (as discussed below in the text). The ionic dissociation of phenolic O-H in aqueous solution upon UV absorption has been reported to enhance by four orders of magnitude in pentafluorophenol (PFP) [50].

Recently, Chakraborty and coworkers reported that discrete vibronic structure of phenol completely washes out in the optical absorption spectrum of PFP [30] which indicated the possibility of existence of close lying interacting electronic states in the vicinity of lowest bright $^1\pi\pi^*$ excited electronic state. These authors also carried out calculation of vertical excitation energies (VEEs) by time-dependent density functional theory (TDDFT)/6-311++G** method using the CAM-B3LYP functional [30] and reported four low-lying electronic excited states of PFP viz., $\pi\sigma^*$ (S_1), $\pi\pi^*$ (S_2), $\pi\sigma^*$ (S_3) and $\pi\sigma^*$(S_4) in the increasing order of energy. The recorded optical absorption spectra by these authors revealed three major discrete peaks at $\sim$ 275 nm, $\sim$ 268 nm and $\sim$ 262 nm for phenol and four hump like structures at $\sim$ 260 nm, $\sim$ 242 nm, $\sim$ 232 nm and $\sim$ 223 nm for PFP [30]. The loss of vibronic structure was attributed to the existence of energetically close lying $\pi\sigma^*$ states in the vicinity of UV absorbing optically bright $\pi\pi^*$ state in PFP. Furthermore, while the resolved absorption band of phenol was assigned to the vibronic structure of S_1 ($^1\pi\pi^*$) state only, the maxima observed in the structureless absorption band of PFP were reported to originate from two energetically close lying optically dark $^1\pi\sigma^*$ states in addition to the bright $^1\pi\pi^*$ state. It therefore appears that optically dark states could be probed in the experiment for PFP, whereas, they could not be in case of phenol.

The interpretation of aforesaid results remain qualitative only in absence of a rigorous theoretical scrutiny which considers the coupling of electronic states within the framework of vibronic coupling theory [1]. Furthermore, the TDDFT vertical excitation energy has been found to provide an incorrect energetic ordering of states in related compounds [30] and therefore it calls for a careful theoretical examination in order to arrive at a justifiable interpretation of experimental results.

The mentioned facts motivated us to undertake the following detail study of electronic structure and nuclear dynamics to elucidate the vibronic structure of the absorption bands of phenol and PFP. Extensive *ab initio* quantum chemistry calculations of electronic energy are carried out and vibronic coupling models of low-lying excited electronic states are established. The nuclear dynamics study on the coupled electronic states is carried out by quantum mechanical methods to calculate the absorption spectra and to study the time-dependent dynamics of excited electronic states. Finally, the theoretical results are assigned and compared with the available literature results [30].

We mention that the $^1\pi\pi^*$ state of phenol is bound in nature and the $^1\pi\sigma^*$ (arising from an excitation to a 3s type of Rydberg orbital of antibonding σ^* character with respect to phenolic O-H bond) is of repulsive type [22]. The latter crosses both the excited $^1\pi\pi^*$ state and S_0 ground state. A viewgraph presented in Fig. 2 of Ref [22] is worth referring at this point. It can be seen that the $^1\pi\pi^*$-$^1\pi\sigma^*$ intersection occurs quite near to the FC region whereas, the crossing with the S_0 state occurs at much larger displacement along the O-H stretch

coordinate. It can also be seen that the $^1\pi\sigma^*$ state is quasibound in nature at the FC zone and its crossing with the $^1\pi\pi^*$ state occurs about an eV above the $^1\pi\pi^*$ minimum. It is emphasized at this point that, we are concerned with the nuclear dynamics in the vicinity of the FC region wherein the states are bound ($^1\pi\pi^*$) and quasibound ($^1\pi\sigma^*$) in nature and therefore the present method (discussed below) can be expected to provide an interpretation and understanding of the experimental results recorded recently [30].

6.2 Theory and Methodology

6.2.1 Electronic Structure Calculations

Equilibrium geometry of the electronic ground state, S_0 (reference state in the present study) of both phenol and PFP is optimized at the second-order Møller-Plesset perturbation (MP2) level of theory employing the aug-cc-pVDZ basis set of dunning [51]. The calculations are carried out using G09 suite of programs [52]. For both phenol and PFP the optimized reference equilibrium geometry of the S_0 state converged to the C_s symmetry point group. Harmonic frequency (ω_i) of vibrational modes of both the molecules is calculated by diagonalizing the kinematic (**G**) and *ab initio* force constant (**F**) matrix of the reference equilibrium structure [53]. These vibrational frequencies of phenol and PFP are listed in Tables 6.1 and 6.2, respectively. It can be seen from the latter that substitution of F atom decreases the frequency of vibrational modes in PFP and the harmonic frequency of the vibrational modes obtained in the present study are in good accord with the theoretical and experimental (fundamental) data available in the literature [30]. The mass-weighted normal coordinate of the vibrational modes is obtained from the eigenvectors of the **GF**- matrix. These coordinates are con-

verted into their dimensionless form ($\mathbf{Q}_i$) by multiplying with $\sqrt{\omega}_i$ (in a.u) [53].

The vibrational modes of phenol and PFP decompose into 23 totally symmetric and 10 nontotally symmetric modes in the C_s symmetry point group. They belong to the a' and a'' irreducible representations of the C_s symmetry point group, respectively. Adiabatic energies of the low-lying singlet electronic states of phenol and PFP are calculated along the dimensionless normal coordinates of the 33 vibrational degrees of freedom. The vertical excitation energies (VEEs) of these electronic states are calculated for a range of nuclear configuration using the equation-of-motion coupled-cluster singles and doubles (EOM-CCSD) method implemented in MOLPRO suite of programs [54]. The energetic ordering of the low-lying electronic states of phenol and PFP obtained at the respective reference equilibrium configuration of the electronic ground state is schematically shown in Fig. 6.1. It can be seen from this figure that the first two $^1\pi\sigma^*$ states of PFP come down in energy as compared to those in phenol. The nature of the energetically low-lying $\sigma*$ orbitals changes upon fluorination. In phenol they are O-H $\sigma*$ whereas, in PFP they are predominantly C-F $\sigma*$. Electronic effect due to F atom stabilizes the latter orbitals.

While the energetic ordering of the first two excited states of phenol is unambiguous, some ambiguity exists in the literature for the same in case of PFP [30]. In order to further confirm the energetic ordering of PFP given in Fig. 6.1, VEEs are calculated at the reference geometry by changing both the basis set and method. With a aug-cc-pVTZ basis and EOM-CCSD method the same energetic ordering is obtained. Multireference configuration interaction (MRCI) combined with CAS(10,11) and CAS(10,12) SCF methods also yield the same energetic

ordering. However, the energetic ordering of the lowest $^1\pi\pi*$ and $^1\pi\sigma*$ states is reversed in the TDDFT calculation [30] and also in a MRCI calculation with a lower active space exercised here. The VEE and oscillator strength of first three excited electronic states of phenol and pentafluorophenol are given in Table 6.3. It can be seen from the table that the results from different calculation are in good accord with each other.

A few remarks are in order at this point. The first two states in PFP are energetically closer compared to those in phenol. The experimental estimate of VEEs understandably relies on the location of the maximum of the recorded spectral band. This may be a correct estimate if the concerned state remains unperturbed by its neighbors. This is not the case in the present situation, in particular with PFP for which the absorbing state is highly perturbed by its neighbors. The latter cause a substantial distortion of the spectral profile of PFP. A correlation of the absorption band maximum with the theoretically calculated VEE in this case seems not appropriate. It can be seen from Table 6.3 that the VEE of both the S_1 and S_2 states of PFP had to be adjusted (number in the parentheses) in order to correctly reproduce the spacing between the maximum and the structure of the recorded experimental band [30]. We note that a CASSCF-MRCI method would have been the best choice for the calculation of electronic energies particularly in the present situation where the states are energetically close. However, such calculations are computationally very expensive and are not affordable. We therefore use the EOM-CCSD method to calculate the electronic energies over a range of nuclear configurations to establish the theoretical model discussed below.

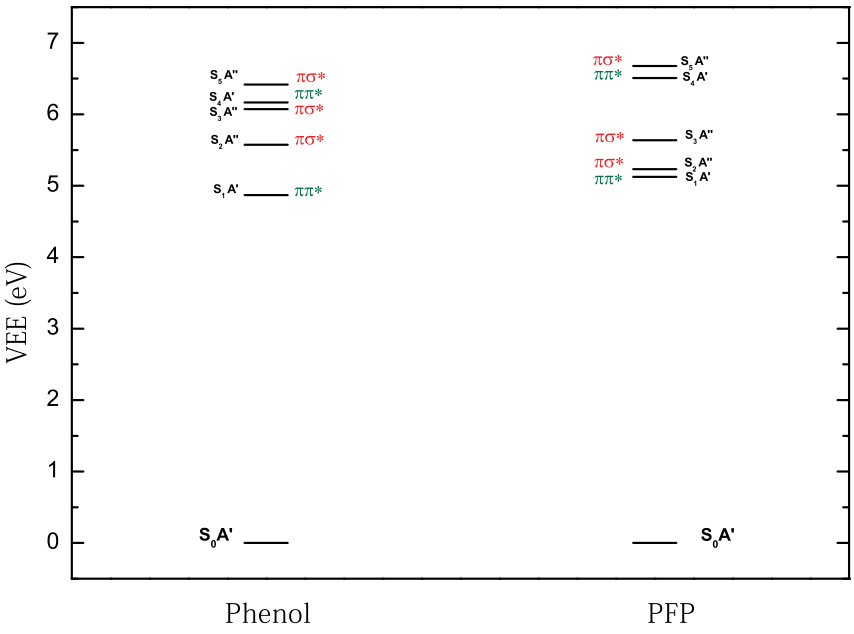

Figure 6.1: Energetic ordering of the lowest five electronic states of phenol and PFP at the reference equilibrium configuration of the electronic ground state.

Table 6.1: Harmonic frequency of the vibrational modes of phenol. The present MP2/aug-cc-PVDZ data are compared with the theoretical and experimental results available in the literature. The experimental data represent fundamental frequency. The frequency values are given in cm^{-1} unit.

symmetry	mode	MP2/aug-cc-PVDZ	B3LYP/cc-PVTZ [44]	Experiment [69]	description
a'	ν_1	3806	3690	3656	in plane O-H stretch
	ν_2	3236	3091	3087	in plane C-H stretch
	ν_3	3229	3085	3070	in plane C-H stretch
	ν_4	3216	3071	3063	in plane C-H stretch
	ν_5	3207	3063	3049	in plane C-H stretch
	ν_6	3191	3045	3027	in plane C-H stretch
	ν_7	1646	1595	1610	in plane C-C stretch
	ν_8	1634	1585	1603	in plane C-C stretch
	ν_9	1501	1484	1501	in plane C-C stretch and C-O-H and C-C-H bending
	ν_{10}	1482	1457	1472	in plane C-C stretch
	ν_{11}	1470	1331	1343	in plane C-C stretch and C-O-H and C-C-H bending
	ν_{12}	1332	1304	1277	in plane C-C-H bend and C-O-H bend
	ν_{13}	1267	1243	1261	in plane C-O stretch and C-C-H bend
	ν_{14}	1194	1155	1176	in plane C-O-H bend
	ν_{15}	1176	1154	1168	in plane C-C-H bend
	ν_{16}	1161	1139	1150	in plane C-C-H bend
	ν_{17}	1083	1060	1070	in plane C-C-H bend
	ν_{18}	1035	1012	1025	in plane C-C-H bend
	ν_{19}	998	985	999	in plane ring bending
	ν_{20}	812	803	823	in plane C-O, C-C stretch and C-C-C bend
	ν_{21}	611	614	619	in plane C-C-C bend
	ν_{22}	520	520	526	in plane C-C-C bend
	ν_{23}	397	393	403	in plane C-C-O bend
a''	ν_{24}	926	960	995	out of plane C-C-H bend
	ν_{25}	910	940	973	out of plane C-C-H bend
	ν_{26}	864	870	881	out of plane C-C-H bend
	ν_{27}	817	801	817	out of plane C-C-H bend
	ν_{28}	742	744	751	out of plane C-C-H bend(wagging)
	ν_{29}	613	683	686	out of plane bend (ring twist)
	ν_{30}	496	501	503	out of plane bend (wagging)
	ν_{31}	406	410	409	out of plane bend (ring twist)
	ν_{32}	332	344	309	out of plane bend (C-O-H torsion)
	ν_{33}	223	224	244	out of plane bend

Table 6.2: Same as in Table 6.1 for PFP

symmetry	mode	MP2/aug-cc-PVDZ	B3LYP/6-311++** [30]	Experiment [30]	description
a'	ν_1	3775	3805	3628	in plane O-H stretch
	ν_2	1697			in plane C-C, C-F and C-O stretch
	ν_3	1687			in plane C-C stretch and C-O-H bend
	ν_4	1562	1552	1541	in plane C-C stretch and C-O-H bend
	ν_5	1541	1530	1524	in plane C-C, C-F and C-O stretch
	ν_6	1509			in plane ring stretch and C-O-H bend
	ν_7	1487	1348	1314	in plane C-C stretch and C-O-H bend
	ν_8	1286			in plane C-O-H bend
	ν_9	1276	1256	1226	in plane C-O, C-F stretch and C-C-C bend and C-O-H bend
	ν_{10}	1149			in plane C-F and C-O stretch
	ν_{11}	1129	1140	-	in plane C-F stretch and C-C-C bend and C-O-H bend
	ν_{12}	1002	1013	1017	in plane C-F and C-O stretch
	ν_{13}	969	979	977	in plane C-F stretch and C-O-H bend
	ν_{14}	772			in plane bend (ring rocking)
	ν_{15}	591			in plane C-C-C bend
	ν_{16}	556			in plane ring stretch
	ν_{17}	442			in plane bend
	ν_{18}	437			in plane bend
	ν_{19}	316			in plane bend (rocking)
	ν_{20}	310			in plane C-C-F and C-C-O bend
	ν_{21}	279			in plane bend (Scissoring)
	ν_{22}	268			in plane bend (Scissoring)
	ν_{23}	264			in plane bend (Scissoring)
a''	ν_{24}	614			out of plane bend
	ν_{25}	597			out of plane bend (ring twist)
	ν_{26}	447			out of plane bend (ring twist)
	ν_{27}	374			out of plane C-O-H bend
	ν_{28}	357			out of plane C-O-H bend
	ν_{29}	349			out of plane bend
	ν_{30}	208	213		out-of-plane C-C-F and C-C-O bend (wagging)
	ν_{31}	180	185		out-of-plane bend (ring twist)
	ν_{32}	138	138		out-of-plane bend
	ν_{33}	135	134		out-of-plane bend

Table 6.3: VEEs (in eV) of energetically low-lying electronic states of phenol and PFP along with the oscillator strength (f) and type of transition. The adjusted VEEs which are used in the dynamics calculations of PFP are given in the parentheses.

Phenol										
State	This work	MRCI(8,8) [23] (aug-cc-pVDZ)	CC2 [48] (aug-(o)-avtz)	CASPT2(10,10) [66] (aug-cc-pVDZ)	CASSCF [22]	TDDFT [67]	Expt [68]	Expt [69]	f	Transition type
S_1 A'	4.869	4.82	4.86	4.52	4.85	4.99	4.51	4.51	0.02	$\pi\pi*$
S_2 A''	5.573	5.70	5.37	5.64	5.44	5.13	5.77	5.12	0.00	$\pi\sigma*$
S_3 A''	6.073	-	-	6.13	-	5.57	6.67	6.01	0.00	$\pi\sigma*$

PFP					
State	This work	TDDFT [30]	Expt [30]	f	Transition Type
S_1 A'	5.124{4.97}	4.49	4.77	0.01	$\pi\pi*$
S_2 A''	5.233{5.49}	4.85	5.34	0.00	$\pi\sigma*$
S_3 A''	5.637	5.76	5.56	0.00	$\pi\sigma*$

6.2.2 Vibronic Hamiltonian

A coupled three states Hamiltonian is constructed in this section. In the spirit of the general approach [1] the Hamiltonian is written in a diabatic electronic basis and in terms of dimensionless normal displacement coordinate of vibrational modes introduced above. Since equilibrium geometry of both phenol and PFP belongs to C_s symmetry point group, the symmetry of the electronic states is either A' or A''. According to symmetry rule the coupling between states of A' and A'' symmetry is caused by vibrational modes of a'' symmetry in first-order. The vibronic Hamiltonian of the S_1, S_2 and S_3 states of phenol and PFP can be symbolically written as [1]

$$\mathcal{H} = \mathcal{H}_0 \mathbf{1_3} + \mathcal{W}, \tag{6.1a}$$

In the above equation, $\mathcal{H}_0 = \mathcal{T}_N + \mathcal{V}_0$, represents the Hamiltonian of the reference electronic ground (S_0) state. Within a harmonic representation

$$\mathcal{T}_N = -\frac{1}{2} \sum_{i \in a',\, a''} \omega_i \frac{\partial^2}{\partial Q_i^2}, \tag{6.1b}$$

and

$$\mathcal{V}_0 = \frac{1}{2} \sum_{i \in a',\, a''} \omega_i Q_i^2. \tag{6.1c}$$

The quantity $\mathbf{1_3}$ is a 3 × 3 diagonal unit matrix. The quantity $\mathcal{W}$ represents the diabatic electronic Hamiltonian and is given by

$$\mathcal{W} = \begin{bmatrix} \mathcal{E}^1 + \mathcal{U}^1 & \sum\limits_{i \in a''} \lambda_i^{1,2} Q_i & \sum\limits_{i \in a''} \lambda_i^{1,3} Q_i \\ & \mathcal{E}^2 + \mathcal{U}^2 & 0 \\ h.c & & \mathcal{E}^3 + \mathcal{U}^3 \end{bmatrix} \tag{6.1d}$$

In the above matrix the quantity $\mathcal{E}^j$ represents the VEE of the j^{th} electronic state. The elements $\mathcal{U}^j$ are expanded in a Taylor series around the reference equilibrium configuration at, $Q = 0$, in the following way

$$\mathcal{U}^j = \sum_{i \in a'} \kappa_i^j Q_i + \frac{1}{2!} \sum_{i \in a',\, a''} \gamma_i^j Q_i^2 + \frac{1}{3!} \sum_{i \in a',} \zeta_i^j Q_i^3 + \frac{1}{4!} \sum_{i \in a',\, a''} \xi_i^j Q_i^4, \tag{6.1e}$$

where the linear, quadratic, cubic and quartic intrastate coupling parameters for the j^{th} electronic state along the i^{th} vibrational mode are given by κ_i^j, γ_i^j, ζ_i^j and ξ_i^j, respectively. The first-order interstate coupling parameter of the i^{th} vibrational mode between the electronic states j and k is given by $\lambda_i^{j,k}$. The symmetry of the vibrational mode i is specified in the summation index. The adiabatic electronic energies calculated *ab initio* (cf., Sec. 6.2.1) are fit to the adiabatic form of the diabatic electronic Hamiltonian of Eq. 6.1d by a least squares procedure to derive the parameters defined above. The estimated complete set of parameters for phenol and PFP are given in Tables 6.4, 6.5, 6.6, 6.7 and 6.8. We mention that we have also estimated bilinear coupling between the symmetric modes and found that they are $\sim 10^{-3}$ eV or less and therefore are not included in the Hamiltonian given above. Owing to a large vibrational degrees of freedom (total 33) all bilinear couplings appeared to be computationally expensive and could not be calculated. It can be seen later in the text that the above Hamiltonian with the

estimated parameter set satisfactorily explains the experimental findings.

A careful inspection of the coupling parameters suggests that all vibrational modes are not relevant in the nuclear dynamics in the considered electronic states of phenol and PFP. Therefore, only the relevant modes (marked with * in Table 6.4 and 6.5) having significant excitation strength are retained in the nuclear dynamics study. The vibronic energy levels and nonradiative decay rate of electronic states are examined below. The spectral intensity is calculated using the Fermi's golden rule equation [1]

$$P(E) \;=\; \sum_{v} \left| \langle \Psi_v^f | \hat{T} | \Psi_0^i \rangle \right|^2 \delta(E - E_v^f + E_0^i), \tag{6.2}$$

where, $|\Psi_v^f\rangle$ represents the eigenstate of the vibronic Hamiltonian of Eq. 6.1a with energy E_v^f. The ket $|\Psi_0^i\rangle$ represents the wavefunction of the initial reference electronic state with energy E_0^i. The quantity $\hat{T}$ is the transition dipole operator and E is the energy of the incident photon. The initial state, $|\Psi_0^i\rangle$, is written as

$$|\Psi_0^i\rangle \;=\; |\Phi_0\rangle|\chi_0^0\rangle, \tag{6.3}$$

with $|\Phi\rangle$ and $|\chi\rangle$ representing the diabatic electronic and vibrational components of the total wavefunction, respectively. The eigenfunctions of the unperturbed harmonic Hamiltonian, $\mathcal{H}_0$ (cf. Eq. 6.1a), of the initial reference state are taken as $|\chi_0^0\rangle$.

In the time-dependent method the spectral intensity given above transforms to Fourier transformation of the autocorrelation function of the WP and is given

by

$$P(E) \approx 2Re \int_0^\infty e^{iEt/\hbar} \langle \mathbf{0}|\boldsymbol{\tau}^\dagger \; e^{-i\mathcal{H}t/\hbar} \; \boldsymbol{\tau}|\mathbf{0}\rangle \; dt, \tag{6.4}$$

$$\approx 2Re \sum_{m=1}^{3} |\tau^m|^2 \int_0^\infty e^{iEt/\hbar} \; C^m(t) \; dt. \tag{6.5}$$

Here, $C^m(t) = \langle \Psi^m(0)|\Psi^m(t)\rangle$ is the time autocorrelation function of the WP initially prepared on the m^{th} electronic state. The ket $|\mathbf{0}\rangle$ represents the vibrational and electronic ground state and $\boldsymbol{\tau}$ is the transition dipole matrix; $\boldsymbol{\tau}^\dagger = (\tau^{S_1}, \tau^{S_2}, \tau^{S_3}, ...)$, with $\tau^m = \langle \Phi^m|\hat{T}|\Phi^0\rangle$ and $\Psi^m(t) = e^{-iHt/\hbar}\tau^m|0\rangle$. The final wavefunction may possess components on each of the vibronically coupled diabatic electronic states (S_1, S_2 and S_3), and understandably, the composite vibronic spectrum would ideally be a weighted sum of the resulting partial spectrum of the component states. In this study the transition dipole matrix elements are treated as constants in accordance with the generalized Condon approximation [55]. The vibronic secular matrix becomes block diagonal upon a suitable ordering of the basic states. When this vibronic symmetry is used, terms like, $|\tau^m|^2$, contributes in Eq. 5 and the mixed terms like, $\tau^m\tau^{n^*}$ present in Eq. (2) vanish [1].

In the time-independent method the spectral intensity is calculated by diagonalizing the Hamiltonian matrix in a harmonic oscillator basis and using the Lanczos algorithm [56]. In the time-dependent calculations the WP propagation is carried out by employing the multi-configuration time-dependent Hartree (MCTDH) method [57–59] implemented in the Heidelberg suite of programs de-

veloped by Meyer and coworkers [60]. The latter utilizes a harmonic oscillator discrete variable representation for the primitive basis. The time-dependent single particle functions are represented in this basis to solve the equation of motion. Furthermore, the vibrational degrees of freedom are combined using its multiset ansatz to form the single particle and to reduce the dimensionality problem in multimode multistate dynamics study. The MCTDH basis set details, as used for quantum dynamical calculations in the present case are given in Tables 6.10 and 6.11. In the latter various mode combination schemes, the time-independent (primitive) basis as well as time-dependent (single-particle functions-SPF) basis are given. The number of basis function for a given mode is estimated from its coupling strength ($\frac{\kappa^2 or \lambda^2}{2\omega^2}$), and the convergence behavior of the spectral envelope. We note that, while the WP calculations yield the broadband spectral envelope and the time development of an electronic state, a precise location of the vibronic eigenvalues are calculated by a time-independent matrix diagonalization approach. The latter calculations are prohibitively difficult for the present systems with large number of electronic and vibrational degrees of freedom. The eigenvectors of the energetically low-lying vibronic levels are also calculated by a block improved Lanczos method [61, 62] to facilitate the spectral assignments and comparison with high-resolution experimental data.

Table 6.4: The linear and quadratic coupling parameters (as defined in Eq. 1e) for the S_1 A', S_2 A'' and S_3 A'' states of phenol obtained from a fitting of calculated *ab initio* electronic energy to the model constructed in Sec. IIB. Dimensionless excitation strengths are given in the parentheses. All data are given in the eV unit.

Symm	Mode	Freq	κ_i	γ_i	κ_i	γ_i	κ_i	γ_i
			S_1 A'		S_2 A''		S_3 A''	
a'	ν_1^*	0.4719	-0.0161(0.00)	0.0004	-0.2138(0.10)	-0.1062	-0.0875(0.02)	-0.0008
	ν_2	0.4013	-0.0324(0.00)	0.0002	-0.0115(0.00)	0.0013	0.0204(0.00)	-0.0154
	ν_3	0.4004	0.0040(0.00)	-0.0001	0.0075(0.00)	0.0020	0.0019(0.00)	-0.0037
	ν_4	0.3988	-0.0134(0.00)	-0.0007	-0.0085(0.00)	0.0011	-0.0053(0.00)	-0.0025
	ν_5	0.3977	0.0153(0.00)	-0.0002	0.0089(0.00)	0.0025	-0.0029(0.00)	-0.0012
	ν_6	0.3957	-0.0112(0.00)	-0.00001	-0.0019(0.00)	-0.0002	-0.0102(0.00)	0.0027
	ν_7^*	0.2041	-0.0109(0.00)	0.0059	0.0882(0.09)	-0.0217	0.0830(0.08)	-0.0357
	ν_8^*	0.2027	-0.0077(0.00)	0.0069	0.1372(0.23)	-0.0193	0.0991(0.12)	-0.0433
	ν_9^*	0.1861	-0.0265(0.01)	-0.0024	-0.0714(0.07)	-0.0071	-0.0171(0.00)	-0.0070
	ν_{10}	0.1837	-0.0264(0.01)	0.0922	-0.0250(0.01)	0.0187	-0.0296(0.01)	0.0271
	ν_{11}	0.1823	0.0057(0.00)	-0.0064	0.0308(0.01)	-0.0061	0.0245(0.01)	-0.0036
	ν_{12}	0.1652	0.0108(0.00)	-0.0004	-0.0089(0.00)	-0.0030	-0.0177(0.01)	-0.0034
	ν_{13}^*	0.1571	-0.1016(0.20)	-0.0002	-0.1006(0.21)	-0.0123	-0.0740(0.11)	-0.0128
	ν_{14}^*	0.1480	-0.0163(0.01)	-0.0031	-0.0648(0.10)	-0.0239	-0.0557(0.07)	-0.0020
	ν_{15}^*	0.1458	0.0070(0.00)	0.0033	-0.0584(0.08)	0.0013	-0.0765(0.14)	-0.0071
	ν_{16}	0.1440	-0.0011(0.00)	0.0050	0.0183(0.01)	0.0008	0.0127(0.00)	-0.0006
	ν_{17}	0.1343	0.0142(0.01)	-0.0065	0.0022(0.00)	-0.0013	0.0035(0.00)	-0.0060
	ν_{18}^*	0.1284	0.1078(0.35)	-0.0018	0.0172(0.01)	0.0020	0.0070(0.00)	-0.0002
	ν_{19}^*	0.1238	0.1060(0.37)	-0.0001	0.0319(0.03)	0.0013	0.0419(0.06)	0.0004
	ν_{20}^*	0.1007	0.0825(0.34)	-0.0018	-0.0061(0.00)	-0.0031	0.0168(0.01)	-0.0057
	ν_{21}	0.0758	-0.0041(0.00)	-0.0211	0.0002(0.00)	-0.0102	-0.0076(0.01)	-0.0144
	ν_{22}^*	0.0645	-0.0306(0.12)	-0.0128	-0.0792(0.75)	-0.0063	-0.0808(0.78)	-0.0078
	ν_{23}^*	0.0492	-0.0036(0.00)	-0.0026	0.0094(0.02)	-0.0017	0.0169(0.06)	0.0008
a''	ν_{24}	0.1148		-0.0676		0.0085	-	0.0043
	ν_{25}	0.1129		-0.0437		0.0011	-	-0.0038
	ν_{26}	0.1071		-0.0418		0.0166	-	0.0210
	ν_{27}	0.1013		-0.0572		-0.0010	-	-0.0117
	ν_{28}	0.0920		-0.0343		-0.0046	-	-0.0259
	ν_{29}	0.0760		-0.0465		-0.0096	-	-0.0044
	ν_{30}	0.0615		-0.0293		-0.0183	-	-0.0202
	ν_{31}^*	0.0504		-0.0561		-0.0111	-	-0.0091
	ν_{32}	0.0412		-0.0215		-0.0679	-	-0.0318
	ν_{33}^*	0.0277		-0.0159		0.0001	-	-0.0379

Table 6.5: Same as in Table 6.4, for the S_1 A', S_2 A'' and S_3 A'' states of PFP. All data are given in the eV unit.

Symm	Mode	Freq	κ_i	γ_i	κ_i	γ_i	κ_i	γ_i
			S_1 A'		S_2 A''		S_3 A''	
a'	ν_1^*	0.4681	-0.0082(0.00)	-0.0003	-0.0768(0.01)	-0.0394	-0.0186(0.00)	-0.0071
	ν_2^*	0.2105	-0.0121(0.00)	0.0141	0.1589(0.28)	-0.0676	-0.1314(0.19)	0.0352
	ν_3^*	0.2092	-0.0078(0.00)	0.0115	0.0113(0.00)	-0.0903	-0.0110(0.00)	0.0665
	ν_4^*	0.1937	-0.0134(0.00)	-0.0074	-0.0279(0.01)	-0.0450	-0.0357(0.02)	-0.0472
	ν_5^*	0.1911	0.0216(0.01)	-0.0064	-0.0327(0.01)	-0.0465	-0.0216(0.01)	-0.0467
	ν_6^*	0.1871	0.1389(0.28)	0.0218	-0.0183(0.00)	-0.0387	-0.0268(0.01)	-0.0299
	ν_7^*	0.1843	0.0633(0.06)	0.1296	0.0037(0.00)	0.0316	-0.0073(0.00)	0.0387
	ν_8^*	0.1595	-0.0092(0.00)	0.0033	-0.0002(0.00)	-0.0184	0.0058(0.00)	-0.0097
	ν_9^*	0.1582	-0.0075(0.00)	-0.0005	0.0229(0.01)	-0.0282	0.0187(0.01)	-0.0309
	ν_{10}^*	0.1425	0.0061(0.00)	-0.0011	-0.0005(0.00)	-0.0247	0.0550(0.07)	-0.0196
	ν_{11}	0.1399	0.0006(0.00)	-0.0013	-0.0069(0.00)	-0.0264	-0.0169(0.01)	-0.0231
	ν_{12}^*	0.1242	-0.0014(0.00)	-0.0045	-0.0195(0.01)	-0.0151	-0.0030(0.00)	-0.0126
	ν_{13}^*	0.1201	-0.0018(0.00)	-0.0039	0.0048(0.00)	-0.0156	0.0078(0.00)	-0.0182
	ν_{14}	0.0957	0.0008(0.00)	-0.0069	0.0027(0.00)	-0.0094	-0.0017(0.00)	-0.0088
	ν_{15}^*	0.0733	-0.0105(0.01)	-0.0010	0.0106(0.01)	-0.0164	-0.0027(0.00)	-0.0183
	ν_{16}^*	0.0689	-0.1054(1.17)	0.0015	-0.0237(0.06)	-0.0055	-0.0415(0.18)	-0.0053
	ν_{17}^*	0.0547	0.0212(0.08)	-0.0127	0.0745(0.93)	-0.0159	-0.0696(0.81)	-0.0039
	ν_{18}^*	0.0542	-0.0096(0.02)	-0.0134	-0.0191(0.06)	-0.0287	0.0223(0.08)	0.0078
	ν_{19}	0.0392	-0.0007(0.00)	-0.0012	-0.0037(0.00)	-0.0080	-0.0029(0.00)	-0.0065
	ν_{20}^*	0.0385	-0.0012(0.00)	-0.0006	0.0026(0.00)	-0.0046	0.0068(0.02)	-0.0066
	ν_{21}^*	0.0345	-0.0019(0.00)	0.0004	0.0013(0.00)	-0.0003	0.0032(0.00)	0.0006
	ν_{22}^*	0.0332	0.0061(0.02)	-0.0033	0.0200(0.18)	-0.0052	-0.0255(0.29)	0.0005
	ν_{23}^*	0.0327	-0.0054(0.01)	-0.0029	-0.0206(0.20)	-0.0029	0.0226(0.24)	0.0002
a''	ν_{24}^*	0.0761		-0.1295		-0.0448		0.0531
	ν_{25}^*	0.0740		-0.3156		0.2677		-0.0605
	ν_{26}^*	0.0554		-0.1065		-0.0170		-0.0222
	ν_{27}^*	0.0463		-0.0340		0.0181		0.0106
	ν_{28}^*	0.0443		-0.0295		-0.0025		0.0090
	ν_{29}^*	0.0433		-0.0642		0.0533		0.0108
	ν_{30}^*	0.0258		-0.0146		-0.0047		-0.0079
	ν_{31}^*	0.0223		-0.0155		-0.0126		-0.0147
	ν_{32}^*	0.0171		-0.0622		0.0309		-0.0055
	ν_{33}^*	0.0168		-0.0700		0.0473		-0.0116

Table 6.6: The 3^{rd} (cubic) and 4^{th} (quartic) order coupling parameters (as defined in Eq. 1e) for the S_1 A', S_2 A'' and S_3 A'' states of Phenol obtained from a fitting of calculated *ab initio* electronic energy to the model constructed in Sec IIB. All data are given in the eV unit.

Symm	Mode	Freq	ζ_i	ξ_i	ζ_i	ξ_i	ζ_i	ξ_i
			S_1 A'		S_2 A''		S_3 A''	
a'	ν_1	0.4719	-0.0000	0.0000	-0.0246	0.0116	0.0000	0.0000
	ν_2	0.4013	-0.0000	0.0000	0.0041	-0.0032	0.0036	0.0016
	ν_3	0.4004	0.0000	0.0000	0.0003	-0.0003	-0.0026	-0.0042
	ν_4	0.3988	-0.0000	-0.0000	0.0020	-0.0013	0.0028	-0.0026
	ν_5	0.3977	0.0000	-0.0000	-0.0000	0.0000	-0.0026	-0.0018
	ν_6	0.3957	-0.0000	-0.0000	0.0107	-0.0067	0.0000	-0.0000
	ν_7	0.2041	0.0031	-0.0027	-0.0071	0.0004	-0.0113	0.0040
	ν_8	0.2027	0.0030	-0.0027	-0.0114	-0.0038	-0.0064	0.0093
	ν_9	0.1861	-0.0000	-0.0000	0.0000	-0.0000	0.0000	-0.0000
	ν_{10}	0.1837	0.0000	-0.0000	0.0000	-0.0000	0.0000	-0.0000
	ν_{11}	0.1823	0.0000	-0.0000	-0.0000	-0.0000	-0.0000	0.0000
	ν_{12}	0.1652	0.0000	-0.0000	-0.0007	-0.0011	-0.0000	-0.0000
	ν_{13}	0.1571	-0.0000	0.0000	0.0000	-0.0000	-0.0000	-0.0000
	ν_{14}	0.1480	0.0000	-0.0008	-0.0134	-0.0145	-0.0000	-0.0000
	ν_{15}	0.1458	-0.0000	0.0000	0.0000	0.0000	-0.0000	-0.0000
	ν_{16}	0.1440	-0.0000	0.0000	0.0000	0.0000	-0.0002	-0.0030
	ν_{17}	0.1343	-0.0000	0.0000	0.0004	-0.0004	0.0000	-0.0000
	ν_{18}	0.1284	-0.0000	0.0000	-0.0000	-0.0000	0.0000	-0.0000
	ν_{19}	0.1238	-0.0000	0.0000	0.0000	-0.0000	0.0000	-0.0000
	ν_{20}	0.1007	-0.0000	0.0000	0.0000	-0.0000	-0.0000	-0.0000
	ν_{21}	0.0758	-0.0000	0.0000	-0.0000	-0.0000	-0.0000	-0.0000
	ν_{22}	0.0645	0.0000	0.0000	-0.0000	-0.0000	-0.0000	-0.0000
	ν_{23}	0.0492	-0.0000	0.0000	-0.0006	-0.0010	-0.0000	-0.0000
a''	ν_{24}	0.1148		0.0096		-0.0013	-	-0.0017
	ν_{25}	0.1029		0.0000		0.0003	-	-0.0000
	ν_{26}	0.1071		0.0000		-0.0022	-	-0.0951
	ν_{27}	0.1013		0.0000		-0.0034	-	-0.0089
	ν_{28}	0.0920		0.0000		-0.0033	-	-0.0044
	ν_{29}	0.0760		0.0000		-0.0000	-	-0.0185
	ν_{30}	0.0615		0.0000		-0.0066	-	-0.0104
	ν_{31}	0.0504		0.0000		-0.0000	-	-0.0016
	ν_{32}	0.0412		0.1546		-0.7446	-	0.0312
	ν_{33}	0.0277		0.0000		-0.0002	-	0.0072

Table 6.7: The 3^{rd} (cubic) and 4^{th} (quartic) order coupling parameters (as defined in Eq. 1e) for the S_1 A', S_2 A'' and S_3 A'' states of PFP obtained from a fitting of calculated *ab initio* electronic energy to the model constructed in Sec IIB. All data are given in the eV unit.

Symm	Mode	Freq	ζ_i	ξ	ζ_i	ξ	ζ_i	ξ
			S_1 A'		S_2 A''		S_3 A''	
a'	ν_1	0.4681	-0.0000	0.0000	-0.0352	-0.0150	-0.0102	-0.0068
	ν_2	0.2105	0.0022	0.0002	-0.0100	0.0364	0.0227	-0.0211
	ν_3	0.2092	0.0016	-0.0019	0.0353	0.0033	0.0353	0.0033
	ν_4	0.1937	0.0000	0.0000	-0.0000	0.0000	0.0000	0.0000
	ν_5	0.1911	0.0000	0.0000	-0.0000	0.0000	0.0000	0.0000
	ν_6	0.1871	0.0000	0.0000	0.0044	0.0019	0.0025	0.0021
	ν_7	0.1843	0.0016	-0.0128	0.0019	-0.0037	0.0005	-0.0039
	ν_8	0.1595	0.0013	-0.0004	-0.0100	-0.0119	-0.0036	-0.0032
	ν_9	0.1582	0.0000	0.0000	-0.0000	0.0000	0.0000	-0.0000
	ν_{10}	0.1425	-0.0002	0.0000	-0.0000	0.0000	0.0000	-0.0000
	ν_{11}	0.1399	-0.0001	0.0000	-0.0000	0.0000	0.0000	-0.0000
	ν_{12}	0.1242	0.0000	0.0000	-0.0000	0.0000	0.0000	-0.0000
	ν_{13}	0.1201	0.0000	0.0000	-0.0000	0.0000	0.0000	-0.0000
	ν_{14}	0.0957	0.0000	0.0000	-0.0000	0.0000	0.0000	-0.0000
	ν_{15}	0.0733	0.0000	0.0000	-0.0000	0.0000	0.0000	-0.0000
	ν_{16}	0.0689	0.0000	0.0000	-0.0000	0.0000	0.0000	-0.0000
	ν_{17}	0.0547	0.0000	0.0000	-0.0093	-0.0051	0.0097	0.0051
	ν_{18}	0.0542	0.0000	0.0000	0.0037	0.0019	-0.0030	-0.0019
	ν_{19}	0.0392	0.0000	0.0000	-0.0000	0.0000	0.0000	-0.0000
	ν_{20}	0.0385	0.0000	0.0000	-0.0000	0.0000	0.0000	-0.0000
	ν_{21}	0.0345	0.0000	0.0000	-0.0006	-0.0003	-0.0002	-0.0002
	ν_{22}	0.0332	0.0000	0.0000	-0.0007	-0.0000	0.0014	-0.0000
	ν_{23}	0.0327	0.0000	0.0000	0.0010	-0.0005	-0.0012	0.0000
a''	ν_{24}	0.0761		0.0361		0.0002		-0.0366
	ν_{25}	0.0740		0.4137		-0.5321		0.0172
	ν_{26}	0.0554		0.0175		-0.0032		0.0002
	ν_{27}	0.0463		0.0017		-0.0239		-0.0061
	ν_{28}	0.0443		-0.0335		-0.0451		-0.0107
	ν_{29}	0.0433		0.0087		-0.0092		-0.0019
	ν_{30}	0.0258		0.0010		-0.0022		-0.0018
	ν_{31}	0.0223		0.0000		-0.0000		-0.0000
	ν_{32}	0.0171		0.0228		-0.0615		-0.0035
	ν_{33}	0.0168		0.0286		-0.0811		0.0056

Table 6.8: Interstate coupling parameters (in eV) of the vibronic Hamiltonian of Eq. 6.1d for the S_1 A', S_2 A'' and S_3 A'' electronic states of phenol and PFP estimated from the *ab initio* electronic structure results (see text for details). Dimensionless excitation strengths are given in the parentheses.

Phenol			
Symm	Mode	$\lambda_i^{1,2}$	$\lambda_i^{1,3}$
a''	ν_{24}	0.1186(0.53)	0.1451(0.79)
	ν_{25}	0.0928(0.34)	0.1002(0.39)
	ν_{26}	0.1063(0.49)	0.1136(0.56)
	ν_{27}	0.1036(0.52)	0.1183(0.68)
	ν_{28}	0.0740(0.32)	0.0548(0.17)
	ν_{29}	0.0842(0.61)	0.1054(0.96)
	ν_{30}	0.0384(0.19)	0.0423(0.23)
	ν_{31}	0.0937(1.72)	0.1225(2.95)
	ν_{32}	0.0000(0.00)	0.0000(0.00)
	ν_{33}	0.0538(1.89)	0.0000(0.00)
PFP			
Symm	Mode	$\lambda_i^{1,2}$	$\lambda_i^{1,3}$
a''	ν_{24}	0.0516(0.27)	0.1649(2.35)
	ν_{25}	0.1903(3.31)	0.2025(3.74)
	ν_{26}	0.0595(0.58)	0.1070(1.87)
	ν_{27}	0.0381(0.34)	0.0759(1.34)
	ν_{28}	0.0292(0.22)	0.0817(1.70)
	ν_{29}	0.0731(1.42)	0.1023(2.79)
	ν_{30}	0.0161(0.19)	0.0274(0.56)
	ν_{31}	0.0088(0.08)	-
	ν_{32}	0.0562(5.40)	0.0893(13.6)
	ν_{33}	0.0656(7.62)	0.0923(15.1)

6.3 Results and Discussion

6.3.1 Adiabatic Potential Energy Surfaces

In this section we examine the topography of the adiabatic PESs of the excited singlet electronic states S_1 A′, S_2 A″ and S_3 A″ of phenol and PFP. One dimensional cuts of the full-dimensional potential energy hypersurface of phenol are plotted along the coordinate of totally symmetric (a') vibrational modes in Figs. 6.2(a-d). There are 23 symmetric vibrational modes in phenol. The potential energy cuts along all 23 modes are examined. To save space, the potential energy cuts in Figs. 6.2 are plotted along four symmetric vibrational modes only. These give a general overview of variation of potential energy along the vibrational modes of phenol. It can be seen from panel a of Fig. 6.2 that S_1 and S_2 states cross along ν_1. The latter is a O-H stretching mode of high frequency, $\sim 3806\ cm^{-1}$. Excitation strength of this mode is negligible in all three states (cf. Table 6.4). The vibrational mode ν_8 (C-C stretch, $\sim 1634\ cm^{-1}$) has larger excitation strength in S_2. It can be seen from panel b of Fig. 6.2 that S_1 and S_2 states are quasi-degenerate at larger displacement along this mode. The vibrational mode ν_{13} (C-O stretch, $\sim 1267\ cm^{-1}$) possesses some excitation strength in all three states (cf. Table 6.4). From panel c of Fig. 6.2, it can be seen that the states are fairly well separated along this mode. This is generally true along all other symmetric vibrational modes of phenol. The vibrational mode ν_{22} has much lower frequency $\sim 520\ cm^{-1}$. The potential energy cuts along this mode are plotted in panel d. This mode has the largest excitation strength in S_2 and S_3 (cf. Table 6.4). As a result the minimum of these states in Fig. 6.2d shifts considerably away from the reference equilibrium minimum at $\mathbf{Q} = 0$.

The potential energy cuts of the first three excited electronic states of PFP are plotted in Figs. 6.3(a-d) along representative ν_1, ν_6, ν_{16} and ν_{18} vibrational modes, respectively. The ν_1 vibrational mode is O-H stretch and has high frequency $\sim 3775\ cm^{-1}$. It can be seen from panel a that the electronic states of PFP are energetically much closer compared to those of phenol. The S_1 and S_2 states become quasi-degenerate in the vicinity of their equilibrium minimum. The low-energy crossing of S_1 state with S_2 and also with S_3 can be clearly seen from the potential cuts of panel b plotted along $\sim 1509\ cm^{-1}$ vibrational mode ν_6. It can be seen from Table 6.5 that the excitation strength of this mode is largest in the S_1 state. The $\sim 556\ cm^{-1}$ vibrational mode ν_{16} also has very large excitation strength in S_1 and except in S_2, this mode is also moderately excited in the remaining states. The potential energy cuts along this mode are shown in panel c of Fig. 6.3. The crossings of S_1 with S_2 and S_3 states can also be seen along this mode. The quasi-degeneracy of the S_1 and S_2 states is found along many other symmetric modes of PFP. For illustration the potential energy cuts along $\sim 437\ cm^{-1}$ vibrational mode ν_{18} are shown in panel d of Fig. 6.3. Because of stronger interactions between the states, the cubic and quartic terms of the Hamiltonian appears to be more relevant in this case as compared to the same in phenol.

It generally appears from the above discussion that the electronic states in PFP are much closer in energy as compared to phenol. In addition, they also exhibit low-energy curve crossings. These crossings develop into conical intersections in multi-dimensional space. The locus of the degeneracy of states forms a seam. The energetic minimum on various crossing seams in phenol and PFP is estimated with a second-order coupling model. The results are given in Table 6.9

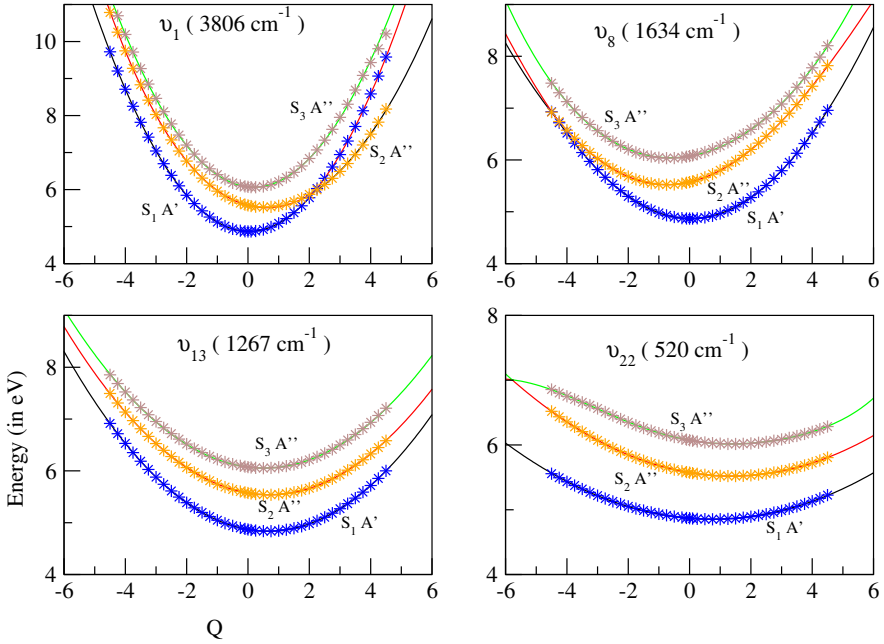

Figure 6.2: Adiabatic potential energies of the S_1 A', S_2 A'' and S_3 A'' electronic states of phenol along the normal coordinates of the totally symmetric vibrational modes ν_1, ν_8, ν_{13} and ν_{22} shown in panel a, b, c and d, respectively. The energies obtained from the present vibronic model and computed *ab initio* are shown by lines and points, respectively.

. In this table the diagonal entries represent the estimated equilibrium minimum of a state and the off-diagonal entries represent the energy minimum on various intersection seam. It can be seen from the Table that the S_1-S_2 intersection minimum in phenol occurs very close to the S_2 minimum but $\sim$ 0.65 eV above the S_1 minimum. The same intersection minimum is much closer to both S_1 and S_2 minimum in PFP. In this case S_1 minimum occurs only $\sim$ 0.1 eV below the S_1-S_2 intersection minimum. Furthermore, while S_1-S_3 intersection in phenol seems not very important for the dynamics on the S_1 and S_2 state, S_1-S_2 and S_1-S_3 intersections appear to have some impact on the S_1-S_2-S_3 coupled states dynamics in PFP.

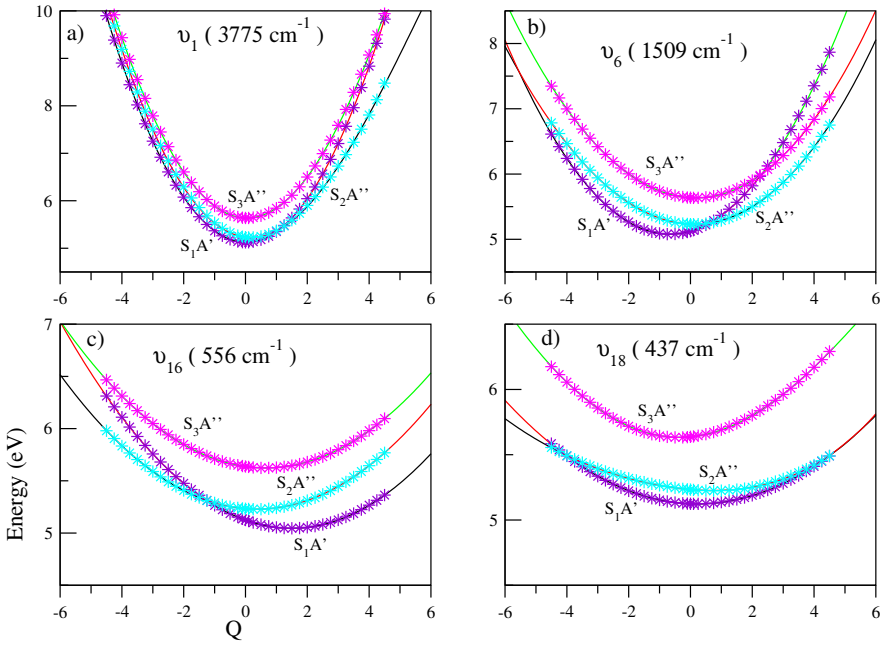

Figure 6.3: Adiabatic potential energies of the S_1 A', S_2 A'' and S_3 A'' electronic states of PFP along the normal coordinates of the totally symmetric vibrational modes ν_1, ν_6, ν_{16} and ν_{18} shown in panel a, b, c and d, respectively. The energies obtained from the present vibronic model and computed *ab initio* are shown by lines and points, respectively.

Table 6.9: Estimated equilibrium minimum (diagonal entries) and minimum of the seam of various conical intersections (off-diagonal entries) of the electronic states of phenol and PFP within a quadratic coupling model. All quantities are given in eV.

Phenol	S_1 A'	S_2 A''	S_3 A''
S_1 A'	4.71	5.36	6.68
S_2 A''	-	5.29	-
S_3 A''	-	-	5.88
PFP	S_1 A'	S_2 A''	S_3 A''
S_1 A'	4.98	5.08	5.52
S_2 A''	-	5.04	-
S_3 A''	-	-	5.48

6.3.2 Optical Absorption Spectrum and Comparison with Experiment

Spectroscopic and photophysical studies revealed that the structured absorption band ($S_1 \leftarrow S_0$) of phenol becomes broad and structureless in PFP [30]. Owing to the energetic proximity of electronic states (cf. Table 6.3), S_1, S_2 and S_3 bands in PFP are highly overlapping. We repeat that the energetic proximity of electronic states in PFP arises from the electronic effect due to F atom, which changes the nature of electronic transition and stabilizes $\sigma*$ orbital of the C-F bond. The S_1-S_2 and S_1-S_3 coupling through the vibrational modes of a'' symmetry in PFP is relatively stronger compared to that in phenol (cf. Table 6.8). Furthermore it can be seen from Table 6.9 that the equilibrium minimum of the participating states is closer to the intersection minimum with their neighbors in PFP. As a result, the S_1-S_2 and S_1-S_3 intersection seems are expected to be more readily accessible to the WP moving on the S_1 electronic state of PFP. Therefore, the nonadiabatic coupling effect on the S_1 and S_2 band is expected to be much stronger in PFP.

In the following the nuclear dynamics calculations are carried out with the coupled states Hamiltonian developed in Sec. 6.2.2 and both by time-independent and time-dependent quantum mechanical methods. The theoretical results are finally compared with the available experimental optical absorption spectrum of both the molecules [30]. In order to understand the vibronic structure of the coupled states spectrum, we first examine the uncoupled state spectra in detail and subsequently add the coupling. The optical absorption spectra of uncoupled electronic states of phenol and PFP are plotted in panel a and b of Fig. 6.4, respectively. The spectrum of each state is calculated including twelve dominant

totally symmetric vibrational modes and the matrix diagonalization method using the Lanczos algorithm [56]. The Harmonic Oscillator basis functions used along each mode in the calculations are given in Table 6.10. Hamiltonian represented in the harmonic oscillator basis is diagonalized using 10000 Lanczos iterations. The theoretical stick spectrum obtained from the diagonalization of the Hamiltonian matrix is convoluted with a Lorentzian line shape function of 15 meV full width at the half maximum (FWHM) to generate the spectral envelopes shown in Fig. 6.4.

A close look at the stick spectrum and the corresponding envelope plotted in Fig. 6.4 reveals that the electronic bands of phenol are relatively well separated in energy and have extended vibrational progressions compared to those of PFP. For the latter, the bands overlap owing to an energetic proximity of electronic states (cf. Fig. 6.4b). It can be seen that in case of phenol the origin line (0_0^0) of the S_1 state has maximum intensity (cf. Fig. 6.4a) whereas, the intensity maximum shifts to the second peak (cf. Fig. 6.4b) in case of PFP. This reveals a geometrical change of PFP in the S_1 state as compared to that in the S_0 state. A close analysis of the progression of peaks in the S_1, S_2 and S_3 bands of phenol (cf., Fig. 6.4a) reveals the following. In the S_1 band strong excitation of the fundamental of ν_{13}, ν_{18}, ν_{19}, ν_{20} and ν_{22} is found. The corresponding peaks are found at $\sim 1266\ cm^{-1}$, $\sim 1028\ cm^{-1}$, $\sim 998\ cm^{-1}$, $\sim 805\ cm^{-1}$ and $\sim 467\ cm^{-1}$ from the 0_0^0 line, respectively. The vibrational modes ν_{19} and ν_{20}, in particular, form extended progressions in the spectrum. The first overtone of these modes is located at $\sim 1996\ cm^{-1}$ and $\sim 1610\ cm^{-1}$, respectively. In addition to these, relatively weak excitation of fundamental of ν_7, ν_8, ν_9, ν_{14} and ν_{15} vibrational modes at $\sim 1669\ cm^{-1}$, $\sim 1661\ cm^{-1}$, $\sim 1491\ cm^{-1}$, $\sim 1182\ cm^{-1}$ and $\sim 1189\ cm^{-1}$, respectively, is revealed by the spectral data. The strongly excited vibra-

tional modes also form numerous combination peaks among themselves and also with the weakly excited ones, for example, the combination peak, $\nu_{19} + \nu_{20}$, with fairly large intensity is found at $\sim 1803\ cm^{-1}$.

In addition to energetic location and excitation strength analyses, the assignment of the peaks is confirmed through a thorough analysis of the nodal pattern of the eigenvectors of the vibrational levels. These eigenvectors are calculated by a block improved Lanczos method as implemented in the MCTDH program module [61, 62]. To illustrate and to save space we present in Fig. 6.5 a few representative eigenvectors only. In these figures the wavefunction probability density is plotted in a suitable reduced dimensional space (as shown in the plot) of normal coordinates. In panel a, b and c the wavefunction of the fundamental of ν_{19}, ν_{20} and ν_{22} is shown, respectively. It can be seen from these plots that the wavefunction acquire a node along the respective normal coordinate. In panel d, e and f the first overtone of these modes revealing two nodes along the respective coordinate is shown. The wavefunction for the combination peaks $\nu_{19} + \nu_{20}$, $\nu_{19} + \nu_{22}$ and $\nu_{20} + \nu_{22}$ is shown in panels g, h and i, respectively. It can be seen that the latter wavefunctions show one quantum excitation along both the modes forming the pair. We note that such a detailed exercise of wavefunction analysis is carried out for all the assignments discussed later in the text.

Unlike in case of S_1 state, the vibrational mode ν_{22} is strongly excited in the S_2 and S_3 states of phenol. The fundamental of this mode is located at $\sim 494\ cm^{-1}$ and $\sim 488\ cm^{-1}$, respectively, in the latter states. Several overtone and combination peaks (with relatively less strongly excited mode) of this mode is found from the calculated spectral data. For example, the first overtone of ν_{22} is

found at $\sim 988\ cm^{-1}$ and $\sim 976\ cm^{-1}$, respectively, in the S_2 and S_3 state. combination peaks of ν_{22} with relatively less strongly excited modes ν_7, ν_8, ν_9, ν_{13}, ν_{14} and ν_{15} are found from the data. The fundamental of the latter modes appears at $\sim 1581\ cm^{-1}$, $\sim 1571\ cm^{-1}$, $\sim 1474\ cm^{-1}$, $\sim 1217\ cm^{-1}$, $\sim 1094\ cm^{-1}$ and $\sim 1182\ cm^{-1}$, respectively, in the S_2 state and $\sim 1520\ cm^{-1}$, $\sim 1465\ cm^{-1}$, $\sim 1470\ cm^{-1}$, $\sim 1215\ cm^{-1}$, $\sim 1118\ cm^{-1}$ and $\sim 1147\ cm^{-1}$, respectively, in the S_3 state of phenol. Relatively stronger excitation, numerous overtones and combination peaks of ν_{22} in the S_2 and S_3 state of phenol contribute to their extended broad structure of the spectral envelope (cf. Fig. 4a) as compared to that of the S_1 state.

It can be seen from Table 6.1 and 6.2 that F atom substitution results into a reduction of frequency of all normal modes in PFP compared to that in phenol. This leads to excitation of many vibrational modes in the absorption spectrum of PFP. In the S_1 state spectrum (cf. Fig. 6.4b) of PFP the vibrational mode ν_{16} is very strongly excited. The fundamental and first two overtones of this mode are found at $\sim 562\ cm^{-1}$, $\sim 1124\ cm^{-1}$ and $\sim 1686\ cm^{-1}$, respectively. The eigenvector of these energy levels are plotted in reduced dimensions in panel a, b and c of Fig. 6.6, respectively. In can be seen that in panel a the eigenvector has one node, whereas, in panel b and c it has two and three nodes, respectively, along ν_{16}. The next strongly excited mode in the S_1 spectrum is ν_6. The fundamental and first overtone of this mode found at $\sim 1595\ cm^{-1}$ and $\sim 3189\ cm^{-1}$, respectively. Fundamental of moderately excited modes ν_5, ν_7, ν_{17}, ν_{18}, ν_{22}, ν_{23} is found at $\sim 1515\ cm^{-1}$, $\sim 1940\ cm^{-1}$, $\sim 388\ cm^{-1}$, $\sim 381\ cm^{-1}$, $\sim 254\ cm^{-1}$ and $\sim 251\ cm^{-1}$, respectively. We note that all the modes discussed above form several combination peaks in the spectrum. To illustrate, the eigenvectors of the combination levels $\nu_{16} + \nu_{17}$, $\nu_{16} + \nu_{18}$ and $\nu_{17} + \nu_{18}$ occurring at $\sim 950\ cm^{-1}$, $\sim$

943 cm^{-1} and $\sim$ 770 cm^{-1} are shown in panels d, e and f of Fig. 6.6, respectively.

In contrast to the above, ν_{17} is the strongly excited mode in both S_2 and S_3 states of PFP. The fundamental of ν_{17} is found at $\sim$ 404 cm^{-1} and $\sim$ 484 cm^{-1}, respectively, in these states. In the latter both ν_{22} and ν_{23} vibrational modes also form extended progressions. The fundamental of these two modes is found at $\sim$ 248 cm^{-1} and $\sim$ 254 cm^{-1} in S_2 and at $\sim$ 274 cm^{-1} and $\sim$ 268 cm^{-1} in S_3 state, respectively. Excitation of the ν_{16} mode is weaker in these states. The high frequency vibrational mode ν_2 also makes an extended progression in the S_2 and S_3 states of PFP. Analyses show that the fundamental of this mode appears at $\sim$ 1398 cm^{-1} and $\sim$ 1940 cm^{-1} in these states, respectively. Apart from this fundamentals, numerous overtone and combination peaks are found from the spectral data which contributes to the huge line density shown under the spectral envelope of all S_1, S_2 and S_3 states of PFP.

We note that coupled states matrix diagonalization calculations were also attempted. The results could not be converged because of the huge computational overheads and are not discussed here. The low-lying vibronic energy levels resulting from the uncoupled state calculations for phenol and PFP are given in Tables 6.12 and 6.13 respectively. In case of phenol the vibronic energies are compared with the vacuum ultraviolet experimental data [63]. The assignments given in the tables are confirmed with a thorough analysis of the vibronic wavefunctions as discussed above. We assign the energy levels in terms of the irreducible representation of vibrational modes of C_s symmetry point group.

The results presented above show that the structured absorption band of the

S_1 state of PFP is quite in disagreement and that of phenol in close agreement to the experiment. In order to unravel the issue we carried out coupled S_1-S_2-S_3 states nuclear dynamics study for both phenol and PFP. The coupled states Hamiltonian developed in Sec. 6.2.2 is employed for the purpose and the calculations are carried out by propagating wave packets employing the MCTDH suite of program [60]. All vibrational modes marked with asterisk in Table 6.4 and 6.5 are included in the calculations. It is stated in the introduction that the signature of the optically dark $^1\pi\sigma^*$ states is not found in the experimental spectrum of phenol. Whereas in case of PFP they appeared as hump like structures. Therefore, although optically dark, the strong vibronic mixing with the bright $^1\pi\pi^*$ state makes the transition sufficiently allowed to be probed in the experiment. Therefore in the theoretical calculations although the initial transition to the $^1\pi\sigma^*$ states of phenol need not be considered, they become important to include to derive the observed band structure of PFP. Within the framework of Condon approximation contribution of three states to the overall band structure is treated equal and also with the weights extracted from the relative height of the peaks of the experimental spectrum. In either case the main results remain the same.

In the following calculations are therefore carried out for an initial excitation of the wave packet corresponding to the reference ground state (taken as a direct product of vibrational wave functions) to the S_1, S_2 and S_3 state separately. After this initial excitation, the wave packet in each case is propagated for 200 fs in the coupled manifold of electronic states. This yields autocorrelation function upto 400 fs [59, 64]. The autocorrelation function from three calculations are combined in case of PFP, damped with an exponential function ($e^{-t/\tau}$, $\tau = 44$ fs)

and Fourier transformed to generate the spectral envelope. The numerical details of the calculations are given in Table 6.11.

The results obtained from the above calculations are plotted in Fig. 6.7 for phenol and PFP in panel a and c, respectively. The experimental results are reproduced from Ref. [30] and shown in panel b and d, respectively. It can be seen that in both cases the experimental results compare well with the theoretically calculated ones. When compared with the uncoupled state spectrum (cf. Fig.6.4) it confirms that the electronic nonadiabatic interactions have profound impact on the overall vibronic structure of the electronic absorption band of PFP. The four hump like structures appearing at $\sim$ 223 nm, $\sim$ 228 nm, $\sim$ 233 nm and $\sim$ 260 nm are in good agreement with their location at $\sim$ 223 nm, $\sim$ 232 nm, $\sim$ 242 nm and $\sim$ 260 nm observed in the experiment. In contrary, sharp peaks appear in the absorption band of phenol (cf. Fig. 6.7 (a and b)) revealing weak nonadiabatic $^1\pi\pi^*$ - $^1\pi\sigma^*$ coupling effects although these states are vertically $\sim$ 0.7 eV apart. It can be seen from Table 6.8 that the interstate coupling strengths in phenol are much weaker as compared to PFP. The peak maxima appearing at $\sim$ 261 nm, $\sim$ 268 nm and $\sim$ 275 nm in case of phenol compare well with their location found in the experimental spectrum at $\sim$ 262 nm, $\sim$ 268 nm and $\sim$ 275 nm, respectively.

To this end we note that the spectra reported above are calculated within the constant transition dipole approximation. While this approximation could be well justified in case of phenol in which the states are well separated and are weakly coupled, it would be worthwhile to ensure the validity of this approximation in case of PFP. Understandably, the consideration of equal weights or their determination from the experimental spectrum is qualitative only to arrive at a

Table 6.10: The number of HO (Harmonic Oscillator) basis functions along with the vibrational modes and the dimension of the secular matrix used in the calculation of the uncoupled stick vibronic spectra presented in various figures in the text.

Molecule	State	Vibrational modes	No. of HO basis	Dimension of secular matrix	Lanczos iteration	Figure(s)
Phenol	S_1	ν_1, ν_7,ν_8,ν_9,ν_{13},ν_{14},ν_{15} ν_{18}, ν_{19},ν_{20},ν_{22},ν_{23}	3,3,3,4,7,3,3, 7,8,9,6,3	61725888	10000	Fig. 4(a)
	S_2	ν_1, ν_7,ν_8,ν_9,ν_{13},ν_{14},ν_{15} ν_{18}, ν_{19},ν_{20},ν_{22},ν_{23}	5,5,8,4,7,4,4, 2,3,2,12,3	38707200	10000	Fig. 4(a)
	S_3	ν_1, ν_7,ν_8,ν_9,ν_{13},ν_{14},ν_{15} ν_{18}, ν_{19},ν_{20},ν_{22},ν_{23}	3,4,5,2,5,4,6, 2,3,3,12,3	9331200	10000	Fig. 4(a)
PFP	S_1	ν_1, ν_2,ν_5,ν_6,ν_7,ν_8,ν_{16} ν_{17}, ν_{18},ν_{21},ν_{22},ν_{23}	3,3,4,9,5,3,12, 5,4,3,4,4	55987200	10000	Fig. 4(b)
	S_2	ν_1, ν_2,ν_5,ν_6,ν_7,ν_8,ν_{16} ν_{17}, ν_{18},ν_{21},ν_{22},ν_{23}	3,9,3,3,3,3,4, 12,4,3,7,7	61725888	10000	Fig. 4(b)
	S_3	ν_1, ν_2,ν_5,ν_6,ν_7,ν_8,ν_{16} ν_{17}, ν_{18},ν_{21},ν_{22},ν_{23}	3,6,3,3,3,3,6, 10,4,3,8,7	58786560	10000	Fig. 4(b)

good representation of the experimental spectrum. A more quantitative study of this subject is beyond the scope of the present study and is deferred to a future publication.

Table 6.11: Normal mode combinations, sizes of the primitive and the single particle basis used in the WP propagation in the coupled three states dynamics of phenol and PFP using MCTDH program module

Molecule	Normal modes	SPF basis[a]	Primitive basis[b]	Figures
Phenol	ν_{22},ν_{20},ν_{19},ν_{18}	(8,8,8)	[12,11,10,10]	Fig. 5(a)
	ν_{13},ν_{8},ν_{15},ν_{31},ν_{33}	(7,7,7)	[8,6,5,7,7]	
	ν_{7},ν_{9},ν_{14},ν_{23}	(5,5,5)	[4,4,4,4]	
PFP	ν_{16},ν_{17},ν_{32},ν_{33}	(9,9,9)	[15,15,12,12]	Fig. 5(c)
	ν_{2},ν_{6},ν_{22},ν_{23},ν_{25}, ν_{29}	(7,7,7)	[10,10,10,9,9,8]	
	ν_{7},ν_{18},ν_{21},ν_{24},ν_{26}, ν_{30},ν_{31}	(5,5,5)	[6,7,7,6,7,6,6]	
	ν_{1},ν_{4},ν_{8},ν_{5},ν_{12}, ν_{13},ν_{27}	(4,4,4)	[5,5,6,5,5,5,5]	
	ν_{3},ν_{9},ν_{10},ν_{15},ν_{28}, ν_{20}	(3,3,3)	[4,4,4,4,5,5]	

[a]The SPF basis is the number of single particle functions used. The WP is propagated for a total of 200 fs to generate the spectrum, for both Fig. 5(a) and Fig. 5(c).

[b]The primitive basis is the number of Harmonic oscillator DVR functions for the relevant mode. The primitive basis for each particle is the product of one dimensional bases; e.g for particle 1 in the set for Fig. 5(a) contains 13200 functions and the full primitive basis (with all twelve modes) consists of a total of 39739392000 functions for a single electronic state. The dimension of the Hamiltonian matrix is 119218176000 for three coupled states. The above numbers for Fig. 5(c) read 32400, 5.59×10^{24} and 16.8×10^{24} in that order.

Table 6.12: Vibrational energy levels of the S_1 A' ($^1\pi\pi*$) electronic state of Phenol along with their assignment.

This work		Ref [63]		Ref [65]	
Energy (eV)	Assignment	Energy (eV)	Assignment	Energy (eV)	Assignment
4.508	0_0^0	4.508	0_0^0	4.507	0_0^0
-	-	-	-	4.512	$4_1^0\ 5_0^1$
-	-	4.513	?	4.513	$4_1^0\ \tau\mathrm{OH}_1^1$
-	-	4.548	$\tau\mathrm{OH}_1^1$	4.548	$\tau\mathrm{OH}_1^1$
-	-	-	-	4.554	$16a_0^2$
4.556	$\nu_{23_0^1}$	4.455	$18b_0^1$	4.556	$18b_0^1$
4.566	$\nu_{22_0^1}$	4.567	$6a_0^1$	4.567	$6a_0^1$
-	-	4.577	$6b_0^1$	-	-
4.606	$\nu_{23_0^2}$	4.601	$18b_0^2$	-	-
4.608	$\nu_{20_0^1}$	4.605	12_0^1	-	-
4.625	$\nu_{22_0^2}$	4.624	$6a_0^2$	-	-
4.632	$\nu_{19_0^1}$	4.626	$18a_0^1$	4.626	$18a_0^1$
4.635	$\nu_{18_0^1}$	4.636	$9a_0^1$	4.629	$9a_0^1$
-	-	4.649	$6b_0^2$	-	-
-	-	4.654	$18b_0^3$	-	-
4.655	$\nu_{14_0^1}$	-	-	-	-
4.655	$\nu_{15_0^1}$	-	-	-	-
4.665	$\nu_{13_0^1}$	4.666	$7a_0^1$	-	-
4.666	$\nu_{22_0^1}\ \nu_{20_0^1}$	4.683	$6a_0^1\ 12_0^2$	-	-
4.690	$\nu_{22_0^1}\ \nu_{19_0^1}$	-	-	-	-
4.693	$\nu_{9_0^1}$	-	-	-	-
4.693	$\nu_{22_0^1}\ \nu_{18_0^1}$	-	-	-	-
4.708	$\nu_{20_0^2}$	4.702	12_0^2	-	-
-	-	4.713	$6b_0^3$	-	-
4.714	$\nu_{8_0^1}$	-		-	-
4.715	$\nu_{7_0^1}$	-	-	-	-
4.723	$\nu_{22_0^1}\ \nu_{13_0^1}$	4.721	$6a_0^1\ 7a_0^1$	-	-
4.725	$\nu_{20_0^1}\ \nu_{22_0^2}$	-	-	-	-
4.732	$\nu_{20_0^1}\ \nu_{19_0^1}$	-	-	-	-
4.735	$\nu_{20_0^1}\ \nu_{18_0^1}$	-	-	-	-
4.749	$\nu_{19_0^1}\ \nu_{22_0^2}$	4.741	$12_0^1\ 6a_0^2$	-	-
4.753	$\nu_{18_0^1}\ \nu_{22_0^2}$	-	-	-	-
4.756	$\nu_{19_0^2}$	-	-	-	-
4.759	$\nu_{19_0^1}\ \nu_{18_0^1}$	-	-	-	-
4.763	$\nu_{18_0^2}$	4.763	$9a_0^2$	-	-
4.765	$\nu_{20_0^1}\ \nu_{13_0^1}$	-	-	-	-
4.765	$\nu_{22_0^1}\ \nu_{20_0^2}$	-	-	-	-
4.782	$\nu_{13_0^1}\ \nu_{22_0^2}$	4.781	$1_0^1\ 7a_0^1$ / $6a_0^2\ 7a_0^1$	4.781	$6a_0^2\ 7a_0^1$
4.789	$\nu_{19_0^1}\ \nu_{13_0^1}$	-	-	-	-
4.792	$\nu_{18_0^1}\ \nu_{13_0^1}$	-	-	-	-
4.793	$\nu_{22_0^1}\ \nu_{20_0^1}\ \nu_{18_0^1}$	4.798	12_0^3 / $6A_0^3\ 12_0^2$	-	-
4.817	$\nu_{22_0^1}\ \nu_{19_0^1}\ \nu_{18_0^1}$	-	-	-	-
-	-	4.818	$1_0^2\ 12_0^2$	-	-
4.822	$\nu_{13_0^2}$	4.822	$7a_0^2$	4.817	$7a_0^2$
4.825	$\nu_{22_0^2}\ \nu_{20_0^2}$	-	-		-
-	-	4.838	$6a_0^3\ 7a_0^1$		-
4.880	$\nu_{22_0^1}\ \nu_{13_0^2}$	4.877	$6a_0^1\ 7a_0^2$		-
-	-	4.896	12_0^4		-

Table 6.13: Vibrational energy levels of the S_1 A' ($^1\pi\pi*$), S_2 A''($^1\pi\sigma*$) and S_3 A'' ($^1\pi\sigma*$) electronic states of PFP along with their assignment.

S_1 A'		S_2 A''		S_3 A''	
Energy (eV)	Assignment	Energy (eV)	Assignment	Energy (eV)	Assignment
4.769	0_0^0	5.344	0_0^0	5.560	0_0^0
4.799	$\nu_{23_0}^1$	5.375	$\nu_{22_0}^1$	5.593	$\nu_{23_0}^1$
4.800	$\nu_{22_0}^1$	5.376	$\nu_{23_0}^1$	5.594	$\nu_{22_0}^1$
4.816	$\nu_{18_0}^1$	5.386	$\nu_{18_0}^1$	5.618	$\nu_{18_0}^1$
4.817	$\nu_{17_0}^1$	5.394	$\nu_{17_0}^1$	5.620	$\nu_{17_0}^1$
4.838	$\nu_{16_0}^1$	5.405	$\nu_{22_0}^2$	5.625	$\nu_{16_0}^1$
4.869	$\nu_{16_0}^1\ \nu_{23_0}^1$	5.406	$\nu_{22_0}^1\ \nu_{23_0}^1$	5.626	$\nu_{23_0}^2$
4.870	$\nu_{16_0}^1\ \nu_{22_0}^1$	5.407	$\nu_{23_0}^2$	5.627	$\nu_{23_0}^1\ \nu_{22_0}^1$
4.886	$\nu_{16_0}^1\ \nu_{18_0}^1$	5.410	$\nu_{16_0}^1$	5.628	$\nu_{22_0}^2$
4.886	$\nu_{16_0}^1\ \nu_{17_0}^1$	5.417	$\nu_{22_0}^1\ \nu_{18_0}^1$	5.652	$\nu_{18_0}^1\ \nu_{22_0}^1$
4.908	$\nu_{16_0}^2$	5.418	$\nu_{23_0}^1\ \nu_{18_0}^1$	5.653	$\nu_{17_0}^1\ \nu_{23_0}^1$
4.939	$\nu_{16_0}^2\ \nu_{23_0}^1$	5.425	$\nu_{22_0}^1\ \nu_{17_0}^1$	5.654	$\nu_{17_0}^1\ \nu_{22_0}^1$
4.939	$\nu_{16_0}^2\ \nu_{22_0}^1$	5.426	$\nu_{23_0}^1\ \nu_{17_0}^1$	5.659	$\nu_{16_0}^1\ \nu_{23_0}^1$
4.955	$\nu_{16_0}^2\ \nu_{18_0}^1$	5.436	$\nu_{18_0}^1\ \nu_{17_0}^1$	5.660	$\nu_{16_0}^1\ \nu_{22_0}^1$
4.956	$\nu_{16_0}^2\ \nu_{17_0}^1$	5.441	$\nu_{22_0}^1\ \nu_{16_0}^1$	5.678	$\nu_{17_0}^1\ \nu_{18_0}^1$
4.956	$\nu_{5_0}^1$	5.444	$\nu_{17_0}^2$	5.680	$\nu_{17_0}^2$
4.966	$\nu_{6_0}^1$	5.453	$\nu_{18_0}^1\ \nu_{16_0}^1$	5.685	$\nu_{16_0}^1\ \nu_{17_0}^1$
4.978	$\nu_{16_0}^3$	5.461	$\nu_{17_0}^1\ \nu_{16_0}^1$	5.686	$\nu_{23_0}^2\ \nu_{17_0}^1$
5.014	$\nu_{6_0}^1\ \nu_{17_0}^1$	5.474	$\nu_{17_0}^2\ \nu_{22_0}^1$	5.687	$\nu_{23_0}^1\ \nu_{22_0}^1\ \nu_{17_0}^1$
5.025	$\nu_{16_0}^3\ \nu_{18_0}^1$	5.475	$\nu_{17_0}^2\ \nu_{23_0}^1$	5.688	$\nu_{22_0}^2\ \nu_{17_0}^1$
5.026	$\nu_{16_0}^3\ \nu_{17_0}^1$	5.486	$\nu_{17_0}^2\ \nu_{18_0}^1$	5.713	$\nu_{23_0}^1\ \nu_{17_0}^2$
5.026	$\nu_{5_0}^1\ \nu_{16_0}^1$	5.494	$\nu_{17_0}^3$	5.714	$\nu_{22_0}^1\ \nu_{17_0}^2$
5.036	$\nu_{6_0}^1\ \nu_{16_0}^1$	5.510	$\nu_{5_0}^1$	5.719	$\nu_{23_0}^1\ \nu_{17_0}^1\ \nu_{16_0}^1$
5.077	$\nu_{7_0}^1$	5.517	$\nu_{2_0}^1$	5.720	$\nu_{22_0}^1\ \nu_{17_0}^1\ \nu_{16_0}^1$
5.083	$\nu_{6_0}^1\ \nu_{16_0}^1\ \nu_{18_0}^1$	5.540	$\nu_{5_0}^1\ \nu_{22_0}^1$	5.738	$\nu_{18_0}^1\ \nu_{17_0}^2$
5.084	$\nu_{6_0}^1\ \nu_{16_0}^1\ \nu_{17_0}^1$	5.541	$\nu_{5_0}^1\ \nu_{23_0}^1$	5.740	$\nu_{17_0}^3$
5.106	$\nu_{6_0}^1\ \nu_{16_0}^2$	5.542	$\nu_{7_0}^1$	5.746	$\nu_{17_0}^2\ \nu_{16_0}^1$
5.147	$\nu_{7_0}^1\ \nu_{16_0}^1$	5.552	$\nu_{5_0}^1\ \nu_{18_0}^1$	5.800	$\nu_{2_0}^1$
5.154	$\nu_{6_0}^1\ \nu_{16_0}^2\ \nu_{17_0}^1$	5.573	$\nu_{7_0}^1\ \nu_{22_0}^1$	5.833	$\nu_{2_0}^1\ \nu_{23_0}^1$
5.164	$\nu_{6_0}^2$	5.574	$\nu_{7_0}^1\ \nu_{23_0}^1$	5.834	$\nu_{2_0}^1\ \nu_{22_0}^1$
5.175	$\nu_{6_0}^1\ \nu_{16_0}^3$	5.585	$\nu_{7_0}^1\ \nu_{18_0}^1$	5.860	$\nu_{2_0}^1\ \nu_{17_0}^1$
5.223	$\nu_{6_0}^1\ \nu_{16_0}^3\ \nu_{17_0}^1$	5.592	$\nu_{7_0}^1\ \nu_{17_0}^1$	5.867	$\nu_{2_0}^1\ \nu_{16_0}^1$
5.234	$\nu_{6_0}^2\ \nu_{16_0}^1$	5.623	$\nu_{7_0}^1\ \nu_{17_0}^1\ \nu_{22_0}^1$	5.894	$\nu_{2_0}^1\ \nu_{22_0}^1\ \nu_{17_0}^1$
5.303	$\nu_{6_0}^2\ \nu_{16_0}^2$	5.624	$\nu_{7_0}^1\ \nu_{17_0}^1\ \nu_{23_0}^1$	5.920	$\nu_{2_0}^1\ \nu_{17_0}^2$
5.373	$\nu_{6_0}^2\ \nu_{16_0}^3$	5.642	$\nu_{7_0}^1\ \nu_{17_0}^2$	5.927	$\nu_{2_0}^1\ \nu_{17_0}^1\ \nu_{16_0}^1$

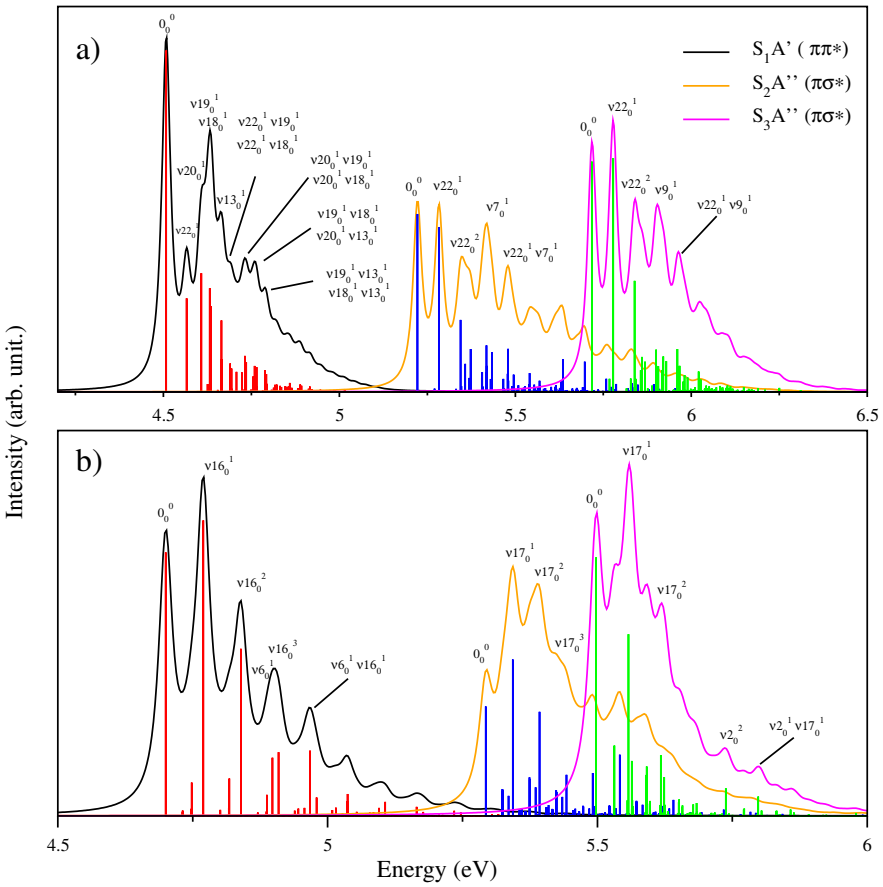

Figure 6.4: The stick vibronic spectrum and the convoluted envelope of the S_1, S_2, S_3 electronic state of phenol (panel a) and PFP (panel b) calculated with the a' vibrational modes (see the text for details). The intensity in arbitrary units is plotted as a function of the energy of the vibronic levels. The zero of energy corresponds to the equilibrium minimum energy of the reference electronic ground state.

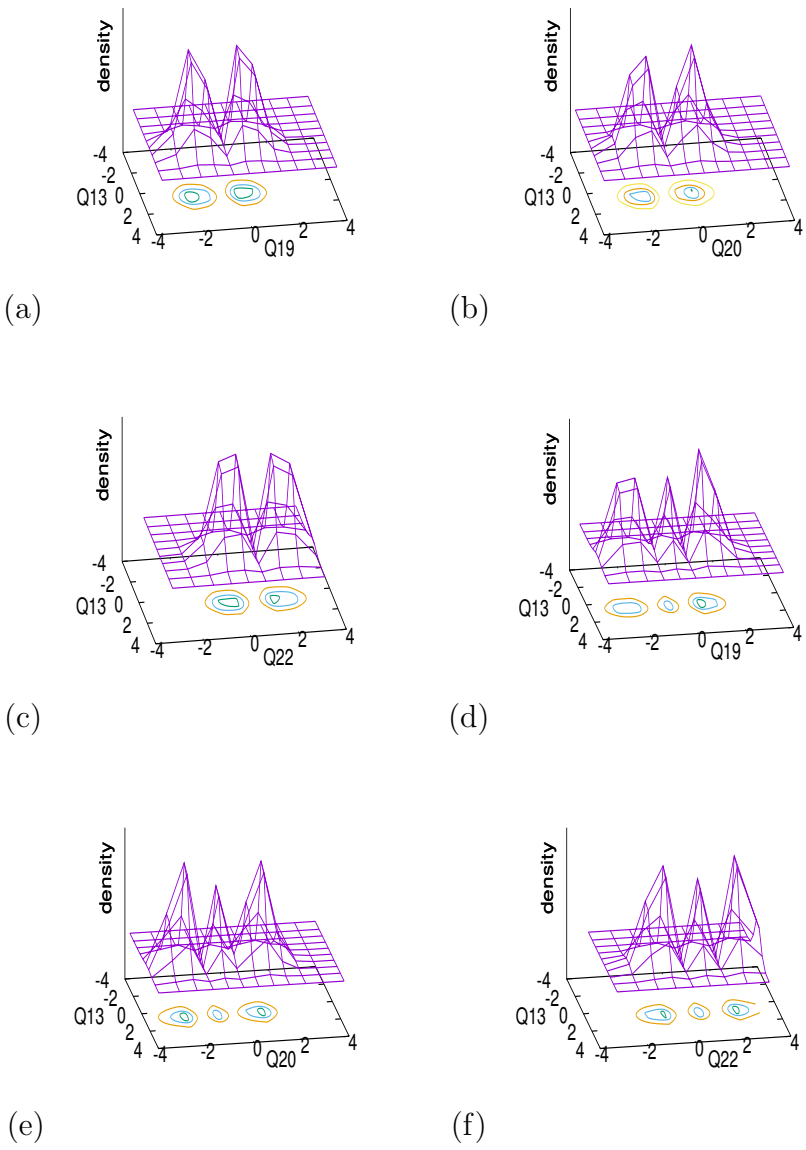

Figure 6.5: Probability density plots of the vibronic wavefunctions of the fundamental (panels a-c, respectively) and first overtone (panels d-f, respectively) of ν_{19}, ν_{20} and ν_{22} vibrational modes, respectively, appearing in the S_1 ($^1\pi\pi*$) state spectrum of Phenol. The wavefunctions in panels g-i represent the combination peak of $\nu_{19} + \nu_{20}$, $\nu_{19} + \nu_{22}$ and $\nu_{20} + \nu_{22}$, respectively.

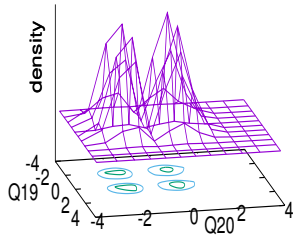

(g)

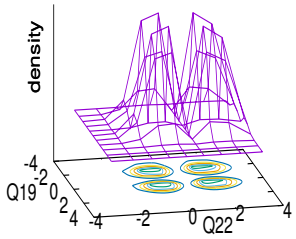

(h)

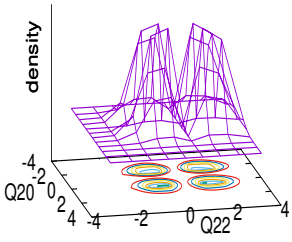

(i)

Figure 6.5: contd.

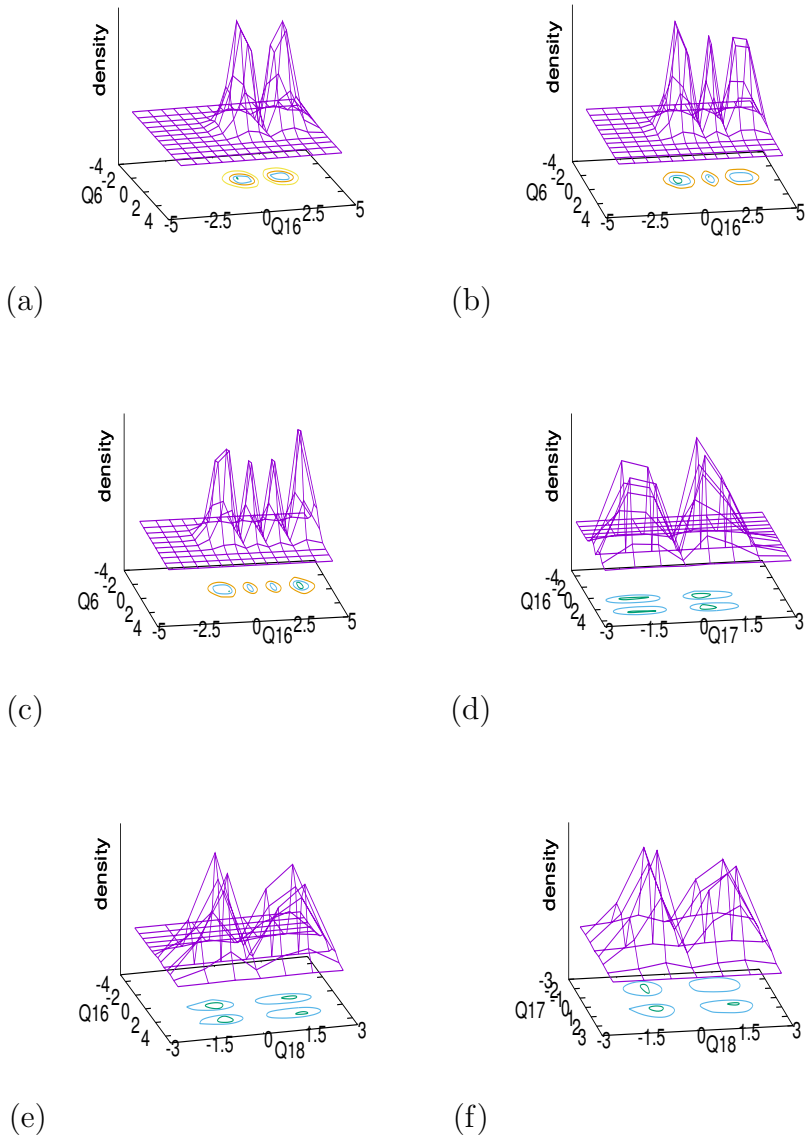

Figure 6.6: Probability density plots of the vibronic wavefunctions of the fundamental and first two overtones (in panels a, b and c) of the ν_{16} vibrational mode appearing in the S_1 ($^1\pi\pi*$) state spectrum of PFP. The wavefunctions in panels d-f represent the combination peak of ν_{16} + ν_{17}, ν_{16} + ν_{18} and ν_{17} + ν_{18}, respectively.

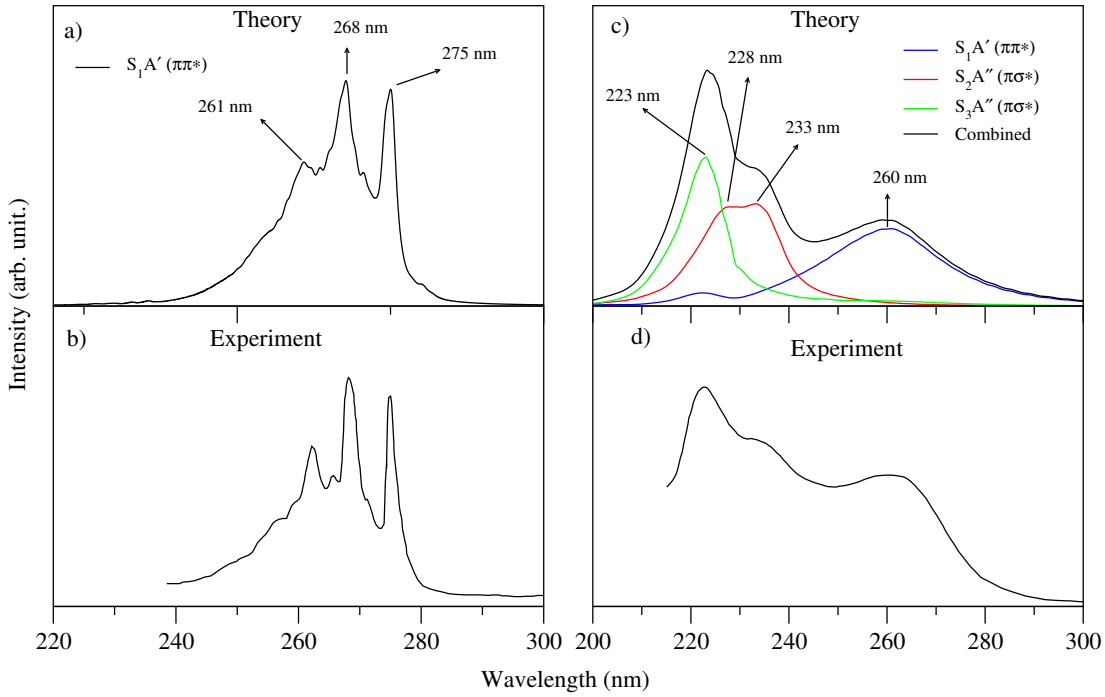

Figure 6.7: Electronic absorption spectrum of phenol and PFP compared with the latest experimental results of Ref. [30]. The spectral profiles are calculated by the wave packet propagation method implemented in the MCTDH program module [57–60]. The intensity in arbitrary units is plotted as a function of the energy of the final vibronic state (in terms of the wavelength).

6.3.3 Electronic Population

In order to unravel further details on the photophysical behavior of phenol and PFP we have examined the time-dependence of diabatic electronic populations in the S_1-S_2-S_3 coupled states dynamics. The results are plotted in Figs. 6.8(a-b). The results of panel a are obtained for an initial excitation of the wave packet to the first excited $^1\pi\pi^*$ state of phenol. The time-dependence of populations of the three electronic states are shown by different color lines and mentioned in the legend. It can be seen from panel a that very little population flows to the

optically dark $^1\pi\sigma^*$ states and the wave packet essentially remains on the optically bright $^1\pi\pi^*$ state in this case. Therefore, the latter state is the dominant emitting state in phenol. This finding convincingly explains the large quantum yield of fluorescence observed in the experimental recording [30] as the transition is optically allowed in this case. Furthermore, the equilibrium geometry of the $^1\pi\pi^*$ state of phenol converges to C_s symmetry point group and essentially remains the same as the ground (S_0) state equilibrium geometry in the coordinate space. This leads to a small Stoke's shift in the fluorescence emission spectrum as observed in the experiment [30].

Contrary to the above, the time-dependence of the electronic population in the S_1-S_2-S_3 coupled state dynamics for an initial excitation to the S_1 state of PFP plotted in panel b shows significant difference. In this case large amount of population flows to the optically dark $^1\pi\sigma^*$ states. This population flow from $^1\pi\pi^*$ to the $^1\pi\sigma^*$ states takes place at a relatively short time. Thereafter, the population remains essentially constant in all three states. Because of the energetic proximity of states (cf. Fig. 6.8) small population flows back and forth among three states (as indicated by the oscillations in the population curves) during the entire period of the dynamics. The initial decay of population of the S_1 ($^1\pi\pi^*$) state of PFP relates to a decay rate of $\sim$ 52 fs. It can be seen from Fig. 6.8b that at longer times the population of optically bright $^1\pi\pi^*$ state saturates at a value of $\sim$ 0.6. On the other hand the combined population of the optically dark $^1\pi\sigma^*$ states reaches a value $\sim$ 0.4. We also carried out five coupled states calculations in case of PFP by including two more excited states S_4 ($^1\pi\pi*$) and S_5 ($^1\pi\sigma*$). While we did not find any significant impact of these states on the broad band spectral profile given in Fig. 6.7, they show quite some impact on the

population dynamics. The latter results are presented in the inset of panel b of Fig. 6.8. It can be seen from the inset that the S_1 ($^1\pi\pi*$) state decays faster and about 50% population is transferred to the other states. More population flows to the optically dark $^1\pi\sigma*$ state in this situation. Owing to a strong nonadiabatic coupling and vibronic mixing the latter states become partially optically allowed and contributes to the fluorescence emission. As a large fraction of the electronic population moves to the $^1\pi\sigma^*$ state of PFP the intensity of the emission drastically reduces as compared to that of phenol.

It is worth recalling that strong coupling between states in PFP, causes a significant distortion of the equilibrium geometry of its first $^1\pi\pi^*$ state. The minimum of the latter shifts to a out-of-plane configuration, as confirmed by the present CASSCF calculations and also discussed in the literature [30]. In order to illustrate further, the potential energy curves of the lowest $^1\pi\pi^*$ and $^1\pi\sigma^*$ states are plotted along strong coupling out-of-plane bending modes ν_{32} and ν_{33} and are shown in panel a and b of Fig. 9. It can be seen that strong repulsion between the states breaks the equilibrium symmetry and shifts the minimum of the states at distorted nuclear configurations. Large Stoke's shift observed in the fluorescence emission spectrum in the experiment [30] can be attributed to this observation. Eventually, emission in this case will be followed by intramolecular vibrational redistribution. Furthermore, the double well shape of the S_1 state of PFP also implies strong repulsion between the states and strong nonadiabatic coupling as discussed above. Significant distortion of the equilibrium geometry and the double well shape of the potential are expected to affect the VEE of the S_1 state for which the experimental absorption maximum may not be a good estimate as already noted in Table 6.3.

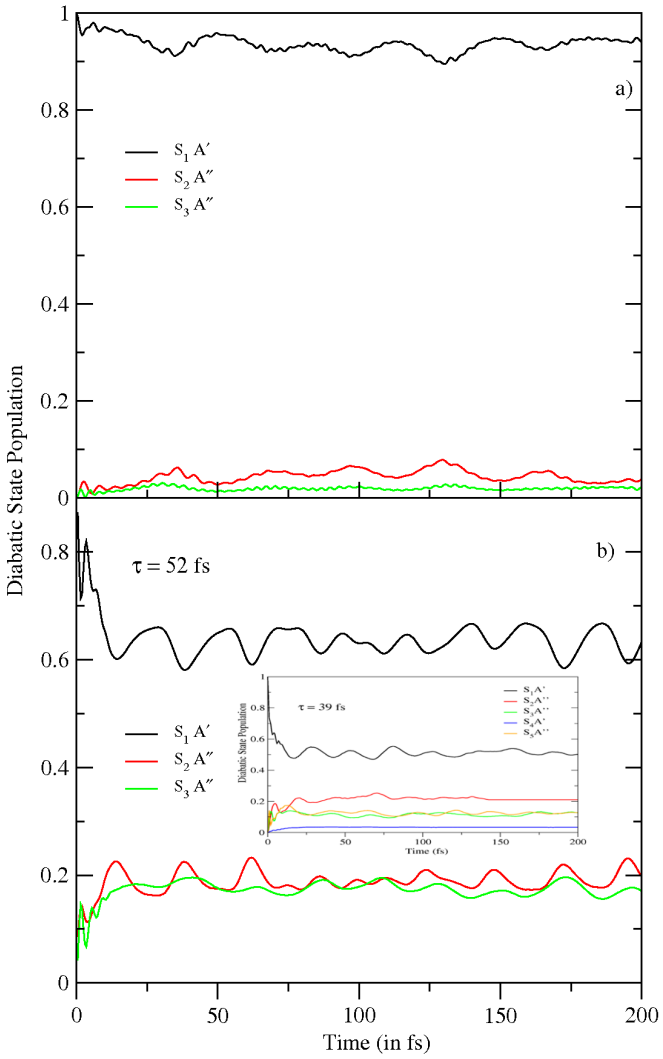

Figure 6.8: Time-dependence of diabatic electronic populations in the S_1-S_2-S_3 coupled states nuclear dynamics of phenol (panel a) and PFP (panel b). The initial wave packet is located on the S_1 state of both molecules. The population obtained in a five coupled state calculations in case of PFP is presented as an inset in panel b (see text for details).

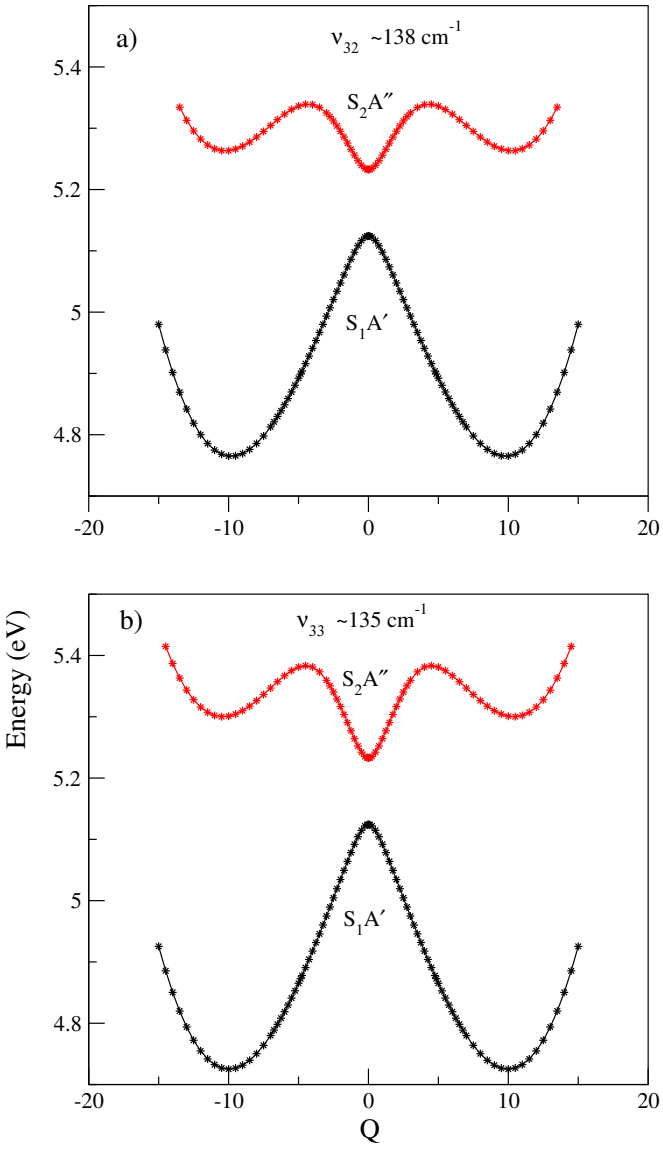

Figure 6.9: Adiabatic potential energies of the S_1 A' and S_2 A'' electronic states of PFP along the normal coordinates of the nontotally symmetric vibrational modes ν_{32} and ν_{33} shown in panel a and b, respectively. The energies computed *ab initio* and their fitting are shown by points and lines, respectively.

6.4 Summarizing Remarks

A detailed theoretical study is carried out to elucidate the role of optically dark $^1\pi\sigma^*$ state on the vibronic structure and dynamics of optically bright $^1\pi\pi^*$ state of phenol and PFP. The potential energy surfaces of the lowest three electronic excited states and their coupling surfaces of each species are calculated by *ab initio* EOM-CCSD method. In the spirit of general approach [1] vibronic Hamiltonians are constructed in a diabatic electronic basis and in terms of dimensionless normal coordinates of vibrational modes. The nuclear dynamics calculations are carried out both by the time-independent matrix diagonalization as well as wave packet propagation methods.

The results show that the low-lying $^1\pi\sigma^*$ states of PFP have predominant C-F σ^* character in contrast to O-H σ^* character of the $^1\pi\sigma^*$ states of phenol. Substitution of F atom lowers the energy of C-F σ^* orbitals and as a result the $^1\pi\sigma^*$ states become energetically very close to the $^1\pi\pi^*$ state in PFP. Strong vibronic coupling between $^1\pi\pi^*$ - $^1\pi\sigma^*$ states in PFP causes a complete loss of structure of its optical absorption band. The latter, calculated theoretically, is in very good accord with the recent experimental recording [30]. Furthermore, reduced dimensional results of resolved vibronic line spectrum of the three electronic states of both the molecules are assigned and the results in case of phenol are compared with the high-resolution VUV recording available in the literature. It is found that while about $\sim$ 10% electron population flows to the $^1\pi\sigma^*$ states in phenol, about $\sim$ 50% population flows to the $^1\pi\sigma^*$ states of PFP when the dynamics is started on the $^1\pi\pi^*$ state. Therefore while the optically bright $^1\pi\pi^*$ state is the major emitting state in phenol, in case of PFP the optically dark $^1\pi\sigma^*$ states equally compete. This reduces the intensity of the fluorescence emission spectrum

of PFP as compared to that of phenol observed in the experiment. Furthermore, both $^1\pi\pi^*$ and $^1\pi\sigma^*$ states of PFP undergoes large geometrical distortion and the emission takes place from this distorted configurations. Emission would be followed by intramolecular vibrational redistribution in this case. This causes a large Stoke's shift observed in the fluorescence emission spectrum of PFP [30]. The geometrical distortions and strong interactions between the states in PFP result into highly asymmetric nature of its absorption bands. The theoretically calculated vertical excitation energies therefore significantly differ from their experimental estimate based on the absorption band maximum in this case.

References

[1] H. Köppel, W. Domcke and L. S. Cederbaum, Adv. Chem. Phys, **57**, 59 (1984) and references therein.

[2] I. B. Bersuker and V. Z. Polinger, *Vibronic Interactions in Molecules and Crystals* Springer-Verlag, Berlin, 1989.

[3] M. Born and J. R. Oppenheimer, Ann. Phys. (Leipzig) **389**, 457 (1927).

[4] *Conical Intersections: Electronic Structure, Dynamics and Spectroscopy*, Eds. by W. Domcke, D. R. Yarkony, and H. Köppel, (World Scientific, Singapore, 2004).

[5] *Conical Intersections: Theory, Computation and Experiment*, Eds. W. Domcke, D. R. Yarkony and H. Köppel, (World Scientific Singapore, 2011).

[6] W. Domcke and D. R. Yarkony, Ann. Rev. Phys. Chem, **63**, 325-352 (2012).

[7] G. A.Worth and L. S. Cederbaum, Ann. Rev. Phys. Chem, **55**, 127 (2004).

[8] S. Mahapatra, Int. Rev. Phys. Chem **23**,483 (2004); Acc. Chem. Res. **42**, 1004 (2009).

[9] E. Gindensperger, I. Bâldea, J. Franz and H. Köppel, Chem. Phys. **338**, 207 (2007).

[10] S. Faraji and H. Köppel, J. Chem. Phys. **129**, 074310 (2008).

[11] T. Mondal and S. Mahapatra, J. Chem. Phys. **133**, 084304 (2010).

[12] T. Mondal and S. Mahapatra, J. Chem. Phys. **133**, 084305 (2010).

[13] T. Mondal, S. R. Reddy and S. Mahapatra, J. Chem. Phys. **137**, 054311 (2012).

[14] T. Mondal and S. Mahapatra, Phys. Chem. Chem. Phys. **11**, 10867 (2009).

[15] J. G. Philis, T. Mondal and S. Mahapatra, Chem. Phys. Lett. **495**, 187 (2010).

[16] C. R. Brundle, M. B. Robin and N. A. Kuebler, J. Am. Chem. Soc. **94**, 1466 (1972).

[17] M. Z. Zgierski, T. Fujiwara and E. C. Lim, J. Chem. Phys. **122**, 144312 (2005).

[18] J. G. Philis, A. Bolovinos, G. Andritsopoulos, E. Pantos and P. Tsekeris, J. Phys. B: At. Mol. Phys., **14**, 3621 (1981).

[19] A. L. Sobolewski and W. Domcke, Chem. Phys. **259**, 181 (2000).

[20] A. L. Sobolewski, W. Domcke, C. Dedonder-Lardeux and C. Jouvet, Phys. Chem. Chem Phys. **4**, 1093 (2002).

[21] M. N. R. Ashfold, B. Cronin, A. L. Devine, R. N. Dixon and M. G. D. Nix, Science. **312**, 1637 (2006).

[22] Z. Lan, W. Domcke, V. Vallet, A. L. Sobolewski and S. Mahapatra, J. Chem. Phys. **122**, 224315 (2005).

[23] O. P. J. Vieuxmaire, Z. Lan, A. L. Sobolewski, and W. Domcke, J. Chem. Phys. **129**, 224307 (2008).

[24] V. Vallet, Z. Lan, S. Mahapatra, A. L. Sobolewski and W. Domcke, Faraday Discussions. **127**, 283 (2004).

[25] M. Sala, *Quantum Dynamics and Laser Control for Photochemistry*, Springer International Publishing, Cham. 87, (2016).

[26] M. Sala, B. Lasorne, F. Gatti and S. Guerin, Phys. Chem. Chem. Phys. **16**, 15957 (2014).

[27] J.-K. Lee, T. Fujiwara, W. G. Kofron, M. Z. Zgierski and E. C. Lim, J. Chem. Phys. **128**, 164512 (2008).

[28] C.-M. Tseng, Y. T. Lee and C.-K. Ni, J. Chem. Phys. **121**, 2459 (2004).

[29] G. L. Loper and E. K. C. Lee, Chem. Phys. Lett. **13**, 140 (1972).

[30] S. Karmakar, D. P. Mukhopadhyay and T. Chakraborty, J. Chem. Phys. **142**, 184303 (2015).

[31] H. Studzinski, S. Zhang, Y. Wang and F. Temps, J. Chem. Phys. **128**, 164314 (2008).

[32] D. V. O'Connor, M. Sumitani, J. M. Morris and K. Yoshihara, Chem. Phys. Lett. **93**, 350 (1982).

[33] D. Phillips, J. Chem. Phys. **46**, 4679 (1967).

[34] S. Schumm, M. Gerhards and K. Kleinermanns, J. Phys. Chem. A **104**, 10648 (2000).

[35] R. J. Lipert, G. Bermudez and S. D. Colson, J. Phys. Chem. **92**, 3801 (1988) .

[36] G. Berden, W. L. Meerts, M. Schmitt and K. Kleinermanns, J. Chem. Phys. **104**, 972 (1996).

[37] C. Ratzer, J. Kpper, D. Spangenberg and M. Schmitt, Chem. Phys. **283**, 153 (2002).

[38] G. Grabner, G. Koehler, J. Zechner and N. Getoff, J. Phys. Chem. **84**, 3000 (1980).

[39] W. Domcke and A. L. Sobolewski, Science, **302**, 1693 (2003).

[40] C.-M. Tseng, Y. T. Lee, M.-F. Lin, C.-K. Ni, S.-Y. Liu, Y.-P. Lee, Z. F. Xu and M. C. Lin, J. Phys. Chem. A, **111**, 9463 (2007).

[41] C. Xie, J. Ma, X. Zhu, D. R. Yarkony, D. Xie and H. Guo, J. Am. Chem. Soc. **138**, 7828 (2016).

[42] X. Xu, J. Zheng, K. R. Yang and D. G. Truhlar, J. Am. Chem. Soc. **136**, 16378 (2014).

[43] M. L. Hause, Y. H. Yoon, A. S. Case and F. F. Crim, J. Chem. Phys. **128**, 104307 (2008).

[44] Y. Yamada, T. Ebata, M. Kayano and N. Mikami, J. Chem. Phys. **120**, 7400 (2004).

[45] T. Ebata, A. Iwasaki and N. Mikami, J. Phys. Chem. A **104**, 7974 (2000).

[46] T. Ebata, N. Mizuochi, T. Watanabe and N. Mikami, J. Phys. Chem. **100**, 546 (1996).

[47] T. Ebata, M. Kayano, S. Sato and N. Mikami, J. Phys. Chem. A **105**, 8623 (2001).

[48] G. A. Pino, A. N. Oldani, E. Marceca, M. Fujii, S.-I. Ishiuchi, M. Miyazaki, M. Broquier, C. Dedonder and C. Jouvet, J. Chem. Phys. **133**, 124313 (2010).

[49] M. N. R. Ashfold, G. A. King, D. Murdock, M. G. D. Nix, T. A. A. Oliver and A. G. Sage, Phys. Chem. Chem. Phys. **12**, 1218 (2010).

[50] J. Han and F.-M. Tao, J. Phys. Chem. A **110**, 257 (2006).

[51] T. H. Dunning, Jr., J. Chem. Phys. **90**, 1007 (1989).

[52] M. J. Frisch, G. W. Trucks, H. B. Schlegel, G. E. Scuseria, M. A. Robb, J. R. Cheeseman, G. Scalmani, V. Barone, B. Mennucci, G. A. Petersson, H. Nakatsuji, M. Caricato, X. Li, H. P. Hratchian, A. F. Izmaylov, J. Bloino, G. Zheng, J. L. Sonnenberg, M. Hada, M. Ehara, K. Toyota, R. Fukuda, J.

Hasegawa, M. Ishida, T. Nakajima, Y. Honda, O. Kitao, H. Nakai, T. Vreven, J. A. Montgomery, J. E. Peralta, F. Ogliaro, M. Bearpark, J. J. Heyd, E. Brothers, K. N. Kudin, V. N. Staroverov, R. Kobayashi, J. Normand, K. Raghavachari, A. Rendell, J. C. Burant, S. S. Iyengar, J. Tomasi, M. Cossi, N. Rega, J. M. Millam, M. Klene, J. E. Knox, J. B. Cross, V. Bakken, C. Adamo, J. Jaramillo, R. Gomperts, R. E. Stratmann, O. Yazyev, A. J. Austin, R. Cammi, C. Pomelli, J. W. Ochterski, R. L. Martin, K. Morokuma, V. G. Zakrzewski, G. A. Voth, P. Salvador, J. J. Dannenberg, S. Dapprich, A. D. Daniels, Farkas, J. B. Foresman, J. V. Ortiz, J. Cioslowski and D. J. Fox, Gaussian 09, Revision C.01, Wallingford CT2010.

[53] E. B. Wilson, J. C. Decius and P. C. Cross, *Molecular Vibrations*, McGraw-Hill, New York 1955.

[54] H.-J. Werner, P. Knowles, G. Knizia, F. Manby, M. Schtz, P. Celani, T. Korona, R. Lindh, A. Mitrushenkov and G. Rauhut, in MOLPRO, version 2010.1, a package of ab initio programs, See http://www. molpro. net2010.

[55] W. Domcke, H. Köppel and L. S. Cederbaum, Mol. Phys. **43**, 851 (1981)

[56] J. K. Cullum and R. A. Willoughby, *Lanczos Algorithms for Large Symmetric Eigenvalue Computations Volumes I and II: Theory*, Birkhuser1985.

[57] M. H. Beck, A. Jckle, G. A. Worth and H. D. Meyer, Phys. Rep., **324**, 1 (2000).

[58] H. D. Meyer, U. Manthe and L. S. Cederbaum, Chem. Phys. Lett. **165**, 73 (1990).

[59] U. Manthe, H. D. Meyer and L. S. Cederbaum, J. Chem. Phys. **97**, 3199 (1992).

[60] Worth. G. A.; Beck. M. H.; Jäckle. A.; Meyer. H. -D. The mctdh package, Version 8.4, (2007), University of Heidelberg, Heidelberg, Geramny. See: http://mctdh.uni-hd.de.

[61] H. -D. Meyer, F. L. Quéré, C. Léonard; F. Gatti, Chem. Phys. **329**, 179 (2006).

[62] L. J. Doriol, F. Gatti, C. Iung, H. -D. Meyer, J. Chem. Phys. **129**, 224109 (2008).

[63] P. Limao-Vieira, D. Duflot, F. Ferreira da Silva, E. Lange, N. C. Jones, S. V. Hoffmann, M. A. Smialek, D. B. Jones and M. J. Brunger, J. Chem. Phys. **145**, 034302 (2016).

[64] V. Engel, Chem. Phys. Lett. **189**, 76 (1992).

[65] M. G. D. Nix, A. L. Devine, B. Cronin, R. N. Dixon and M. N. R. Ashfold, J. Chem. Phys. **125**, 133318 (2006).

[66] R. N. Dixon, Thomas A. A. Oliver, and Michael N. R. Ashfold, J. Chem. Phys. **134**, 194303 (2011).

[67] B. Jones, G. B. da Silva, R. F. C. Neves, H. V. Duque, L. Chiari, E. M. de Oliveira, M. C. A. Lopes, R. F. da Costa, M. T. d. N. Varella, M. H. F. Bettega, M. A. P. Lima and M. J. Brunger, J. Chem. Phys. **141**, 074314 (2014).

[68] J. Lorentzon, P. Malmqvist, M. Fülscher and B. O. Roos, Theoretica chimica acta, **91**, 91 (1995).

[69] H. D. Bist, J. C. D. Brand and D. R. Williams, J. Mol. Spectrosc. **21**, 76 (1966); *ibid.* **24**, 402 (1967); *ibid.* **24**, 413 (1967).

Chapter 7

Summary and outlook

A detailed description of the photoinduced nonadiabatic quantum dynamics on the coupled electronic states of polyatomic molecules, clusters and molecular radical cations is investigated theoretically in this thesis. The investigations are carried out with the aid of *ab initio* electronic structure calculations and quantum dynamical simulations of underlying nuclear motion. Clearly, the study of multimode molecular dynamics on the multistate coupled electronic surfaces reveals a challenging theoretical and computational problem. Several vibronic coupling models are developed to solve them. The most important result of VC is occurrence of conical intersections (CIs) in nonlinear molecules or Glancing intersections (GIs) in linear molecules of electronic states. Theoretical treatment of VC in polyatomic molecules becomes tedious. The essential simplifications are the assumptions of harmonic diabatic potentials and truncation of Taylor series (around the equilibrium geometry of the neutral molecule and along the dimensionless nuclear coordinates) in low-order. The typical spectroscopic effects of CIs (or Glancing intersections, GIs) have been identified. Photoabsorption spectra of neutral linear carbon clusters, C_{2n+1} (n=7-10), phenol and PFP and the

photoelectron spectra diacetylene radical cation are studied.

Structures and dynamics of the ten (including degeneracy) energetically closely lying electronic states ($^1\Sigma_u^+$, $^1\Delta_u$, $^1\Delta_g$, $^1\Pi_g$, $^1\Pi_u$ and $^1\Sigma_g^+$) of neutral bare linear carbon clusters, C_{2n+1}, (n=7-10) have been investigated to examine the photoabsorption spectrum of the corresponding clusters. It is found that all these clusters have linear chain structure at the equilibrium minimum of their electronic ground state and an excited state of $^1\Sigma_u^+$ term is strongly absorbing. There are states of Π_g, Π_u, Δ_g and Δ_u symmetry, in the immediate vicinity of the $^1\Sigma_u^+$ state, which are optically dark but gain intensity through vibronic coupling. Such a coupling scheme is developed in this chapter with the aid of the calculated *ab initio* quantum chemistry results. A detailed theoretical account of the multimode RT and PRT interactions in some selected electronic states of linear C_{2n+1}, where n=7-10 cluster is presented in this chapter to elucidate the lifetimes of its excited electronic state of $^1\Sigma_u^+$ term. The vibronic Hamiltonian is constructed in a diabatic electronic basis, including the RT coupling within the degenerate $^1\Pi_g$ and $^1\Pi_u$ electronic states and the PRT couplings of these RT split states with the nondegenerate $^1\Sigma_u^+$ and $^1\Sigma_g^+$ electronic states of C_{2n+1}, where n=7-10. The RT effect in the $^1\Pi_g$ and $^1\Pi_u$ electronic states of these clusters is found to be very weak. The PRT coupling between the $^1\Pi_g$ and $^1\Pi_u$ states dominates the RT coupling. Due to a clustering of the four excited states within $\sim$ 1.0 eV, the nonradiative processes are found to be dominanting in predicting the vibronic structure and the transfer of diabatic electronic population among these states. The initial decay of the diabatic population of $^1\Sigma_u^+$ state is estimated to be $\sim$76 fs for C_{15}, $\sim$64 fs for C_{17}, $\sim$189 fs for C_{19} and $\sim$337 fs for C_{21} which lie in the much anticipated range $\sim$70-200 fs. So, it is found that for linear odd numbered

carbon chains one particular excited electronic state ($^1\Sigma_u^+$) has a very high oscillator strength (f) value and their absorption also happens within the 400-800 nm range and the lifetime of the $^1\Sigma_u^+$ state is in the anticipated range. So these are likely to be a potential DIBs carrier.

In this thesis only odd numbered long carbon chains are investigated. As a continuation, one can study the even numbered carbon chains also which possesses $^3\Sigma_g^-$ ground electronic state term symbol. The present study is restricted to the vibronic coupling of electronic states with same spin multiplicities. It will be interesting to investigate VC for electronic states of different spin multiplicities and including the spin-orbit coupling in the VC models developed in this thesis. A detailed theoretical investigation can be done for linear silicon chains, like carbon chains, which are also proposed to be potential DIBs carrier.

Vibronic interactions in the $\widetilde{X}^2\Pi_g$ and $\widetilde{A}^2\Pi_u$ band system of diacetylene radical cation is theoretically investigated with the aid of *ab initio* quantum chemistry calculations, vibronic coupling theory and time-independent and time-dependent quantum dynamics methods. Both the RT coupling within the $\widetilde{X}$ and $\widetilde{A}$ states and also the coupling between them are considered and the impact of these couplings on the vibronic dynamics of each electronic state is carefully examined. It is found that the RT coupling within each $\widetilde{X}$ and $\widetilde{A}$ state is weak. However, this coupling triggers the excitation of degenerate vibrational modes within each electronic states. The pseudo-Jahn-Teller type of $\widetilde{X}$ - $\widetilde{A}$ coupling through the vibrational modes of σ_u^+ symmetry has, in particular, no effect on the dynamics. The nonadiabatic coupling among the two electronic states is quenched by the large energy separation, which leads to a sharp band structure of the two states.

The X $\rightarrow$ A transition in $C_4H_2^+$ do not occur very close to the DIB position at 506.9 nm. Our results are not in agreement with this.

Polyacetylenes are the building blocks for polycyclic aromatic hydrocarbons (PAHs). It would be useful to study the bond breaking and bond formation mechanism in these PAHs. Besides that, mono- or di- substituted fluoro-, methyl- or cyanide- derivatives are also proposed to be a DIBs carriers. A full theoretical calculations is also necessary for this systems.

A detailed theoretical study is carried out to elucidate the role of optically dark $^1\pi\sigma^*$ state on the vibronic structure and dynamics of optically bright $^1\pi\pi^*$ state of phenol and PFP. The results show that the low-lying $^1\pi\sigma^*$ states of PFP have predominant C-F σ^* character in contrast to the O-H σ^* character of phenol. Substitution of F atom lowers the energy of C-F σ^* orbitals and as a result the $^1\pi\sigma^*$ states become energetically very close to the $^1\pi\pi^*$ state in PFP. Strong vibronic coupling between $^1\pi\pi^*$ - $^1\pi\sigma^*$ states in PFP causes a complete loss of structure in its optical absorption band. Furthermore, reduced dimensional results of resolved vibronic line spectrum of the three electronic states of both the molecules are assigned and the results in case of phenol are compared with the high-resolution VUV recording available in the literature. It is found that while about $\sim$ 10% electron population flows to the $^1\pi\sigma^*$ states in phenol, about $\sim$ 50% population flows in PFP when the dynamics is started on the $^1\pi\pi^*$ state. Therefore while the optically bright $^1\pi\pi^*$ state is the major emitting state in phenol, in case of PFP the optically dark $^1\pi\sigma^*$ states equally compete. This reduces the intensity of the fluorescence emission spectrum of PFP as compared to that of phenol observed in the experiment. Furthermore, both $^1\pi\pi^*$ and $^1\pi\sigma^*$

states of PFP undergoes large geometrical distortion and the emission takes place from this distorted configurations. Emission would be followed by intramolecular vibrational redistribution in this case. This is the reason behind a large Stoke's shift observed in the fluorescence emission spectrum of PFP.

This study can be further extended into the heterocyclic aromatic ring systems like pyridine, pentafluoropyridine etc.

Publications:

1. **Arpita Ghosh**, Samala Nagaprasad Reddy, S. Rajagopala Reddy, and S. Mahapatra*, "*Vibronic Coupling in the* $X^2\Pi_g$ – $A^2\Pi_u$ *Band System of Diacetylene Radical Cation*" *J. Phys. Chem. A*, **120**, 7881 (2016).

2. Karunamoy Rajak, **Arpita Ghosh** and S. Mahapatra*, "*Photophysics of phenol and pentafluorophenol: The role of nonadiabaticity in the optical transition to the lowest bright* $^1\pi\pi^*$ *state.* " *J. Chem. Phys.*, **148**, 054301 (2018).

3. **Arpita Ghosh**, S. Rajagopala Reddy and S. Mahapatra*, "*Electronic Spectroscopy of Carbon Clusters (*C_{2n+1}*, n=7-10). I. Quantum Chemistry* ". (Manuscript under preparation).

4. **Arpita Ghosh**, S. Rajagopala Reddy and S. Mahapatra*, "*Electronic Spectroscopy of Carbon Clusters (*C_{2n+1}*, n=7-10). II. Quantum Dynamics* ". (Manuscript under preparation).

5. Sabari Ghosh, Sathish Kumar Kurapati, **Arpita Ghosh**, Ankit Kumar Srivastava, and Samudranil Pal* "*Di-*μ*-acetato Diuranyl(VI) Complexes with N-(2-pyridyl)-N′-(5-R-salicylidene)hydrazines: Syntheses, Structures, Properties and Extraction Studies*". (Manuscript under revision).